



Measurement of Atmospheric Electricity During
Different Meteorological Conditions

Alec Bennett

A thesis submitted for the degree of Doctor of Philosophy

Department of Meteorology

July 2007

Declaration

I confirm that this is my own work and the use of all material from other sources has been properly and fully acknowledged.

Alec Bennett

Abstract

The Earth's atmosphere is continually electrified. Our understanding of the global atmospheric electrical circuit has improved since its discovery in the early twentieth century, although this area of geophysics still provides both theoretical and experimental scientific challenges. The variability of the electric field and current density measured at the surface is attributed to meteorological sources, both global and local in origin. By investigating the variability in electrical parameters under different atmospheric conditions, these global and local sources can be separated. As a consequence, information on global thunderstorm and shower cloud activity can be retrieved, which is of direct relevance to research on global climate change.

A historical review of the global atmospheric electric circuit concept is presented, which includes both theoretical and experimental development. A new high vertical-resolution vertical profile model is described for calculating the total electrical resistance of an atmospheric column during fair-weather conditions. This model incorporates the effect of cosmic and terrestrial sources of ion production with ion loss due to aerosol attachment and ion recombination. The sensitivity of surface measurements to columnar changes in ionisation rate, temperature and aerosol number concentration has been quantified using the model. Aerosol number concentration was identified as the dominant source of variability during fair-weather conditions.

Instruments based on an entirely new principle of measuring a fundamental electrical parameter; the air-Earth conduction current density, are developed and tested in a range of atmospheric conditions. Using these measurements, both global and local sources of electrical variability were identified, and the atmospheric conditions most favourable to measurement of the global circuit determined.

Surface electrical parameters were demonstrated to be sensitive to convective cloud, fog, rain and snow. A spectral "window" was identified where diurnal variability in surface electrical parameters were most likely to be dominated by global sources. The duration of this window ranged from 0-4UT during summer, to all day during the winter. A shallow boundary layer was found to be most favourable for global circuit monitoring using the air-Earth current density, with a deep, uniformly varying boundary layer preferred when using the surface electric field.

“There can be no doubt but the electric indications, when sufficiently studied, will be found important additions to our means for prognosticating the weather...”

Lord Kelvin, 1872

Acknowledgements

The Natural Environment Research Council provided the funding for this project, and I have also benefited from a C N Davies Award from The Aerosol Society. Firstly, I would like to thank my supervisor Giles Harrison for his enthusiasm, good humour and invaluable guidance, which greatly contributed to my enjoyment of this project. I am also indebted to all the technicians who cheerfully welded, soldered, fixed, assembled, cleaned, and installed all the numerous instruments this project involved, including the digging of an enormous pit on my request. I am especially grateful to Stephen Gill and Andrew Lomas for their patience, technical expertise and resisting the temptation to run upon seeing me enter the labs with yet another question.

My Monitoring Committee members Keith Shine and Robin Hogan provided support and kept me focussed, for which I am grateful. Robin Hogan and Martin Füllekrug offered helpful and perceptive comments on my thesis during my viva. I would like to thank the team at Chilbolton Observatory for allowing me to use their site and data, and Ewan O'Connor for generating the radar and lidar plots. I also acknowledge the data generously provided by Ferenc Märcz of the Hungarian Academy of Sciences.

I was fortunate to be a member of a social and friendly department during this project, of which I will retain fond memories, not least that of dressing as a giant goose for the departmental Christmas pantomime. I would particularly like to thank my fellow PhD students for providing support, sofas and good company.

My family and friends offered unreserved encouragement and support during my project, allowing me to retain motivation and perspective during challenging times. I thank them all. My brother Matt was particularly helpful in providing guidance in computer programming. Finally, I would like to thank Marie, who has been there for me throughout.

Contents

List of Figures	VIII
List of Tables	XIX
Nomenclature.....	XXI
1 Introduction	1
1.1 Historical overview	1
1.2 Motivation	2
1.3 The global atmospheric electric circuit	5
1.4 Measurement of current density	7
1.5 Thesis structure	8
2 Conceptual origins and measurement of the global atmospheric electric circuit	9
2.1 Introduction	9
2.2 The Carnegie cruises 1915-1921 (cruises 4,5 and 6).....	10
2.2.1 Cruise geographical details.....	11
2.2.2 Overview of measurements made during cruises IV-VI.....	12
2.2.3 Diurnal variation of the potential gradient measured by the Carnegie	13
2.3 The origin of the global circuit concept.....	13
2.4 Evidence for the global atmospheric electric circuit concept.....	15
2.4.1 Modern measurement of the global circuit	21
2.5 Modelling the global circuit.....	26
2.6 Solar activity and the global circuit	29
2.7 Measurement of the atmospheric conduction current density.....	34
2.7.1 Methods of displacement current density correction.....	36
2.7.2 Summary of J_C measurement methods.....	38
2.8 Discussion	40
3 Modelling the atmospheric electrical columnar resistance	42
3.1 Overview.....	42
3.2 General aspects of previously published columnar resistance models	45
3.3 Model outline	47
3.4 Model Assumptions.....	47
3.5 Model equations and processes.....	55
3.6 Comparison between modelled and observed profiles	66
3.6.1 Ionisation rate	66
3.6.2 Air conductivity.....	67
3.6.3 Aerosol profile.....	69
3.7 Model sensitivity.....	70
3.7.1 Aerosol	72
3.7.2 Ionisation rate	74

3.7.3	Temperature	77
3.8	Discussion	79
4	Instrumentation for atmospheric electrical research	81
4.1	Overview.....	81
4.2	Passive Wire (PW).....	81
4.2.1	Use of the PW to measure air conductivity.....	83
4.3	Field Mill (FM).....	86
4.4	Programmable Ion Mobility Spectrometer (PIMS)	91
4.4.1	Comparison of PIMS and PW derived total conductivity.....	93
4.5	The Air-Earth Current Pyramid (AECP).....	94
4.5.1	Requirements	94
4.5.2	The AECP current collector geometry.....	96
4.5.3	AECP collector insulation.....	99
4.5.4	AECP picoammeters.....	101
4.5.5	Initial results from the AECP	106
4.5.6	Modelling of J_C and J_D around the AECP	108
4.5.7	AECP insulator durability	112
4.6	The Geometrical Displacement and Conduction Current Sensor (GDACCS) ..	117
4.6.1	The GDACCS current collectors	118
4.6.2	The GDACCS collector insulation	120
4.6.3	Current source verification	123
4.6.4	Modelling the GDACCS distortion.....	126
4.6.5	Verification of GDACCS model parameters.....	128
4.6.6	Comparison between AECP and GDACCS measurements	131
4.6.7	Summary of the GDACCS	132
4.7	The Electric Potential gradient And Current (EPAC) Sensor	133
4.8	Discussion	133
5	Analysis of local atmospheric electrical parameters	135
5.1	Introduction.....	135
5.2	Operational times of RUAO atmospheric electrical instrumentation.....	135
5.3	RUAO atmospheric electrical annual mean climatology for 2006	137
5.3.1	Potential gradient (PG)	138
5.3.2	Air-Earth conduction current density (J_C).....	141
5.3.3	Measurement of the turbulent current density (J_T).....	144
5.3.4	Total conductivity (σ_T)	146
5.3.5	Small ion number concentration and mobility.....	149
5.4	RUAO atmospheric electrical diurnal and seasonal variations.....	151
5.4.1	Potential gradient (PG)	151

5.4.2	Air-Earth conduction current density (J_C).....	158
5.4.3	Total conductivity (σ_T)	161
5.5	Inter-comparison of atmospheric electrical parameters	166
5.6	Comparison between fair-weather atmospheric electrical and standard meteorological parameters	171
5.7	Disturbed-weather case studies	178
5.7.1	Fog	179
5.7.2	Convective cloud	184
5.7.3	Precipitation.....	191
5.8	Discussion	194
6	Observation of the global atmospheric electric circuit.....	195
6.1	Introduction	195
6.2	Diurnal variations of fair-weather PG and J_C at Lerwick.....	196
6.3	RUAO fair-weather PG and J_C diurnal cycles compared to those of the Carnegie 200	
6.4	Retrieval of global circuit diurnal variation from measurements made at a polluted site 207	
6.5	Simultaneous observations of PG at Reading, Durlston Head and Chilbolton. 215	
6.6	Comparison between RUAO and Nagycenk fair-weather PG.....	223
6.7	Discussion	229
7	Conclusions and suggestions for further work.....	231
7.1	Overview of studies completed	231
7.2	Summary of measurement findings.....	232
7.3	Summary of R_C model.....	233
7.4	Discussion of applicability of Ohm's Law.....	233
7.5	Insights into the global circuit	234
7.6	Further work.....	236
	Appendix A	238
	Appendix B	244
	References	245

List of Figures

Figure 1.1 Basic components of the global atmospheric electric circuit. The air-Earth current density (J_C) is denoted by the fair-weather current, and the columnar resistance (R_C) is shown as a combination of boundary layer and free tropospheric resistance. 6

Figure 2.1 Average diurnal variation of the potential gradient measured on cruises 4, 5 and 6 of the Carnegie, as percentage of the mean. This has become known as the “Carnegie curve”. 13

Figure 2.2 Comparison between average diurnal PG cycles from clean-air sites and estimated global thunderstorm area diurnal variation for the Northern Hemisphere summer, as a percentage of the mean from Whipple (1929). 15

Figure 2.3 Average diurnal variation of R_C of a 1cm^2 column from the surface to 4.57km with local time (from Sagalyn and Faucher, 1956). 17

Figure 2.4 Global thunderstorm frequency as measured by the annual number of days when thunder was heard using the WMO 1956 dataset (adapted from Krumm, 1962). 19

Figure 2.5 Estimated global (top line) and regional (Asia/Australia, Africa/Europe, America and Ocean (lowest line)) mean number of thunderstorms at 2-hour intervals in Universal Time from Krumm (1962). 19

Figure 2.6 Diurnal variation of thunderstorm area over the entire world (top line) and major land regions calculated by Whipple (1929) from Krumm (1962). 20

Figure 2.7 Cumulative global lightning flash frequency per 2.5° grid box as monitored by the satellite-based OTD (Optical Transient Detector) instrument between April 1995 and March 2000 (from Nickolaenko et al., 2006). 24

Figure 2.8 Comparison between the mean diurnal variation of global lightning flash number (April 1995 to March 2000) and the Carnegie curve (from Nickolaenko et al., 2006). 24

Figure 2.9 Percentage variation of daily mean J_C from the normal due to solar flares observed in Hawaii (Cobb, 1967). 30

Figure 2.10 The effect of a solar flare and Forbush decrease in air conductivity with (a) altitude and (b) latitude (Hays and Roble, 1979). The numbered lines in (a) represent measured conductivity profiles (see Hays and Roble (1979) for more detail on these observed profiles). 31

Figure 2.11 Modelled deviation of J_C and PG from the unperturbed condition as a result of the Forbush decrease in cosmic ray ionisation, as a function of colatitude along 72.5°E . (Sapkota and Varshneya, 1990). 33

Figure 3.1 Illustration showing atmospheric properties that are used by the vertical profile model in the calculation of columnar resistance. 45

Figure 3.2 Effect of aerosol charge on conductivity. Solid line represents the calculated mean aerosol particle charge (in elementary charge units, e) using equation (3.5) using the observations of mean atmospheric polar conductivity ratios of Woessner et al., (1958). The dashed line is the percentage increase in total conductivity resulting from the charged aerosol, relative to the conductivity for neutral aerosol, using the Gunn (1954) theory of ion-aerosol attachment for charged aerosol. The temperature was fixed at 273K. An aerosol effective radius of $0.05\mu\text{m}$ and $10,000\text{cm}^{-3}$ number concentration was used, with an ionisation rate of $10\text{cm}^{-3}\text{s}^{-1}$ to replicate near-surface conditions..... 50

Figure 3.3 Summary of the main inputs and outputs of the vertical profile model. 56

Figure 3.4 Schematic of model pre-processing steps at each level. The input values for each numbered step are identified by a square box, with the details on the governing equation described in later in this section..... 58

Figure 3.5 Schematic of model main processing steps at each level. Profiles from the pre-processing stage are outlined by a bold box, with the details on the governing equation described in later in this section. 59

Figure 3.6 Schematic of model post-processing steps, showing the final output parameters of columnar resistance (R_C), potential gradient (PG) and air-Earth conduction current density (J_C)..... 60

Figure 3.7 Modelled (dashed line) and measured (grey points) ionisation rate, scaled to standard surface atmospheric conditions to avoid the effect of air density change with height. A least-squares best-fit line for the measured points (solid line) is given for comparison to the model (Bennett and Harrison, 2006c)..... 67

Figure 3.8 Comparison between modelled and observed air conductivity profiles. Air conductivity data obtained during Gerdien's 30th August 1905 ascent over Berlin (Gerdien, 1905) is shown (squares). The solid and dashed lines are from the model, with a boundary layer surface aerosol concentration $N_{\text{OBL}} = 20,000$ and $N_{\text{OBL}} = 2,000$ particles per cm^3 respectively and $z_{\text{BL}} = 300\text{m}$. Both profiles have $N_{\text{OBG}} = 2300$ particles per cm^3 and $z_{\text{BG}} = 10,000\text{m}$, from Harrison and Bennett (2007a). 68

Figure 3.9 Model fit to conductivity expressions of Woessner et al. (1958). Geomagnetic latitude set at 50° , corresponding to the location of observations of Woessner et al. (1958). A best-fit aerosol profile of $N_{\text{OBL}} = 10,000\text{cm}^{-3}$, $z_{\text{BL}} = 500\text{m}$, $N_{\text{OBG}} = 1500\text{cm}^{-3}$ and $z_{\text{BG}} = 7,000\text{m}$ was used for the model. 69

Figure 3.10 Columnar resistance as a percentage of that at 50km ($223\text{P}\Omega\text{m}^2$), as a function of height from the surface to 25km, using typical parameters for an urban site at a geomagnetic latitude of 50°N , found in Table 3.4... 71

Figure 3.11 Sensitivity of R_C , J_C and PG at 1m to a doubling of boundary-layer aerosol number concentration N_{OBL} from $10,000\text{cm}^{-3}$ to $20,000\text{cm}^{-3}$, with varying boundary-layer scale height z_{BL} . Sensitivity corresponds to the magnitude of parameter change. 73

Figure 3.12 Aerosol number concentration (N) profiles used to calculate model sensitivities to change in N_{0BL} with varying z_{BL} , shown in Figure 3.11. The dashed and unbroken lines represent N for $N_{0BL}=10,000\text{cm}^{-3}$ and $20,000\text{cm}^{-3}$ respectively, both with a z_{BL} of 500m.	73
Figure 3.13 Sensitivity of R_C , J_C and PG at 1m to a doubling of terrestrial ionisation rate Q_0 from $8\text{cm}^{-3}\text{s}^{-1}$ to $16\text{cm}^{-3}\text{s}^{-1}$, with varying terrestrial ionisation scale height z_{si} . Sensitivity corresponds to the magnitude of parameter change.	75
Figure 3.14 Variation of R_C , J_C and PG at 1m to a change in cosmic ray ionisation rate q_C , relative to the standard q_C profile for 50°N using the equations of Makino and Ogawa (1985). R_C was truncated at 100% for clarity of presentation.....	77
Figure 3.15 Assumed air temperature profile for the model, using equations (3.18) to (3.20) and the coefficients.....	78
Figure 4.1 The Passive Wire (PW) installed on the RUAO 1m above the surface, showing main features. The horizontal wire was positioned 1m above the surface and was approximately 20m long. An identical support structure was at the far end of the instrument, except without the electrometer.	82
Figure 4.2 The thin wire used for the PW instrument shown in Figure 4.1, seen here emerging from the end of the insulator.....	83
Figure 4.3 PW potential measured simultaneously for wires at 0.5m, 1.0m, 2.0m and 2.85m above the surface, as well as output potential from a field mill system (From Barlow, 1999).....	83
Figure 4.4 PG from calibrated field mill (FM) and voltage on the passive wire (PW) after grounding, with modelled charging curve of theoretical equation (4.2) (from Bennett and Harrison, 2006a).	85
Figure 4.5 Total air conductivity derived from the best model fits using different lengths of the passive wire charging curve (from Bennett and Harrison, 2006a).....	86
Figure 4.6 Basic schematic of the constant capacitance-type field mill (from Chubb, 1990).	87
Figure 4.7 Laboratory test of FM to investigate effect of power supply voltage on FM output.....	88
Figure 4.8 The FM and support pole installed at the RUAO in part (a) and (b) the modelled distortion of potential and therefore PG around the earthed FM and pole itself. The black lines are lines of equipotential (starting with 20V near the surface and increasing in 20V intervals with height), with the filled colour representing the PG. The ambient PG was 100V/m (i.e. green). It can be seen that the presence of the 2m structure causes an increase in PG of more than a factor of two at the top of the FM, where the PG is sensed. The figure (b) was generated using Maxwell SV electrostatic modelling software,	

assuming the air has zero conductivity, with the surface and all objects being perfect conductors.	89
Figure 4.9 Raw output voltage of screened FM versus air temperature as five minute means between 2-6 February, 2007, with linear trend line.	90
Figure 4.10 Comparison between PG recorded by the PW at 1m above the ground and the FM at 2m during fair-weather (from Bennett and Harrison, 2006a), using the manufacturer's suggested calibration. The line of best fit was then used to calculate the actual FM calibration equation (4.3).	91
Figure 4.11 The Programmable Ion Mobility Spectrometer 2 (PIMS2) installed at the RUAO, with basic components labelled.....	92
Figure 4.12 Scatter plot of total conductivity derived from the PIMS and passive wire instruments (circles), compared to the line of unity gradient, indicating an exact agreement.....	94
Figure 4.13 The AECF installed at the RUAO. (a) identifies the two collectors and (b) describes the dimensions of the collectors. The pit required for the pyramid plate to be flush with the surface and not touching anything other than the insulated supports at the top pyramid corners is also shown. A separation of 0.1m was allowed between the BP and P collectors to avoid accidental bridging by water, blowing leaves, grass etc.....	99
Figure 4.14 PTFE insulators used to support the border (BP) and pyramid plate (P) collectors of the AECF. The BP was supported by eight vertical PTFE cylinders approximately 4cm high and approximately 1cm diameter, with conical tops to minimise the contact surface, reducing the probability of leakage currents. The P collector was supported by four cylinders approximately 16cm long and 26mm in diameter positioned on the corners of the pit. The blade-like edge of the P collector resulting from the requirement to weld the sides together meant that contact area was kept to a minimum as the collector rested only on its edges.	100
Figure 4.15 Circuit diagram for the picoammeters used in the AECF. (From University of Reading, Department of Meteorology electronics laboratory technical guide number 018-3, based on the designs of Harrison, 1997b). Component details are provided in Table 4.2.	102
Figure 4.16 The picoammeters used for the AECF. Part (a) identifies the large value feedback resistor (R3) and smoothing capacitor of the picoammeter input stage within the circuit, and part (b) shows the two picoammeters housed in the AECF logging box, connected to the two collecting plates.....	104
Figure 4.17 Calibration of the picoammeters using a Keithly 6512 electrometer to measure current generated by a voltage source and 10G Ω resistor. The equation for the line of best-fit (using the least squares method) is given for the two picoammeters (PA1 and PA2).....	105

Figure 4.18 Five-minute mean current measured by the border plate (BP) and pyramid plate (P) as well as Potential gradient (PG) using a field mill 2m from the AECF, 28 January 2006. From Bennett and Harrison (2006b).....	106
Figure 4.19 Scatter plot of field mill-derived displacement current calculated using equation (4.8) versus displacement current derived from AECF geometrical measurements and equation (4.7). Points are one-minute values between 01-10 UT 28 January 2006. From Bennett and Harrison (2006b).....	108
Figure 4.20 Vertical cross section of modelled PG around the AECF. The ambient PG was modelled as 100V/m so the contour values represent the percentage of ambient PG around the instrument. An enhancement of ambient PG of approximately 25% is modelled for the surface of the BP collector, with a reduction in PG around the P collector.....	109
Figure 4.21 Gradients of 1Hz BP vs P current measurements for 5 minute intervals between 18UT 26 February and 03UT 27 February, 2006. During this time, the weather was fair and calm, with 1Hz current variation attributed to J_D	110
Figure 4.22 Vertical cross section of modelled PG vectors around the AECF. The direction of the conduction current J_C is parallel to these vectors (directed downward); with the line's length proportional to ion drift speed. Current remains vertical to the BP collector, verifying the assumption of a vertical current. Although current divergence is found within the P collector, the collector receives a near-vertical current.....	112
Figure 4.23 An example of leakage currents resulting from insulation water absorption on the border (BP) and pyramid (P) collecting plates of the AECF during times of high atmospheric relative humidity (RH). All measurements displayed as five-minute means.	114
Figure 4.24 The percentage increase in mass of a PTFE cylinder of length 159mm and diameter 26mm completely immersed in water (at room temperature). The observed increase (Obs) has been modelled using a power law trendline, indicating that the percentage mass increase is approximately related to the square root of immersion time. The starting mass was 117.40g.	115
Figure 4.25 Use of additional Sapphire ball and rod to reinforce the BP and P insulators respectively, whilst retaining minimal contact area with the collector surface.	116
Figure 4.26 Picture and dimensions of the GDACCS. The sensor installed at the RUAO is shown in part (a) and dimensions, including the positioning of the collector support and picoammeter below the plates, can be seen in part (b).	119
Figure 4.27 Design of the GDACCS combined collector support and current connection to the picoammeter, incorporating heated PTFE insulation. (a) shows the support mounted on the electronics housing box, with a cross-section of the support identifying the internal conducting rod shown in (b). The yellow tape shown at the base of the metal support was	

used as a temporary guard against bridging by water drops, until the surrounding shield was installed.	122
Figure 4.28 Results showing a strong linear relationship between one minute mean currents measured from the FP and CP collectors (green circles). The lack of similar variation once the FP collector is removed from the support is also shown (red crosses).	124
Figure 4.29 Modelled geometrical distortion of local electrical variables around the GDACCS. Part (a) shows the PG, in V/m, with contours at 10V/m intervals. Ambient (undisturbed) PG was set to 100V/m so the values displayed represent the percentage PG relative to ambient. Part (b) shows the electric field vectors, which J_c will flow parallel to. The length of the line represents its magnitude, with the line parallel to the vector direction (i.e. vertically downward above the GDACCS).....	126
Figure 4.30 Modelled mean PG as percentage of ambient on different sections of the CP collector. The mean PG for the whole collector was found to be approximately 95% of ambient.	127
Figure 4.31 Change in FP and CP current over one second resulting from 27 nearby lightning strikes (of both positive and negative polarity), during storms on different days in October and December 2006.....	128
Figure 4.32 Effect of high frequency noise induced on the support cylinder from the heating coils of the FP and CP collectors. Part (a) shows the high frequency nature of the noise, with a similar current change of amplitude approximately 5pA and frequency of 0.3Hz, registered by both picoammeters. Part (b) demonstrates that both picoammeters are measuring the same induced current, with a linear relationship that may be closely approximated as passing through the origin and with a unit gradient.	130
Figure 4.33 Comparison between five minute mean AECP and GDACCS derived J_c . (a) shows variation of the two J_c measurements during the time period, with (b) a scatter plot using the same values as (a) to quantifying this relationship. The correlation coefficient is shown to be 0.960, with the equation for the least squares best fit line also displayed. The error bars identify the estimated uncertainty based on a single measurement for each instrument.	131
Figure 5.1 Operational times of all atmospheric electrical instrumentation at the RUAO indicated by a solid line, from the start of this investigation in October 2004. In addition to previously described acronyms (chapter 4), SP refers to a Simple Plate sensor, initially used to measure air-Earth current density.....	136
Figure 5.2 Atmospheric electrical equipment of the RUAO on 12 July 2006. Only the FP collector of the GDACCS is shown as the CP collector was not installed at the indicted location until 14 July 2006.....	137

Figure 5.3 Histograms of: (a) hourly mean PG for 2006, in 5Vm^{-1} bins, from 8654 operational hours (98.8% of the total year), (b) standard deviation of the twelve five minute means used to calculate each hourly mean.	139
Figure 5.4 Periodogram of hourly mean PG between 1 May 2005 and 1 March 2007, with prominent cycles identified. Dashed line represents the 99% significance threshold amplitude for white noise.	141
Figure 5.5 Histogram of hourly mean J_C for 2006, derived from the AECP until 31 July, and GDACCS thereafter. The 4.2pAm^{-2} bin has been removed as difference of saturation outputs from the AECP collectors (BP and P) produce a spurious J_C of 4.1pAm^{-2} , which otherwise would appear as a large spike in the histogram.....	143
Figure 5.6 Periodogram of hourly mean fair-weather J_C between 1 January 2006 and 1 March 2007, with prominent cycles identified. Dashed line represents the 99% significance threshold amplitude for white noise.....	144
Figure 5.7 Equipment layout at the RUAO for J_T measurement during 15 June 2007....	145
Figure 5.8 Histogram of total conductivity (σ_T) from small ions for 2006. Any PIMS σ_T data below 2fSm^{-1} or above 20fSm^{-1} was considered spurious and excluded from the dataset.	147
Figure 5.9 Periodogram of hourly mean σ_T for 2006, with prominent cycles identified. Dashed line represents the 99% significance threshold amplitude for white noise.	148
Figure 5.10 Histograms of small ion (a) number concentration and (b) mobility for positive and negative ions during 2006.	150
Figure 5.11 Monthly mean fair weather PG recorded at the RUAO during 2006.....	152
Figure 5.12 (a) Annual mean diurnal cycle and (b) contour plot of monthly fair-weather PG diurnal variations for 2006.....	154
Figure 5.13 Monthly mean fair-weather (FW) PG for 2006, including standard deviation of hourly mean FW PG values observed during the month.	156
Figure 5.14 Standard deviation of the twelve five minute means that were used to calculate each hourly mean value for 2006, displayed as a function of time and day of year. The colour key was chosen to indicate times of typical and high PG sub-hourly variability.....	157
Figure 5.15 Mean diurnal cycle of five minute PG standard deviation within an hour for all PG measurements in 2006, including standard error bars.....	158
Figure 5.16 Seasonal mean diurnal variation of fair-weather J_C for 2006. Seasonal definitions are Winter (Dec,Jan,Feb), Spring (Mar-May) Summer (Jun-Aug) and Autumn (Sep-Nov). Standard error bars are included.....	159
Figure 5.17 Annual mean fair-weather J_C diurnal variation for 2006, including standard error.	160

Figure 5.18 Monthly mean fair-weather J_C and standard deviation of hourly measurements within the month. The grey line (August to December) represents measurements made by GDACCS.	161
Figure 5.19 Seasonal mean diurnal variation of σ_T during 2006. Months used were restricted to data availability (Table 5.4), with Winter (Feb), Spring (Mar, May), Summer (Jun, Jul) and Autumn (Sep, Oct, Nov). Standard error bars included.	162
Figure 5.20 Annual mean σ_T diurnal cycle for 2006, including standard error bars.	163
Figure 5.21 Diurnal variation as percentage of mean for July 2006 of (a) total conductivity (TC), total small ion number concentration (n) and mean small ion mobility (μ). Diurnal variation of total conductivity (with axis reversed) and aerosol mass concentration for July 2006 are shown in (b).	165
Figure 5.22 Monthly mean σ_T and standard deviation of samples within the month, for 2006. Number of samples per month are provided in Table 5.4.	166
Figure 5.23 PG versus J_C for July 2006, as five minute means. Values were chosen when σ_T was approximately $\pm 5\%$ of the median, at $5\text{-}6\text{fSm}^{-1}$	168
Figure 5.24 Resistivity (σ_T^{-1}) versus PG for July 2006. Values were chosen when J_C was approximately $\pm 5\%$ of the median, at $2.7\text{-}2.9\text{pAm}^{-2}$. PG values are five minute means corresponding to the time of σ_T , which represents an average of approximately 18 minutes.	169
Figure 5.25 σ_T versus J_C for July 2006. Values were chosen when PG was approximately $\pm 5\%$ of the median, at $90\text{-}100\text{Vm}^{-1}$. J_C values are five minute means corresponding to the time of σ_T , which represents an average of approximately 18 minutes. R^2 value of 0.0004.	170
Figure 5.26 Mean diurnal variation of the standard meteorological parameters during July 2006, as a percentage of the mean. Standard error bars have been included for mean wind speed (U) and aerosol, but omitted from Tdry and RH due to their small size ($<1\%$).	174
Figure 5.27 Mean diurnal variation of atmospheric electrical parameters during July 2006, as a percentage of the mean. Standard error bars included.	174
Figure 5.28 Histogram of aerosol mass concentration measured at the RUAO by the Dust Trak instrument for July 2006, with the aerosol mass $<30\mu\text{gm}^{-3}$ corresponding to 54% of total aerosol samples highlighted.	177
Figure 5.29 PG at the RUAO before and after fog (identified by the difference in dry-bulb and dew point temperatures, Tdry and Tdew respectively). Measurements were made every second (Bennett and Harrison, 2007b).	180
Figure 5.30 (a) J_C and PG during three days of near-continuous fog at the RUAO between 19-21 December 2006, with (b) corresponding Tdry and RH. Values are five minute means.	181

Figure 5.31 Comparison of histograms during the foggy days of 19-21 December 2006 with the mean histogram for 2006 for (a) J_C and (b) PG.	182
Figure 5.32 (a) Temperature and PG and (b) J_C and voltage on the passive wire (PW) during the foggy days of 19-21 December 2006.	184
Figure 5.33 PG (as 1minute means) during the passage of convective clouds over the RUAO, separated by periods of fair-weather, between 1-2 April, 2006.	185
Figure 5.34 PG during positive and negative polarity lightning, near to (order 10km) the RUAO on 25 August, 2005.	186
Figure 5.35 Field mill measuring PG positioned approximately 100m from the Chilbolton cloud radar facility. Picture taken by Stephen Gill.	187
Figure 5.36 (b) PG (5min means) during the passage of an isolated shallow Cumulonimbus cloud identified by (a) the cloud radar reflectivity factor (the intensity of radar signal reflected from the cloud droplets) over the Chilbolton Observatory around midnight 17 November 2006.	188
Figure 5.37 (a) Schematic of the modelled charge distribution of an isolated Cumulonimbus cloud that passed over the RUAO on 28 July 2005, with (b) a comparison between modelled and observed PG at 1m. The x-axis "horizontal distance" represents the location of the cloud when PG observation began, found by converting the measurement times to distance, assuming a constant cloud speed of 8.3ms^{-1} (Bennett and Harrison, 2007b).	190
Figure 5.38 (b) PG (5min means) during the passage of a complex cloud structure identified by (a) the cloud radar reflectivity factor over the Chilbolton Observatory between 12UT on 19 and 12UT on 20 November 2006. The complexity was caused by the arrival of multiple fronts during this time, identified in (c), the section of UK Met. Office synoptic chart for midnight on 20 November 2006.	191
Figure 5.39 PG and accumulated rainfall amount at the RUAO during steady moderate rainfall (1030-1400UT) and heavy rain (1400-1500UT) on 22 September 2006. Data are five minute means.	192
Figure 5.40 PG and global shortwave solar radiation (S_g) during a snow shower between 15:30 and 15:33UT on 28 February 2006 (Bennett and Harrison, 2007b).	193
Figure 6.1 Comparison of mean diurnal PG measured at Lerwick during 1968-73 and that of the standard Carnegie curve (adapted from Harrison, 2003).	197
Figure 6.2 Difference between Lerwick and Carnegie PG diurnal variation, as a difference in percentage variation from their respective means.	198
Figure 6.3 Mean J_C diurnal variation for Lerwick between 1979-1983.	199
Figure 6.4 Difference in J_C and PG diurnal variations for Lerwick, between 1979-1983. Values expressed as a difference in percentage variation from their respective means.	200

Figure 6.5 Mean diurnal fair-weather PG for Reading (RUAO) during 2006 and the standard Carnegie curve, as a percentage of the mean.....	201
Figure 6.6 Difference between PG (as percentage of mean) for RUAO 2006 and Carnegie.....	202
Figure 6.7 Difference between percentage RUAO monthly mean fair-weather PG with the standard Carnegie curve, for each hour. Monthly means averaged between May 2005 and April 2007.....	202
Figure 6.8 Correlation of RUAO monthly mean fair-weather PG with the standard Carnegie curve. Monthly correlations averaged between May 2005 and April 2007.....	204
Figure 6.9 Five minute mean PG measured at the RUAO during 23 January 2006. The standard Carnegie curve is shown for comparison. Both data are shown as percentages of their respective means.....	205
Figure 6.10 Comparison of fair-weather J_C and PG mean diurnal variation for January 2007 and the mean November-January Carnegie curve (averaged over all cruises). The standard errors associated with the J_C and PG monthly means are ~2%.	206
Figure 6.11 Comparison of fair-weather J_C and PG mean diurnal variation for August 2006 and the mean August-October Carnegie curve (averaged over all cruises). The standard errors associated with the J_C and PG monthly means are ~2%.	207
Figure 6.12 Estimated diurnal variation of boundary layer height (z_{BL}) based on Dupont et al. (1999), including height error bars of $\pm 10\%$ of mean, with observed variation of surface aerosol mass concentration (assumed to be proportional to number concentration). The retrieved diurnal cycle of surface terrestrial ionisation rate from observed σ_T and N_{OBL} is also shown. All values are relative to their respective means.	211
Figure 6.13 Observed and modelled (a) J_C and (b) PG for July 2006 assuming no diurnal variation of V_I (i.e. the local component of modelled variability) as a percentage of their respective means.....	212
Figure 6.14 Retrieved V_I diurnal cycle based on J_C , PG and σ_T variability for July 2006, and the summer Carnegie curve. Error bars on V_I used to assess the uncertainty in boundary layer height at 06UT and 18UT are shown.	213
Figure 6.15 Difference between observed and modelled PG (relative to the mean) for July 2006, once the effect of aerosol and terrestrial ionisation rate variability is removed.....	214
Figure 6.16 Map of South East England showing location of the RUAO, Chilbolton Observatory and Durlston Head.....	216
Figure 6.17 Five minute mean fair-weather PG measured simultaneously at the RUAO and Durlston Head between 24-31 October 2006 (year days 297-304 respectively), showing (a) the PG with time and (b) a scatter plot comparing PG from the two sites... ..	218

Figure 6.18 Mean diurnal cycles for PG measured at the RUAO and Durlston Head between 24-31 October 2006, compared to the standard Carnegie curve. Values are expressed as a percentage of their respective means.....	219
Figure 6.19 (a) Scatter plot between five minute mean coincident fair-weather PG for the RUAO and Chilbolton Observatory between 1 November and 4 December 2006. (b) The mean fair-weather PG diurnal variation for the two sites and the standard Carnegie curve, as a percentage of their respective means.....	221
Figure 6.20 (a) PG measured at Chilbolton on 21 November 2006 compared to the Carnegie variation. Vertical scales have been adjusted to show the similarity in variation, although the magnitudes are different, with variability in Chilbolton PG about the mean being three times that of the Carnegie. The corresponding RHI radar reflectivity factor is shown in (b) identifying convective cloud as the source of rapid PG deviations from the Carnegie curve.....	222
Figure 6.21 Five minute mean fair-weather PG for the RUAO and Chilbolton Observatory during 21 November 2006.....	223
Figure 6.22 Mean fair-weather PG diurnal cycle for the RUAO and Nagycenk during (a) January 2006 and (b) August 2006.	224
Figure 6.23 Correlation of RUAO and Nagycenk monthly mean fair-weather PG diurnal cycles. Monthly correlations averaged between July 2005 and December 2006.	225
Figure 6.24 Difference in percentage RUAO and Nagycenk monthly mean fair-weather PG diurnal cycles. Monthly differences for each hour averaged between July 2005 and December 2006.	226
Figure 6.25 Mean fair-weather PG diurnal variation for the RUAO, Nagycenk and Chilbolton Observatory during November 2006, along with the standard Carnegie curve. Values are shown as a percentage of their respective means.....	227
Figure 6.26 Comparison between RUAO and Nagycenk fair-weather PG at 03UT between July 2005 and December 2006, as (a) a scatter plot and (b) over time, with the latter smoothed over 10 days.....	228

List of Tables

Table 2.1 Approximate minimum, mean and maximum values of the parameters measured during the Carnegie cruises IV, V and VI.....	12
Table 2.2 Comparison of basic global circuit model properties discussed in this section.	29
Table 2.3 Authors (and year of publication) of different methods of J_C measurement considered in this section.....	34
Table 2.4 Comparison of different methods to directly measure the conduction current density.	40
Table 3.1 Mean ion drift distance for aerosol (near-surface) and ion (upper atmosphere) dominant heights. The value of β is from Hoppel et al. (1986) and the ion-dominant mean n and α from Harrison and Carslaw (2003).	52
Table 3.2 Key to the abbreviations used in the model schematics.....	57
Table 3.3 Observations of PG and J_C with corresponding modelled aerosol profile variables as described in equation (3.13).	69
Table 3.4 Values of the coefficients used in the model R_C profile in Figure 3.10.....	70
Table 3.5 Coefficients used in equations (3.18) to (3.20) for the standard temperature profile of the model.....	77
Table 3.6 Percentage sensitivity of R_C , J_C and PG at 1m to atmospheric temperature change between 0-50km.....	78
Table 4.1 Results of the PW relaxation and PIMS methods of total conductivity measurement for different fair-weather days in summer 2006 (Bennett and Harrison, 2006a).....	94
Table 4.2 Components used for the picoammeter described in Figure 4.15. (From University of Reading, Department of Meteorology electronics laboratory technical guide number 018-3).	102
Table 5.1 Mean and standard deviation of J_T for samples made on different days, calculated from 4Hz measured PG gradient and vertical wind speed.....	146
Table 5.2 Summary statistics for atmospheric electrical parameters measured at the RUAO during 2006. J_C has been constrained to -5 to 10pAm ⁻² to remove suspected leakage values whilst containing the fair-weather distribution of Figure 5.5.....	151
Table 5.3 The standard error in monthly mean PG diurnal variation during 2006 (averaged over all hours), as shown in Figure 5.11.....	153
Table 5.4 Number of PIMS samples made during each month of 2006. Each sample represents a single PIMS measurement cycle, lasting approximately 18 minutes. Months in italics were not used for monthly statistics due to under/lack of sampling.....	161
Table 5.5 Results of the hypothesis testing for the validity of Ohm's Law in measured atmospheric electrical parameters at the RUAO during fair weather in July 2006.....	171

Table 5.6 Correlation coefficients and corresponding confidence levels for hourly mean surface fair-weather atmospheric electrical and standard meteorological parameters during 2006. Tdry is dry bulb temperature, RH is relative humidity, U is mean wind speed at 2m and aerosol represents the aerosol mass concentration measured by the Dust Trak instrument. A total of 512 coincident data points for each parameter was used.....	172
Table 5.7 Correlation coefficients and corresponding confidence levels for hourly mean standard meteorological parameters used to compare against PG, J_C and σ_T during 2006.	172
Table 5.8 Correlation coefficients and corresponding confidence levels for five minute mean surface fair-weather atmospheric electrical and standard meteorological parameters during July 2006. Tdry is dry bulb temperature, RH is relative humidity, U is mean wind speed at 2m and aerosol represents the aerosol mass concentration measured by the Dust Trak instrument. A total of 548 coincident data points for each parameter was used.	173
Table 5.9 Correlation between σ_T and isolated meteorological parameters for July 2006, with the remaining parameters set at a narrow range to limit their influence. These ranges were chosen to include the modal value, and were $20^\circ\text{C}<\text{Tdry}<22^\circ\text{C}$, $62\%<\text{RH}<67\%$, $2\text{ms}^{-1}<\text{U}<3\text{ms}^{-1}$ and $10\mu\text{gm}^{-3}<\text{aerosol}<15\mu\text{gm}^{-3}$	176
Table 5.10 Correlation coefficients for aerosol versus atmospheric electrical parameters during July 2006, using aerosol mass concentrations less than $30\mu\text{gm}^{-3}$. To test PG, J_C was kept between $2.2\text{-}2.4\text{pAm}^{-2}$ and σ_T between $5\text{-}6\text{fSm}^{-1}$	177
Table 5.11 Summary of significant (>95%) independent correlations (tick mark) for the atmospheric electrical and standard metrological parameters investigated. The sign of the correlation (+ or -) is displayed next to the tick mark.	178
Table 5.12 Modelled atmospheric electrical parameters due to a 100m deep layer of fog, relative to the values for fog-free conditions.	179
Table 6.1 Observed monthly mean fair-weather atmospheric electric parameters and dry-bulb temperature for July 2006.....	208
Table 6.2 Model parameters used to simulate the mean electrical conditions of July 2006.	209
Table 6.3 Modelled parameters and profiles that were kept constant and those with an assumed diurnal cycle.....	211
Table 6.4 Correlation coefficients for the mean diurnal variation of J_C , PG and retrieved V_i for July 2006.	215
Table 7.1 Summary of conditions most favourable to the observation of global circuit variability in surface measurements of J_C and PG at the RUAO.	235

Nomenclature

Symbol	Description	Units
α	Ion-ion recombination coefficient	cm^3s^{-1}
β	Ion-aerosol attachment coefficient	cm^3s^{-1}
$\overline{\beta}_0$	Mean ion-aerosol attachment coefficient for uncharged aerosol	cm^3s^{-1}
ϵ_0	Permittivity of free space	Fm^{-1}
μ	Mean ion mobility, $\mu = \frac{1}{2}(\mu_+ + \mu_-)$	$\text{cm}^2\text{V}^{-1}\text{s}^{-1}$
μ_+	Positive ion mobility	$\text{cm}^2\text{V}^{-1}\text{s}^{-1}$
μ_-	Negative ion mobility	$\text{cm}^2\text{V}^{-1}\text{s}^{-1}$
μ_0	Reference ion mobility at a specified temperature	$\text{cm}^2\text{V}^{-1}\text{s}^{-1}$
ρ	Total bipolar air electrical resistivity	Ωm
ρ_I	Ionic space charge density	cm^{-3}
ρ_{SC}	Total (ionic and aerosol) space-charge density	cm^{-3}
ρ_{air}	Air density	Kgm^{-3}
σ_T	Total bipolar air electrical conductivity	fSm^{-1}
σ_+	Positive air electrical conductivity	fSm^{-1}
σ_-	Negative air electrical conductivity	fSm^{-1}
τ	Electrical relaxation time of the air	s
C	Electrical capacitance	F
e	Ion (elementary) unit charge	C
E	Electric field	Vm^{-1}
F	Potential Gradient (when used in equations) where $F = -E$	Vm^{-1}
g	Gravitational acceleration	ms^{-2}
I_{BP}	Current from the border plate of the AECP	pA
I_{CP}	Current from the corrugated plate electrode of the GDACCS	pA
I_{FP}	Current from the flat plate electrode of the GDACCS	pA
I_{P}	Current from the pyramid plate of the AECP	pA
j	Mean number of elementary charges on aerosol particle	e
J_{C}	Conduction current density	pAm^{-2}
J_{D}	Displacement current density	pAm^{-2}
$J_{\text{D(FM)}}$	Displacement current density calculated by the field mill	pAm^{-2}
J_{P}	Precipitation current density	pAm^{-2}
J_{S}	Total air-Earth current density	pAm^{-2}
J_{T}	Turbulent current density	pAm^{-2}
k	Boltzmann's constant	JK^{-1}
m_+	Positive ionic mass	kg
m.	Negative ionic mass	kg

M	Molecular mass of air	kg
n_+	Positive ion number concentration	cm^{-3}
n_-	Negative ion number concentration	cm^{-3}
n	Total ion number concentration, $n = (n_+ + n_-)$	cm^{-3}
\bar{n}	Mean ion number concentration, $\bar{n} = \frac{1}{2}(n_+ + n_-)$	cm^{-3}
N	Aerosol number concentration	cm^{-3}
N_{OBG}	Background surface aerosol number concentration	cm^{-3}
N_{OBL}	Boundary layer aerosol number concentration	cm^{-3}
P	Air pressure	Pa
P_0	Reference atmospheric pressure	Pa
P_S	Air pressure at the surface	Pa
P_{SD}	Standard air pressure	Pa
PG	Potential Gradient (assigned F when in equation)	Vm^{-1}
q	Ion pair production rate	$\text{cm}^{-3}\text{s}^{-1}$
q_c	Cosmic ray component of the ionisation profile	$\text{cm}^{-3}\text{s}^{-1}$
q_L	Local ion pair production rate	$\text{cm}^{-3}\text{s}^{-1}$
Q_0	Surface-generated (terrestrial) ionisation rate	$\text{cm}^{-3}\text{s}^{-1}$
Q_a	Cosmic ionisation rate at the reference height	$\text{cm}^{-3}\text{s}^{-1}$
Q_{max}	Maximum cosmic ionisation rate	$\text{cm}^{-3}\text{s}^{-1}$
r	Ionic radius	m
r_a	Aerosol radius	m
R_C	Columnar resistance	$\text{P}\Omega\text{m}^2$
R_d	Gas constant for dry air	$\text{JK}^{-1}\text{mol}^{-1}$
S_a	Lower cosmic ionisation rate scale height	m
S_b	Upper cosmic ionisation rate scale height	m
S_{J_c}	Sensitivity of modelled air-Earth conduction current density	cm^3
S_{PG}	Sensitivity of modelled potential gradient	cm^3
S_{R_C}	Sensitivity of modelled columnar resistance	cm^3
t	Time	s
t_A	Ion-aerosol attachment timescale	s
t_R	Ion recombination timescale	s
T	Air temperature	K
T_0	Reference air temperature	K
T_S	Air temperature at the surface	K
T_{SD}	Standard air temperature	K
V_D	Mean ion drift velocity	ms^{-1}
V_I	Ionospheric potential	kV

y	y-intercept	pA
z	Height	m
z_a	Reference height of ionisation rate	m
z_{BG}	Background aerosol number concentration scale height	m
z_{BL}	Boundary layer aerosol number concentration scale height	m
z_{max}	Height of maximum cosmic ionisation rate	m
z_{si}	Surface-generated ionisation rate and scale height	m
z_{ST}	Height of the tropopause-stratosphere interface	m
z_{TP}	Height of the troposphere-tropopause interface	m
z_{VI}	Height of the ionospheric potential	m

Instrument Acronyms

AECP	Air-Earth Current Pyramid
BP	Border Plate electrode (of AECP)
CP	Corrugated Plate electrode (of GDACCS)
EPAC	Electric Potential And Current (sensor)
FM	Field Mill
FP	Flat Plate electrode (of GDACCS)
GDACCS	Geometrical Displacement And Conduction Current Sensor
P	Pyramid Plate electrode (of AECP)
PIMS	Programmable Ion Mobility Spectrometer
PW	Passive Wire
SP	Simple Plate
RUAO	Reading University Atmospheric Observatory

1 Introduction

This chapter gives a historical overview of key concepts in atmospheric electricity, and the motivation and objectives for this study. An introduction to fundamental concepts that will be investigated in more detail as part of this thesis will be provided. A guide to the thesis structure is also given.

1.1 Historical overview

Before more specific details on this study are provided, a brief historical introduction to key revelations in atmospheric electricity (to be discussed in more detail in chapter 2) is given in this section to introduce the general background of this area of research.

The quantitative study of atmospheric electricity in the UK began over 250 years ago, with detection of electric charge in a clear atmosphere reported by John Canton in 1753. From his experiments, Canton (1753) discovered that the air was generally positively charged with respect to the ground during fair-weather, with changes in this charge associated with different meteorological phenomena, such as precipitation and fog. The mid-nineteenth century marked an advancement of atmospheric electrical sensors, noticeably Lord Kelvin's "water dropper" electric field sensor. When combined with the newly-discovered method of photographic recording, the water-dropper allowed continuous measurement of the electric field at Kew Observatory, London in 1861 (Everett, 1868; Harrison and Aplin, 2002). The close connection between the electrical state of the atmosphere and changes in the weather provided motivation for continued study of atmospheric electricity. Lord Kelvin confidently predicted that electric field measurements were to eventually form a basis for weather forecasting (Thomson, 1872), and was reported as saying:

"There can be no doubt but the electric indications, when sufficiently studied, will be found important additions to our means for prognosticating the weather; and the speaker hoped soon to see the atmospheric electrometer generally adopted as a useful and convenient weather-glass."

Kelvin and previous researchers such as Canton observed a continuous and varying electric field in the atmosphere. The air was also known to be weakly electrically conductive from experiments by Gerdien (1905a), implying the presence of an atmospheric electrical current. A vertical current flowing through the electrically resistive atmosphere was considered to be the source of the fair weather electric field by the Nobel Prize winner C.T.R. Wilson in 1906. The concept of a global atmospheric electrical circuit

and the description of a new type of sensor capable of directly measuring this vertical current density, as well as the associated electric field, were given by Wilson (1906). The personal significance of this direct measurement of the air-Earth current density was recalled by Wilson in a later publication about his work (Wilson, 1960):

“I remember the satisfaction I had when my work led to the fulfilment of my dream of isolating a portion of the earth’s surface and measuring the charge upon it and the current flowing into it from the atmosphere.”

An additional motivation to investigate temporal patterns in atmospheric electricity measurements came later in the early twentieth century, with the discovery of a universal global diurnal variation in electric field. Careful measurements made in clear oceanic air during the 1915-1928 cruises of the geophysical research ship Carnegie, showed a distinct diurnal cycle that was independent of geographical location. This significant finding suggested a global source of diurnal variation of surface electric field. The global source was thought to directly relate to the intensity of global thunderstorm activity, as demonstrated by Whipple (1929), who found the shape and phase of the observed cycle to be closely related to the estimated diurnal variation of global thunderstorm area with universal time.

A global signal in surface atmospheric electric field measurements (thereafter called the Carnegie curve) was further evidence for the suggestion originally proposed before the cruises by Wilson (1906), that the diurnal variation of the electric current and field had global origins, visible when local meteorological influences were low. Wilson’s air-Earth current density has since been recognised as the most fundamental electrical parameter of the global electric circuit that can be measured at the surface (e.g. Chalmers (1967), Dolezalek (1978)).

1.2 Motivation

Climate-global circuit interaction

A modern motivation for the study of atmospheric electricity is to determine what extent the global electric circuit is a forcing effect on climate. The global circuit provides a physical link between solar and geophysical change with the Earth’s climate, through the effect of the air-Earth current density on cloud microphysics¹, although further research is

¹ Hadley Centre Technical Note HCTN 62 (January 2005), Met Office, UK

required to understand the exact mechanisms involved. Evaluating the importance of this link requires detailed observations, analysis and modelling of electrical properties.

Global thunderstorm and shower cloud activity is considered the primary source of the global circuit, as discussed in more detail in the next section. A feedback of the global circuit-climate interaction exists as increased global surface temperature is expected to cause an increase in convection and therefore global thunderstorm activity (Williams, 1992), with associated enhancements of the global circuit. Measurement of the intensity of this circuit may therefore provide insight into global climate change (Markson, 2007), providing the only method of global climate monitoring to use a single point on the Earth's surface.

Aerosol concentration

Atmospheric electrical quantities are sensitive to aerosol. If the electrical parameters are known for a site, information on the aerosol concentration can be retrieved (although further research is required to quantify the electrical-aerosol relationships sufficiently for general acceptance by the scientific community). As highlighted by the International Panel on Climate Change (IPCC) a large contribution ($\sim\pm 50\%$) of the uncertainty in the radiative forcing of climate models is due to inadequate knowledge in the areas of chemical and microphysical properties of anthropogenic aerosol and their interaction with cloud, as well as their geographical and vertical distribution (IPCC Working Group I Report, 1995). Measurement of atmospheric electricity may provide a further method of studying global aerosol profiles as well as improving the understanding of aerosol-cloud interactions, as the charge associated with atmospheric electrical processes is expected to modify aerosol-cloud microphysics and affect the formation of clouds. Although satellite and surface-based optical methods of aerosol profile retrievals provide estimates of aerosol radiative properties, they do not provide information on the ultrafine particle spectrum, unlike atmospheric electrical methods.

A general motivation for study of the global circuit is therefore a better understanding of the extent of climate forcing through interaction of the air-Earth current density with cloud microphysics (Harrison, 2004c). In order that this can be achieved, detailed measurements of surface electrical parameters and how they can be used to monitor the global circuit are required. The variability of these parameters results from local and global sources, so it is crucial that a method of separation of these sources is found.

The objectives of this project are to provide detailed measurements of surface atmospheric electrical parameters for analysis, and separate their observed variability into that due to local and global sources.

Thesis objectives

A list of key thesis objectives is now provided. These will address the requirements for detailed atmospheric electrical measurements and their use in monitoring of the global circuit.

- *Measurement of atmospheric electrical parameters at the surface during different meteorological conditions, including the design and operation of new sensors.*

This will form the dataset which will be analysed during this study. As sensors such as those used for air-Earth current density measurement are not commercially available, they will need to be constructed to specific requirements for accuracy and durability, as discussed in chapter 4.

- *Separation and analysis of observed local and global effects on electrical variability at the surface.*

As variability attributed to both local and global sources provides information on separate local meteorological and global climatological phenomena, separation of these two signals in the relevant surface atmospheric electrical measurements is necessary for analysis, which is provided in chapters 5 and 6. The separation will be made using both model simulation and direct measurements, including simultaneous observation at different sites that are sufficiently horizontally displaced to exceed the expected length scale of local variability sources.

- *Modelling the influence of the local atmospheric column on fair-weather atmospheric electricity.*

As surface atmospheric electrical measurements are a function of many processes both locally and in the atmospheric column above, my approach will be to use a vertical profile model to explore the relative contributions of different sources to measured variability during fair-weather, and will be used to help distinguish between local and global effects.

1.3 The global atmospheric electric circuit

The basic concept of the global atmospheric circuit is described in this section, with a review of the published literature provided in chapter 2. More detail can also be found in MacGorman and Rust (1998) which provides a brief overview of the basic principles of the global circuit and considers in detail atmospheric electrical characteristics during disturbed weather. Harrison (2004c) provides details on all aspects of the global electrical circuit, including historical instrumentation, observations and the proposed connection with climate.

Thunderstorms and shower clouds cause separation of electric charge between the ground and ionosphere, an electrically conductive layer about 60km above the surface (the term electrically conductive layer refers to a layer with sufficiently high conductivity compared to the lower (tropospheric) atmosphere to be considered a perfect conductor). This charge separation causes the ionosphere to have a potential (V_I) of approximately +300kV with respect to the surface. Ionisation from cosmic rays and terrestrial sources produce cluster ions (small ions) which make the atmosphere weakly electrically conductive. These ions flow vertically because of the vertical potential difference, causing the air-Earth conduction current density, J_C , of order 10^{-12} Am⁻². The total electrical resistance for a unit area of the atmospheric column from the surface to the ionosphere is called the columnar resistance, R_C . A schematic of the global circuit is given in Figure 1.1.

The ionosphere-earth potential difference (V_I), columnar resistance and conduction current are related by Ohms law,

$$V_I = J_C \cdot R_C \quad (1.1).$$

The physical units of R_C are Ωm^2 (or more commonly $\text{P}\Omega\text{m}^2$ due to the inherently large values). This is because R_C is the integral of resistivity (units Ωm) with height (equation (3.1)). V_I represents the electric potential of a layer at a height above the surface (the zero potential reference) so the units are in volts (usually quoted in kV).

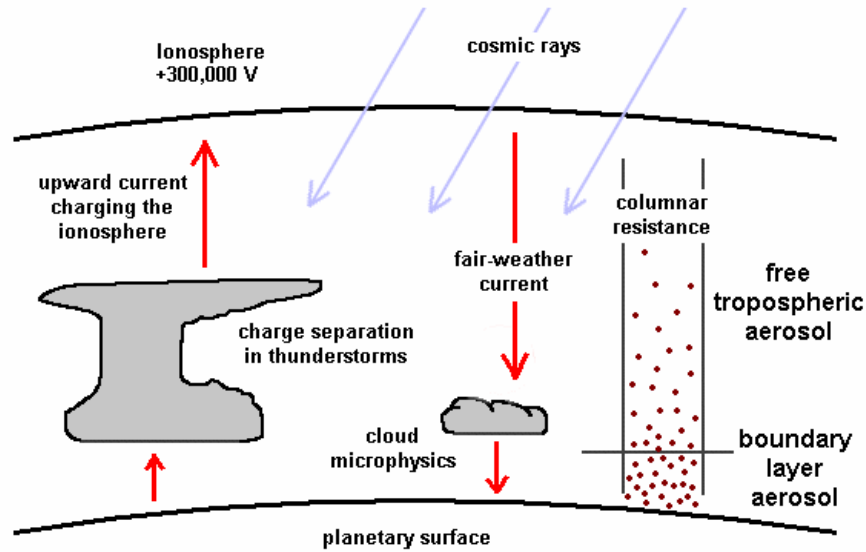


Figure 1.1 Basic components of the global atmospheric electric circuit. The air-Earth current density (J_C) is denoted by the fair-weather current, and the columnar resistance (R_C) is shown as a combination of boundary layer and free tropospheric resistance.

By convention, the electric field (E) is referred to as the potential gradient (F in equations, PG in text), defined as the negative of electric field:

$$F = -E \quad (1.2).$$

At the surface, the PG arises because of J_C flowing through the electrically conductive air. It is therefore J_C that is the parameter that permits the effect of the global circuit to be measured at the surface, either directly through measurement of J_C itself, or by PG. However, PG is also a function of the local air conductivity (σ_T). Away from sources of charge separation, the air conductivity (σ_T), potential gradient (F) and conduction current density are related by Ohm's Law:

$$F = \frac{J_C}{\sigma_T} \quad (1.3).$$

The atmosphere is positively charged with respect to the ground during fair weather. This produces a downward pointing (negative) electric field (E) so PG is positive for fair weather conditions from equation (1.2).

In the fair-weather part of the circuit, small ions dominate the charge transport since they have a large electrical mobility. Therefore an increase in small ion concentration will

increase the air conductivity by providing more charge carriers. Aerosol in the atmosphere removes small ions by attachment. An increase in aerosol number concentration therefore reduces the ion number concentration and decreases the air conductivity. A change in aerosol number concentration subsequently modifies the total columnar resistance (R_C) between the ionosphere and the surface, and therefore J_C directly through equation (1.1) and consequently has an indirect effect on PG through equation (1.3).

1.4 Measurement of current density

Of the quantities which can be measured at the surface, the air-Earth conduction current density (J_C) presents one of the most fundamental parameters of the global circuit (Chalmers, 1967). It is therefore of great importance in this study, with its continuous measurement being one of the aims of this thesis. A positive current density occurs when positive charge is moved downward. The conduction current density is one of several components contributing to the total current density, J_S , received by a horizontal conducting electrode at the earth's surface, electrically isolated from the ground. J_S comprises contributions from turbulence J_T , conduction J_C , displacement J_D and precipitation J_P ,

$$J_S = J_C + J_D + J_T + J_P \quad (1.4),$$

where J_C is the component flowing as a result of the global electric circuit (Rycroft et al. 2000). The displacement current density (J_D) is induced by changes in the PG. The turbulent current density (J_T) arises due to the transport of space charge by air turbulence. Charged precipitation falling on the electrode will also transfer a precipitation charge, J_P . The current density is considered positive if positive charge is brought from the atmosphere to the surface (or electrode to surface in the case of J_D).

As J_C is the contribution to J_S arising from the global atmospheric electric circuit, a distinction is required between this component and J_D , which is effectively a local source of noise. J_P is of course confined only to times of falling precipitation. A description of instrumentation to measure J_C (when the J_T and J_P components are negligible), and the methods used to separate J_D and J_C from the directly measured J_S are discussed in Chapters 2 and 4.

1.5 Thesis structure

In this thesis chapter 2 provides a review of the published literature regarding measurement of the conduction current density and the global circuit. Chapter 3 describes a vertical profile model used to simulate changes in fair-weather electrical parameters measured at the surface from variation of temperature, aerosol number concentration and ionisation rate profiles. The instrumentation used to measure atmospheric electric parameters is described in chapter 4. An electrical climatology of the observation site and observed variability of these parameters in the context of local meteorological effects are analysed in chapter 5. This chapter also includes an investigation into the validity of Ohm's Law during fair weather at the surface and in the atmospheric column. Observation of global circuit diurnal variability is given in chapter 6, including the use of the vertical profile model in retrieving global signals from surface electrical observations by accounting for local sources of variability. Conclusions and suggestions for further work resulting from this study are summarised in chapter 7.

2 Conceptual origins and measurement of the global atmospheric electric circuit

2.1 Introduction

The scientific study of atmospheric electricity began in the 18th century, with investigation into the electrical nature of thunderstorms such as that famously undertaken by Benjamin Franklin, producing a spark from his aerial apparatus in 1750. Realisation that the atmosphere was electrified even in fair weather was made by the French botanist and physicist L.G. Le Monnier (Watson, 1746) who reproduced Franklin's experiment with an aerial in 1752 (although he removed the grounding pole from the aerial and placed some dust particles near the apparatus to investigate electrostatic attraction). This positive atmospheric charge was also found by John Canton in 1753. Le Monnier later went on to demonstrate the clear-sky electrification of the atmosphere and the diurnal variation of atmospheric electricity, by observing changes in the electrostatic attraction of a suspended wire insulated from the ground and exposed to the atmosphere. The English physicist Benjamin Wilson visited Le Monnier in Paris in 1753, who stated in a letter to the President of the Royal Society:

“...he [Le Monnier] had great reason to believe the electric matter did not come from the earth at all, but from the air...”

B. Wilson, 1753

The regular diurnal variation of electric field found by Le Monnier was also found by the Italian physicist Giambatista Beccaria, (Beccaria, 1775). An advocate of the scientific ideas of Benjamin Franklin, Beccaria determined that the atmosphere was positively charged with respect to the Earth during fair weather in 1775. Ten years later the French physicist Charles Coulomb discovered that atmospheric air was not a perfect electrical insulator as previously thought, but was in fact weakly conductive. Unfortunately however, this aspect of his work was ignored at the time.

In the 1860s William Thomson (later Lord Kelvin) invented the water-dropping discharger (Thompson, 1910). With this instrument it was possible to transport charge induced by an insulated tube in equilibrium with the atmosphere on water droplets from a reservoir, being collected by a metal funnel that was connected to an electrometer. That way charge could be measured from a collector whilst still being electrically isolated from the ground, allowing the atmospheric potential (and therefore electric field, given a further reference

potential) to be determined. Kelvin recognised the necessity for regular recordings of atmospheric electricity, preferably simultaneously at different locations in the study of atmospheric electricity, following what was described by Kelvin as the “incessant” recordings by Beccaria a century before (Thomson, 1859).

Almost fifty years later, C.T.R. Wilson developed a method to measure the air-earth conduction current density (J_c) at the surface in Kew Observatory, London (Wilson, 1906). By this time the presence of ions in the air was known and the Wilson instrument could also measure total air conductivity (σ_T) and potential gradient (PG) simultaneously, as described in detail by Harrison and Ingram (2005). This invention permitted the beginning of regular measurements of all three major variables in atmospheric electricity in the UK – air-earth current density, potential gradient and air conductivity.

In addition to knowledge that natural radioactivity had sources in the ground that ionised the air, a balloon flight in 1912 by Austrian physicist Victor Hess carrying an ionisation chamber demonstrated that ionisation rate actually increased with height (after an initial decrease), demonstrating that the ground was not the only source of ionisation (Hess, 1912). The extra-terrestrial source of this ionisation was determined to be cosmic radiation, with ionisation rate increasing with height as the absorbing mass of atmosphere above decreased. The cosmic origins that produced an increased ion production rate (and therefore air conductivity) with height offered an explanation in addition to decreased aerosol concentration with height for the results from previous balloon flights measuring atmospheric electrical parameters (e.g. Gerdien, 1905a, 1905b), that noticed an increase in conductivity and decrease in potential gradient with height.

2.2 The Carnegie cruises 1915-1921 (cruises 4,5 and 6)

The research vessel Carnegie was built in New York for the Carnegie Institution of Washington, USA with the purpose of scientific investigation and logging of geomagnetic and atmospheric electrical phenomena throughout the world's oceans. It was a sailing ship constructed out of wood or, if wood was not possible, non-magnetic metal (to prevent local magnetic distortion). Indeed, even the crew's cutlery was made from Mexican silver (Bunker, 1982). The ship was nearly 48m long, weighed 323 Tons and robust enough to withstand heavy seas. After 20 years of successful deployment, the Carnegie tragically caught fire during the seventh global cruise in 1929: it was not replaced.

Of the many new discoveries during the cruises, the Carnegie showed the global presence of “penetrating radiation” (now known to be produced by cosmic rays), of

approximately uniform intensity at the surface (Fleming, 1949), although a variation with geomagnetic latitude was present (Aplin et al. 2005). In confirmation of the earlier discovery by Hess (1912) it was shown from air and sea-water radioactivity measurements that penetrating (cosmic) radiation could not be attributed to any known source from within the oceans (Fleming, 1949).

It was noted that no significant variation of PG with small-scale position was found at sea (unlike on land) with an average PG of about 130Vm^{-1} (Fleming, 1949). However, PG was found to be about 10 percent less in low latitudes than in high latitudes, or even up to 20 percent allowing for observed annual change in PG (Fleming, 1949). This annual variation is likely to be due to changes in local air conductivity since although PG had an annual variation, the average air-earth current (found as a product of PG and total air conductivity) was found to be nearly constant (Fleming, 1949).

2.2.1 Cruise geographical details

The Carnegie surveyed all oceans from 80°N to 60°S , covering a distance of nearly 480,000 kilometres over 7 cruises (Fleming, 1949). The three longest, most instrumented cruises were IV, V and VI, details of their tracks are as follows.

Cruise IV

The ship began cruise IV from Brooklyn on 6 March 1915. The first stop was Hawaii, followed by Alaska (60°N) then New Zealand. From New Zealand the Carnegie began a four-month circumnavigation of the globe, generally confined to between 50°S and 60°S . After reaching New Zealand again, the ship travelled clockwise near the Pacific Rim, past Japan, before arriving at San Francisco in September 1916. The final leg of the cruise was down the western coast of North and South America, round Cape Horn and concluding the cruise in Buenos Aires on 2 February 1917.

Cruise V

The Carnegie set sail from Buenos Aires on 4 December 1917. The route went round Cape Horn and up the western coast of South America, through the Panama Canal and ending at Washington, USA on 10 June 1918.

Cruise VI

From Washington on 9 October 1919, the Carnegie began a global circumnavigation cruise, confined mostly between 40°N and 40°S , arriving back in Washington on 10 November 1921.

2.2.2 Overview of measurements made during cruises IV-VI

Typical values obtained during cruises IV, V and VI

The instruments on board the Carnegie were refined and improved for cruises IV, V and VI but remained essentially the same as the preceding cruises, with observational procedure and skill also improving with time (Ault and Mauchly, 1926). The atmospheric electrical instruments measured PG, small ion number concentration and mobility (both polarities), air conductivity (both polarities), “penetrating” (gamma) radiation and terrestrial (beta/alpha) radiation. The conduction current density was determined indirectly using PG and total air conductivity.

Table 2.1 is the suggested typical mean, maximum and minimum values of the parameters measured on cruises IV, V and VI of the Carnegie based on inspection of the data tables (the total volume of printed data is too large for statistical values to be produced over all the cruises, although individual cruise summary statistics were given in the Carnegie reports).

Parameter	Minimum	Mean	Maximum	Units
Potential Gradient	-80	130	1000	Vm ⁻¹
Small ion number concentration (+ve)	50	400	900	cm ⁻³
Small ion number concentration (-ve)	150	500	900	cm ⁻³
Air conductivity (+ve)	2.2	11.1	25.6	fSm ⁻¹
Air conductivity (-ve)	1.7	8.9	23.4	fSm ⁻¹
Small ion mobility (mean)	0.30	1.50	9.00	cm ² V ⁻¹ s ⁻¹
Air-earth current density (indirect)	-3.0	4.0	27.0	pAm ⁻²
“Penetrating radiation” (cosmic)	1.8	3.7	8.0	cm ⁻³ s ⁻¹
Ionisation (terrestrial)	0.0	2.0	250.0	cm ⁻³ s ⁻¹

Table 2.1 Approximate minimum, mean and maximum values of the parameters measured during the Carnegie cruises IV, V and VI.

Ault and Mauchly (1926) stated that each instrument for all the cruises showed considerable variation even under ideal conditions and even with the same observer. This was thought to be due to a lack of appreciation of the importance of contact potential effects and the adequate screening of all connections against inductive effects. Despite this, it was found that accuracy (compared to the calibration equipment) better than 5 percent was possible during the voyages for all the measurements, assuming normal precautions were observed. However, with an electrometer of suitable sensitivity and a

more highly refined 10-observation technique, probable errors in the atmospheric electrical measurements could be reduced to about 1 percent (Ault and Mauchly, 1926).

2.2.3 Diurnal variation of the potential gradient measured by the Carnegie

Perhaps the most significant finding of the Carnegie cruises for the study of atmospheric electricity was that of the mean diurnal variation of PG away from the polluted continents. Despite limitations when the PG could be accurately measured (involving the orientation of the ship's boom and mainsail) and correction factors that needed to be made even for ideal boom and sail positions (Ault and Mauchly, 1926), a characteristic diurnal cycle emerged that would later form the standard for diurnal variation of the global atmospheric electric circuit. This average variation is shown in Figure 2.1, for cruises 4-6.

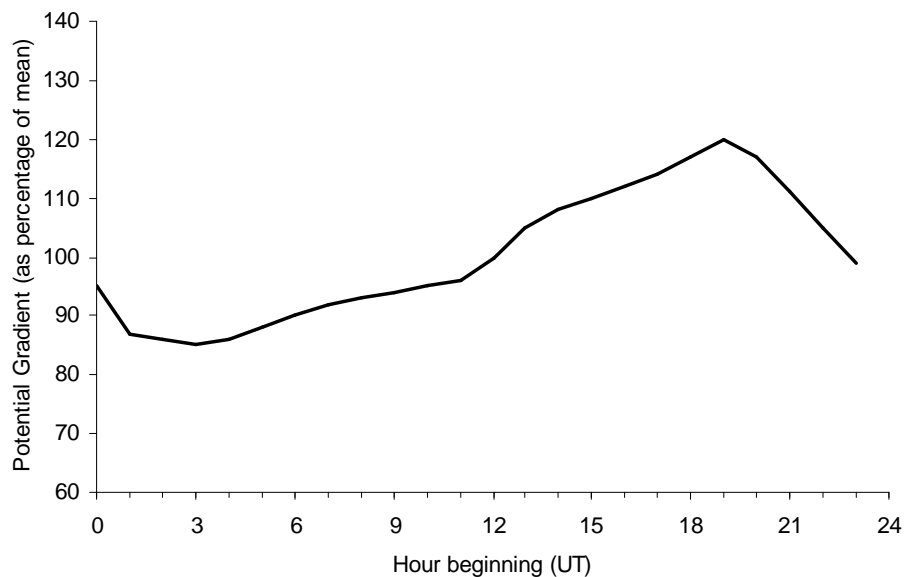


Figure 2.1 Average diurnal variation of the potential gradient measured on cruises 4, 5 and 6 of the Carnegie, as percentage of the mean. This has become known as the “Carnegie curve”.

2.3 The origin of the global circuit concept

It was Wilson (1906) who proposed that the air-earth current (and consequent potential gradient) had its source in “wet weather” areas, and flowed large distances in the conductive upper atmosphere to areas of fair weather as a conduction current, produced from the movement of free ions due to the potential difference (of order 100,000V) between the surface and upper atmosphere. Wilson even theorised an effect of aerosol on

the circuit (Wilson, 1906). It was these “showers of the appropriate kind” that act as batteries to the global atmospheric electrical circuit.

By the late 1920s there was gathering evidence that the diurnal variation of potential gradient with respect to Universal Time was similar for stations throughout the world, especially at unpolluted sites such as during the oceanographic cruises of the Carnegie. Evidence for the universal diurnal variation of potential gradient was first published by S.J. Mauchly from observations made on board the Carnegie, as shown in Figure 2.1 (Mauchly, 1921).

With the establishment of a global network of meteorological stations it became possible to compare the diurnal variation reported by Mauchly (1921) with the diurnal cycle of global thunderstorm activity. This was first investigated by Whipple (1929) who compared the diurnal variation of thunderstorm area² and assumptions about the typical storm occurrence in local time and the frequency of oceanic storms, with the Carnegie, Maud, Arctic and Antarctic diurnal variation of potential gradient (Figure 2.2). There appeared to be good agreement, with the minima and maxima of both curves occurring at approximately the same time, thereby strongly supporting the Wilson theory of a global circuit (Whipple, 1929). However, this conclusion ignored shower clouds and other areas of disturbed weather, since thunderstorms were expected to be the main, but not only, mechanism for powering the global circuit. Harrison (2004c) extrapolated the linear fit between PG from the Carnegie curve and thunderstorm area and found that the intercept on the PG axis was non-zero, demonstrating that thunderstorm activity accounted for most, but not all, of the Carnegie PG variation.

² based on the observer hearing thunder at the site

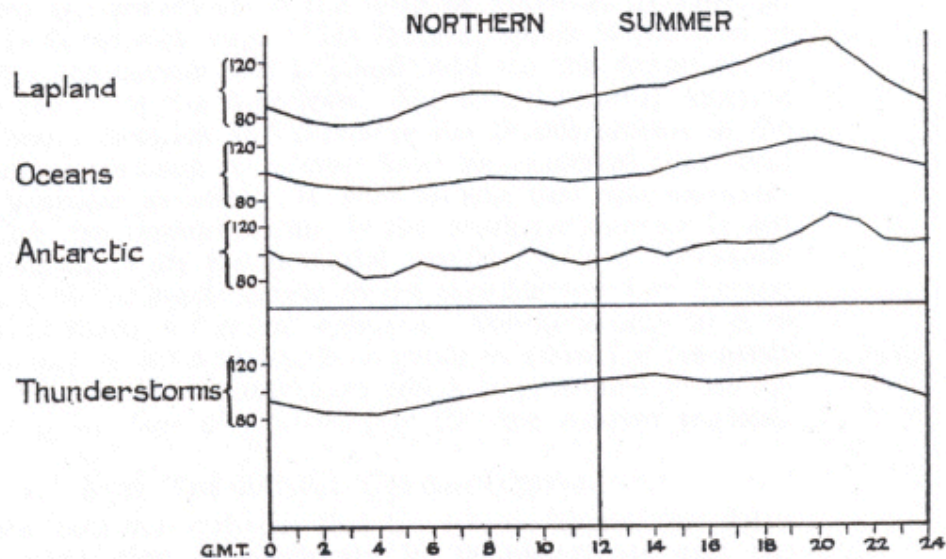


Figure 2.2 Comparison between average diurnal PG cycles from clean-air sites and estimated global thunderstorm area diurnal variation for the Northern Hemisphere summer, as a percentage of the mean from Whipple (1929).

Despite the close agreement between global thunderstorm area and diurnal variation of PG, the Wilson theory was not universally accepted, with leading authorities on atmospheric electricity of the time such as G.C. Simpson remaining to be convinced that there was any physical support to Wilson's hypothesis (Whipple, 1929).

As the source of the fair weather PG is the air-Earth conduction current density (J_C), the Carnegie curve would also be expected to be observed in the diurnal variation of J_C during times of negligible variability in columnar resistance (R_C). Such a similarity of J_C diurnal variation to the Carnegie curve has indeed been reported (e.g. Cobb (1967), Anderson (1969), Retalis (1991), Isrealsson and Tammet (2001)).

2.4 Evidence for the global atmospheric electric circuit concept

The theory of Wilson's global atmospheric electrical circuit concept is still regarded as the best explanation for the global variation of PG and J_C , due to the increasing weight of observations in agreement with the main principles of the theory, the details of which will be discussed in this section.

Columnar Resistance

During fair weather (away from any local sources of charge separation), the conduction current density J_C is related only to the ionospheric potential V_I and columnar resistance

R_C (Chapter 1). Since J_C is the most fundamental parameter of the global circuit measurable from the surface due to it being largely unaffected by local surface conditions (e.g. Dolezalek, 1978), it offers the best method of global circuit monitoring. For this, the variation of R_C must either be known or assumed to be negligible for the diurnal variation of J_C to represent the strength of the global circuit via ionospheric charging by global thunderstorm activity. It is therefore of significant importance to investigate changes in R_C at all timescales and under different conditions.

One of the principal components to the Wilson theory of a global electric circuit is that of the large but finite electrical resistance between the ionosphere and surface. This resistance, termed the columnar resistance, R_C , by Gish (1944) can be determined experimentally by measuring the vertical profile of total air conductivity (Chapter 1). This was first done using the stratospheric balloon flight of *Explorer II* in 1935 (Gish, 1944), obtaining a columnar resistance of the order $100\text{P}\Omega\text{m}^{-2}$ (Sagalyn and Faucher, 1954). The relative contribution of the atmosphere to this columnar resistance was strongly height dependent, with Sagalyn and Faucher (1954) reporting columnar resistances of between $90\text{-}250\text{P}\Omega\text{m}^{-2}$, of which 40-73% originated from the surface boundary layer. These observations have been used to explain the large air-earth current densities found at the summit of mountains (e.g. Kasemir, 1951 reported a J_C of up to ten times higher than at sea level) where the mass of atmosphere above is less (and generally cleaner).

The first investigation of the diurnal variation of R_C was made by Sagalyn and Faucher (1956) using equipment carried by balloons to measure the total conductivity profile from the surface to 4.57km (Figure 2.3). The shape of the profile was demonstrated to be a function of the height of the boundary layer, with the upward transport of aerosols by turbulent mixing around midday increasing the total aerosol number concentration in the column and hence R_C . The shape of the curve and the 40% daily variation are in approximate agreement with modern estimation of the diurnal variation of boundary layer turbulence (Hoppel et al., 1986).

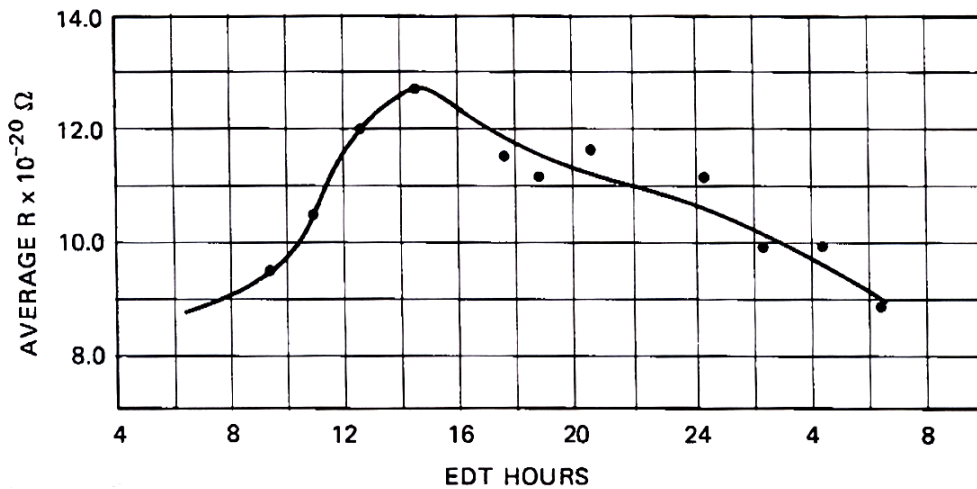


Figure 2.3 Average diurnal variation of R_C of a 1cm^2 column from the surface to 4.57km with local time (from Sagalyn and Faucher, 1956).

Tropospheric balloon flights measuring negative conductivity between 1957-1962 were used to calculate the seasonal variation in R_C near Tokyo, Japan (Uchikawa, 1972). It was found that a distinct seasonal variation existed, being proportionally greater in the winter (December) than the summer (June). However, no seasonal variation was found over the Hachijojima, an island in the Pacific Ocean, 200km south of Tokyo, making the clean-air site more suitable for assessing seasonal variation of V_I using measurements of J_C as any seasonal variation would be attributed to V_I alone. The difference between these two results may be attributed to the greater influence of air pollution near Tokyo than at Hachijojima, as aerosol removes small ions in the column by attachment, increasing R_C . The seasonal variation in R_C over Tokyo varied in the opposite sense to the air-earth current density calculated in the stratosphere by the balloon soundings, but only half the relative amplitude. This difference in variations of R_C and current density was approximately equal to the variation in V_I observed in Weissenau, Germany, thereby suggesting an Ohmic relationship (Uchikawa, 1972).

The Ohmic assumption between J_C and V_I was used more recently by Harrison (2005b) to calculate R_C using coincident J_C data from the Wilson apparatus at Kew, London and V_I soundings from Weissenau. The R_C over Kew varied between ~ 50 to $400\text{P}\Omega\text{m}^2$. The reason for this variability was not straightforward, with cosmic ray-induced aerosol formation being a suggested factor. A method of remotely detecting the total number of cluster ions in the atmospheric column using infrared absorption was investigated by Aplin and McPheat (2005). Remote sensing of total number of ions in the atmospheric column

could provide a method of measuring R_c , providing appropriate assumptions about the vertical distribution of the ions and the ion mobility vertical profile are made.

Source of the global circuit

More work was done on the source term of the global circuit by Krumm (1962) who re-investigated the relationship between global thunderstorm area and the Carnegie curve using more modern and extensive data (from the 1956 World Meteorological Organisation thunder days dataset) than available during the first investigation by Whipple (1929). Although the variation found by Krumm (Figure 2.5) appears to have a similar minima time as the Carnegie curve (Figure 2.1), the maximum number of global of thunderstorms appears to be at a sooner time than that found by Whipple (Figure 2.6) and the Carnegie curve, although an offset between thunderstorm area and the Carnegie was also acknowledged by Whipple.

Reasons for this discrepancy between the Whipple (1929) and Krumm (1962) analyses seem to be due to the inclusion of oceanic data with a maximum of around 13UT (unlike Whipple who included no maximum time for oceanic storms) and the similar maximum amount of Asian/American storms used by Krumm (Figure 2.5), with Whipple using a lower occurrence of Asian storms relative to American, although conversely, the annual global thunder days used by Krumm (Figure 2.4) still appear to imply a greater occurrence of American storms. The differences between Whipple and Krumm's thunderstorm estimations are likely to be a result of improved spatial representatively of global thunderstorm occurrence due to a longer recording history of more frequent and reliable meteorological stations in 1959 than those available to Whipple in 1929. It is therefore of interest that the departure of estimated global thunderstorm area produced by Krumm (1962) from the Carnegie curve is greater than that of Whipple (1929).

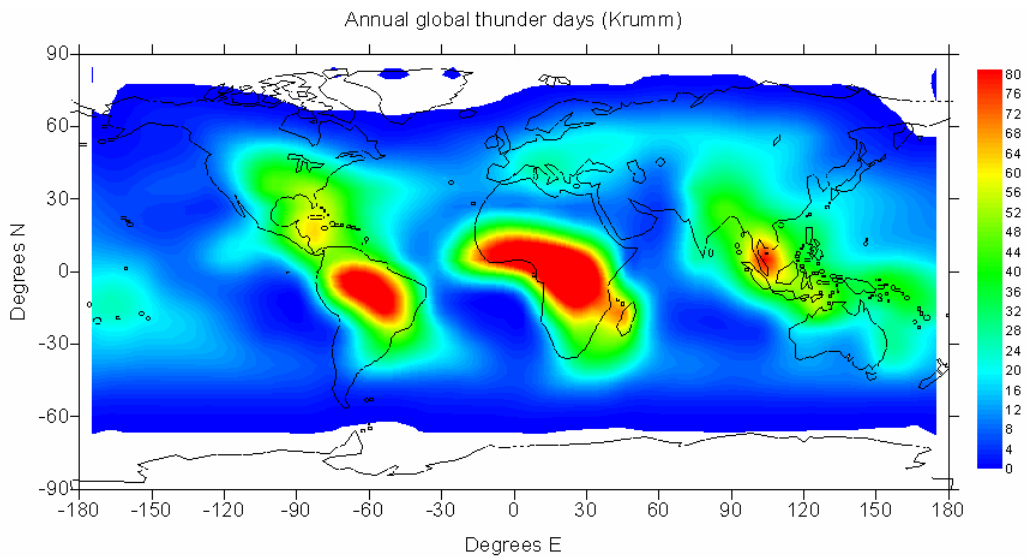


Figure 2.4 Global thunderstorm frequency as measured by the annual number of days when thunder was heard using the WMO 1956 dataset (adapted from Krumm, 1962).

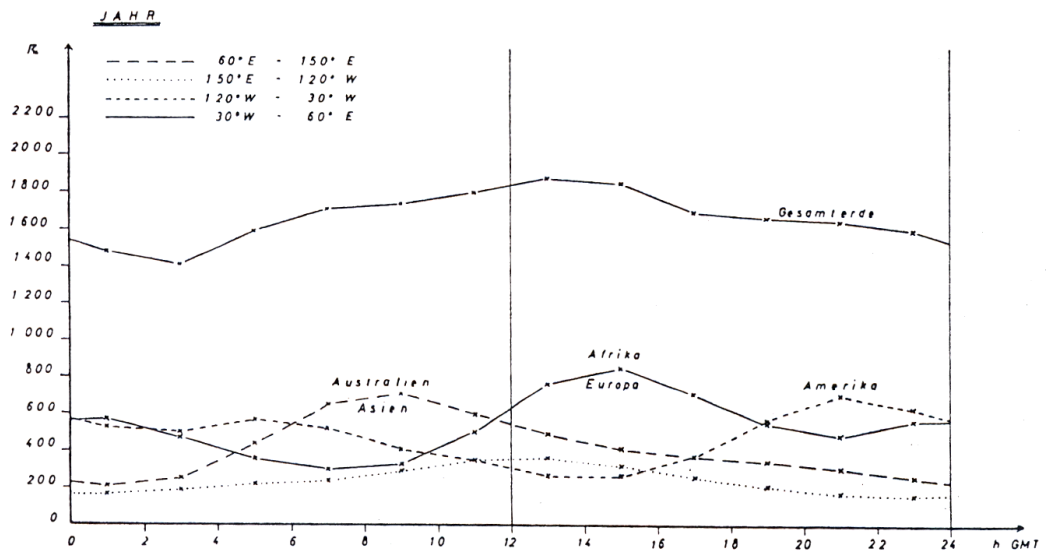


Figure 2.5 Estimated global (top line) and regional (Asia/Australia, Africa/Europe, America and Ocean (lowest line)) mean number of thunderstorms at 2-hour intervals in Universal Time from Krumm (1962).

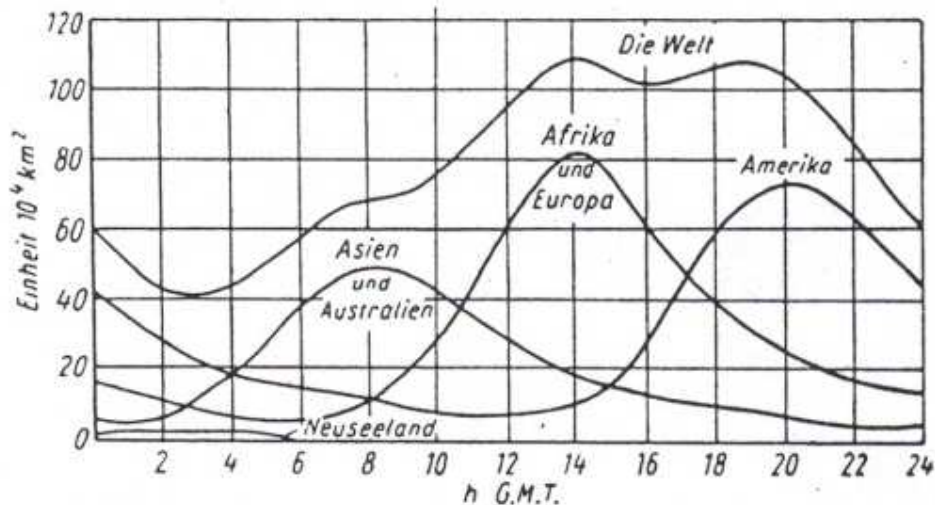


Figure 2.6 Diurnal variation of thunderstorm area over the entire world (top line) and major land regions calculated by Whipple (1929) from Krumm (1962).

The discrepancy between the calculated thunderstorm areas of Krumm (1962) and Whipple (1929) was discussed by Dolezalek (1972) where concern was expressed over the lack of more recent evidence supporting the close correlation between global thunderstorm area and the Carnegie curve as suggested by Whipple (1929). Due to this lack of modern evidence, Dolezalek (1972) states that:

“...It is obvious that the assessment of the global thunderstorm activity is the weakest point in our attempts to understand the global circuit...”

Dolezalek (1972) does not, however, dispute the observed uniform global diurnal cycle of (clean-air) PG and J_c . Dolezalek (1972) suggests that the air-earth current density was the “safest” surface parameter for investigating the diurnal cycle of the global circuit, with thunderstorm numbers being the most tenuous. Reasons suggested are due partly to the questionable accuracy and limited density of global thunderstorm observations at the time and also the unproven assumption of a linear proportionality between thunderstorm area and ionospheric charging, or that this charging rate does not vary with the geographical source of the thunderstorm generators. As was then suggested by other researchers (e.g. Kasemir, 1972) that long term monitoring of ELF or VLF (extremely and very low radio frequency respectively) intensity generated by global lightning activity, especially in Polar regions, would provide a more reliable (and in near-real time) method of determining the global thunderstorm activity than meteorological statistics in order to further investigate this fundamental aspect of the global circuit theory. The technique of using ELF measurements in the Antarctic and Greenland as a means of global circuit monitoring was

investigated by Füllekrug et al. (1999). A remarkably close correlation in both shape and phase between the mean diurnal variation of the ELF magnetic field intensity and the surface PG at the South Pole during December 1992 was found. However, correlations between hourly values of ELF and PG were low, suggesting the presence of local variations in PG at hourly timescales. From the ELF and PG comparison, Füllekrug et al. (1999) estimated that global cloud-to-ground lightning activity contributed to $\sim 40 \pm 10\%$ of the strength of the atmospheric electric field.

It has always been noted (e.g. Wilson, 1906 and Kasemir, 1972) that mechanisms other than just global thunderstorm activity may be responsible for modulation of the global circuit, such as shower clouds. A more recent investigation of the possible contribution of shower clouds on the global electric circuit (as originally hypothesised by Wilson, 1906) has been discussed by Williams and Satori (2004), suggesting a significant contribution of electrified shower clouds in South America. Mechanisms for charge separation within thunderstorms have been investigated recently by Bürgesser et al. (2006), with the importance of rapid convective updrafts and the presence of mixed-phase cloud hydrometeors shown.

2.4.1 Modern measurement of the global circuit

The use of instrumented aircraft to study the worldwide variations in atmospheric electricity was seen as the most promising technique by Anderson (1967), who also criticised the lack of “care and effort” employed by aircraft campaigns in the past. In particular, Anderson (1967) states that surface-based instrumentation is subject to too much local variation caused by the turbulent motion of space charge, terrain and electrode layers, even for “exotically placed” instrumentation. Instrumented aircraft measuring both potential gradient and air conductivity in order that J_C could be derived and flying over a large body of water during fair-weather conditions was suggested to be the most reliable method of monitoring the global circuit, with a collection of such measurements suggested to be able to provide the “final” answer to the source(s) and variability of the global atmospheric electrical circuit (Anderson, 1967).

Continuing the initiative of using J_C measured indirectly by aircraft to study variation of the global circuit, Anderson compared measurements of the mean UT diurnal cycle of J_C made in this manner above the Mediterranean and Tasman Seas, although separated by four months (Anderson, 1969). Both diurnal cycles exhibited similar general patterns, although with different emphasis in parts. This was expected to be due to the proximity of the storm group that caused the global variation to the point of observation, such that

accentuations of the global pattern due to storm activity in the same hemisphere would occur, with attenuation of that from further away (Anderson, 1969). A similar result was also reported by Takagi and Masahiro (1972) who found that better correlations between clean-air stations measuring PG were found when the stations were in the same hemisphere. More recently, Kamra et al., (1994) measured the mean PG diurnal variation during a cruise in the Bay of Bengal and obtained a curve with characteristics dominated more by the contribution of local (Asian) thunderstorms than seen in the typical Carnegie curve. This implies that although thunderstorm activity is propagated across the entire globe as expected by the Wilson theory, the signal does attenuate with distance from source to point of observation, particularly when crossing the equator. An attenuated global signal is likely to be overpowered by local sources of variability.

Aircraft measurements were later used by Markson (1976) to calculate the mean diurnal variation of V_I from profiles of PG, to further investigate the global circuit hypothesis. This percentage variation was shown to agree well with the Carnegie curve (correlation coefficient of 0.96) as expected from the Wilson theory if R_C remained constant, which was likely as measurements were conducted over the ocean. In addition, a comparison between PG using an aircraft at constant altitude over the Bahamas and J_C measured near-simultaneously by an aircraft over the Gulf of Alaska. The same Carnegie curve-type variation was apparent at both sites, adding confidence to the global circuit hypothesis (Markson, 1976). Similar trends in coincident ionospheric potential measurements, as well as surface PG have also been reported (Harrison, 2005b). Additionally, it was suggested by Markson (1976) that aircraft measurements were capable of recording temporal variation of V_I with a resolution of minutes, which as not possible with ground instrumentation. This was presumably due to the improved signal-to-noise ratio for measurements above the boundary layer and the reduced electrical relaxation time in the mid-upper troposphere, allowing more rapid coupling between the airborne measurements and the Ionosphere. Interestingly, Markson commented that the overall average of 120 V_I soundings was lower than estimates made 10-20 years earlier, suggesting a possible decrease in the strength of the global circuit with time (Markson, 1976). However, the effect of nuclear weapons testing in the 1960s may have had an influence on this, an effect mentioned earlier by Uchikawa (1972).

It is also noted during research in the 1970s that despite the term “ionospheric potential” V_I the majority of this potential is reached within the troposphere (in accordance with the majority of columnar resistance, R_C) as illustrated by Israelsson (1978) who found the diurnal variation of V_I (using radiosonde ascents) to be of a similar appearance to the Carnegie curve as expected, with the potential at the top of the tropopause being 88%

(standard deviation of 9%) of the assumed V_1 (by extrapolation) based on 24 soundings. This finding illustrates the importance of the troposphere, and therefore meteorological processes, in the global atmospheric electrical circuit, as well as the significant meteorological influence on local atmospheric electrical parameters, especially during high static stability in the boundary layer (Israelsson, 1978). However, it is quite possible that meteorological phenomena either directly or indirectly affect ionosphere even at altitudes such as the F2-layer (~100km) (Rishbeth, 2006).

More recent investigations of the global circuit diurnal and seasonal variation have been made by Burns et al. (2005). In this paper, the mean diurnal and seasonal variation of PG measured in Antarctica between 1998-2002 was analysed. It is evident that the diurnal variation was very much like that of the Carnegie curve, although even in Antarctica, local influences such as wind speed and blowing snow were still evident under certain meteorological conditions. Seasonal trends in this diurnal cycle were also observed, such as a reduction in the diurnal range (as a % of the mean) in May-June (29% variation) compared to November-December (59%) as well as seasonal changes to the curve shape, expected to be due to changes in the location of main global thunderstorm activity. Although suggestive of seasonal variation in the global circuit, the authors advise that care should be taken when considering the global generators as the only source of this variation in PG due to the relative sparseness of fair-weather measurements around the time of the November-December minimum and the influence of local meteorological conditions on the measurements (Burns et al, 2005). Due to the cross-polar cap potential, a model must be used to account for this influence on surface atmospheric electrical effects, which would also have possibility of introducing errors. It was also emphasised that measurement of the air-earth conduction current density (J_C) would potentially provide more reliable measurements of the global circuit as they are less influenced by changes in local air conductivity than the PG (Burns et al., 2005), especially as significant seasonal variation of air conductivity at the South Pole occurs (Reddell et al., 2004). A list of preferred measurements and locations for global circuit monitoring is given by Märcz and Harrison (2005), which states that V_1 is the primary quantity of interest, followed by J_C then PG in oceanic, mountain, continental rural and finally urban air.

The advent of modern, satellite-based instrumentation suitable for monitoring lightning flashes (both day and night) has allowed a detailed investigation of the link between diurnal variation of global lightning activity and that of the global circuit as seen by the Carnegie curve. Using data from the OTD (Optical Transient Detector, based on sensors originally designed for the detection of atmospheric nuclear explosions) between April

1995 and March 2000 Nickolaenko et al. (2006) produced a map of the global distribution of lightning activity (Figure 2.7) and compared the diurnal variation with the Carnegie curve (Figure 2.8).

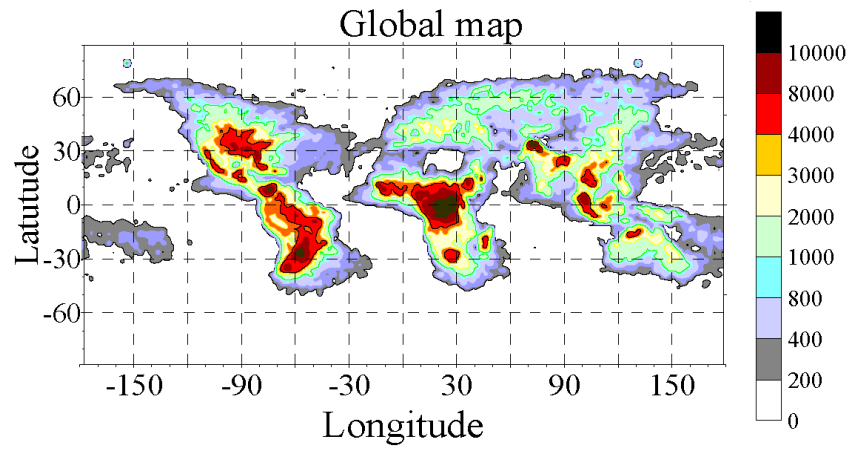


Figure 2.7 Cumulative global lightning flash frequency per 2.5° grid box as monitored by the satellite-based OTD (Optical Transient Detector) instrument between April 1995 and March 2000 (from Nickolaenko et al., 2006).

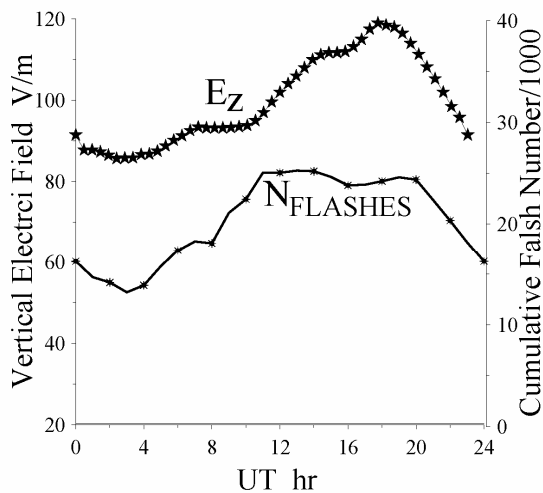


Figure 2.8 Comparison between the mean diurnal variation of global lightning flash number (April 1995 to March 2000) and the Carnegie curve³ (from Nickolaenko et al., 2006).

Comparing thunderstorm area estimated from the 1956 WMO statistics by Krumm (1962) in Figure 2.4 to the OTD-derived global distribution of lightning flash rate (Figure 2.7) compiled by Nickolaenko et al. (2006) it can be seen that both maps are in general agreement as to the main sources of lightning. However, the increased spatial detail of the OTD dataset allows more localised sources to be separated from the general regions of high activity that was not apparent in the Krumm (1962) analysis. Strong,

³ Note that the y-axis label is incorrect and should read potential gradient as a percentage of the daily mean, not the absolute value of vertical electric field (which would be negative in any case).

localised lightning activity over the Himalayas and northern Australia are examples of these, and were probably underrepresented in the 1956 WMO statistics due to their remote locations and consequent lack of regular observations.

Comparison between the diurnal cycle of global flash rate and the Carnegie curve (Figure 2.8) shows that the curves are generally similar in appearance, but with noticeable differences. In particular, Nickolaenko et al. (2006) remarks that the amplitude of the flash rate is 30% whereas it is only 20% for the Carnegie. The peak in flash rate is broader and earlier than that of the Carnegie making it more like the thunderstorm area cycle estimated by Krumm (1962), although both minimums occur at the same time. Reasons for this discrepancy are suggested by Nickolaenko et al. (2006), such as if cloud-to-ground flashes (primarily detected by the OTD) were not a fair representation of all the strikes, or if individual lightning events produced different amounts of charging (not a one-to-one relationship as would be required for the two curves to be the same) as well as differences in measurement accuracy of PG and flash rate. Nickolaenko et al. (2006) further suggest that the different time and form of the flash maximum could be attributed to lightning over the Himalaya and Karakorum highlands being below average efficiency at charging the ionosphere, so their contribution (around 12UT) would be lower when seen in the global circuit cycle than directly in the global flash rate. The Himalaya and Karakorum highlands contribution to global lightning activity was suggested to be a recent addition, perhaps due to climate change (Nickolaenko et al., 2006). The suggestion of mountain storms being somehow less effective at charging the ionosphere is in opposition to those made earlier by Dolezalek (1972) and the model results of Hays and Roble (1979) and Makino and Ogawa (1985), due to a more effective electrical connection between the storm and ionosphere from the low columnar resistance above mountainous areas. Further evidence for the non-linear relationship between lightning activity and the global circuit may be the observed difference between the diurnal variation of Schumann resonance and the Carnegie curve (e.g. Füllekrug and Fraser-Smith, 1997; Price and Melnikov, 2004) over all seasons.

The contribution of intense lightning discharges to the global circuit was investigated by Füllekrug (2004) during April 1998. The results indicated that intense positive cloud-to-ground lightning decreased the global circuit intensity by bringing positive charge to the surface, causing a net decrease of ~ 0.005 - 0.04% on the ~ 1 minute time scale. This finding therefore suggests a further source of uncertainty when using ELF or optical methods of global circuit intensity inferred from global lightning activity, as the sign of the flash (and therefore its contribution to the global circuit) can not be determined by these methods.

In summary, it is clear that observations made throughout the 100 years since the concept of a global atmospheric electrical circuit (Whipple, 1906) continue to support its hypothesis. Perhaps the greatest uncertainty lies in quantitative connection between global thunderstorm activity and ionospheric potential (Dolezalek, 1972) as well as the physical mechanisms of charge separation and transport to the upper atmosphere, although the recent discovery of upward plasma discharges from the tops of thunderstorms (e.g. "Sprites") are likely to provide clues to this missing link. The attenuation of this thunderstorm signal as it passes along the ionosphere has been noticed (Anderson (1969), Takagi and Masahiro (1972) and Kamra et al., 1994), offering further insights into the interactions present in this circuit. Despite the increasing evidence, further research and suitably dense networks of good quality and simultaneous monitoring of J_C , PG, air conductivity and preferably V_I and R_C via radiosondes or other vertical profiling as well as global thunderstorm activity are required for more conclusive proof of the Wilson (1906) global electric circuit theory.

2.5 Modelling the global circuit

A summary of the five models to be discussed in this subsection are given in Table 2.2. One of the first detailed, quantitative calculations of the vertical profile of atmospheric electric parameters was made by Shreve (1970). This model was for the surface to 60km altitude, and included profiles of small ion concentration, total air conductivity, space charge density, PG and ion production rate. The model was calculated for steady state, where the ion production rate was in equilibrium with ion loss and charge was conserved (i.e. constant J_C with height). However, the effect of aerosol attachment in the ion loss term was not considered, making the results of this aerosol-free profile rather unrealistic, especially for the lower troposphere where aerosol concentration is high. Additionally, the effect of large ions (not considered by Shreve, 1970) has been calculated to contribute to air conductivity by nearly 10% for moderate urban boundary layer aerosol number concentrations of $2 \times 10^4 \text{ cm}^{-3}$ with an ionisation rate of 10 ions cm^{-3} (Dhanorkar and Kamra, 1997).

The model proposed by Hays and Roble (1979) was the first three dimensional numerical model of the global circuit. The model incorporated both vertical profile and geographical location, with model resolution in spherical coordinates. Model output was averaged at 5° latitude and longitude grid resolution. Vertically, the model was composed of four coupled layers (lower tropospheric boundary, upper troposphere, stratosphere and mesosphere, with the magnetosphere as the upper layer). As magnetospheric interaction was

considered, the Earth's magnetic field was also modelled to allow for field line curves away from the vertical with height (and therefore the lines of greatest conductivity). The latitudinal variation of cosmic ray intensity was modelled using a simple cosine dependence (and constant from the poles to 30°). There was a relatively crude representation of surface orography (5° resolution) but, like Shreve (1970), aerosol was not considered, with the vertical profile of air conductivity modelled by an exponential decrease and a function only of modelled cosmic ray intensity. The model was primarily used to investigate the effect of orography and electrical coupling between the thunderstorm source terms (modelled as vertical dipoles and distributed globally according to thunderstorm probability using climatological statistics) and the ionosphere, including the effects of solar flares and subsequent Forbush decrease in cosmic ray intensity (Figure 2.10).

Makino and Ogawa (1985) proposed a further three-dimensional global model that concentrated on the lower atmosphere between 0-60km altitude. Important advances were the inclusion of an empirical formula for the latitudinal variation of cosmic ray intensity based on actual measured vertical profiles of Neher (1967) for various geographic locations. Secondly, the model incorporated an aerosol vertical profile, allowing the air conductivity to be a function of both cosmic ray and surface radioactive sources for ion production and, crucially, aerosol attachment for ion loss in addition to simply recombination. Surface orography was also incorporated and model results were calculated on a 5° latitude-longitude grid. Vertical resolution was height dependent, with a resolution near sea level of 50m, increasing to 500m at an altitude above 20km. The ionosphere was assumed to be a global equipotential and like Hays and Roble (1979), thunderstorms were considered as the only source term, with the air-earth current flowing vertically and in steady-state, therefore being constant with height. The aerosol vertical profile was represented with a simple exponential profile, using surface value and scale height, as was the surface-generated component of the ionisation rate profile.

A similar model to Makino and Ogawa (1985) was later developed by Sapkota and Varshneya (1990). The main differences of this newer model was the inclusion of the global distribution of anthropogenic aerosol production based on population density (again, using a simple exponential decrease) and volcanic aerosol based on the location of global volcanic activity, allowing for volcanic aerosol in the stratospheric section of the aerosol number concentration profile. The surface component of ionisation rate was set at 8.6 ions cm^{-3} , with a scale height of 1km (i.e. the same as the aerosol profile), values also used by Makino and Ogawa (1985). Additionally the effect of ionisation due to coronal

discharges beneath thunderclouds were represented, which made the global resistance also a function of thunderstorm activity.

More recently, a further development in modelling of the global circuit was made by Tinsley and Zhou (2006). The basic structure of the model was similar to Makino and Ogawa (1985), with a 5° horizontal resolution (of independent columns) and variable vertical resolution of 50m near the surface to 500m at the upper limit of the model at 60km. One of the main differences however was the inclusion of stratospheric conductivity increases due to varying charged particle fluxes from space, namely relativistic electron, RE and Solar energetic particle (SEP) events, in addition to the background cosmic ray intensity. This additional ionisation increased stratospheric ionisation by a factor of two compared to Makino and Ogawa (1985) and Sapkota and Varshneya (1990). The model also parameterised atmospheric dynamics that produced horizontal variability in radon gas (and therefore the surface component of ionisation rate). The surface value of ionisation rate was also geographically dependent, with the effects of surface cover (wet soil, ice, ocean etc) on radon emission taken into consideration.

Like Sapkota and Varshneya (1990), the spatial variability of anthropogenic and volcanic aerosol emissions was modelled, although the size distribution and species were also considered. Aerosol profiles were modelled from a global dataset of measured aerosol profiles (Global Aerosol Data Set, GADS), including supplemental observations of stratospheric aerosol. In addition, simple assumptions on the seasonal dependence of surface-generated (Radon) and aerosol production and scale heights were introduced. Using their model, the authors suggest inferred changes in the global circuit due to climate change on interannual to Milankovich timescales. Principally, they suggest that variations in tropical and sub-tropical solar radiation on Milankovich timescales would affect global thunderstorm intensity, and therefore air-earth current. Changes in air-earth current are further suggested to effect global cloud cover, which may be a forcing agent for climate change on this timescale.

Model	Horizontal resolution	Vertical resolution	Maximum Height	Ionisation Profile	Aerosol Profile
Shreve (1970)	N/A	Not specified	60km	Empirical from measured at 50/51N	Aerosol not considered
Hays and Roble (1979)	5° global grid	4 coupled layers	105km	Exponential, different for each layer	Aerosol not considered
Makino and Ogawa (1985)	5° global grid	265 points, 50m to 500m	60km	Empirical from measured, 4 layer formula	Simple exponential, land/sea difference
Sapkota and Varshneya (1990)	5° global grid	Not specified	Not specified, but appears to be 60km	Empirical from measured, 4 layer formula (from M&O85)	Simple exponential, pop density dependent. Volcanic aerosol
Tinsley and Zhou (2006)	5° global grid	335 points, 50m to 500m	60km	Empirical from measured, includes RE, SEP	Empirical, divided into layers using measured dataset

Table 2.2 Comparison of basic global circuit model properties discussed in this section.

2.6 Solar activity and the global circuit

The total electrical resistance of the global circuit is determined by the amount of small ions, which are mostly produced by cosmic radiation. Therefore any process that modulates the strength of cosmic radiation below the ionosphere will also effect the global circuit. As the activity of the Sun increases (such as during the peak of the 11-year cycle) so too does its magnetic field. This magnetic field diverts galactic cosmic rays from the Earth, causing a decrease in the ionisation of the atmosphere and subsequent increase in R_C .

Shorter period solar activity can also produce variation of the solar field strength and therefore the intensity of galactic cosmic rays reaching the Earth's atmosphere. Coronal mass ejection (CME) causes a rapid decrease in the observed galactic cosmic rays reaching Earth a few days after the event due to the enhanced magnetic field carried by the solar wind (called a Forbush decrease) thereby increasing R_C . However, a solar flare event will cause an increase in cosmic ray intensity originating from the Sun itself (solar cosmic rays) that will enhance the ionisation of the Earth's atmosphere and decrease R_C .

The air-earth conduction current density, J_C , is a function of both V_I and R_C so any change in cosmic radiation that alters R_C will consequently be observed in J_C at the surface, for a

given V_i . Of course, R_C varies naturally at timescales of hours to seasons with changes in the aerosol vertical profile, so if modulation by cosmic ray changes is to be observed, the observation site must be unpolluted so that variation of R_C due to aerosol is kept to a minimum. This criterion makes remote sites such as oceanic or polar stations best suited to monitor changes in the global circuit from solar activity (although the effects are believed to be latitude dependent as will be discussed later). However, for the case of polar sites, the cross-polar cap potential (a horizontal potential difference between the nocturnal and daylight sides of the ionosphere), makes changes in cross-polar ionospheric potential unrepresentative of global variation and a model is required to account for this additional (non-global circuit) source of V_i variability.

Direct measurements of J_C using an automatic “Wilson-plate” at the relatively unpolluted site of the Pacific Island of Hawaii were made by Cobb (1967). The observations identified an increase of approximately 10% in daily mean J_C (and PG) above their normal values following solar flare events, demonstrating an effect of solar flares on the global circuit. The effect of an individual flare caused an increase of about 5 or 6% with the increase usually lasting less than a day although the clustered nature of solar flare emissions meant that the cumulative effect of a rapid sequence of flares produces the typical 10% overall increase, visible over the duration of the flare cluster arrivals (Figure 2.9). Short periods of greatly enhanced J_C were also observed following a multiple flare burst, where J_C increased by 75% for a 6-hour period (Cobb, 1967). A similar increase in J_C and PG after solar flares was also observed at two European mountain top sites (Ogawa, 1985).

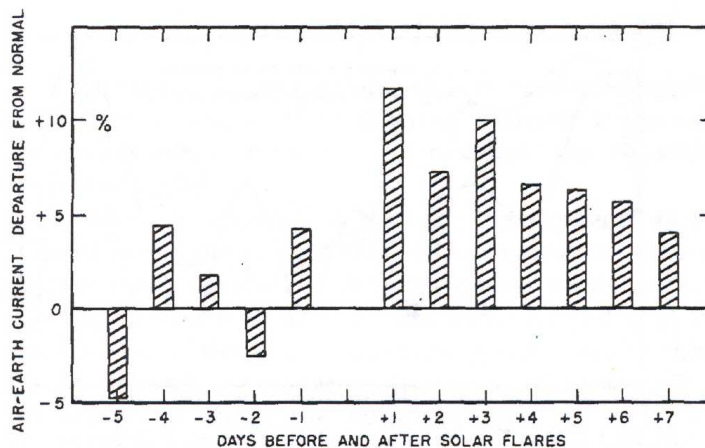


Figure 2.9 Percentage variation of daily mean J_C from the normal due to solar flares observed in Hawaii (Cobb, 1967).

Hays and Roble (1979) modelled the effect of a solar flare and Forbush decrease on the total air conductivity at different altitude and latitude (Figure 2.10). The results show an altitude variation parallel to the modelled conductivity profile, of noticeable but reasonably small magnitude compared to the variation of observed profiles. The decrease in conductivity due to the reduction in galactic cosmic rays during a Forbush decrease appears to be approximately equal to the increase in conductivity with increased solar cosmic rays after a solar flare.

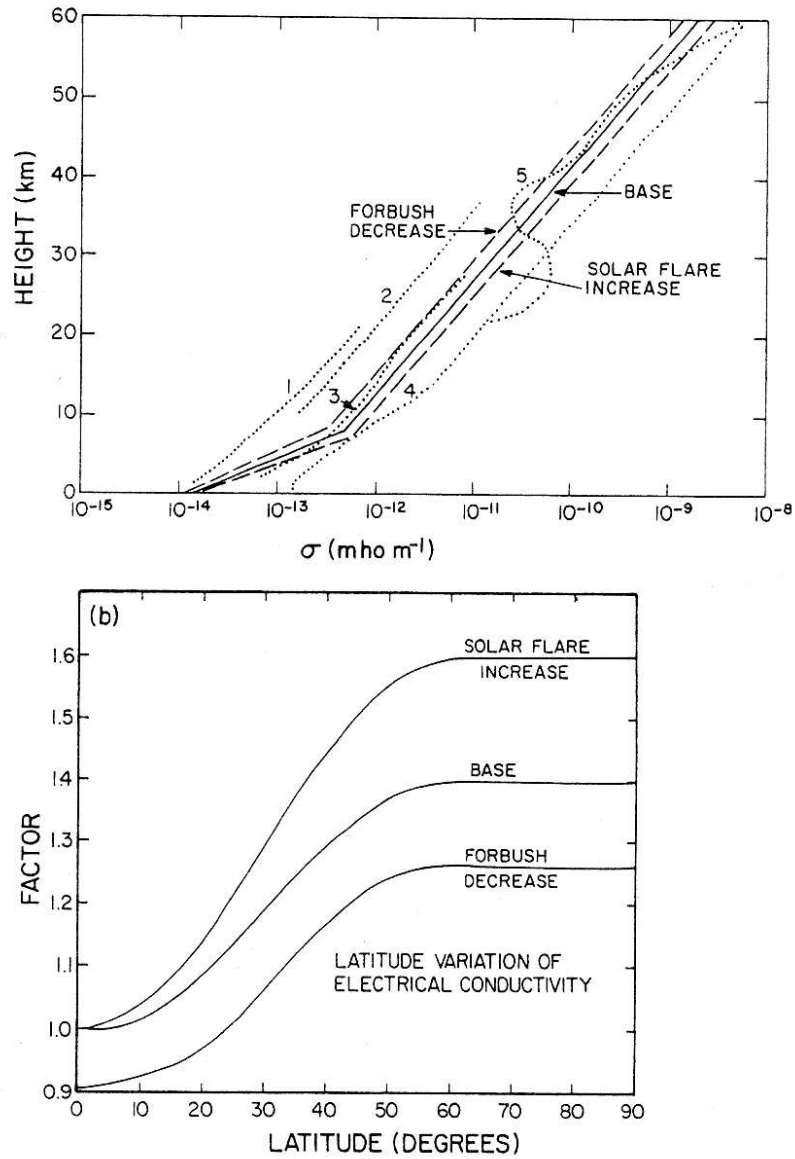


Figure 2.10 The effect of a solar flare and Forbush decrease in air conductivity with (a) altitude and (b) latitude (Hays and Roble, 1979). The numbered lines in (a) represent measured conductivity profiles (see Hays and Roble (1979) for more detail on these observed profiles).

The latitude dependency of the effect of a Forbush decrease and solar flare appears to differ for both magnitude and form. As compared to the natural variation of air conductivity with latitude (base), the model suggests little or no effect of a solar flare in equatorial regions, a larger and more latitude-dependent effect at tropical and extra-tropical regions, and the greatest but latitude-independent effect for high ($>60^\circ$) latitudes. The reduction in air conductivity due to a Forbush decrease is independent of latitude. It is of note that the approximate 5-6% increase in J_C (and therefore air conductivity via R_C) due to an individual solar flare observed in Hawaii at 20° latitude by Cobb (1967) is in reasonable accordance with the modelled effect of Hays and Roble (1979) for that latitude.

Sapkota and Varshneya (1990) produced a more detailed model to investigate the effect of a Forbush decrease on J_C and PG with colatitude. The effect of this decrease was modelled for both altitude dependent and independent assumptions, with a latitudinal-dependent change in cosmic ray intensity (between 2-35% global variation) applied to their model, and the effect on surface J_C and PG described. As identified in Figure 2.11 the latitudinal response is quite different for J_C and PG and is more complicated than the earlier model of Hays and Roble (1979) that suggested a latitude-independent decrease of total air conductivity (therefore increase in R_C and decrease in J_C).

The reason for this discrepancy in latitudinal-dependent J_C and PG change between the two models is that the more sophisticated Sapkota and Varshneya (1990) model calculates the perturbation of V_I resulting from the reduction in cosmic ray ionisation and the redistribution of R_C with latitude due to the latitude-dependent cosmic ray ionisation rate (in turn resulting from the latitudinal variation of the geomagnetic field). For instance, the increase in V_I that results from a Forbush decrease causes an increased J_C near the equator, as the change in R_C is low (owing to the strong geomagnetic shielding that reduces the cosmic ray intensity). However, at the poles, the increase in R_C outweighs the increase in V_I so causes a decrease in J_C in accordance with Ohm's Law. As PG is a function of both J_C and the local air conductivity (which will also be a function of latitude as the distribution of aerosol is also included in this model) the perturbation with latitude will be different than for J_C alone.

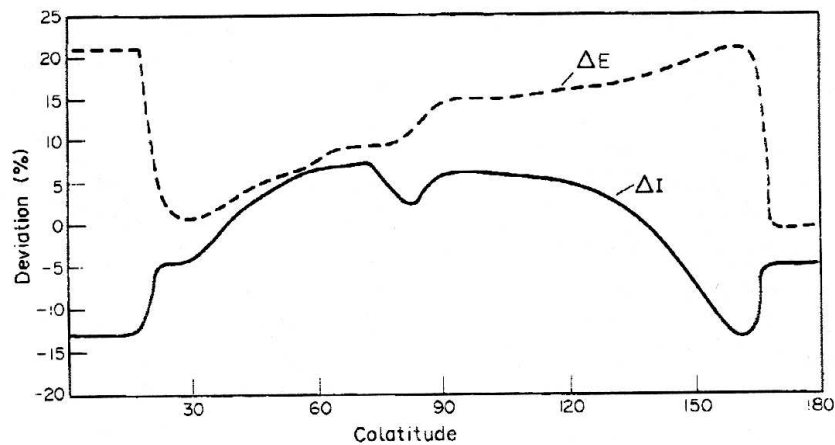


Figure 2.11 Modelled deviation of J_C and PG from the unperturbed condition as a result of the Forbush decrease in cosmic ray ionisation, as a function of colatitude along 72.5°E . (Sapkota and Varshneya, 1990).

More recently, an increase in observed J_C after a geomagnetic substorm (such as that initiated by a solar flare) was detected by Belova et al. (2001), even against the background of daily variation. J_C was measured using a long-wire antenna in Sweden during 1998-99. Additionally, the short-period (order minutes) variability of J_C was reported to increase during the geomagnetic storm events in addition to the increase in mean.

Solar influences over long-term (decadal) variation of the global circuit have also been proposed as changes to the solar magnetic field intensity modulate the amount of galactic cosmic rays that enter the Earth's atmosphere, (McCracken et al., 2004) which in turn will modify R_C . This was proposed as a cause of the observed twentieth century secular decrease in the atmospheric electric circuit by Harrison (2002, 2004b) and Märcz and Harrison (2005). However, Harrison (2006a) found no evidence of galactic cosmic ray modulation of more recent surface PG measurements made at Kennedy Space Centre, USA, between 1997-2005. As cosmic ray intensity showed little change during this time, the effect may have been unclear in the PG measurements, compared to the longer timescales studied by Harrison (2002, 2004b) and Märcz and Harrison (2005). A change in measured early twentieth-century air conductivity vertical profiles over central Europe was found by Harrison and Bennett (2007a), that was also consistent with a decrease in cosmic ray intensity during this time.

2.7 Measurement of the atmospheric conduction current density

The conduction current density (J_C) is generally considered to be the most representative electrical parameter measured at the surface for investigation of the global electric circuit (e.g. Chalmers, 1967), although the Potential Gradient (PG) is by far the most frequently sampled parameter spatially and temporally (Harrison, 2004c). Due to the importance of J_C for global circuit monitoring, a review of published methods of J_C measurement is included in this chapter.

As described in chapter 1, the conduction current density is one of several components contributing to the total current J_S received by a horizontal conducting electrode at the earth's surface, electrically isolated from the ground. With no precipitation, J_S (the total air-Earth current density) comprises contributions from turbulence J_T , conduction J_C and displacement J_D

$$J_S = J_C + J_D + J_T \quad (2.1)$$

where J_C is generally regarded as the component flowing as a result of the global electric circuit. The displacement current density J_D is induced by changes in the PG. The turbulent current density J_T arises due to the transport of space charge by air turbulence. As J_C is the contribution to J_S arising from the global atmospheric electric circuit (Rycroft et al. 2000), a distinction is required between this component and J_D , which is effectively a local source of noise. This section describes instrumentation to measure J_C (when the J_T component is negligible), and the methods used to separate J_D and J_C from the directly measured J_S are discussed. A table of collectors to be discussed in this section and their author and year of publication is provided in Table 2.3.

Air-earth current collector	Author
Plate, flush with ground	Wilson (1906)
Plate, flush with ground	Simpson (1910)
Plate, flush with ground	Scrase (1933)
Metal plate or mesh	Kasemir (1955)
Hemispherical bowl flush with ground	Adamson (1960)
Spherical collector, 2.7m above the ground	Burke and Few (1978)
Disc and hemispherical bowl, flush with ground (proposed)	Mukku (1984)

Table 2.3 Authors (and year of publication) of different methods of J_C measurement considered in this section.

Methods of air-Earth current density measurement can be categorised as being either direct or indirect (Chalmers, 1967). Direct methods measure the current density received

at an electrode. Indirect methods measure the PG and total air conductivity (σ_T) independently, and calculate the current density from Ohm's Law (equation (1.3)).

Wilson (1906) was the first to use the direct method of J_C measurement, as recently described by Harrison and Ingram (2005). Another direct method was that of Simpson (1910), who connected an electrically isolated 17m² horizontal metal plate to a Kelvin water dropper. The water dropper equalised the potential of the plate with Earth, and the total charge carried away from the plate was measured by collecting the water droplets' charge using an electrometer. The total charge measured by the electrometer was measured every two minutes, providing a method of continuous J_S measurement.

A more recent direct approach to measuring J_C is that of Burke and Few (1978). Their sensor consisted of a 15cm radius hollow aluminium sphere (which also housed the electronic components), suspended 2.7m above the surface by a horizontal insulated wire strung between wooden supports spaced at the corners of a 6m equilateral triangle. The spherical sensor was split into two hemispheres, electrically separated by an insulating disk. (For insulation, Byrne *et al.* (1993) used Polytetrafluoroethene, PTFE). In principle, the sensor operates by flow of the conduction current flow from the air into one of the hemispheres and out of the other. The current passing between the two hemispheres was measured by an integral electrometer, and the readings transmitted by radio to allow the sphere to remain electrically isolated. Sensors of other geometry have also been used, notably an insulated long horizontal wire. The use of a horizontal wire antenna for direct measurement of the air-Earth current density was described by Kasemir (1955a) and more recently investigated by Tammet *et al.* (1996). Retalis (1991) measured the air-Earth current density directly using a flat plate collector. Recent indirect measurements at the surface include Israelsson and Tammet (2001). This indirect method of J_C determination multiplied PG measured by radioactive collector and field mill with total air conductivity found by bipolar Gerdien-type aspirated condensers, in accordance with equation (2.2),

$$J_C = \sigma_T F \quad (2.2).$$

The mean value of J_C at their low-pollution Swedish site between 1993-1998 was 2.44pAm⁻², with a standard deviation of 5.57pAm⁻² (Israelsson and Tammet, 2001). Airborne methods for J_C measurement have been either indirect (e.g. Anderson, 1967 using aircraft measurements of PG and σ_T) or direct (e.g. Rosen *et al.*, 1982) who used a vertical long wire antenna (Kasemir (1955) below a balloon. However, Hamilton (1969) expressed concern that J_C directly measured above the surface would have greater

uncertainty than measurements made flush with the ground due to the turbulence current J_T affecting both the top and bottom of the sensor electrode.

Differences in J_C using the direct and indirect methods have been reported, for instance Oluwafemi et al (1975) reported “substantial differences” between direct and indirect J_C determination, which they attributed to the presence of space charge near the surface. The space charge would prevent the Ohmic assumption (equation (2.2)) from applying exactly, and advection of space charge would invalidate its use in one dimension.

2.7.1 Methods of displacement current density correction

Calculation from Potential Gradient measurement

The displacement current (J_D) arises from changes in the PG, which is a major error term in determining the conduction current density (J_C) from the total current density (J_S) received by a collecting plate. The relationship between PG variation and J_D is given by Chalmers (1967) as:

$$J_D = -\epsilon_0 \frac{d}{dt} F \quad (2.3)$$

where ϵ_0 is the permittivity of free space, t is time in seconds and F is PG. If the PG decreased by 100Vm^{-1} in one hour, equation (2.3) gives $J_D = 0.25\text{pAm}^{-2}$, approximately 25% of the typical J_C . A change in PG of 100Vm^{-1} per hour or more is not uncommon near the surface during fair-weather, especially over short (~10 minute) timescales over land, from movement of local space charge.

The atmospheric existence of J_D was confirmed by the measurements of Wilson (1906). In this early system, the displacement current was accounted for by adjusting a compensating capacitor to maintain zero potential on the current collecting plate (with respect to earth) when the plate was first exposed to the electric field (Harrison and Ingram (2005)). The Wilson method was subsequently modified for continuous recording. J_D was found using a continuous PG record (Simpson, 1910) who recorded the potential gradient before and after the current measurement, therefore determining the overall J_D . (Such a method did not allow for fluctuations with periods less than the few minutes required to measure the current). This approach required a separate PG instrument, and an assumption that the measured PG represented the PG at the plate. Any difference between the response time of the J_S and PG sensors must also be considered for the J_D correction to be applied correctly. In a further development, Scrase (1933) placed a wire net connected to a radioactive potential equaliser over the Wilson collecting plate,

choosing the time constant to be longer than that of the measuring instrument. As the potential equaliser was slow to respond, the net would not have always been at earth potential, and the current from the collecting plate would not have been exactly that expected for a fully exposed plate.

Adamson (1960) accounted for J_D using a similar principle to Scrase (1933), but with the advantage of electronic methods to account for the changing PG: Adamson used a double electrometer valve instead of Scrase's quadrant electrometer arrangement. Additionally, the time constants of the collecting and electric field measuring circuits were adjusted to be as equal as possible, including the capacitance of the shielded cable between the collecting plate and the electrometer. Adamson (1960) reported reduction of the J_D component to less than 20 per cent of its previous value, for the majority of PG changes.

Matching circuit method

An electronic method for suppressing J_D was investigated by Kasemir (1955b). This used a capacitor C in parallel with a resistor R , connected between the collecting plate and ground. The RC time constant was chosen to approximate the electrical relaxation time of the lower atmosphere. This arrangement permitted the displacement current to pass to ground through the capacitor, whilst the conduction current passed through the resistor for measurement. The main disadvantage is the assumption of constant air conductivity, so that any change of potential due to a conductivity change would not be accounted for. Since the surface air conductivity varies, the Kasemir (1955) method can only realistically provide a partial compensation of J_D (Gherzi, 1967). Additionally, short-period (order minutes) J_C variability can not be resolved due to the required instrument lag of ~ 1000 s. Despite this, the Kasemir compensation method has proved popular (e.g. Burke and Few (1978), Retalis (1991) and Gherzi (1967)).

Geometrical cancellation method

A new concept in air-earth current density measurements was proposed by Mukku (1984), based on the physical principle that J_D is proportional to the collector *surface area*, but J_C is proportional to the collector's *cross-sectional area*. Two electrically isolated collecting plates for current measurement were considered, of equal surface areas, but one a circular disk and the other a hemispherical shell. As both collectors receive the same J_D owing to their identical surface areas, the difference between the collector currents would be directly proportional to J_C , with J_D cancelled. The same approach could measure J_D , if the horizontal cross sectional areas were equal, since this would cause each collector to receive the same J_C . Mukku (1984) also suggests that the effect of contact potentials

could be minimised by using similar materials for both collectors. Such a geometrical method has clear benefits over other established methods, as

- It does not rely on assumptions of constant local air conductivity
- The simplicity of the geometrical method depends on collector geometry and requires no additional compensating electronics
- J_D is measured in addition to J_C and not simply diverted straight to ground

The geometrical method has not hitherto been investigated experimentally and its first practical use in the atmosphere is reported in chapter 4.

2.7.2 Summary of J_C measurement methods

A summary of the different methods of conduction current measurement is given in Table 2.4. All of the methods to measure J_C involve the rate of collection of charge on a collector isolated from earth but kept at a voltage as close to earth potential as possible (so that it does not generate its own field that will affect the flow of charge onto the collector) and measure the current flowing from the air to the plate. An exception to this is the Burke and Few (1978) sensor that is not at earth potential but the potential of the atmosphere at the height of installation. In order not to allow the apparatus to modify the electric field over the collector, the collector (and even entire apparatus in the case of Wilson's method in Kew) is kept flush with the surface and consequently near-horizontal sites are chosen. Again, an exception to this is the spherical-shaped collector of Burke and Few (1978) that is suspended above the surface and measures the current flowing between the two hemispheres.

Additionally, a successful method for global circuit monitoring must discriminate between the displacement and conduction currents. The methods of this discrimination are based either on adjustment of the plate voltage using a compensator (Wilson, 1906), calculation of the displacement current using an independent field mill such as Simpson (1910) and Adamson (1960). Choosing an RC time constant to approximate the electrical relaxation time of the atmosphere is a popular choice that has been incorporated in designs since the suggestion by Kasemir (1955), such as Burke and Few (1978) although the drawback to this method is that constant air conductivity must be assumed (although this is not observed in reality). By far the most simple and seemingly robust method of displacement current compensation is the use of two collecting plates of differing geometry (Mukku, 1984), that take advantage of the physical difference between the induced displacement

current and the current caused by an actual accumulation rate of charge from the air such as the conduction current.

The effect of the possible surface electrode layer must also be considered since any gradient in space charge adjacent to the collector is liable to be converted into a turbulence current by turbulent mixing. This current may be comparable to the conduction current so care must be taken in the interpretation of current measurements when this process is expected to have occurred, when comparing current derived from direct and indirect methods or between current measured at the surface (which will only receive the positive component of the conduction current) and above the surface (such as the Burke and Few (1978) sensor) as although both components of the conduction current are measured by this sensor, the assumptions that no space-charge gradient exists between the top and bottom of the sensor and that conductivity is essentially uniform (the Kasemir (1955a) method of displacement current elimination) are unlikely to persist through the measuring interval.

Although the geometry of the Mukku (1984) apparatus directly cancels the displacement current, the method or equipment are still unable to account for the turbulence current. Methods for measurement and compensation for the turbulence current density (J_T) are as yet unproven, although research into the eddy diffusivity, the surface electrode effect and space charge gradients (such as Oluwafemi *et al.*, 1975, Vitta, 1974 and Mareev *et al.*, 1996) and the development of rapid response turbulence sensors such as sonic anemometers represent advancement in this area. J_T at the surface is however considered small compared to J_C during fair weather (Hamilton (1969), Gherzi (1967)), see chapter 5 for experimental verification of this assumption.

Author	Air-earth current collector	Current detection	Displacement current correction	Operating potential	Time constant/sampling frequency
Wilson (1906)	Plate, flush with ground	Gold leaf electrometer	Manual correction (compensator)	Earth	5 minute collection
Simpson (1910)	Plate, flush with ground	Gold leaf electrometer	PG measurement before and after collection	Earth	Registration every 2 minutes
Scrase (1933)	Plate, flush with ground	Quadrant electrometer	Wire net connected to equalizer	Earth	10 minutes
Kasemir (1955)	Metal plate or mesh	Electrometer (one stage d.c. thermionic amplifier)	Time constant set similar to atmospheric relaxation time	Earth	Order 10 minutes
Adamson (1960)	Hemispherical bowl flush with ground	Feedback thermionic amplifier	Valve circuit and field mill incorporated directly into electrometer stage.	Earth	20 seconds
Burke and Few (1978)	Spherical collector, 2.7m above the ground	Specialist amplifier circuit	Time constant set similar to atmospheric relaxation time	Same potential as surrounding air	Order 10 minutes
Mukku (1984)	Disc and hemispherical bowl, flush with ground (proposed)	Voltage drop and opamp follower proposed	Geometrical	Earth	Not implemented; freedom of choice using this theory

Table 2.4 Comparison of different methods to directly measure the conduction current density.

2.8 Discussion

Since the discovery of atmospheric electricity in the 18th century, an increasing amount of evidence has been gathered to support the hypothesis originally proposed by Wilson (1906) of some form of global atmospheric circuit. All the major components of this circuit (such as ionospheric potential, columnar resistance and global lightning activity) have now been measured, although a complete, global quantitative account linking all these factors is yet to be made. Attempts to numerically model this circuit have successfully demonstrated the fundamental aspects such as the effect of the aerosol profile and cosmic ray variability, although there is still a high level of uncertainty for some of the parameters used in the model. Areas of greatest model uncertainty include fundamental values such as global mean ionospheric potential and total upward current (Tinsley and Zhou, 2006). A high-resolution columnar resistance model used to test sensitivity of surface atmospheric electrical parameters to aerosol, temperature and ionisation rate vertical profiles is described in chapter 3.

The surface parameter most fundamental to the global circuit is the air-Earth conduction current density, J_C , as it is only a function of ionospheric potential and columnar resistance under fair weather, Ohmic conditions (equation (1.1)). There is a range of published methods to measure J_C , in particular on its separation from the displacement current component. A common method (Kasemir, 1955) attempts to match the RC time constant of the sensor to that of the atmosphere, with the main disadvantages of having to assume constant air conductivity and an inability to measure short-period (order minutes) J_C variability, as the instrument results in a lag of ~ 1000 s. A method to separate J_C and J_D using two electrodes of different geometry has been proposed (but yet to be experimentally verified) which does not have these disadvantages. This geometrical cancellation theory was experimentally tested during this thesis using instrumentation described in chapter 4, with results given in chapters 5 and 6.

3 Modelling the atmospheric electrical columnar resistance

3.1 Overview

The study of atmospheric electricity links local and remote processes that contribute to the nature of parameters measured at the surface. For example, the air-Earth current density J_C is the source of fair-weather PG at the surface. This current is modulated by properties of the entire atmospheric column above the surface measurement. The two factors that control this current density are the columnar resistance, R_C , and the ionospheric potential, V_i . The model presented in this chapter calculates R_C , allowing J_C and PG to be calculated for a given value of V_i . As ionisation rate from cosmic ray intensity is an important factor in determining R_C , the strength of the geomagnetic field (which varies spatially) must also be considered as this regulates cosmic ray intensity. In addition to integrated columnar properties, there are local contributing factors which further modify the calculation of electrical parameters such as local ionisation rate (when the cosmic ray ionisation component is small compared to terrestrial sources such as near the land surface), aerosol number concentration and ion mobility, all of which must be represented in the model.

In order that surface measurements of atmospheric electrical parameters such as PG, J_C and σ_T and their interrelations are better understood in terms of relative importance of local and global effects, a numerical model is required. J_C flows vertically between the lower ionosphere at about 50km altitude to the surface. The greatest variation of atmospheric properties such as air density (which largely defines the ionisation rate profile) is also in the vertical direction. Therefore, a vertical profile model is best suited for investigation of atmospheric electricity. Thunderstorms and shower clouds generate complex perturbations in most atmospheric electrical parameters (MacGorman and Rust, 1998). Fair-weather is the more usual atmospheric situation (away from the main thunderstorm source regions in the tropics) and will consequently be most representative of mean observations. The fair-weather condition shows the least horizontal disturbance and key processes such as the balance between ion generation and loss are considered to be in steady-state. These conditions make fair-weather the simplest and conventionally modelled situation (e.g. Tinsley and Zhou (2006), Makino and Ogawa (1985)).

Details of a fair-weather (steady-state) vertical profile model will be presented in this chapter. The model is designed to be used to investigate measurements made at the

RUAO (Reading University Atmospheric Observatory), including expected magnitudes of atmospheric electrical parameters and the relative contribution of local and global effects on surface PG and J_c .

A detailed account of the processes and equations relating to the R_c calculation will be given in later sections. However, to aid explanation of the principles used for the columnar resistance model, some important equations will be presented in this introductory section, and a further overview of the model and governing equations may also be found in Harrison and Bennett (2007a).

In order to calculate the columnar resistance, R_c in Ω , the air electrical resistivity (i.e. inverse of total conductivity, σ_T , in Sm^{-1}) vertical profile must be calculated and integrated between the surface and upper height limit of the model (in m), which is considered to be the height above which the contribution to R_c is negligible.

$$R_c = \int_0^{Z_{VI}} \frac{1}{\sigma_T(z)} dz \quad (3.1),$$

where z is height and Z_{VI} is the upper height limit (in m), which corresponds to the height of the ionospheric potential. The conductivity of the air is a product of the mean ion number concentration (\bar{n}), charge (e) and mean ion mobility (μ)

$$\sigma_T = 2e\bar{n}\mu \quad (3.2).$$

The ion charge (e) will be equal in magnitude to the electron charge, which is a physical constant at approximately $1.6 \times 10^{-19} \text{C}$. The ion mobility relates to the speed an ion will move when subjected to an external electric field, given as the speed per unit electric field strength. The ion mobility is fundamentally controlled by the mass of the ion, which relates to its chemical composition. However, like any object travelling in a fluid, the actual speed of the ion in an electric field is also influenced by the density of the fluid it is passing through. If the ion mobility is known for a reference air density (i.e. for standard temperature and pressure) then the mobility for a specific air density can be found by the scaling equation:

$$\mu(z) = \mu_0 \cdot \frac{P_0}{P(z)} \cdot \left(\frac{T(z)}{T_0} \right)^{\frac{1}{2}} \quad (3.3)$$

Where μ_0 is a reference mobility at a temperature T_0 and pressure P_0 , $\mu(z)$ is found for air temperature T and pressure P . From this equation it is apparent that the vertical temperature and pressure structure of the atmosphere is required by the model.

The mean ion number concentration, \bar{n} , (units of cm^{-3}) is the second parameter that is required for calculation of air conductivity by equation (3.2) and therefore ultimately R_C . The model uses the steady-state ion-aerosol balance equation which describes ion generation by ionisation of neutral air molecules and ion loss by recombination or attachment to aerosol. The equation for steady-state is given as (Harrison and Carslaw, 2003):

$$\bar{n}(z) = \frac{\left[\sqrt{(\beta^2 N^2 + 4\alpha q)} - \beta N \right]}{2\alpha} \quad (3.4),$$

where α and β are the ion-ion recombination and ion-aerosol attachment coefficients respectively, q is the ion pair production rate and N the aerosol number concentration. Both of these coefficients are height dependent as they are related to air temperature and pressure, the details of which are described in a later section of this chapter. The ion-pair production rate is a function of both the ionisation rate and air density, which will also be described in a later section. From equation (3.4) it can be seen that ionisation rate and aerosol number concentration determines the ion number concentration for a specific air density once the coefficients are calculated, so their input into the model is of considerable importance.

From the parameters needed in equations (3.1)-(3.4) a summary of the main atmospheric properties that are used by the model for the calculation of columnar resistance is shown in Figure 3.1. The ionospheric potential (V_i) is included in Figure 3.1 as it needed in combination with R_C to determine PG and J_C , although V_i is not required for calculation of R_C itself.

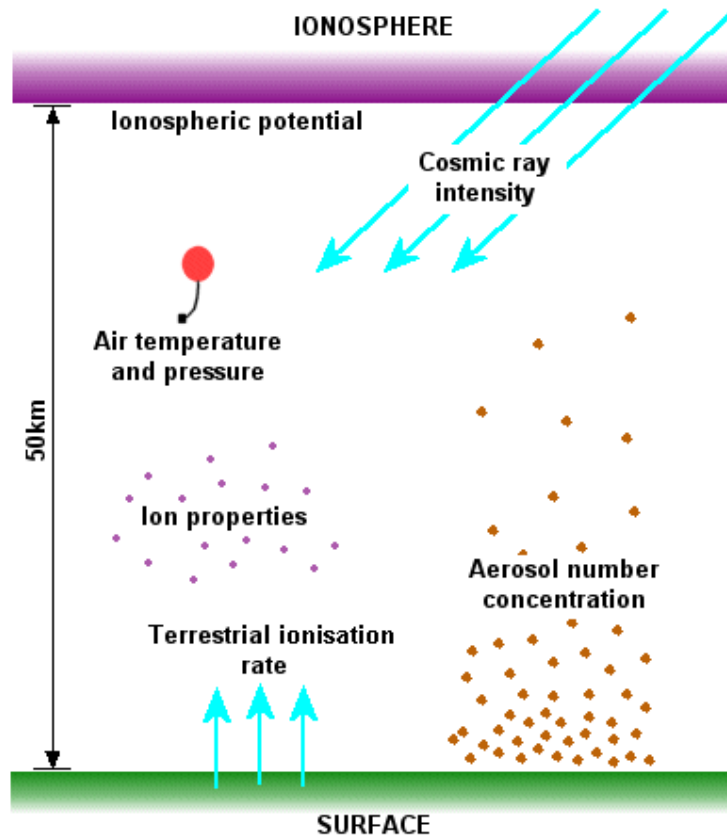


Figure 3.1 Illustration showing atmospheric properties that are used by the vertical profile model in the calculation of columnar resistance.

3.2 General aspects of previously published columnar resistance models

A comparison between previously published models has been described in chapter 2, either in their entirety if they are purely vertical profilers or considering an individual grid point in the case of global models. This section identifies key aspects required for a columnar resistance model based on previously published models, including a discussion on the atmospheric parameters required to model R_C and how they are likely to vary with height.

The resolution of a columnar resistance model must take into consideration the rate of change of input parameters with height, as the ultimate function of the model is to integrate the resistivity profile with height as in equation (3.1). If the resistivity profile changes rapidly with height, then a finer vertical resolution is required. Considering this, some models have a varying vertical resolution (Makino and Ogawa (1985), Tinsley and Zhou (2006)), with higher resolution (50m) near the surface where the greatest vertical

gradient of resistivity is found (Hoppel et al. 1986), reducing to 500m in the upper region of the model.

Aerosol number concentration is strongly related to total conductivity near the surface (Harrison, 2006), so regions with a strong gradient of aerosol number concentration will also have sharp conductivity gradient. The aerosol vertical gradient is pronounced at the top of the planetary boundary layer, (Pruppacher and Klett, 1997). Any vertical resolution near the surface must therefore be high enough to adequately resolve the sharp conductivity gradient in the boundary layer, as this layer provides significant contribution to the total R_C (Sagalyn and Faucher, 1956). The height of the boundary layer varies both diurnally and seasonally, with values over an urban environment down to below 200m (Harrison and Aplin, 2003). Del Guasta (2002) used a LIDAR to estimate aerosol scale height (assuming an exponential decrease in concentration from the surface) in an urban boundary layer, obtaining values commonly between 100-300m. According to Hoppel et al. (1986) the first 2km contributes to approximately 50% of R_C , corresponding to an average sensitivity of 2.5% per 100m height. This emphasises the importance of adequate representation of the lowest region of the atmosphere.

Considering a typical boundary layer depth of around 100-300m, and a mean height sensitivity to R_C of 2.5% per 100m below 2km, a resolution of 50m for previously published models is likely to be sufficient for identifying the presence of a boundary layer, but of course the finest resolution possible for the model assumptions (as detailed later in this chapter) would be ideal.

The aerosol number concentration vertical profile is commonly modelled using an exponential decrease from the surface (Makino and Ogawa (1985), Del Guasta (2002)) or a surface exponential with additional stratospheric contribution (Sapkota and Varshneya). However, an aerosol profile that considers both the large value and rapid reduction in aerosol number concentration with height in the boundary layer, whilst retaining the exponential characteristics of the lower value and more gradually decrease of aerosol in the free troposphere (Pruppacher and Klett, 1997) is considered preferable (Harrison and Bennett, 2007a). The ionisation rate profile should include both a terrestrial and cosmic ray component in accordance with observations over a land surface (Hoppel et al. 1986). An empirical formula incorporating both these effects has been constructed by Makino and Ogawa (1985) that was used by themselves and Sapkota and Varshneya (1990) in a columnar resistance model, although a physically-based (yet more complicated) cosmic-ray ionisation model such as Usoskin et al. (2002) may provide more accurate representation.

The height of previous columnar resistance models extends to an altitude of 60km (Makino and Ogawa (1985), Tinsley and Zhou (2006)). Considering the first 13km is reported by Hoppel et al. (1986) to contribute to 95% of R_C , then any value of model upper height greater than 13km would be expected to be representative of R_C to within 5%.

Based on previous published models and reported observations of the columnar resistance and aerosol number concentration profiles, a columnar resistance model that incorporates these aspects has been designed. The details of which will be provided in the following sections.

3.3 Model outline

Direct measurements of atmospheric electrical parameters are not routinely observed and their accurate observation is usually difficult. However, this model uses simple meteorological profiles such as those of air temperature and pressure with geophysical, aerosol and ion properties to predict atmospheric electrical profiles. The model (written in C++, see appendix for full code) requires knowledge of fundamental constants (such as the elementary charge, atomic mass unit etc) and user-defined input parameters. These may be separated into parameters that do not change with height and those that require a height value for their calculation.

As vertical profiles are calculated, pre-processing is needed to determine those input parameters that are height dependent before the model can begin the main processing steps. Once the main processing has been completed for each height, post-processing is needed to determine the principal model outputs, which are atmospheric electrical parameters. This stage includes integration through all the model heights.

3.4 Model Assumptions

The model described in this section is primarily for use as a tool to investigate surface values of P_G , J_C and σ_T . The first two require a value of the columnar resistance, R_C . Therefore the total conductivity vertical profile must be calculated, which in turn requires knowledge or assumptions about the ionisation rate and aerosol profiles, together with assumptions about the ions that are produced and how they interact with aerosol and each other over a range of atmospheric temperatures and pressures. The basic assumptions of this model (and their justifications) are as follows:

1. *Ion pairs are produced by cosmic ray ionisation and from terrestrial radioactive sources near the surface.*

Cosmic ray ionisation and terrestrial radioactivity are regarded as the main sources of ion pair production below approximately 50km (MacGorman and Rust, 1998). Other sources of stratospheric ion pairs are relativistic electrons precipitated from the radiation belts and solar energetic particle events (Tinsley and Zhou, 2006). These additional sources only appear intermittently such as during geomagnetic storms and do not usually penetrate into the troposphere (Tinsley and Zhou, 2006), where the majority of columnar resistance is found. Therefore, this assumption is appropriate for the majority of the time (i.e. non-geomagnetic storm conditions) and especially for the region of atmosphere containing the largest columnar resistance component (the troposphere). Terrestrial ionisation occurs over land due to the presence of natural radioactivity such as Radon gas (Hoppel et al. 1986).

2. *Aerosol particles are assumed spherical and monodisperse.*

Although aerosol particles have a broad range of shapes depending on their individual coagulation and formation characteristics, a spherical shape is used to represent an aerosol particle (Prauppacher and Klett, 1997) as this size is easily quantified; requiring only a value of radius. The simplicity of this shape therefore allows more straightforward mathematical modelling of ion-aerosol interaction. Spherical particles have been assumed for all of the published atmospheric electrical models which include aerosol, the latest being Tinsley and Zhou (2006). In addition, all previous models with the exception of Tinsley and Zhou (2006) assume a monodisperse aerosol population (i.e. with a constant effective radius) for each vertical profile. This is justified providing the aerosol size distribution is narrow enough and concentrated about a single radius. A single peak in aerosol size distribution does appear to occur in the ultrafine region (around 0.05 μm) over the continents, based on observations described by Prauppacher and Klett (1997).

3. *Aerosol particle charge can be neglected for calculations of total conductivity.*

Aerosol particles will become charged by attachment to ions. If ions of a particular sign are preferentially attached to the aerosol, it will assume this net charge. The amount of net charge an aerosol particle is capable of carrying is dependent on its size, the ambient temperature and the relative difference in ion mobility and concentration for the two signs of ions. In reality, a distribution of aerosol charge exists (Clement and Harrison, 1991) although it is the mean aerosol charge of this distribution that is of important for the model calculations. The theoretical mean aerosol charge j (Gunn, 1955) is:

$$j = \frac{4\pi\epsilon_0 r_a kT}{e^2} \ln \left[\frac{n_+ \mu_+}{n_- \mu_-} \right] \quad (3.5)$$

where e is the elementary charge ($1.6 \times 10^{-19} \text{C}$), ϵ_0 the permittivity of free space, T the absolute temperature, r_a the aerosol radius and k is Boltzmann's constant. n and μ are ion number concentration and mobility respectively, with the ion sign denoted in subscript. The mean aerosol charge has in itself no physical units, as it represents the number of elementary charges (e) on the aerosol (the units of which are in Coulombs). The equation component within the square brackets can also be described as the ratio of the polar ionic conductivities (or the ion asymmetry factor). This ratio was found experimentally by Woessner et al., (1958) who made simultaneous measurements of both polarities of conductivity from the ground to 26km over Washington D.C., USA. The polar conductivity ratio was found to be approximately 0.63 near the surface before increasing to 1.00 above 25km (MacGorman and Rust, 1998). Using equation (3.5) with an aerosol effective radius of $0.05 \mu\text{m}$, temperature of 273K and a ratio of polar ionic conductivity between 0.63-1.00 (Woessner et al., 1958) the theoretical mean aerosol particle charge can be calculated. The Gunn (1954) theory of ion-aerosol attachment for charged aerosol (the same theory used in this model) also allows the relative effect of aerosol charge on the total air conductivity to be calculated. This is achieved by comparing total conductivity calculated using charged aerosol particles to that derived using only neutral particles. Aerosol number concentration and ionisation rate were kept constant at $10,000 \text{cm}^{-3}$ and $10 \text{cm}^{-3} \text{s}^{-1}$ respectively, to simulate conditions near the surface where the ratio was lowest. The results of these calculations are shown in Figure 3.2.

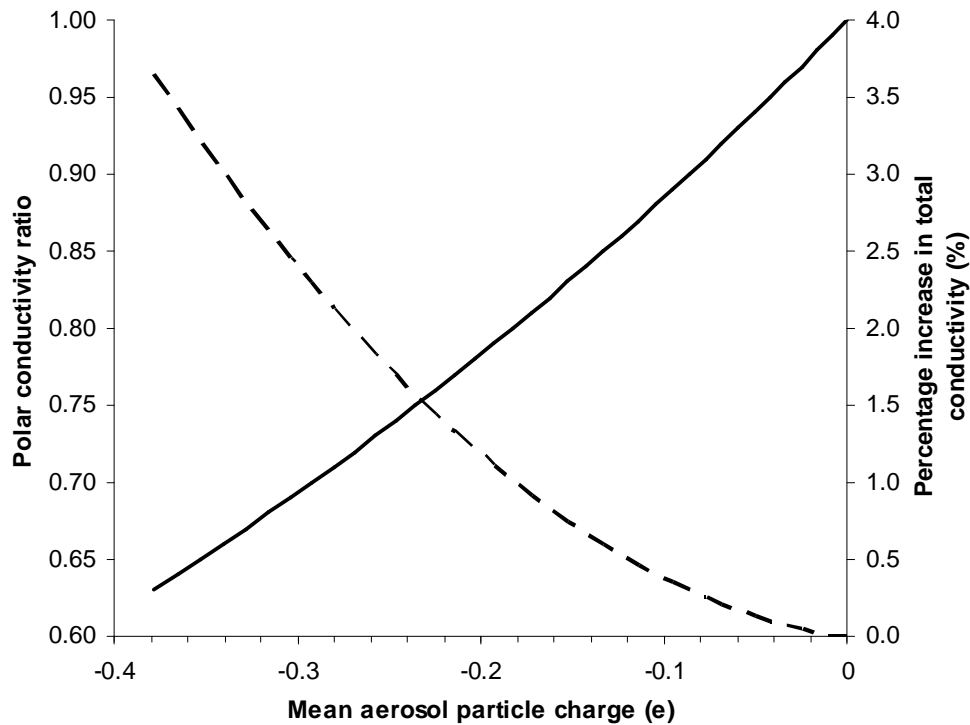


Figure 3.2 Effect of aerosol charge on conductivity. Solid line represents the calculated mean aerosol particle charge (in elementary charge units, e) using equation (3.5) using the observations of mean atmospheric polar conductivity ratios of Woessner et al., (1958). The dashed line is the percentage increase in total conductivity resulting from the charged aerosol, relative to the conductivity for neutral aerosol, using the Gunn (1954) theory of ion-aerosol attachment for charged aerosol. The temperature was fixed at 273K. An aerosol effective radius of $0.05\mu\text{m}$ and $10,000\text{cm}^{-3}$ number concentration was used, with an ionisation rate of $10\text{cm}^{-3}\text{s}^{-1}$ to replicate near-surface conditions.

From the results shown in Figure 3.2 it can be seen that for a range of typical atmospheric polar conductivity ratios and aerosol effective radius of $0.05\mu\text{m}$, the aerosol charge is no less than $-0.38e$ under near-surface conditions. This corresponds to a maximum percentage error in total air conductivity by assuming the aerosol was neutral of 3.7%, for a temperature of 273K, aerosol number concentration of $10,000\text{cm}^{-3}$ and ionisation rate of $10\text{cm}^{-3}\text{s}^{-1}$. This temperature would be expected near the surface where the smallest ratio was observed. As the temperature decreases with height, the magnitude of aerosol charge (and associated model error) will be less than the already small amount indicated by Figure 3.2 as charge is proportional to temperature from equation (3.5). Aerosol number concentration usually decreases and ionisation rate increases with height, and both will act to significantly reduce the sensitivity of aerosol particle charge on total conductivity, as ion loss by recombination becomes dominant over loss by aerosol attachment. Therefore a relative error of 3.7% is effectively an upper limit for calculation of

total conductivity for typical atmospheric conditions, with the error being significantly lower away from the surface.

The mean polar conductivity ratio vertical profile from Woessner et al., (1958) was measured over continental Europe, so would have likely experienced considerable aerosol concentration in the lower troposphere. This accounts for the low polar conductivity ratio near the surface as negative ions were preferentially attached to aerosol owing to their greater mobility (hence the aerosol has a net negative charge in Figure 3.2). The polar conductivity ratios of Woessner et al., (1958) are somewhat lower than that found by Gringel (1978) who determined the polar conductivity ratio during ten ascents, with a mean of about 0.87 at 6km, compared to approximately 0.72 by Woessner et al., (1958) for the same height. This further suggests that the Woessner et al., (1958) ascents were made during rather polluted conditions so act as an upper end value of the likely aerosol unit charge during fair-weather conditions over land.

It is therefore apparent that the relative error in assuming an aerosol particle is uncharged for the calculation of total conductivity is not high enough under fair-weather conditions to warrant the greatly increased model complexity required to account for aerosol charging.

4. *There is no net vertical flux of ions of either polarity.*

The assumption that there is no net flux of ions of either polarity can be justified by considering the ion drift velocity and lifetime. The mean ion drift velocity is the product of the mobility and PG. Ions will drift parallel to the direction of PG, which is vertical. This velocity is found by:

$$V_D = \mu \cdot F \quad (3.6)$$

where V_D is the mean ion drift velocity (in ms^{-1}) and μ the mean ion mobility. Using the Ohmic assumption, PG can be substituted by:

$$F = \frac{J_C}{\sigma_T} \quad (3.7)$$

Where J_C is the air-Earth conduction current density and σ_T is the total conductivity. Substituting this into equation (3.6) gives:

$$V_D = \frac{\mu \cdot J_C}{\sigma_T} \quad (3.8)$$

The total conductivity σ_T can be re-written as equation (3.2). This can be substituted into equation (3.8) to produce the equation:

$$V_D = \frac{J_C}{2ne} \quad (3.9)$$

To assess the validity of a zero net vertical flux of ions assumption, the drift velocity must be multiplied by the typical ion lifetime. This is found by considering the ion-aerosol attachment and ion recombination timescales (t_A and t_R respectively) found in the limiting cases of:

$$t_A = \frac{1}{\beta N} \quad (3.10)$$

$$t_R = \frac{1}{\alpha n} \quad (3.11)$$

Where α is the mean ion recombination coefficient, β the mean ion-aerosol attachment coefficient and N is the aerosol number concentration. The ion lifetime in an aerosol-dominated environment (i.e. near the surface) will approximate to t_A , and in the low-aerosol, high-ion concentration environment in the free troposphere and stratosphere, the lifetime is approximated by t_R . By combining equations (3.9), (3.10) and (3.11) it is possible to estimate the mean ion drift distance. The results of these calculations for heights where ion loss is dominated by aerosol attachment (near the surface) and ion recombination (upper atmosphere) are shown in Table 3.1.

	Mean n (cm^{-3})	N (cm^{-3})	α (cm^3s^{-1})	β (cm^3s^{-1})	J_C (pAm^{-2})	Drift distance (m)
<i>Aerosol dominant</i>	100	10000		2.0×10^{-6}	1.0	1.6
<i>Ion dominant</i>	2500		1.6×10^{-6}		1.0	0.3

Table 3.1 Mean ion drift distance for aerosol (near-surface) and ion (upper atmosphere) dominant heights. The value of β is from Hoppel et al. (1986) and the ion-dominant mean n and α from Harrison and Carslaw (2003).

From Table 3.1 it is seen that the mean ion drift distances for the typical values used are small for both aerosol and ion dominated ion loss, so assuming no net vertical flux of ions

is indeed justified at model resolutions greater than order 10m, where ~90% of ions should be contained within the model layer.

5. *The reduced positive and negative ion mobilities are constant with height.*

Reduced mobility is the mobility of an ion once corrected to standard temperature and pressure (STP) conditions. A change in reduced mobility with height implies a change in ion chemical composition (such as ion mass). The assumption that reduced ion mobility (and therefore ion composition) is constant with height can be justified by experimental data. For instance, the measured results of Gringel et al. (1983) and Rosen and Hofmann (1981) both show that the vertical profiles of positive small ion reduced mobility are generally constant with height especially above the first few kilometres.

6. *Any inequality between positive and negative ion number concentration (i.e. ionic space charge) for a given height is due only to selective attachment to aerosol, which results from differences between positive and negative ion mobilities. No dynamical local charge separation is permitted.*

The assumption of no ionic space charge generated by means other than selective attachment to aerosols must always be considered as an approximation as ionic space charge will always exist in reality due to the act of J_c flowing through a conductivity gradient. However, the ionic space charge (and therefore aerosol space charge by attachment) is usually small compared to the local ion concentration. This can be demonstrated using the theoretical calculation of ionic space charge density ρ_I along a conductivity gradient due to J_c using the equations of Hoppel (1967) with PG substituted by equation (3.7):

$$\rho_I = J_c \frac{\epsilon_0}{\sigma_T^2} \cdot \frac{d\sigma_T}{dz} \quad (3.12)$$

where z is height. If a strong vertical conductivity gradient existed near the surface such that $\sigma_T=10\text{fSm}^{-1}$ increased to 100fSm^{-1} within a vertical distance of 10m, producing a gradient $d\sigma_T/dz$ of 9fSm^{-2} , the ionic space charge generated by J_c of 1pAm^{-2} flowing through this gradient would be nearly 800pCm^{-3} . A conductivity gradient of this size will represent a well-defined cloud boundary where conductivity within the cloud drops to about 10% of the cloudless value (MacGorman and Rust, 1998). A conductivity gradient of this size is unlikely to be found in the typical aerosol profile. For example, for an ionisation rate of $10\text{cm}^{-3}\text{s}^{-1}$ and aerosol radius of $0.05\mu\text{m}$ a gradient of this size would be produced if the 16500cm^{-3} aerosol number concentration required for $\sigma_T=10\text{fSm}^{-1}$ dropped to only 300cm^{-3} 10m above this layer, which would be a very sharp aerosol concentration gradient indeed. Even if all the 800pCm^{-3} ionic space charge was transferred to the

aerosol population, this would produce an aerosol particle charge of $0.3e$ (assuming the 800pCm^{-3} is shared evenly between the 16500cm^{-3} local aerosol population). From Figure 3.2 this would have produced a $\sim 2.5\%$ relative error in total conductivity calculation if this aerosol charge was neglected.

In fair-weather conditions, such sharp conductivity gradients are unlikely to be produced even near the surface, so errors incurred by neglecting dynamically-produced local space charge (and assuming it is all transferred to the local aerosol) in the conductivity calculation are expected to be negligible for normal conditions, when typically observed fair-weather space-charge densities are less than 3pCm^{-3} near the surface and 0.1pCm^{-3} above the boundary layer (MacGorman and Rust, 1998). Any space charge caused by a strong conductivity gradient will only reside along the horizontal interface (i.e. cloud boundary), which would have only been 10m thick for the 800pCm^{-3} cloud boundary example. A 10m thick layer of 10fSm^{-1} would contribute to 1% of the total R_C if a typical value of $100\text{P}\Omega\text{m}^{-2}$ is assumed (Sagalyn and Faucher, 1954). A 2.5% error on a 1% component would therefore become insignificant in the calculation of R_C , which is the model's primary objective. Additionally, as ρ_l is proportional to σ_T^{-2} the effect will reduce rapidly with height as σ_T increases.

7. A steady-state exists between ion pair production and ion loss by recombination and attachment to aerosol.

The assumption states that a steady-state exists between ion pair production and ion loss by recombination and attachment to aerosol. For this assumption to be justified the ions must reside in the layer they were generated in for long enough to be lost either by recombination or attachment to aerosol. From the product of typical ion drift velocity and lifetime used to justify assumption 4, it was seen that the ions drift vertically by less than 10m (and even by less than 1m above the highest aerosol concentrations near the surface). Therefore all the aerosol and ion interactions required to reach a steady-state can be justifiably contained within 10m thick layers of the atmosphere under typical fair-weather conditions. Exceptions to this (and assumption 4) in reality would be significant vertical air movement carrying aerosol and ions mechanically, observed as turbulent current densities (J_T). As such, this fair-weather model will not adequately represent times and heights of notable convection.

8. All the columnar resistance exists between the surface and a height of 50km.

The assumption of the model is that all the columnar resistance (R_C) exists between the surface and a height of 50km. This can be justified by considering the typically observed conductivity profile. Such a profile was measured by Sagalyn and Faucher, (1954) who

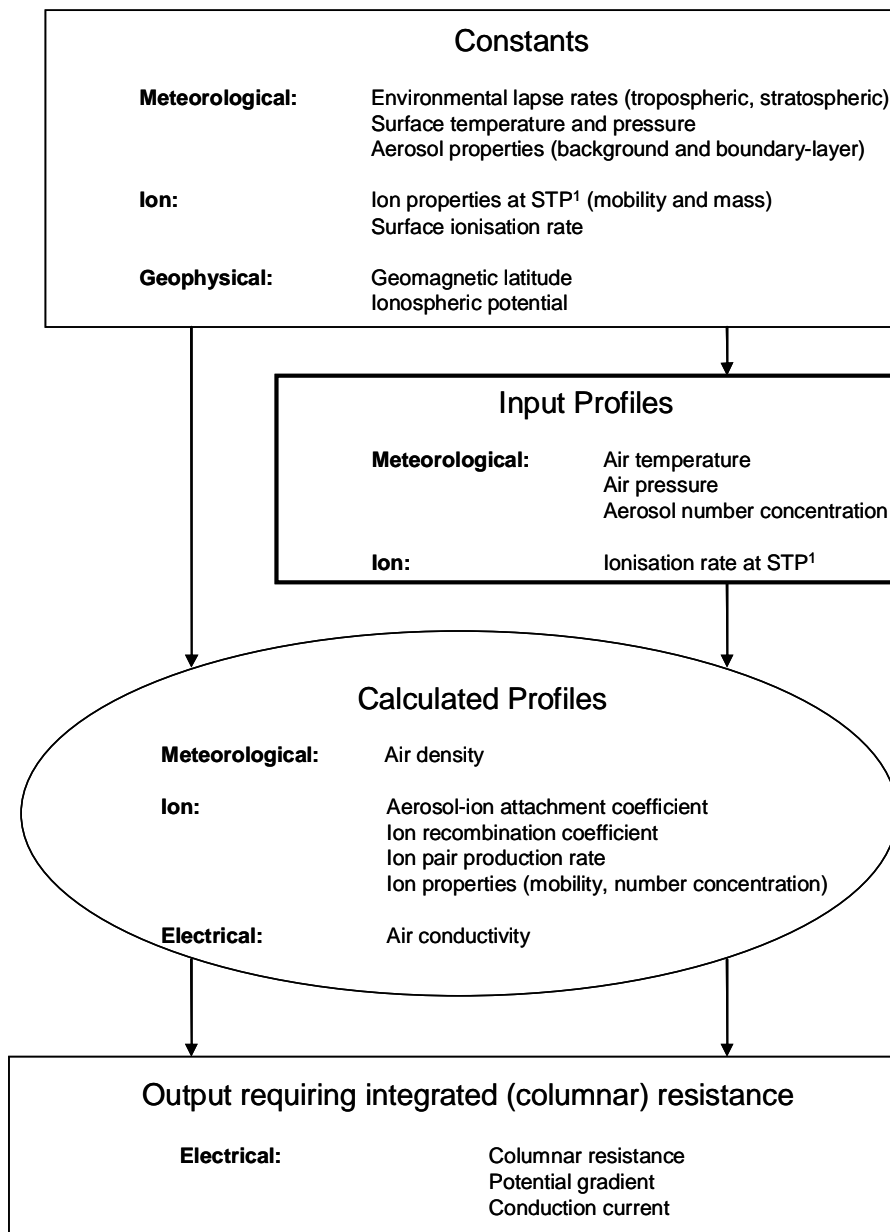
reported that 40-73% of R_C originated from the surface boundary layer (layer of air adjacent to the surface of order 1km thick). The first 13km usually comprise 95% of R_C (Gringel et al. 1986). As σ_T increases with height due to the increased ionisation rate, a negligible component of R_C would be expected to remain above 50km. This is especially likely as conductivity increases even more rapidly above this height when ionisation due to solar ultraviolet radiation exceeds that due to cosmic rays (Roble and Tzur, 1986).

9. *The air-Earth conduction current density is an Ohmic current resulting from the product of Ionospheric potential and columnar resistance; flowing vertically and uniform with height.*

In order that there is no accumulation of space charge gathering in the atmosphere, the air-Earth current density, J_C , must be constant with height. This assumption has been demonstrated by indirect measurements of J_C from balloon ascents such as that of Gringel et. al. (1986) and Rosen et al (1982) over continental landmass and Gringel et. al. (1978) over the ocean. All show a constant J_C with height during fair-weather conditions.

3.5 Model equations and processes

Before a detailed account of the model steps is presented, a summary of the model input and output profiles is given in Figure 3.3. The input profiles refer to data describing the atmospheric temperature and pressure structure (used for calculation of ion mobility, for example) and factors that control the ion number concentration, which are ionisation rate (for ion generation) and aerosol number concentration (for ion loss).



¹STP as 0°C and 1013hPa

Figure 3.3 Summary of the main inputs and outputs of the vertical profile model.

The steps involved in this model can be grouped into three main stages that relate to the order in which they are used by the model. These are:

- *pre-processing*

Steps required to convert raw inputs (single values) into vertical profiles of basic parameters (e.g. temperature profile) that are needed for subsequent profile calculations. These steps are shown in Figure 3.4.

- *Main processing*

The steps that use the basic input profiles calculated during pre-processing and calculate further vertical profiles of parameters which are required for the air conductivity profile. This is the key profile as from this the columnar resistance (R_C) can be found. These steps are shown in Figure 3.5.

- *Post-processing*

These steps use the air conductivity profile to find R_C , which is required for calculation of PG and J_C given V_i . These steps are shown in Figure 3.6.

A key describing the abbreviations used in the schematics is given in Table 3.2. In the model schematics, each step is given a number (generally coinciding with the sequence of execution within the model). The specific details of these individual steps are provided in a list after the schematics. A further description of this model, including sensitivity tests and output profiles can also be found in Harrison and Bennett (2007a), where it is demonstrated to closely follow measured profiles.

Symbol	Description	Units
AR	Aerosol radius	μm
BAC	Background aerosol number concentration at the surface	cm^{-3}
GML	Geomagnetic latitude	degrees
IM	Ionic mass (positive or negative)	amu
K_0	Standard ion mobility (positive or negative)	$\text{cm}^2\text{V}^{-1}\text{s}^{-1}$
SAC	Surface aerosol number concentration	cm^{-3}
SELR	Stratospheric environmental lapse rate	Km^{-1}
SIR	Terrestrial ionisation rate at the surface	$\text{cm}^{-3}\text{s}^{-1}$
SP	Surface air pressure	Pa
ST	Surface air temperature	K
SZ	Stratospheric base height	m
TELR	Tropospheric environmental lapse rate	Km^{-1}
TPELR	Tropopause environmental lapse rate	Km^{-1}
TPZ	Tropopause base height	m
VI	Ionospheric potential	V
Z	Height	m
ZBA	Background aerosol scale height	m
ZSA	Surface aerosol scale height	m
ZSQ	Terrestrial ionisation scale height	m

Table 3.2 Key to the abbreviations used in the model schematics.

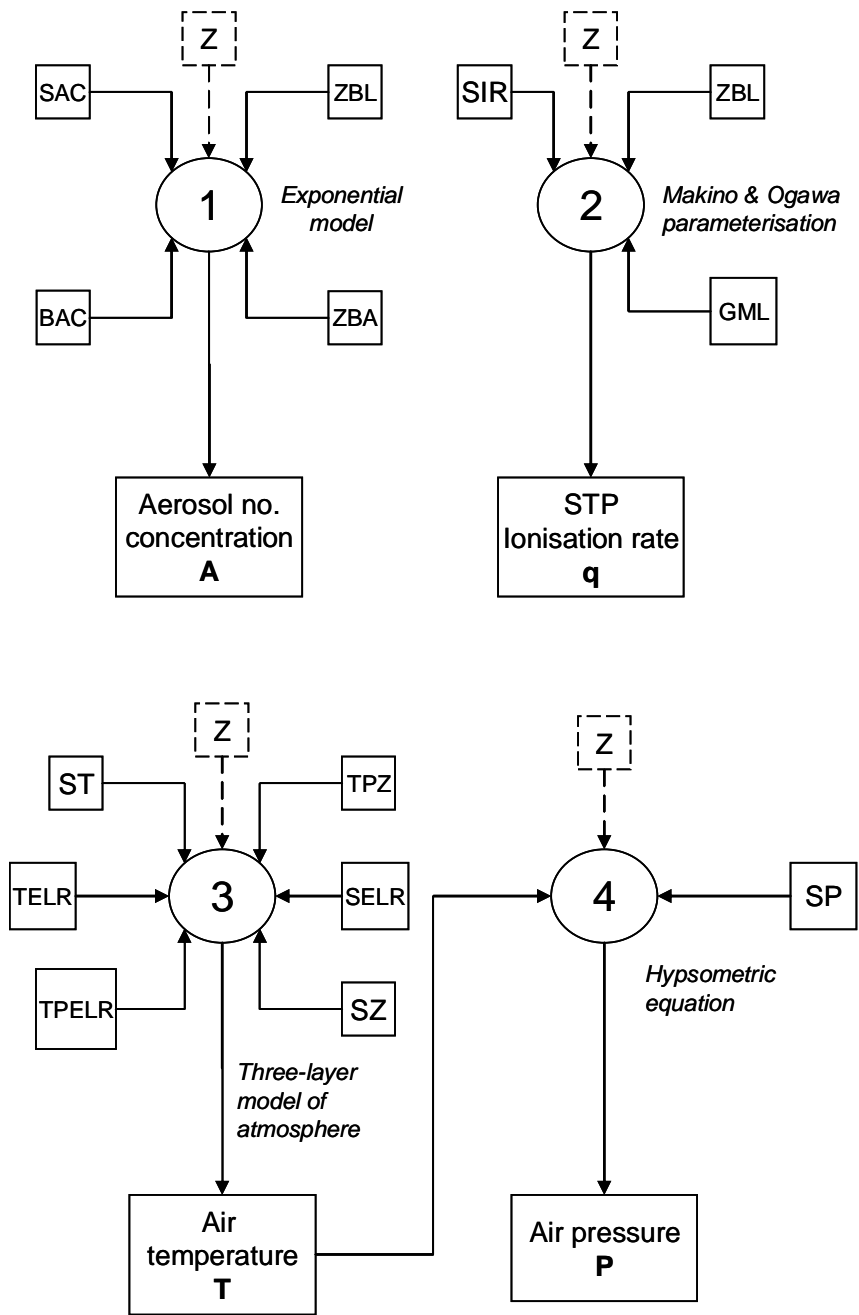


Figure 3.4 Schematic of model pre-processing steps at each level. The input values for each numbered step are identified by a square box, with the details on the governing equation described in later in this section.

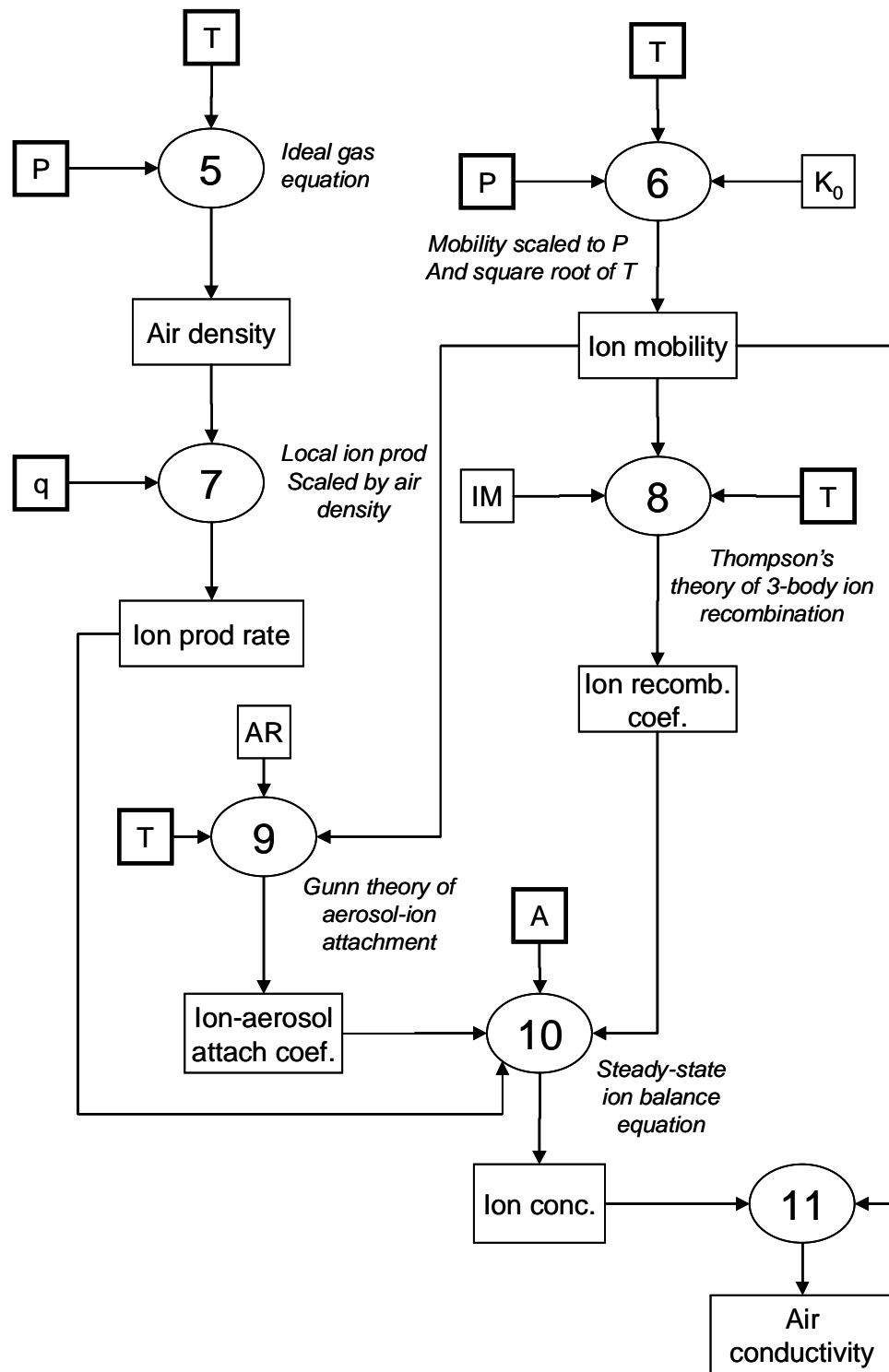


Figure 3.5 Schematic of model main processing steps at each level. Profiles from the pre-processing stage are outlined by a bold box, with the details on the governing equation described in later in this section.

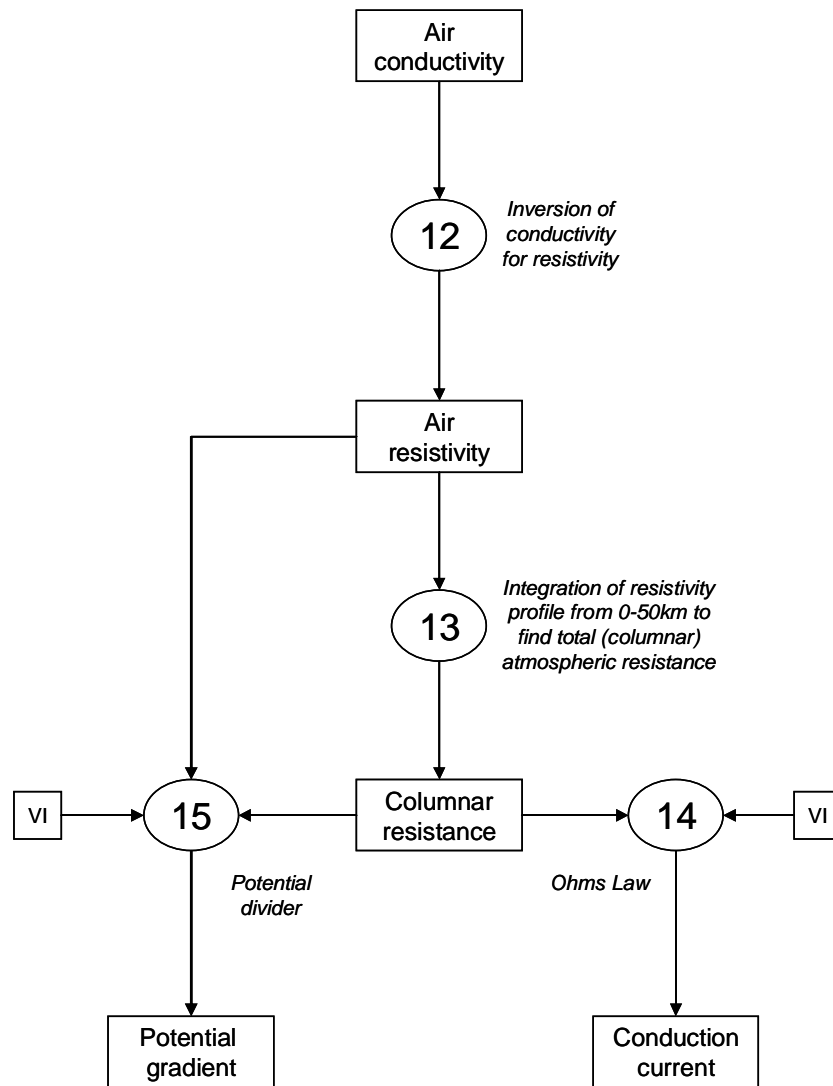


Figure 3.6 Schematic of model post-processing steps, showing the final output parameters of columnar resistance (R_C), potential gradient (PG) and air-Earth conduction current density (J_C).

Step 1 – Exponential model of aerosol number concentration

The aerosol profile can be represented as a number concentration decreasing exponentially with height (Pruppacher and Klett, 1978) in the mid to low troposphere. However, consideration must also be given for upper tropospheric/stratospheric aerosol, since the columnar resistance is particularly sensitive to upper level aerosol concentrations (Meyerott et al. 1983), where there is substantial ion production from cosmic rays. In light of this, the aerosol profile is represented using two exponential decreases (Harrison and Bennett, 2007a); one for the background aerosol concentration and another for the additional (and more variable) aerosol load of the planetary boundary layer. Such an approach is consistent with the double exponential model for the average PG vertical profile reported by Chalmers (1967). The equation used by this model is:

$$N(z) = N_{0BG} e^{-\frac{z}{z_{BG}}} + N_{0BL} e^{-\frac{z}{z_{BL}}} \quad (3.13),$$

where z is the height in metres, N_{0BG} and z_{BG} are the background surface aerosol number concentration and scale height, respectively, and N_{0BL} and z_{BL} are the boundary layer aerosol number concentration and scale height, respectively. For simplicity, the aerosol is considered monodisperse, usually with a prescribed effective radius of $0.05\mu\text{m}$. The choice of an effective radius of $0.05\mu\text{m}$ was based on the typically most abundant radius in the aerosol size distribution (Pruppacher and Klett, 1997).

Step 2 – STP Ionisation rate

The STP (standard temperature and pressure) ionisation rate profile $q(z)$ (units of $\text{cm}^{-3}\text{s}^{-1}$) is given by the parameterisation of Makino and Ogawa (1985) and requires the geomagnetic latitude and scale height of terrestrial ionisation. This profile is calculated using the following equations (Harrison and Bennett, 2007a):

$$q(z) = Q_0 e^{-\frac{z}{z_{si}}} + q_c(z) \quad (3.14),$$

where

$$q_c(z) = Q_a e^{-\frac{(z-z_a)}{S_a}} \quad \text{when } (z < z_a) \quad (3.15),$$

$$q_c(z) = Q_{\max} e^{-\left(\frac{z-z_{\max}}{S_b}\right)^2} \quad \text{when } (z_a \leq z < z_{\max}) \quad (3.16),$$

$$q_c(z) = Q_{\max} \cdot \frac{z}{z_{\max}} \cdot e^{-\left[\frac{1}{2}\left(\frac{z}{z_{\max}}\right)^2 + \frac{1}{2}\right]} \quad \text{when } (z_{\max} \leq z \leq 30\text{km}) \quad (3.17),$$

with Q_0 and z_{si} being the surface-generated ionisation rate and scale height respectively, q_c is the cosmic ray component of the ionisation profile, z_a is the reference height of ionisation rate, Q_a is the cosmic ionisation rate at the reference height, Q_{\max} is the maximum cosmic ionisation rate at a height of z_{\max} which is a function of latitude. Additionally, the scale heights S_a and S_b are used to scale the exponential profile below z_a and between z_a and z_{\max} , respectively (equations (3.15) and (3.16)). These scale heights are both functions of latitude, z_a and Q_a . The constants for the cosmic ray component of ionisation are based on latitude and an empirical fit to the data gathered by Neher (1967), full details of which are described in Makino and Ogawa (1985). The ionisation rate profile $q(z)$ is produced by adding the surface-generated component to either equations (3.15), (3.16) or (3.17) depending on height. For heights exceeding 30km, the ionisation rate is

fixed at the value for 30km. A recent experimental confirmation of this parameterisation has been given by Harrison (2005b) for mid-latitude air over Reading.

Step 3 – air temperature

A simple air temperature profile is included in this model to calculate temperature at each model height which is required for, example, in the calculation of the air density and components of the ion balance equation. The temperature profile $T(z)$ is calculated using the following equations:

when $z \geq z_{TP}$

$$T(z) = T_s + z \left(\frac{dT}{dz} \right)_{TR} \quad (3.18),$$

when $z_{TP} < z < z_{ST}$

$$T(z) = T_s + z_{TP} \left(\frac{dT}{dz} \right)_{TR} + (z - z_{TP}) \cdot \left(\frac{dT}{dz} \right)_{TP} \quad (3.19),$$

when $z \geq z_{ST}$

$$T(z) = T_s + z_{TP} \left(\frac{dT}{dz} \right)_{TR} + (z - z_{TP}) \cdot \left(\frac{dT}{dz} \right)_{TP} + (z - z_{ST}) \cdot \left(\frac{dT}{dz} \right)_{ST} \quad (3.20),$$

where TR , TP and ST denote the troposphere, tropopause and stratosphere respectively, $\left(\frac{dT}{dz} \right)$ is the environmental lapse rate corresponding to the atmospheric layer in subscript. By definition the lapse rate in the tropopause would normally be zero, although this is left as a variable in case a slight change with height is required. T_s is the air temperature at the surface, with z_{TP} and z_{ST} denoting the height of the tropopause and stratospheric base respectively.

Step 4 – air pressure

The air pressure is calculated using the hypsometric equation. This allows changes in air pressure (and therefore density) that result from a prescribed change in the air temperature profile. The air pressure profile $P(z)$ is found by:

$$P(z) = P_s \exp \left[- \frac{g}{R_d} \int_0^z \frac{1}{T} dz \right] \quad (3.21),$$

where P_s is air pressure at the surface, g is gravitational acceleration and R_d is the gas constant for dry air.

Step 5 – air density

The air density is derived using the ideal gas equation:

$$\rho_{air}(z) = \frac{P}{R_d T} \quad (3.22).$$

Step 6 – ion mobility

The vertical profile of ion mobility, $\mu(z)$, arises from a temperature and pressure dependence. Mobility is calculated using equation (3.3). The surface (reduced) ion mobility μ_0 was chosen as $1.4\text{cm}^2\text{V}^{-1}\text{s}^{-1}$ for positive ions and $1.9\text{cm}^2\text{V}^{-1}\text{s}^{-1}$ for negative ions, based on the findings of Bricard (1965).

Step 7 – local ion pair production rate

The STP ionisation rate calculated in step 2 must be converted into the local ion pair production rate $q_L(z)$ (which takes the air density into account), before its use in the ion balance equation. This step utilises the following equation:

$$q_L(z) = q(z) \left(\frac{\rho_{air}(z) \cdot R_d T_{SD}}{P_{SD}} \right) \quad (3.23).$$

With T_{SD} and P_{SD} denoting standard air temperature (273K) and pressure (101300Pa) respectively.

Step 8 – ion-ion recombination rate

Thomson's theory of 3-body ion recombination (Thomson, 1924) was used to calculate the recombination rate of atmospheric ions in this model. The strength of electrostatic force surrounding each positive and negative ion is considered as a spherical shell, and recombination of ions will occur if any third body passes within this shell. The equation used is complicated, and as such is broken down into components for clarity (McDaniel, 1964).

These components are combined make the complete ion recombination equation (units cm^3s^{-1}):

If $z < 40\text{km}$,

$$\alpha(z) = \pi a^2 \sqrt{(c_+^2 + c_-^2)} \left\{ 2 - \frac{\lambda_+}{2a} \left(1 - \exp \left[-\frac{2a}{\lambda_+} \right] \right) - \frac{\lambda_-}{2a} \left(1 - \exp \left[-\frac{2a}{\lambda_-} \right] \right) \right\} \quad (3.24).$$

If $z \geq 40\text{km}$

$$\alpha(z) = 1.3 \times 10^{-7} \quad (3.25).$$

The component a represents a critical distance (in units of metres) around each ion which relates to the longest ion separation distance required to cause a collision event, defined as:

$$a = \frac{e^2}{6\pi\epsilon_0 kT} \quad (3.26),$$

where e is the elementary charge ($1.6 \times 10^{-19}\text{C}$), ϵ_0 the permittivity of free space, r the ionic radius, and k is Boltzmann's constant.

$$c_+ = \sqrt{\left(\frac{8kT}{\pi m_+} \right)} \quad (3.27),$$

$$c_- = \sqrt{\left(\frac{8kT}{\pi m_-} \right)} \quad (3.28),$$

$$\lambda_+ = \frac{8\mu_+}{3e} \left[\frac{kTm_+M}{(M + m_+)} \right]^{\frac{1}{2}} \quad (3.29),$$

$$\lambda_- = \frac{8\mu_-}{3e} \left[\frac{kTm_-M}{(M + m_-)} \right]^{\frac{1}{2}} \quad (3.30).$$

Where m is the ionic mass (the polarity of which is denoted by the subscript) and M is the molecular mass of air. The c_+ and c_- components are the root mean square speeds for positive and negative ions respectively (units of ms^{-1}) and λ_+ and λ_- are the mean free paths of positive and negative ions respectively (units of metres).

The setting of $\alpha(z)$ to be constant with height after 40km is required so that the solution of $\alpha(z)$ does not get too unrealistically small; tending to zero as the density of air (and therefore local ion pair production) becomes very low above this height. This adjustment physically represents the contribution of two-body recombination process at upper levels.

Step 9 – ion-aerosol attachment coefficient

The process of ion attachment to aerosol particles (that may also be charged) used for this model was proposed by Gunn (1954). The ion-aerosol attachment coefficient requires knowledge of the aerosol unit charge (in units of elementary charge). For this model however, the aerosol is considered uncharged. The equations used for this step are discussed by Harrison and Carslaw (2003). The Gunn (1954) solution for the mean value of β for uncharged aerosol ($\overline{\beta}_0$) with radius r_a is:

$$\overline{\beta}_0(z) = \frac{4\pi\mu k T r_a}{e} \quad (3.31).$$

Step 10 – ion-balance equation

The steady-state ion balance equation sets the local ion pair production rate $q_L(z)$ to be equal to the ion loss rate by both ion recombination and ion-aerosol attachment. This allows the mean steady-state ion number concentration to be found (\overline{n}) for a given set of aerosol, environmental and ionisation conditions (equation (3.4)). This equation is discussed further by Harrison and Carslaw (2003).

Step 11 – air conductivity

Once the mean mobility and concentration of ions has been calculated, the total air conductivity can be found by equation (3.2). The total conductivity is simply twice the mean polar conductivity as negative conductivity equals positive conductivity for steady state and uncharged aerosol.

Step 12 – air resistivity

The total air resistivity (ρ) is defined as the inverse of the total air conductivity:

$$\rho(z) = \frac{1}{(\sigma_T)} \quad (3.32).$$

Step 13 – columnar resistance

The columnar resistance (R_C) is the total resistance of a column of air of 1m^2 horizontal area and a vertical extent between the surface and ionosphere (set at 50km in this model). This equates to the integral of the air resistivity profile (equation (3.1)). The integral is solved using Simpson's Rule with constant height increments (set at 1m).

Step 14 – air-Earth conduction current density

The air-Earth conduction current density (J_c) is found by Ohm's Law such that:

$$J_c = \frac{V_I}{R_c} \quad (3.33).$$

From this equation, it can be seen that the value of J_c is uniform with height, in accordance with Ohm's Law.

Step 15 – potential gradient

The potential gradient (F in equations) at a particular height is found by the potential divider concept, which is that the fraction of potential gradient between two heights within a total potential division is proportional to the fractional difference in resistance, used in this case as:

$$F(z) = V_I \frac{\rho(z)}{R_c} \quad (3.34),$$

where V_I is the prescribed ionospheric potential.

3.6 Comparison between modelled and observed profiles

As the model's primary function is to calculate the total conductivity profile (and therefore determine R_c) the emphasis of this comparison will be on total conductivity. However, other comparative data relating to this determination is also presented here. Without the simultaneous aerosol number concentration and total conductivity vertical profile it is not possible to completely constrain this model against observations. As such, certain assumptions about the aerosol profile must be made. Indeed, this model offers a method of estimating basic properties of the aerosol profile if suitably constrained with atmospheric electrical measurements at the surface and/or aloft.

3.6.1 Ionisation rate

An ionisation rate sensor attached to a meteorological radiosonde was launched from the RUAO to measure the STP ionisation rate profile (Harrison, 2005a). This can be compared with the modelled STP ionisation rate for the geomagnetic coordinates of Reading (Bennett and Harrison, 2006c). The results of this comparison are shown in Figure 3.7. From this, it can be seen that the modelled and observed STP ionisation rates are in close agreement, especially considering the variability of the observed values.

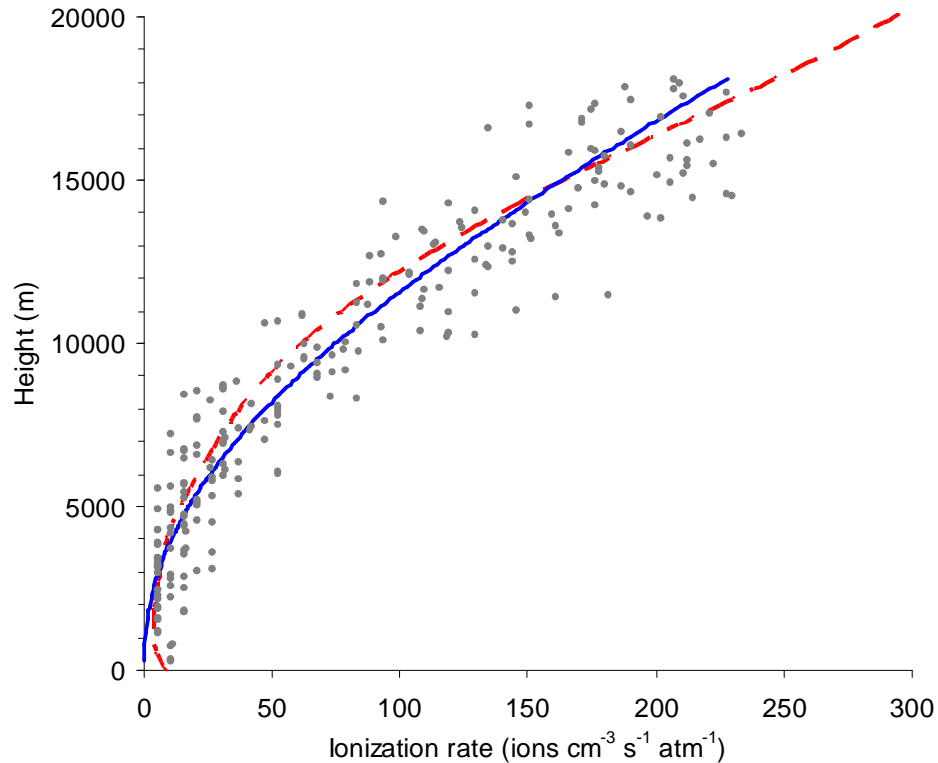


Figure 3.7 Modelled (dashed line) and measured (grey points) ionisation rate, scaled to standard surface atmospheric conditions to avoid the effect of air density change with height. A least-squares best-fit line for the measured points (solid line) is given for comparison to the model (Bennett and Harrison, 2006c).

3.6.2 Air conductivity

There are currently no observations of the air conductivity profile made above the RUAO. Instead, the model output is compared to ascents made by other investigators. The total air conductivity measured during a balloon ascent over Berlin, Germany on 30 August 1905 (Gerdien, 1905) is compared to model output simulating the conditions of this ascent in Figure 3.8 (Harrison and Bennett, 2007a). The Gerdien ascent was chosen as the instrumentation was clearly described, made over a land surface and was at a similar geomagnetic latitude to Reading. Details of model parameters used for this comparison are given by Harrison and Bennett (2007a). It can be seen that the modelled and observed profiles are in good agreement at all heights when a surface aerosol number concentration of $N=20,000\text{cm}^{-3}$ is used. The similarity of both the low and high surface aerosol profiles above 1500m highlights the need for observations within the boundary layer if realistic estimations of R_C and the aerosol number concentration profile are to be made as the lowest 2km contributes to approximately 50% of R_C (Hoppel et al. 1986).

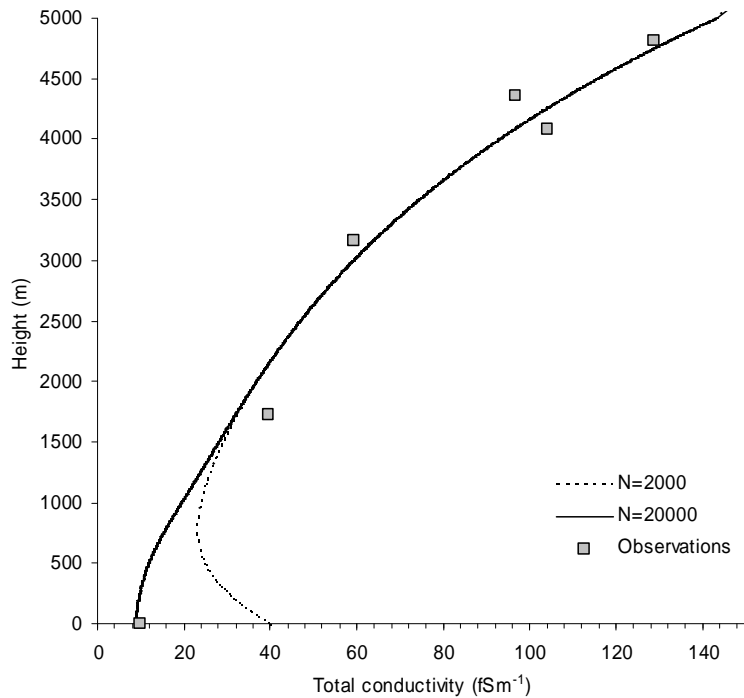


Figure 3.8 Comparison between modelled and observed air conductivity profiles. Air conductivity data obtained during Gerdien's 30th August 1905 ascent over Berlin (Gerdien, 1905) is shown (squares). The solid and dashed lines are from the model, with a boundary layer surface aerosol concentration $N_{0BL} = 20,000$ and $N_{0BL} = 2,000$ particles per cm^3 respectively and $z_{BL} = 300\text{m}$. Both profiles have $N_{0BG} = 2300$ particles per cm^3 and $z_{BG} = 10,000\text{m}$, from Harrison and Bennett (2007a).

An expression for the mean conductivity profile observed up to 26km for the Washington D.C area of the USA (geomagnetic latitude 50°) was derived by Woessner et al. (1958), using an exponential profile. The numerical parameters were converted to MKS units by MacGorman and Rust (1998). This profile was compared to the calculated profile using the model. An approximate best-fit aerosol profile was found to have parameters of $N_{0BL} = 10,000\text{cm}^{-3}$, $z_{BL} = 500\text{m}$, $N_{0BG} = 1500\text{cm}^{-3}$ and $z_{BG} = 7,000\text{m}$. However, the Woessner et al. (1958) conductivity expression appears to have a rather unrealistically high total conductivity near the surface for a continental site (approx 80fSm^{-1}), so is used to compare with heights above the Gerdien profile at 5km. Above this height, the model conductivity profile is in reasonable agreement to the conductivity expression derived by Woessner et al. (1958), as seen in Figure 3.9.

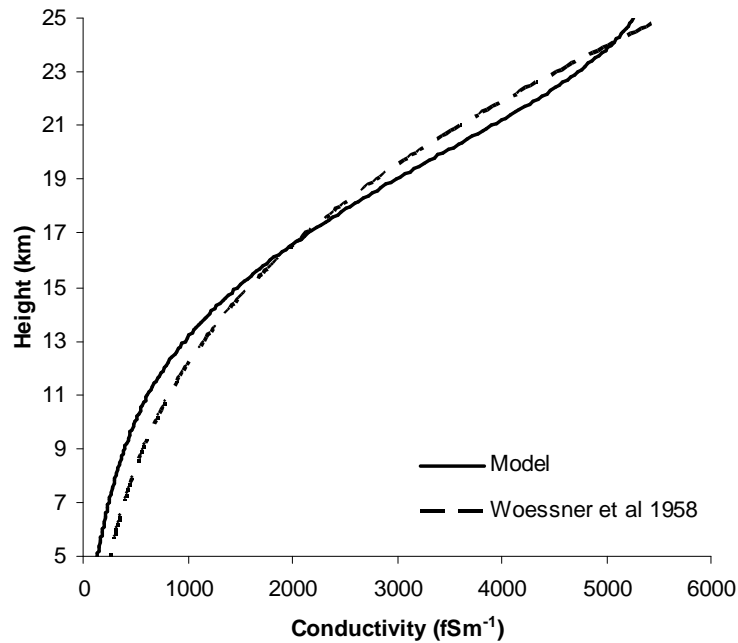


Figure 3.9 Model fit to conductivity expressions of Woessner et al. (1958). Geomagnetic latitude set at 50°, corresponding to the location of observations of Woessner et al. (1958). A best-fit aerosol profile of $N_{0BL} = 10,000\text{cm}^{-3}$, $z_{BL} = 500\text{m}$, $N_{0BG} = 1500\text{cm}^{-3}$ and $z_{BG} = 7,000\text{m}$ was used for the model.

3.6.3 Aerosol profile

Observed PG and J_C measured at surface level at the RUAO were modelled using an assumed aerosol profile, the details and results are described in Bennett and Harrison (2006c). The measured PG and J_C were used to constrain the modelled aerosol number profiles, which were shown to be consistent with the meteorological conditions for the time. A table showing the modelled aerosol number concentration coefficients for equation (3.13) that corresponded to the observed PG and J_C is shown in Table 3.3 (Bennett and Harrison, 2006c).

Date	Time	Mean PG	Mean J_C	N_{0BG}	N_{0BL}	z_{BG}	z_{BL}
25/01/06	14-15UT	140Vm ⁻¹	1.81pAm ⁻²	400cm ⁻³	14,500cm ⁻³	10,000m	650m
28/01/06	17-21UT	200Vm ⁻¹	1.82pAm ⁻²	400cm ⁻³	21,000cm ⁻³	10,000m	350m

Table 3.3 Observations of PG and J_C with corresponding modelled aerosol profile variables as described in equation (3.13).

The meteorological synoptic situations for the two dates in Table 3.3 were different due to the height of a subsidence inversion, with trapped aerosol below. Although there were no direct observations of aerosol above the surface, a difference in the aerosol profile

between the two days was expected due to the change of inversion height that retained aerosol near the surface. The aerosol profile change resulting from the inversion height was modelled by varying the surface aerosol number concentration exponent of equation (3.13), whilst keeping the background contribution the same. By changing the aerosol profile, the model successfully represented the observed change in PG between the two days whilst allowing for the similar J_C that occurred despite an observed change in surface aerosol concentration (Bennett and Harrison, 2006c).

3.7 Model sensitivity

The model function is to calculate R_C from profiles of atmospheric temperature and pressure, ionisation rate and aerosol number concentration. Using values of these parameters typical of the atmosphere over an urban surface at a geomagnetic latitude of 50°N (Table 3.4), the modelled columnar resistance as a function of height has been calculated and shown in Figure 3.10.

	P_s	T_s	Q_0	z_{si}	N_{0BG}	N_{0BL}	z_{BG}	z_{BL}
<i>Value</i>	1013hPa	15°C	8cm ⁻³ s ⁻¹	500m	2000cm ⁻³	20000cm ⁻³	5000m	500m

Table 3.4 Values of the coefficients used in the model R_C profile in Figure 3.10.

The majority of R_C is found in the lowest few kilometres, with 47% of R_C at 50km attributed to the lowest 1km and 99% below 20km, from the results shown in Figure 3.10. These results are similar to those described by Hoppel et al. (1986). The dominance of the troposphere in contributing to R_C implies that meteorological processes that cause variation in this atmospheric region are also likely to influence R_C and therefore surface measurements of J_C and PG for a given V_I .

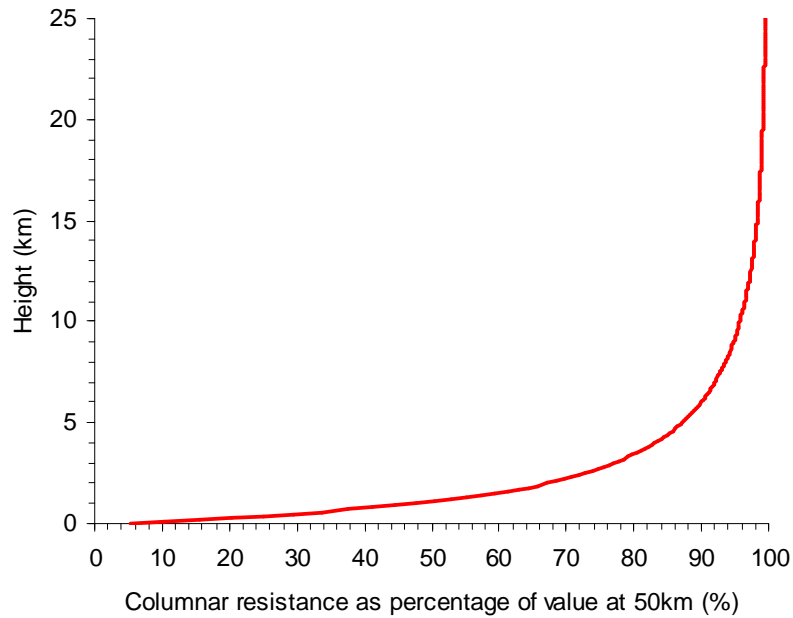


Figure 3.10 Columnar resistance as a percentage of that at 50km ($223\text{P}\Omega\text{m}^2$), as a function of height from the surface to 25km, using typical parameters for an urban site at a geomagnetic latitude of 50°N , found in Table 3.4.

Equations (3.33) and (3.34) are used to calculate J_C and PG respectively. From these equations it can be seen that variation in V_I (which would correspond to variations of the global circuit intensity) will be the only cause of variation of J_C if R_C remained constant with time. However, for PG to show only this global variation, the fraction $\frac{\rho}{R_C}$ must remain

constant with time. These relationships can be used to identify whether variation in J_C or PG will be attributed more to global (V_I) or local (R_C or ρ) sources. For instance, in the case where the local air resistivity (ρ) is variable over a shallow depth near the surface, the change in R_C associated with this local conductivity change may only be slight if the layer represents only a small fraction of total R_C . This will mean that J_C , which is related to the whole R_C and not just the local conductivity, will experience a larger relative contribution to any variability from global sources, whilst the PG which is proportional to local resistivity changes will have a greater relative contribution to variability attributed to local sources. This would make J_C a more reliable source of global variation. However, the opposite would be true if local resistivity varied by the same fractional amount as R_C .

The sensitivity of J_C and surface PG measurements to changes in the aerosol, ionisation and temperature profiles (all of which would be expected to vary in the troposphere) are investigated in this section.

3.7.1 Aerosol

The sensitivity of modelled R_C , J_C and PG at 1m to a doubling of boundary-layer aerosol number concentration (N_{0BL}) for different boundary layer scale heights (z_{BL}) is shown in Figure 3.11. All other model variables were kept constant, with the same values as shown in Table 3.4. The absolute sensitivity S for a particular parameter X (R_C , J_C or PG) and scale height z_{BL} was calculated by:

$$S_X = \left| \frac{X_2 - X_1}{X_1} \cdot 100 \right| \quad (3.35),$$

where the numbers 1 and 2 denote the value of X when $N_{0BL}=10,000\text{cm}^{-3}$ and $N_{0BL}=20,000\text{cm}^{-3}$ respectively. The aerosol number concentration profiles for situations 1 and 2 are shown in Figure 3.12.

The results of this aerosol sensitivity test identify the boundary-layer aerosol scale heights where J_C and PG become relatively more sensitive to variation in boundary-layer aerosol number concentration and therefore least likely to be representative of global variation through V_1 . The choice of V_1 will not affect the sensitivity analysis results as only relative variation of J_C and PG is investigated. As background aerosol uses the same exponential decrease function as boundary layer aerosol (just with different values of the coefficients) the characteristics of the sensitivity analysis will be identical to that from the boundary layer component, so will not be investigated separately.

The sensitivity of R_C and J_C to the aerosol number concentration profile follow similar trends with varying z_{BL} , although with different magnitudes. This similarity can be explained by J_C being proportional to the inverse of R_C , corresponding to a sensitivity of J_C that is related to the R_C sensitivity by:

$$S_{J_C} = S_{R_C} \cdot \frac{R_{C1}}{R_{C2}} \quad (3.36).$$

As $R_{C1} < R_{C2}$ due to the reduced aerosol load, the sensitivity of J_C to a change in N_{0BL} is proportionally lower than that of R_C , with the greatest difference occurring at higher z_{BL} when the difference between R_{C1} and R_{C2} is largest due to a greater depth of aerosol variation.

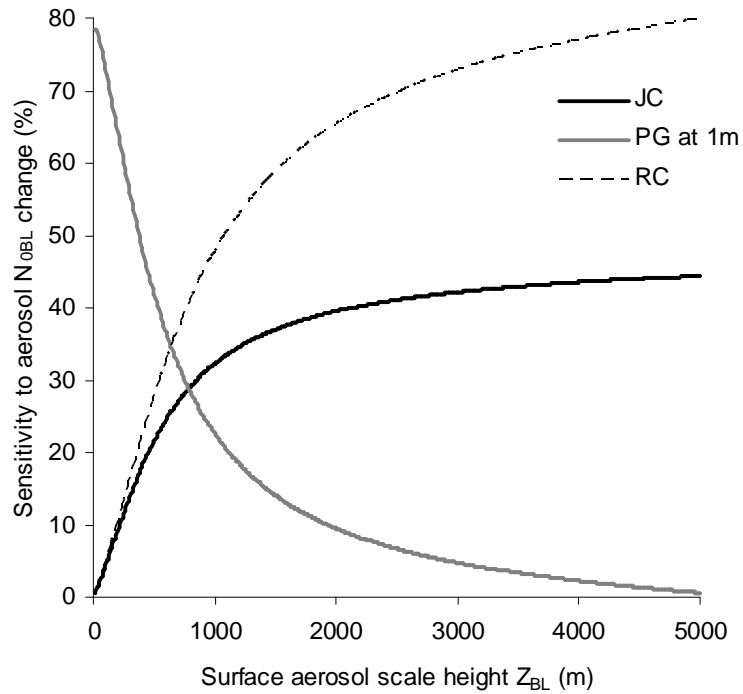


Figure 3.11 Sensitivity of R_C , J_C and PG at 1m to a doubling of boundary-layer aerosol number concentration N_{OBL} from $10,000\text{cm}^{-3}$ to $20,000\text{cm}^{-3}$, with varying boundary-layer scale height z_{BL} . Sensitivity corresponds to the magnitude of parameter change.

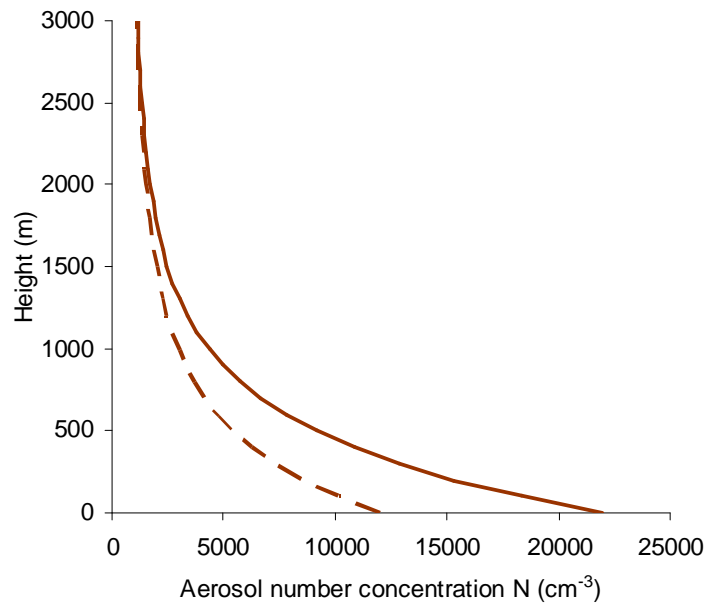


Figure 3.12 Aerosol number concentration (N) profiles used to calculate model sensitivities to change in N_{OBL} with varying z_{BL} , shown in Figure 3.11. The dashed and unbroken lines represent N for $N_{OBL}=10,000\text{cm}^{-3}$ and $20,000\text{cm}^{-3}$ respectively, both with a z_{BL} of 500m.

The sensitivity of PG to the change in aerosol varies with z_{BL} in the opposite sense to R_C and J_C , being most sensitive at low z_{BL} heights. This is because the PG response is determined by the fraction of local resistivity and columnar resistance (equation (3.34)). From Figure 3.12 it can be seen that N increases near the surface where the PG is calculated (at 1m) with an associated 78% increase in resistivity when $z_{BL}=10m$. Although the local resistivity is strongly affected by this shallow layer of aerosol variation, the effect on the combined R_C is small by comparison, at only 0.4%. However, the influence of the boundary layer aerosol component on R_C increases with z_{BL} so the variation in R_C tends towards the variation of local resistivity near the surface:

$$\frac{\rho_1}{R_{C1}} \rightarrow \frac{\rho_2}{R_{C2}} \text{ as } \Delta R_C \rightarrow \Delta \rho \quad (3.37).$$

This will act to reduce the difference in local resistivity and R_C fractions and therefore lower PG sensitivity to the change in aerosol number concentration profile.

The different aerosol sensitivity responses of J_C and PG to a change in boundary layer depth, z_{BL} , identifies the boundary layer aerosol conditions when the source of variation in J_C is either more or less likely to be global compared to that of PG. For $z_{BL}<800m$, J_C is less sensitive to N_{0BL} change and global variation (through changes in V_i) are more likely to be identified than from PG. However, PG becomes less sensitive than J_C at z_{BL} heights exceeding 800m, so will instead be the favoured parameter for investigation of global (V_i) variation. The boundary layer height was observed to be below 800m over an urban environment by Harrison and Aplin 2003, and Del Guasta, 2002), implying that J_C is more likely to be globally representative under typical urban boundary layer conditions. However, for situations where boundary layer aerosol number concentration is the dominant source of R_C variability (i.e. $\Delta R_C \rightarrow \Delta \rho$) such as when aerosol number concentration changes uniformly over a deep boundary layer, then PG variation is most likely to be globally representative.

3.7.2 Ionisation rate

Variation of terrestrial and cosmic ray ionisation rates are treated separately for this sensitivity analysis as both originate from independent sources.

Terrestrial ionisation rate

The sensitivity of modelled R_C , J_C and PG at 1m to a doubling of terrestrial ionisation rate (Q_0) for different terrestrial ionisation scale heights (z_{si}) is shown in Figure

3.13. All other model variables were kept constant, with the same values as shown in Table 3.4. The absolute sensitivity was calculated from equation (3.35), with the numbers 1 and 2 denoting the value of X when $Q_0=16\text{cm}^{-3}\text{s}^{-1}$ and $Q_0=8\text{cm}^{-3}\text{s}^{-1}$ respectively.

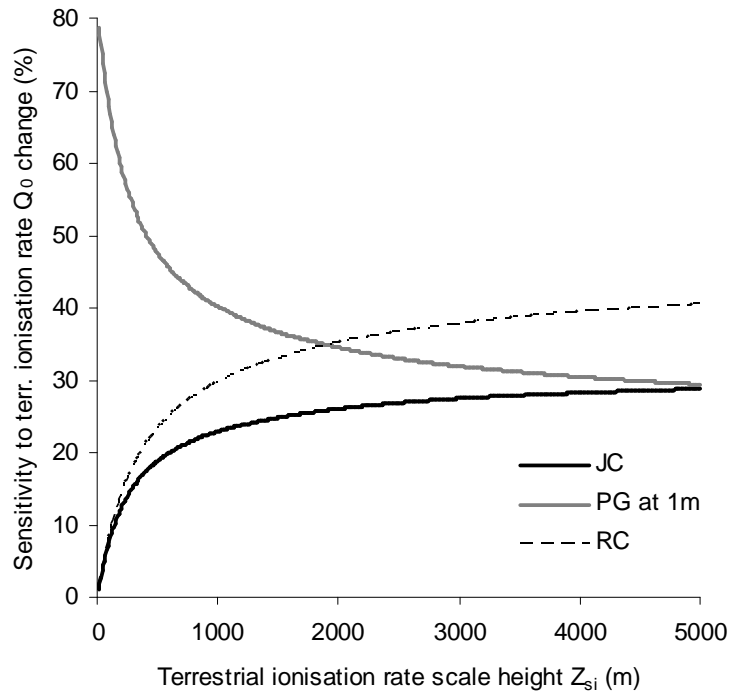


Figure 3.13 Sensitivity of R_C , J_C and PG at 1m to a doubling of terrestrial ionisation rate Q_0 from $8\text{cm}^{-3}\text{s}^{-1}$ to $16\text{cm}^{-3}\text{s}^{-1}$, with varying terrestrial ionisation scale height z_{si} . Sensitivity corresponds to the magnitude of parameter change.

The results of this sensitivity analysis shown in Figure 3.13 appear qualitatively similar to the boundary layer aerosol profile sensitivity analysis of Figure 3.11. The similar response of the three parameters sensitivities to Q_0 change for increasing z_{si} is due to the same exponential decrease of both terrestrial ionisation rate and boundary layer aerosol number concentration profiles, as seen by inspection of equations (3.14) and (3.13) respectively. Both an increase in aerosol number concentration and a decrease in terrestrial ionisation rate will produce a decrease in small ion number concentration (equation (3.4)), which will reduce air conductivity through equation (3.2). The same reasoning used to explain the aerosol sensitivity analysis can therefore also be applied to explain the terrestrial ionisation rate sensitivity, with equations (3.36) and (3.37) applying for both effects.

Although qualitatively similar, the results of the sensitivity analysis for variation of terrestrial ionisation rate differs from that of boundary layer aerosol number concentration regarding the asymptotic value of the three sensitivities with increase scale heights. For

aerosol, PG sensitivity (S_{PG}) tended towards zero as $\Delta R_C \rightarrow \Delta \rho$, the S_{PG} for terrestrial ionisation rate change tends to ~26%, not ~0% like aerosol. This means that a change in Q_0 will always produce a change in PG for any z_{si} , as the change in local resistivity ρ associated with this will not be completely balanced by a change in R_C . The sensitivity of J_C to a change in Q_0 is lower than that of PG for the entire range of z_{si} investigated (Figure 3.13) making J_C the preferred parameter to investigate global (V_I) variability, although continuing the trends observed in Figure 3.13 the two sensitivities may become at least equal for $z_{si} > 5000m$.

Cosmic ray ionisation rate

The variation of R_C , J_C and PG to a change in cosmic ray ionisation rate q_C , relative to the standard q_C profile for a geomagnetic latitude of 50°N is shown in Figure 3.14. The standard q_C was calculated using the same coefficients and formulae of Makino and Ogawa (1985) described by equations (3.15) to (3.17). The aerosol number concentration and terrestrial ionisation profiles were kept constant, with values for coefficients given by Table 3.4.

As q_C decreases, less atmospheric ions are produced, increasing R_C . The increase in R_C is most sensitive to q_C change for low q_C as indicated by the larger gradient, with the value of R_C rising to 279% of standard for a q_C of 10%. Variation of J_C and PG with changing q_C are similar as q_C affects the whole depth of the atmosphere, particularly upper regions where cosmic ray intensity is highest. This means that the main variability comes from R_C (which both PG and J_C are inversely proportional to) and not the 1m resistivity ρ , which is the factor that separates the sensitivity characteristics of PG and J_C . This whole-atmosphere influence of q_C variability is in contrast to that found by variation of boundary layer aerosol number concentration and terrestrial ionisation rate, which only affect the lower troposphere. Despite the dominance of terrestrial ionisation over cosmic ray ionisation at the land surface (Hoppel et al. 1986) the modelled cosmic ray component q_C of ionisation rate at 1m comprises 17% of the total q (for a Q_0 of $8cm^{-3}s^{-1}$). As previously identified in this section, there exists a partial compensation mechanism (equation (3.37)) that reduces PG sensitivity to a change in R_C providing this relative change is similar to that of ρ at 1m, which makes PG less sensitive to vertical conductivity profile variation than J_C . This local ρ and R_C “balance” mechanism is shown to operate for q_C change above the standard value, where PG is less sensitive to q_C variation than J_C , as seen in Figure 3.14.

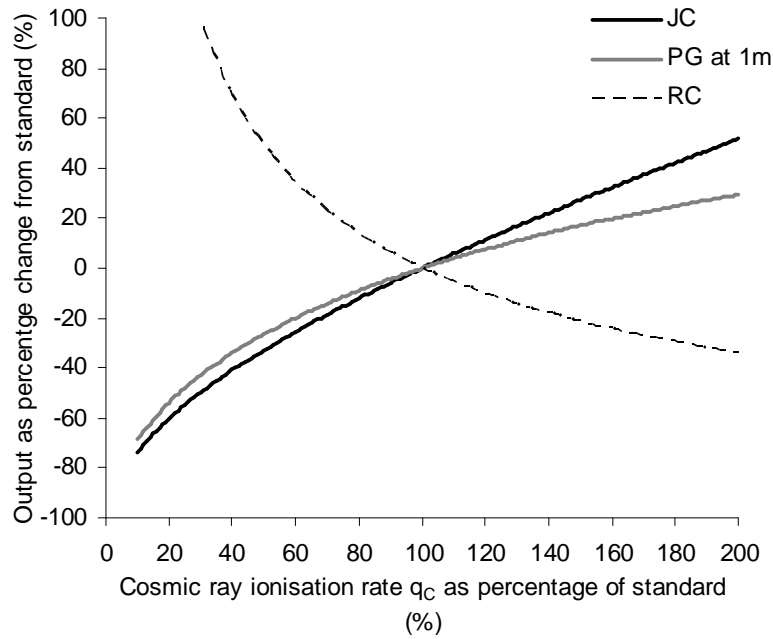


Figure 3.14 Variation of R_C , J_C and PG at 1m to a change in cosmic ray ionisation rate q_C , relative to the standard q_C profile for 50°N using the equations of Makino and Ogawa (1985). R_C was truncated at 100% for clarity of presentation.

3.7.3 Temperature

The model's standard temperature profile uses the coefficients shown in Table 3.5 for equations (3.18) to (3.20). The values were chosen to approximate to the 1976 US standard atmosphere.

	T_S	Z_{TP}	Z_{ST}	$\left(\frac{dT}{dz}\right)_{TR}$	$\left(\frac{dT}{dz}\right)_{TP}$	$\left(\frac{dT}{dz}\right)_{ST}$
Value	15°C	11km	20km	$-6.5 \times 10^{-3} \text{K m}^{-1}$	0K m^{-1}	$1.5 \times 10^{-3} \text{K m}^{-1}$

Table 3.5 Coefficients used in equations (3.18) to (3.20) for the standard temperature profile of the model.

As pressure is derived from the hypsometric equation (3.21), changes in atmospheric temperature will alter the air pressure profile accordingly, although the surface value is still defined. A graph of the temperature profile based on these coefficients is shown in Figure 3.15.

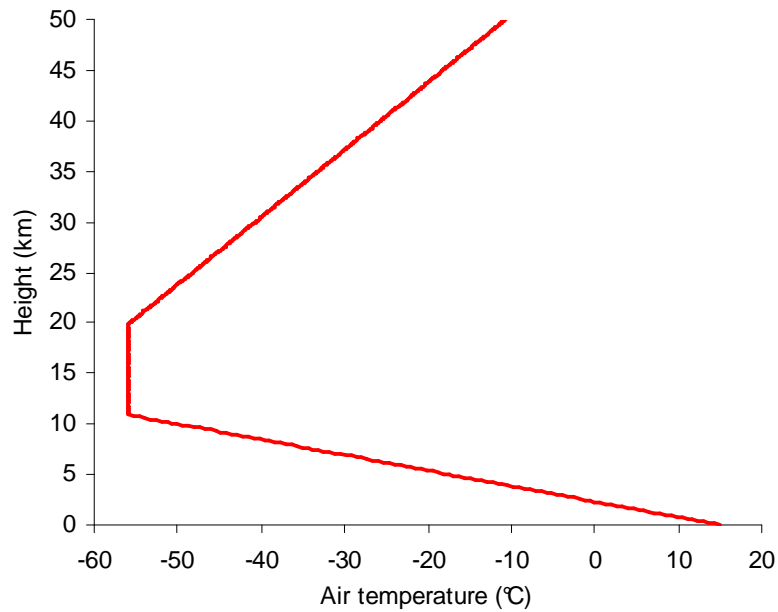


Figure 3.15 Assumed air temperature profile for the model, using equations (3.18) to (3.20) and the coefficients

In order to investigate the sensitivity of R_C , J_C and PG at 1m to atmospheric temperature, these parameters were calculated using the standard temperature profile described by the coefficients in Table 3.5, with an aerosol and ionisation rate profile using the coefficients in Table 3.4. The temperature of the entire atmospheric column was then varied about this standard temperature profile (with aerosol and ionisation rate profiles kept constant) by changing T_S , with associated changes in R_C , J_C and PG at 1m calculated as a percentage of the values found using the standard temperature profile. Unlike variation caused by aerosol and ionisation rate, the variation in R_C , J_C and PG at 1m is linear with atmospheric temperature change between T_S of -10°C to 30°C , the gradients of which are shown in Table 3.6.

	R_C	J_C	PG at 1m
<i>Sensitivity</i>	$0.41\%K^{-1}$	$-0.43\%K^{-1}$	$0.27\%K^{-1}$

Table 3.6 Percentage sensitivity of R_C , J_C and PG at 1m to atmospheric temperature change between 0-50km.

Temperature will affect R_C through changes in the air density profile which will affect ion mobility and ion production rates, as well as changes in ion-aerosol attachment and ion-ion recombination coefficients. The percentage sensitivities to atmospheric temperature change were calculated for a uniform change in atmospheric temperature, so these values should be considered as maximum sensitivities. For example, the diurnal range of air

temperature due to solar heating of the land surface may have an upper limit of approximately 20°C at a mid-latitude site in summer. However, this temperature variation will not penetrate into the entire depth of the atmosphere, rather only the lowest few hundred metres (at most) corresponding to the net vertical heat flux (Stull, 2000). Even if the temperature of the lowest 1km of the atmosphere changed by 20°C, this would only correspond to a change in R_C , J_C and PG at 1m of 2%, -2% and 4% respectively. These changes are small compared to those of a moderate change in boundary-layer aerosol number concentration over a similar boundary layer height (Figure 3.12 and Figure 3.13).

3.8 Discussion

The R_C model assumes a zero ion and aerosol flux, with ions and aerosols existing in steady-state for each horizontal layer. Aerosol particles are considered neutral, spherical and monodisperse. Any dynamical source of local space charge that would result when J_C flows through a conductivity gradient is assumed to have a negligible effect on the overall conductivity profile and therefore R_C . For layer thicknesses (i.e. vertical resolution) of order 10m or larger, and fair-weather conditions (i.e. no sharp aerosol concentration boundaries, local space charge or significant vertical mixing) these assumptions are expected to be valid. From these assumptions it is possible to calculate the total conductivity profile from the surface to 50km. As 95% of R_C occurs in the lowest 13km (Hoppel et al. 1986), this region below 50km is expected to contain all the R_C , which is found by integration of the resistivity profile. Once R_C is known, J_C and PG can be calculated for a given value of V_I . The model ionisation rate and conductivity profiles are in good agreement with observed profiles, once a suitable aerosol profile is assumed for the latter. This model allows the influence of factors such as the aerosol profile on the surface measurements of J_C , PG and σ_T to be investigated, and the relative contribution of local and global effects on these atmospheric electrical observations at the surface.

The model is sensitive to changes in the main input parameters; aerosol number concentration, ionisation rate and air temperature. The relative sensitivity of the model outputs (R_C , J_C and PG at 1m) is not fixed, but is dependent not only on the size of the change in input but also the scale heights. This is due to differences in the relative importance of changes in local and columnar resistance (ρ and R_C) to the three output parameters, and the relative importance of R_C change with height, with nearly half of total R_C residing in the lowest 1km. It is primarily the aerosol number concentration, followed by ionisation rate that controls R_C , with atmospheric temperature change being of negligible importance.

The next chapter describes instrumentation used to measure atmospheric electrical parameters, including a new type of sensor to directly measure J_C at the surface.

4 Instrumentation for atmospheric electrical research

4.1 Overview

The three main atmospheric electrical parameters used for the study of atmospheric electricity at the RUAO are the potential gradient (PG), air-Earth conduction current density (J_c) and total air conductivity (σ_T). Details of all the instruments used to make these measurements will be given in this chapter. Of these instruments, two were developed by the University of Reading Department of Meteorology before the commencement of this study. These were the Passive Wire (PW) for PG measurement, and the Programmable Ion Mobility Spectrometer (PIMS) for measurement of σ and small ion properties. The JCI 131 Electrostatic Field Mill (FM) is a commercially available instrument which measures the PG and was installed at the start of this study in Autumn 2004. The FM and PIMS will be used to determine the atmospheric electrical climatology of the Reading University Atmospheric Observatory (RUAO) site, with shorter periods selected for case studies. The instruments for direct measurement of the air-Earth current density were designed and developed as part of this study and will consequently be discussed in particular detail here. Like the FM and PIMS, the aim is to use the J_c instrumentation to produce a dataset capable of indicating the electrical climatology and providing data for case studies, such as investigation of the validity of Ohms Law, which requires simultaneous measurement of all three parameters (J_c , PG and σ_T).

4.2 Passive Wire (PW)

The Passive Wire (also referred to as the long or stretched wire antenna in the literature) is primarily used for the absolute measurement of electric potential (with the ground as the zero reference potential) at a given height, but can also be used to determine the total air conductivity using a method described later in this section.

The basic principle of the PW is that a well-insulated horizontal wire positioned at a known height above ground level will naturally assume the atmospheric electrical potential for that height. The time taken to reach this potential depends on the air conductivity. Since the resultant voltage on the wire is not artificially generated by an equaliser, the instrument is called the passive wire. Crozier (1963) provides a thorough account of the PW principle. The voltage on the wire is measured using a high impedance voltmeter (Harrison, 1997a). The voltmeter also applies a guard voltage to the support wires to

ensure ultra-low leakage ($<5\text{fA}$) from the sensing wire electrode. Further details of the operation and use of the PW at the RUAO are given by Barlow (1999).

A picture of the PW installed at the RUAO can be seen in Figure 4.1, with the main components of this instrument labelled. The actual wire used is kept under constant tension by weights and a pulley at one of the support posts. The wire is thin (0.5mm diameter) and can not be seen in Figure 4.1. A close-up view of the wire and insulator end can however be seen in Figure 4.2.

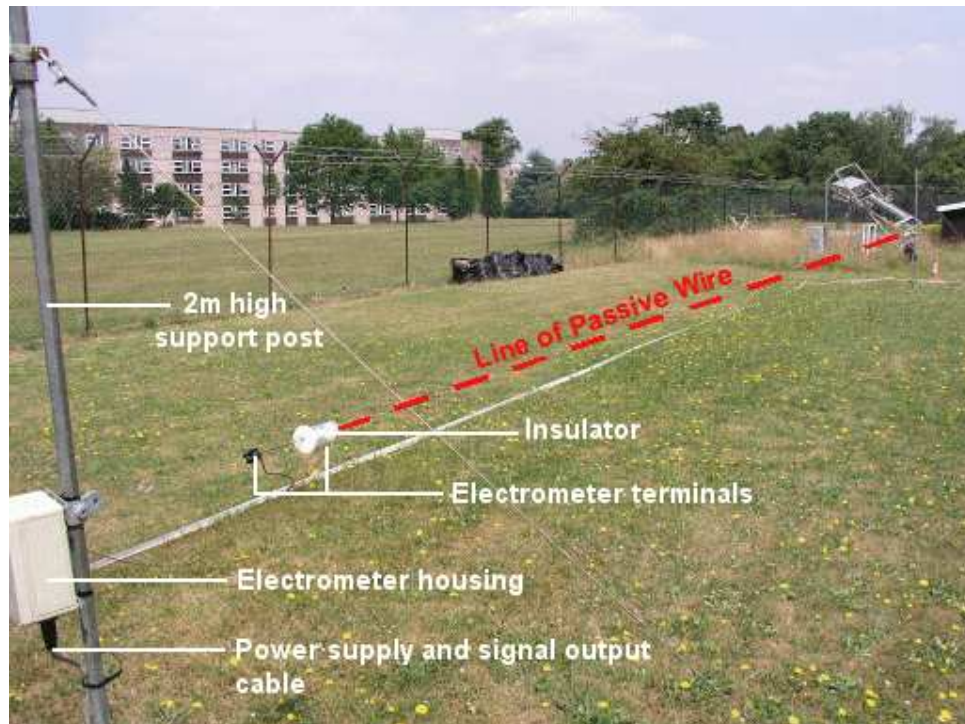


Figure 4.1 The Passive Wire (PW) installed on the RUAO 1m above the surface, showing main features. The horizontal wire was positioned 1m above the surface and was approximately 20m long. An identical support structure was at the far end of the instrument, except without the electrometer.

Once the potential is known for the height of the wire, the mean PG between the surface and wire can be determined by simply dividing the potential by the height of the wire. If the PG is considered uniform between the wire and surface, the potential of the PW positioned at 1m above the surface is therefore the same value as the PG at 1m. The uniformity of PG at this height is demonstrated by the results of Barlow (1999), where the potential was measured simultaneously on wires positioned at 0.5m, 1.0m, 1.5m, 2.0m and 2.85m above the surface (Figure 4.3). The potential increased uniformly with height, implying a constant PG between the surface and 2.85m. Similarity in the time variability of

the passive wire potentials correspond closely to each other and to that of a nearby field mill (Barlow, 1999). As no calibration or geometrical corrections are required, the value of PG at 1m measured using the PW is considered absolute.



Figure 4.2 The thin wire used for the PW instrument shown in Figure 4.1, seen here emerging from the end of the insulator.

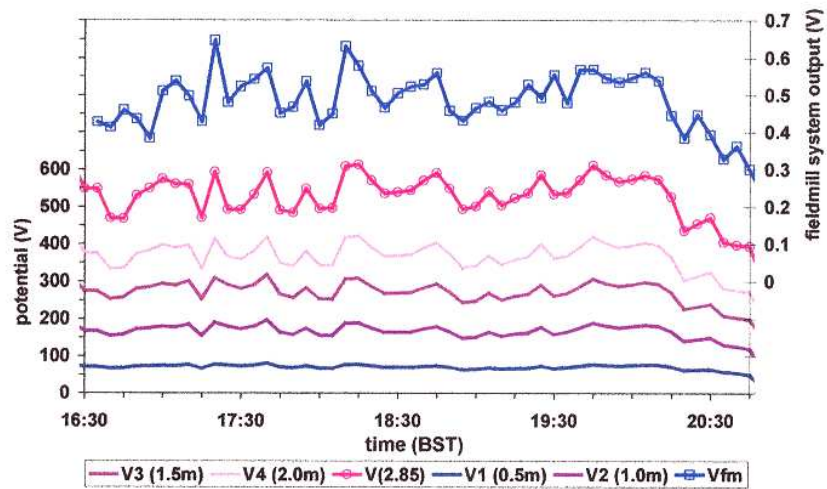


Figure 4.3 PW potential measured simultaneously for wires at 0.5m, 1.0m, 2.0m and 2.85m above the surface, as well as output potential from a field mill system (From Barlow, 1999).

4.2.1 Use of the PW to measure air conductivity

In addition to the absolute measurement of PG, the PW can also be used to measure total air conductivity (Bennett and Harrison, 2006a). This is achieved by grounding the wire (by

briefly touching the electrode wire with a wire connected to Earth) and measuring the rate of increase in potential of the wire as it comes back into equilibrium with the surrounding air. After being earthed the time taken by the wire to reach atmospheric potential will depend on the total electrical resistivity (i.e. inverse of conductivity) of the air, ρ and electrical capacitance, C . It is the total conductivity (σ_T) that is measured since the wire is charged to that of its surroundings by both positive ions from above and negative ions from below. Since ρ and C both depend on the same geometrical factors, which cancel, the total conductivity is given by (e.g. Chalmers, 1967)

$$\sigma_T = \frac{\epsilon_0}{\rho C} = \frac{\epsilon_0}{\tau} \quad (4.1),$$

where ϵ_0 is the permittivity of free space and τ is the electrical relaxation time of the air between the surface and the wire. τ can be found using the time series of voltage on the wire after being earthed. The passive wire potential V with respect to ground is described in equation (4.2) in accordance with established theory for RC circuits

$$V = V_0 \cdot \left(1 - e^{-\frac{t}{\tau}} \right) \quad (4.2),$$

where t is the time elapsed since grounding and V_0 is the potential of the air at the height of the wire. Since the wire is at one metre above the surface, this corresponds to PG in the first metre above the surface. This provides a method to determine total air conductivity as an exponential fit can be made to the voltage time series, the relaxation time τ (typically of order 1000s) found and thereby total conductivity using equation (4.1). An example of the close agreement between measured and theoretical PW voltage after grounding is shown in Figure 4.4. The period prior to grounding shows the agreement between passive wire and field mill derived PG.

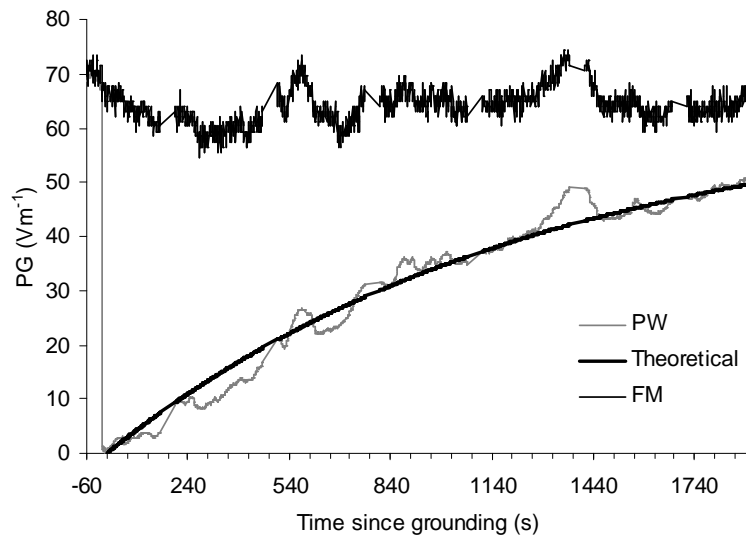


Figure 4.4 PG from calibrated field mill (FM) and voltage on the passive wire (PW) after grounding, with modelled charging curve of theoretical equation (4.2) (from Bennett and Harrison, 2006a).

As the calculated relaxation time is a time-averaged quantity, the derived total conductivity is an average value for the sampling period. This method assumes that changes in the PG during the charging time are small compared to the rate of increase in the voltage on the wire. This assumption is valid either nearer the start of charging when the rate of increase in V is greatest, or as is more usually the case in practise after a duration long enough for the short-period (order one minute) fluctuations in PG to be averaged out. The time taken to achieve a consistent estimation of the total conductivity was found to be approximately 15 minutes (Figure 4.5), when the charging time exceeded the electrical relaxation time of the atmosphere (Bennett and Harrison, 2006a).

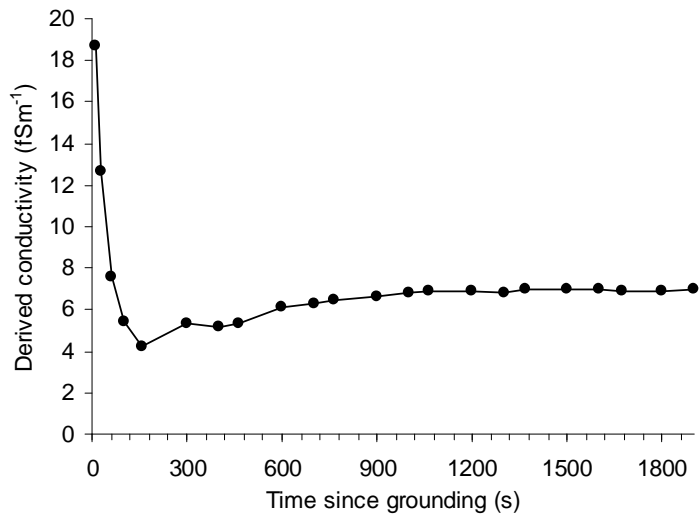


Figure 4.5 Total air conductivity derived from the best model fits using different lengths of the passive wire charging curve (from Bennett and Harrison, 2006a).

4.3 Field Mill (FM)

A JCI 131 electrostatic field mill (FM) was installed at the RUAO in October 2004 (although reliable continuous records did not begin until April 2005). The instrument is commercially available (John Chubb Instrumentation, their website detailing the FM is <http://www.jci.co.uk/jci131.html>). Field mills have been successfully used for continuous recording of PG at other sites (e.g. Isrealsson and Tammet (2001), Harrison (2006a), De et al., (2006)). The basic design of a FM is a rotating metal electrode beneath an earthed case with electrode-shaped slots at the top, allowing the rotating electrode beneath to be alternately exposed and shielded from the atmospheric PG. This action induces a charge on the electrode, measured as a displacement current with magnitude proportional to the PG above the aperture. Most field mills require the electrode to be earthed at a certain point in their cycle, which is usually done with a metal brush permitted to make and break electrical contact with the electrode (Chubb, 1990). However, the JCI 131 FM is designed to use capacitive coupling between the electrode current and electrometer, thereby removing the requirement of any contact brush (which inevitably degrades with time) and thereby increasing the durability of the instrument. The rotation rate is determined by an optical sensor, so no contact is required for this either. A basic schematic of this FM type can be seen in Figure 4.6.

In addition to the brushless design, the FM is unaffected by mains frequency (50/60Hz) electric fields (useful for urban measurement sites such as the RUAO). There is a large gap between the rotating electrode and outer case to avoid bridging by water droplets,

and drainage holes near the base, making this FM suitable for all weather conditions (see JCI 131 user manual at <http://www.jci.co.uk/jci131.html> for further details).

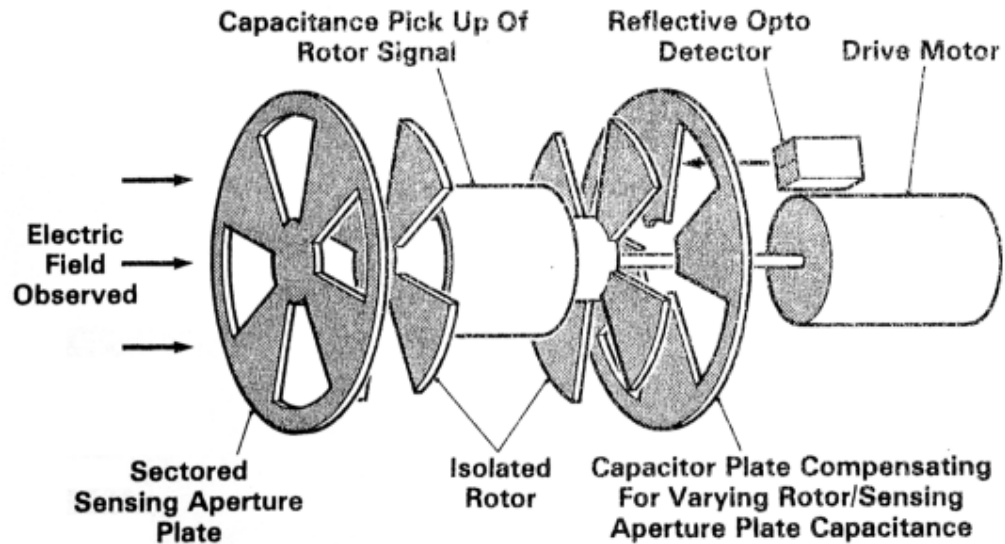


Figure 4.6 Basic schematic of the constant capacitance-type field mill (from Chubb, 1990).

Before installation on the RUAO the field mill was tested in the laboratory to ensure the output was linearly proportional to an applied PG ($\sim 100\text{-}800\text{Vm}^{-1}$). Additionally, the power supply voltage was changed to determine any voltage effect on FM output. The experimental setup was to clamp the FM vertically and position a horizontal metal plate approximately 3cm above the sensing aperture. The rectangular plate was insulated from the surroundings and connected to the positive terminal of a power supply, thereby allowing a known positive voltage to be applied to the plate, with respect to ground (common to the voltmeter and FM). The plate dimensions were such that a uniform vertical PG would exist between the sensing aperture and plate (i.e. the plate was larger than the sensor aperture, being approximately 25cm by 35cm). The FM was powered by another DC power supply which allowed a variable output voltage. The results of this test are shown in Figure 4.7, for power supplies of 10, 12 and 18V. As illustrated, the FM output was linear with respect to applied PG and appeared unaffected by the input power supply voltage. Further tests revealed a stable FM output with supply voltages down to 7V, well below the minimum expected at the RUAO.

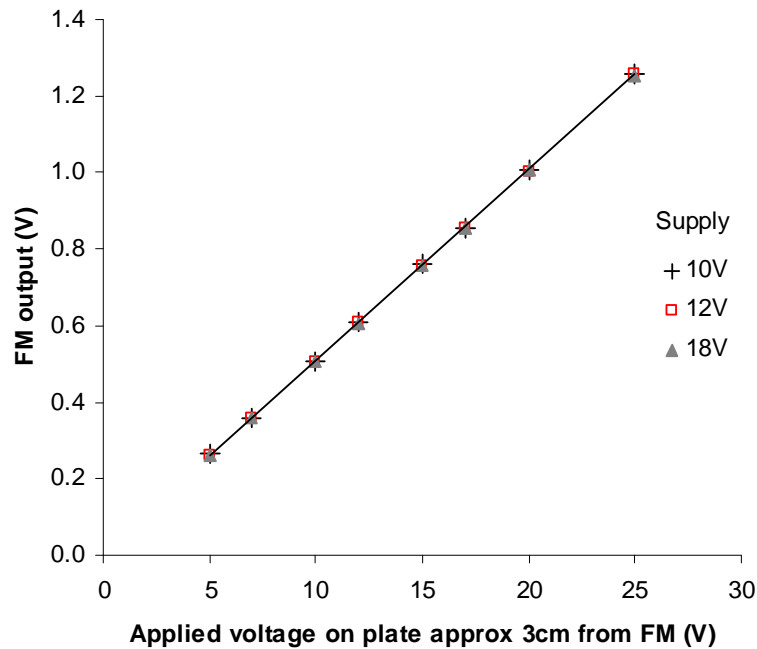


Figure 4.7 Laboratory test of FM to investigate effect of power supply voltage on FM output.

The FM has an auto range capability, allowing automatic switching of sensitivity range settings between 2, 20, 200 and 2000kV m^{-1} for a full scale output of 2V, with a quoted accuracy of within 1% of operating range sensitivity. Due to the possibility of confusion caused by the auto range setting being activated (monitoring of the actual range set would require a further two research channels, which were not available for this purpose) the range was fixed. This was achieved by supplying 5V to the required range-fixing terminal using power from the RUAO supply (modified to 5V) via a break-out box fixed to the bottom of the support pole. This small box can be seen in part (a) of Figure 4.8 attached to the support pole approximately 30cm from the ground.

Once the FM was installed at the RUAO at the top of a pole, with aperture pointing vertically upward, the instrument required in situ calibration due to the inevitable distortion of the ambient PG by the instrument and support pole. This distortion will be large (greater than a factor of 2) as can be seen in Figure 4.8b. For this model, both the ground and equipment were assumed to be perfect conductors, and the air a perfect insulator. Although a theoretical equation based on the electric field around an earthed vertical pole is suggested for calibration by the FM user manual, the PW was used as an absolute method of calibration, as the wire was suspended 1m in the air, away from the support poles. The closest end of the PW was situated approximately 2m from the FM pole, and measurement of raw FM output voltage was compared to PG measured by the PW 1m

above the surface (see section 3.2), allowing the FM aperture at 2m elevation to be calibrated to give PG at 1m. From this comparison, the calibration equation was determined to be

$$F_{1m} = 387 \cdot FM_{raw} + 12 \quad (4.3),$$

where F_{1m} is the PG at 1m in Vm^{-1} , FM_{raw} is the output of the FM at 2m in V.

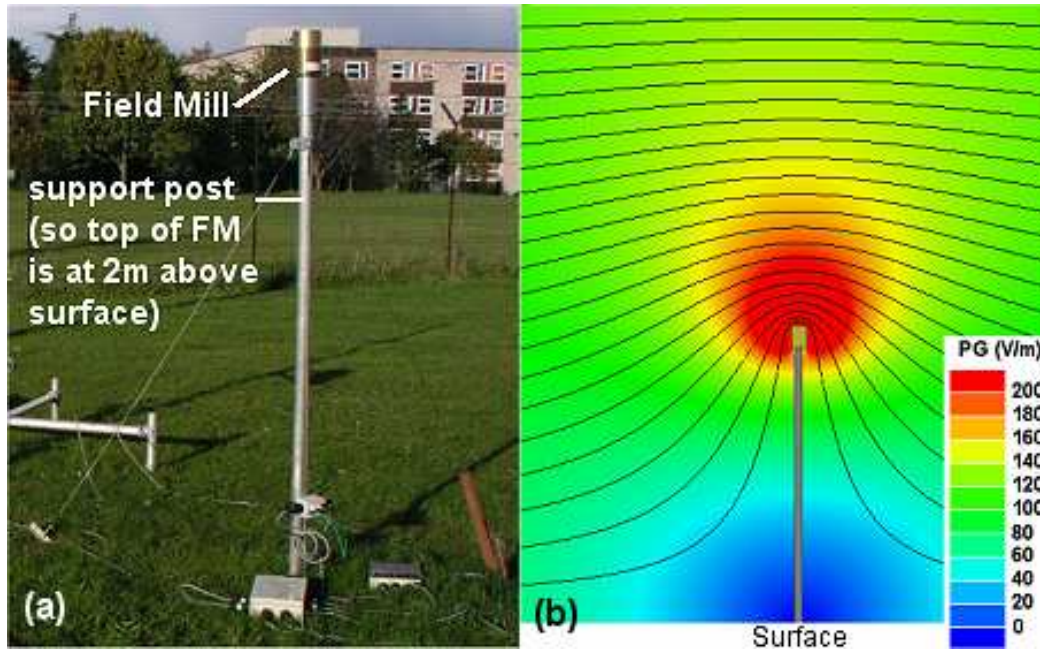


Figure 4.8 The FM and support pole installed at the RUAO in part (a) and (b) the modelled distortion of potential and therefore PG around the earthed FM and pole itself. The black lines are lines of equipotential (starting with 20V near the surface and increasing in 20V intervals with height), with the filled colour representing the PG. The ambient PG was 100V/m (i.e. green). It can be seen that the presence of the 2m structure causes an increase in PG of more than a factor of two at the top of the FM, where the PG is sensed. The figure (b) was generated using Maxwell SV electrostatic modelling software, assuming the air has zero conductivity, with the surface and all objects being perfect conductors.

To test for an instrument for temperature dependence, the FM was screened with an earthed metal cover over the sensing aperture so that no electric field would be experienced. The instrument was left like this for five days to measure output voltage at different air temperatures. The results of this experiment are shown in Figure 4.9. From these results it can be seen that a small negative response to increasing temperature is apparent, at $-6.2 \times 10^{-4} VK^{-1}$. Using equation (4.3) this is equivalent to a PG drift of $-0.24 Vm^{-1}$

$^1\text{K}^{-1}$. Assuming a large diurnal temperature range of 30K, this would therefore mean a corresponding variation of 7.2Vm^{-1} , which considering the usual mean fair-weather PG value of approximately 100Vm^{-1} , represents a “worst-case” temperature-induced diurnal PG variability of 7% of the mean. A low mean output voltage (0.009V) during this experiment confirms a negligible electric field experienced by the FM as it was covered by the metal plate.

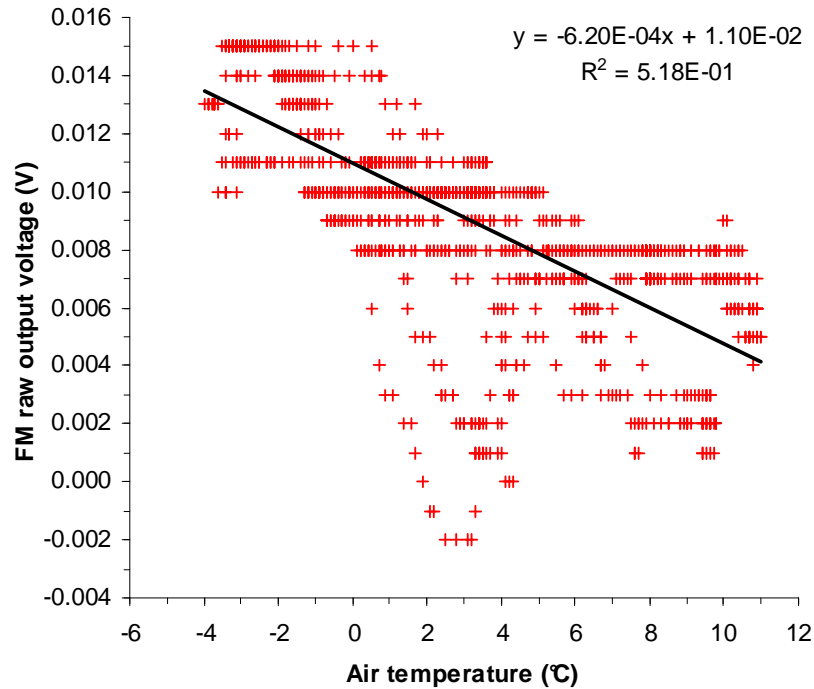


Figure 4.9 Raw output voltage of screened FM versus air temperature as five minute means between 2-6 February, 2007, with linear trend line.

A scatter plot of five minute average field mill-derived PG (using equation (4.3)) and the PG measured using the PW, taken over 16 days, is shown in Figure 4.10. Unlike the FM that is suitable for all-weather recording, the PW is only functional during dry, turbulent conditions when the insulation is not degraded by moisture and there is sufficient air movement adjacent to the wire to allow a continuous supply of ions (Harrison, 2004a) This is typically for a few hours either side of midday, but can be significantly longer during the summer. When both instruments were working it can be seen that a linear relationship exists, in accordance with the derived linear calibration equation (4.3).

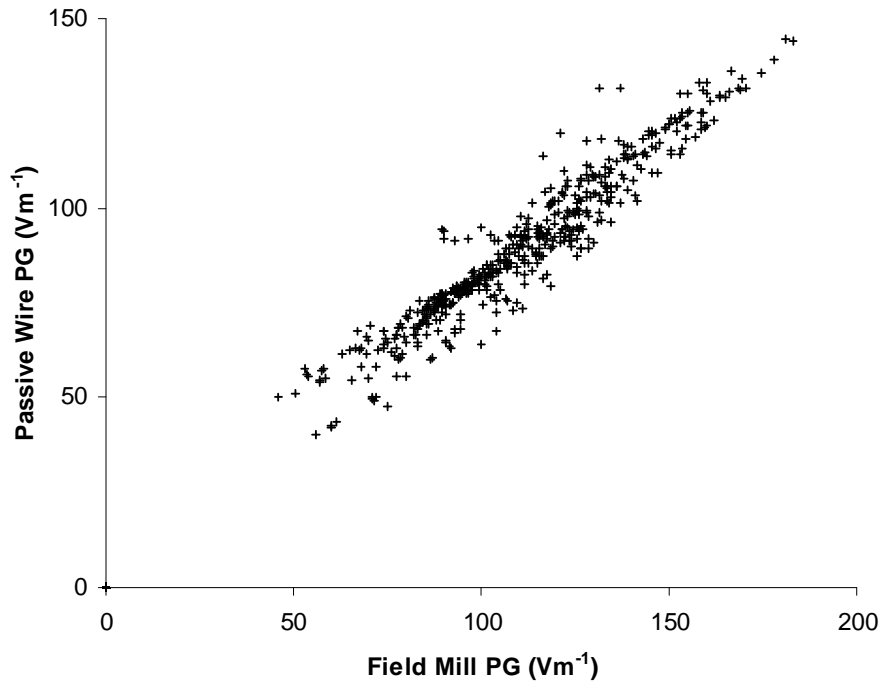


Figure 4.10 Comparison between PG recorded by the PW at 1m above the ground and the FM at 2m during fair-weather (from Bennett and Harrison, 2006a), using the manufacturer's suggested calibration. The line of best fit was then used to calculate the actual FM calibration equation (4.3).

The range was set to allow a PG range of $\pm 1947 \text{Vm}^{-1}$ corresponding to a raw output voltage of $\pm 5 \text{V}$ (RUAO logging range) once the calibration equation (4.3) is applied. This setting, when combined with the calibration equation (4.3) gives a manufacturer's quoted accuracy of within 7.7Vm^{-1} (corresponding to 1% of uncalibrated range sensitivity). This quoted accuracy is expected to be a considerable overestimate for routine measurement, based on results such as Figure 4.7 and the observed variability of the FM under both laboratory and operational conditions. This PG range was found to be adequate for routine fair-weather observation, whilst keeping a high resolution of 0.4Vm^{-1} for the RUAO logging system voltage resolution of $\sim 2.4 \text{mV}$ (10V range at 12-bit resolution).

4.4 Programmable Ion Mobility Spectrometer (PIMS)

The Programmable Ion Mobility Spectrometer (PIMS) was designed and built at the University of Reading Department of Meteorology (Aplin, 2000). The PIMS is based on a long-established approach for measuring the atmospheric ion spectrum by collecting the ions at the central electrode of an aspirated cylindrical capacitor, to which a deflecting (bias) voltage is applied to the outer electrode. The bias voltage is generated by a digital-to-analogue converter, which permits a wide variety of sampling voltage sequences for the ion spectrum (Harrison and Wilding 2005). The PIMS can measure either the voltage

decay or current flow, although the latter is usually preferred. The tube electrode voltage steps during the sampling cycle include both positive and negative values, allowing both ion signs to be analysed. There are currently three PIMS types; PIMS1, PIMS2 and PIMS3, all of which share the same general design and characteristics, but with successive advancements such as a metallic case and heated electrometer for improved all-weather durability. In addition, there are small-ion and large-ion PIMS, which have a smaller and larger electrode tube deflection fields respectively, to analyse different parts of the ion mobility spectrum. The instrument used most often during the investigation period was a small-ion PIMS2 instrument (number 010) as pictured in Figure 4.11. Small ions are generally most abundant, making them the main source of air conductivity at the RUAO.

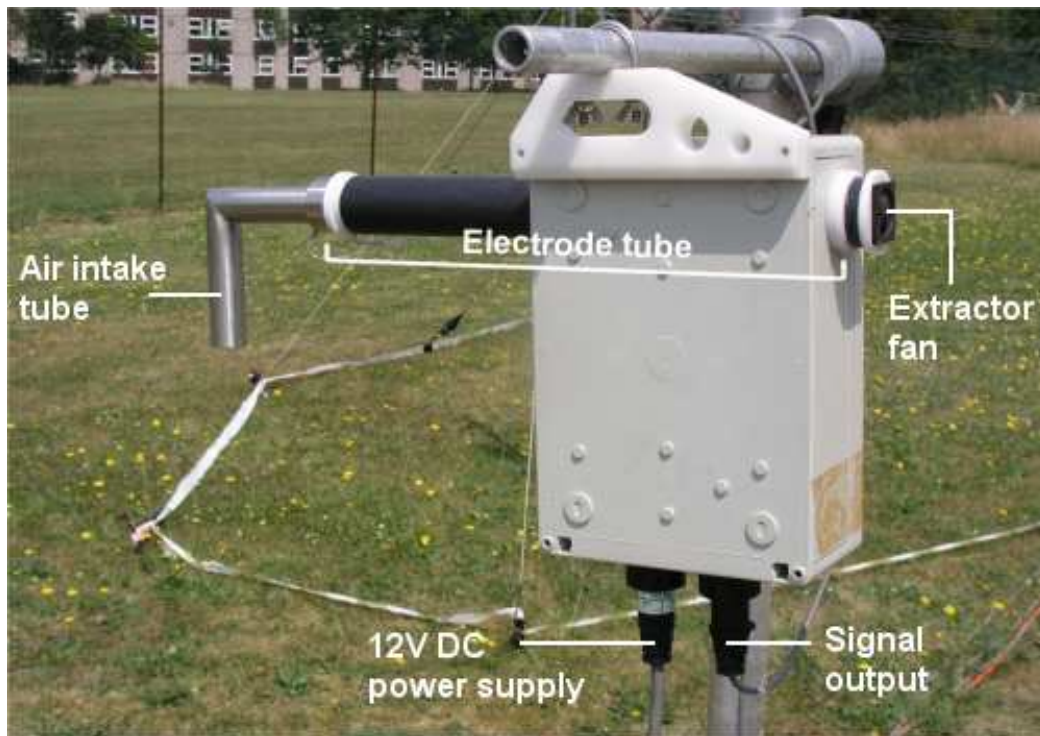


Figure 4.11 The Programmable Ion Mobility Spectrometer 2 (PIMS2) installed at the RUAO, with basic components labelled.

Once the PIMS output is logged using the custom-designed logging program PIMSPECT, a data processing program called SPECPROC is used to convert the raw current and tube voltages into atmospheric electrical parameters, such as air conductivity, ion mobility, ion number concentration, ion radius and space charge for both positive and negative small ions. The SPECPROC procedure is described by Harrison and Aplin (2007). A detailed account of the design and operation of the PIMS can be found in (Aplin (2000), Aplin and

Harrison (2001) and further measurements and improvements to PIMS by Harrison and Wilding (2005).

4.4.1 Comparison of PIMS and PW derived total conductivity

The PIMS instrument measured positive and negative air conductivity simultaneously and co-located with a series of PW charging experiments made on different fair-weather days in summer 2006 (Bennett and Harrison, 2006a). This allowed comparison between the two techniques for estimation of total air conductivity. Providing the assumption that the relaxation time measured by the PW technique is due solely to atmospheric properties i.e. that equation (4.1) is obeyed, the PW relaxation technique provides a near absolute reference conductivity determination in atmospheric conditions. This is because the measurement does not require knowledge of any air intake flow speed and is independent of instrument geometry, capacitance, or assumptions concerning the ambient ion mobility spectrum.

The voltages that capture the largest ions sampled by the small-ion PIMS are -18.5V and +17.9V. This corresponds to a minimum positive and negative critical ion mobility sampled by the PIMS of 0.95 and 0.99 $\text{cm}^2\text{V}^{-1}\text{s}^{-1}$ respectively. Five comparisons on different fair-weather days of the average total conductivity during the data collection intervals (typically 40-50 minutes) were made, the results of which are given in Table 4.1 and displayed in Figure 4.12. These results indicated that measurements made by the two instruments were in close agreement, with an average magnitude of 0.84fSm^{-1} and a mean difference of zero, although a maximum difference of 1.2fSm^{-1} was observed for one sample. Reasons for this discrepancy include possible spatial variations in average air conductivity during this period, or a substantial contribution of large ions (not detected by the small-ion PIMS) to the total conductivity (Dhanorkar and Kamra, 1997).

Since there was no identified systematic discrepancy between the two instruments (with any individual comparison usually under 1fSm^{-1}) there was consequently no evidence to suggest that the PIMS total air conductivity is different to the derivation made by the atmospheric relaxation measurement technique of the PW. The variation between consecutive experiments of the ion mobility spectrum was therefore concluded to be small.

Total Conductivity (fSm^{-1})		Difference (fSm^{-1})
Passive Wire	PIMS	
6.9	5.9	1.0
4.3	4.8	-0.5
6.4	5.2	1.2
3.6	4.6	-1.0
3.3	3.8	-0.5
Mean		0.0

Table 4.1 Results of the PW relaxation and PIMS methods of total conductivity measurement for different fair-weather days in summer 2006 (Bennett and Harrison, 2006a).

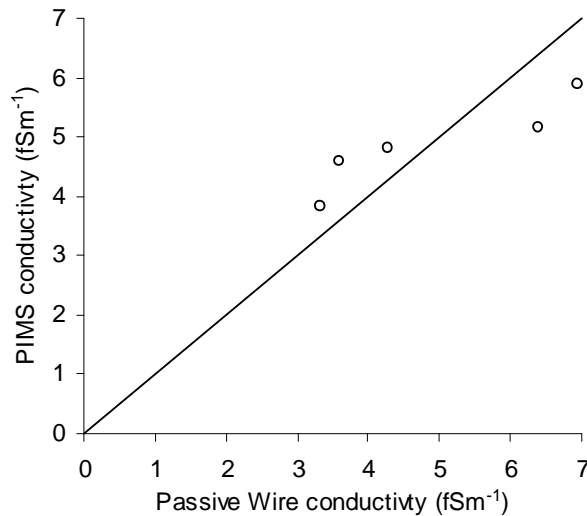


Figure 4.12 Scatter plot of total conductivity derived from the PIMS and passive wire instruments (circles), compared to the line of unity gradient, indicating an exact agreement.

4.5 The Air-Earth Current Pyramid (AECF)

The AECF was the first current density measuring instrument designed and installed at the RUAO. The instrument is the first to use a geometrical method of current density determination, the theory of which was discussed in chapter 2. Confirmation of the operating principles and initial results of the AECF have been reported in Bennett and Harrison (2006b).

4.5.1 Requirements

As discussed in the current measurement section of chapter 2, there are a variety of ways in which the conduction current density (J_c) component of the air-Earth current density (J_s) can be directly measured. During fair-weather, it is the displacement current density

(J_D) that produces the greatest “interference” when attempting to measure J_C and so all methods attempt to separate or remove this component.

Of these different compensation methods, it is the geometrical method originally suggested by Mukku (1984) that is investigated here. The main reasons for this choice are:

- The geometrical method does not rely on assumptions about the local air conductivity, required by the Kasemir (1955) method, which assumes a known and constant conductivity. Since the air conductivity is known to vary at the RUAO (Bennett and Harrison 2006a) as indeed at any location, the Kasemir (1955) method can only realistically provide a partial compensation of J_D .
- The simplicity of the geometrical method based only on collector geometry requires no additional electronics or insulation other than that for the collectors themselves, reducing the risk of leakage currents or possibility of compensator degradation in addition to the insulation.
- J_D is measured in addition to J_C (not simply diverted straight to ground as in the popular Kasemir (1955) method) providing additional data.

Although the basic concept was proposed by Mukku (1984) the idea had not been put into practise until this investigation. As the fair-weather current density is small (of order 1pAm^{-2}) the surface area of the collector must be large enough to collect a detectable current by the ammeter used, but not too large as to be impractical to construct and install. The requirement for a three-dimensional collecting plate to be placed with its top flush with the surface to avoid distortion of the ambient PG also requires some sort of pit to be dug to accommodate this collector, so for practical purposes, consideration of the depth of pit required must also be made.

As the geometrical method involves an effective surface area (the difference in horizontal cross-sections of the two collectors), rather than the areas of the individual collectors, the most efficient design for the two collectors required will have a maximum difference in cross-section relative to their overall size, whilst retaining the same total surface areas, in accordance with the geometrical method principle. A list of design criteria is given to summarise the requirements:

List of design criteria:

- Two collectors each having the same total surface area, but different horizontal cross-sections.
- Collector geometry which maximises the difference in horizontal cross section.
- The cross-section of an individual collector should ideally be large enough to act as a collector of J_c in its own right (and not just J_D), allowing comparison and cross-checking between the two collectors.

Therefore, the best geometry will be that which permits the largest absolute difference in cross sectional area between the two collectors, for the lowest ratio of cross sections to avoid one plate being disproportionately large to compensate for the other. Mathematically, the ideal solution is a hemispherical-shaped collector and a horizontal flat (e.g. disk-shaped) collector. This allows an absolute difference in cross-sectional area equal to that of the hemispherical collector itself, allowing one collector to have only twice as large cross section as the other, as described by the original equations of Mukku (1984).

In practise however, a suitably large hemispherical shell of the required material and properties would be too difficult (and likely expensive) to construct using the resources available. A cube-shaped design would have a high cross section ratio, but this would make one collector cross-section very small relative to the other, requiring one collector to be very large to allow the other to have a cross-section capable of collecting a measurable J_c . For instance, a 5m² flat collector would be required to allow the cubic collector to have a 1m² cross-section, i.e. factor of five larger, compared to a factor of two for the hemispherical collector.

4.5.2 The AECF current collector geometry

After consideration of the balance between the ideal design criteria and ease of construction, it was decided that a pyramid-shaped collecting plate (hence the name of the instrument) would be the best supplement for the hemispherical shell originally proposed by Mukku (1984). This was due mainly to the cross sectional ratio being low enough not to require an impractically large second collecting plate to compensate, whilst retaining simplicity of construction. Due to the three-dimensional nature of this pyramid collector, the depth of the collector (and therefore of pit required to allow the top to be flush with the ground) must also be calculated, as the tip of the inverted pyramid must not be allowed to make contact with the pit bottom or edges.

For the second collecting plate, the simplest and most efficient design would be horizontal and flat, but the actual shape is not important as the cross section will always be equal to the surface area for an essentially two-dimensional object. The turbulence-dependency of some components of J_T and J_D mean that spatial variation is likely to occur on a broad range of length-scales. It was therefore considered that the two collectors should be positioned as close to each other as possible. Constructing a flat horizontal plate collector that actually bordered the perimeter of the upturned pyramid would satisfy this requirement as much as possible, since both collectors would be centred about the same point. The precise dimensions of the two collectors depend on the required effective collecting area (i.e. the difference in cross sectional area of the two collectors). As previously stated, a compromise between having large collectors that will gather more current and therefore increase the signal-to-noise ratio and ease of construction and instalment at the RUAO must be made, as a pit is required to accommodate the pyramid collector.

It was decided that an effective collecting area of 1m^2 would be ideal as this would correspond to a current of order 1pA , which would be suitable for the picoammeters used, and have the additional benefit of being a unit-area measurement, i.e. the output current would be equal to the current density in m^2 . For simplicity and ease of construction, the surface area of the horizontal flat plate surrounding the pyramid (termed the border plate, BP) and the pyramid collector (termed the pyramid plate, P) was set to be 2m^2 . The cross-section of the pyramid plate must therefore be 1m^2 for an effective collecting area of 1m^2 . These areas allow simple calculation of J_C from the currents collected by BP and P (Bennett and Harrison, 2006b) such that:

$$I_{BP} = 2J_C + 2J_D \quad (4.4)$$

$$I_P = J_C + 2J_D \quad (4.5)$$

where I denotes collector current for BP and P in pA , identified by the appropriate subscript, with J_C and J_D being in pAm^{-2} and assumed proportional to the cross section and surface areas respectively. Therefore J_C and J_D (in pAm^{-2}) are found simply by

$$J_C = I_{BP} - I_P \quad (4.6)$$

$$J_D = \frac{I_{BP} - 2 \cdot (I_{BP} - I_P)}{2} \quad (4.7)$$

as the identical surface areas of BP and P allow J_D to cancel in equation (4.6) on subtraction, leaving only J_C . Equation (4.7) is used to determine J_D . Strictly, equation (4.6) is valid only for $J_T \ll J_C$, (J_T is indistinguishable from J_C without separate measurements using Ohmic assumptions or the local space charge gradient and turbulent theory such as that of Vitta, 1974). J_T is however expected to be small in fair-weather conditions (Gherzi, 1967). An experimental verification that $J_C \gg J_T$ during fair-weather conditions is provided in chapter 5.

An image of the AECP installed at the RUAO and the dimensions of the collecting plates and pyramid pit are given in Figure 4.13. The AECP was constructed out of marine-grade stainless steel for all-weather durability and good electrical conduction. The metal sheet was 1mm thick, which was considered a compromise between durability, ease of construction/installment on RUAO, and weight (since the plates have to be supported on high-quality insulation using the smallest possible surface area to avoid leakage currents). Despite the thin sheet metal, the AECP weighed 31.4kg in total. A layer of wooden reinforcement was added to the underside of the BP to reduce the metal flexing under its own weight. The AECP was finally installed at the RUAO on 7 October 2005.

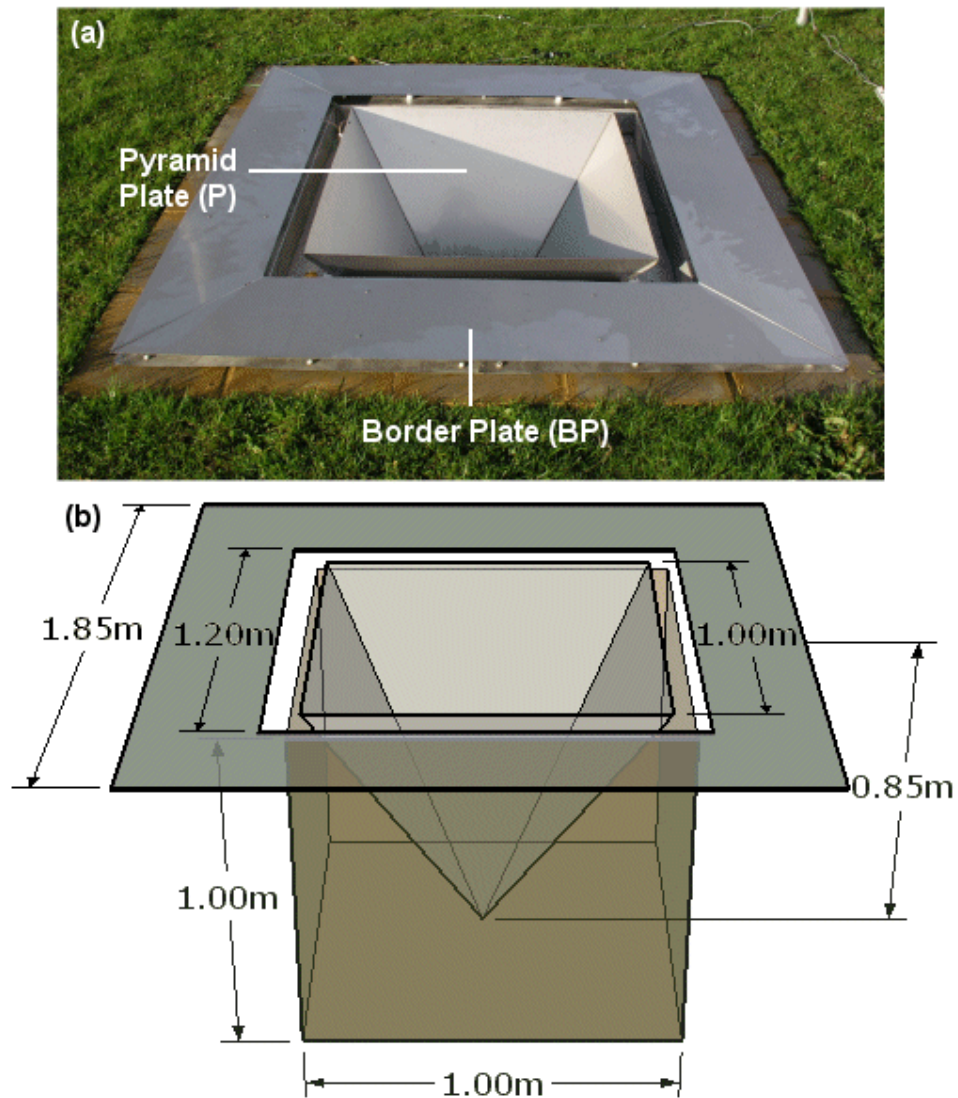


Figure 4.13 The AECP installed at the RUAO. (a) identifies the two collectors and (b) describes the dimensions of the collectors. The pit required for the pyramid plate to be flush with the surface and not touching anything other than the insulated supports at the top pyramid corners is also shown. A separation of 0.1m was allowed between the BP and P collectors to avoid accidental bridging by water, blowing leaves, grass etc.

4.5.3 AECP collector insulation

Good quality electrical insulation is an essential aspect of air-Earth current instruments (Kasemir, 1951) so much attention was given to the method of electrically isolating the two collecting plates of the AECP from the ground. Polytetrafluoroethylene (PTFE) was used as the insulator material due to its extremely high resistivity (of order $1 \times 10^{18} \text{ Ohm cm}$). In addition, this soft polymer is easily machined to any desired shape and is chemically inert, preventing any chemical reactions from altering its properties over time or generating

spurious currents. PTFE is non-stick (the material is also known as Teflon[®]) so this also helps to prevent dirt and other impurities sticking to the surface and lowering the resistivity. PTFE has been used for the insulation of air-Earth current instrumentation by other researchers (e.g. Gherzi, 1967, Retalis, 1991 and Byrne et al., 1993).

The PTFE insulators used to support the AECF collectors is shown in Figure 4.14. The pyramid collector (P) was supported at each edge by a cylindrical PTFE rod, with the border plate (BP) supported by PTFE columns at the corners and the middle of each side. Therefore twice as many supports are required for the BP than the P as although by definition both have the same surface area, thickness and hence weight, the flat BP collector is less rigid than the P collector so requires further support to prevent flexing, and the subsequent risk of ground contact. As the metal used for the BP collector was only 1mm thick, the collector had a tendency to bow towards the ground away from the supports, increasing the risk ground contact. The later addition of wooden reinforcement to the underside of the BP improved its rigidity but 8 insulators were still required for adequate support, as supports positioned only at the corners were ineffective at preventing bowing in the middle of the sides, especially after rain when the BP was wet and therefore heavier.



Figure 4.14 PTFE insulators used to support the border (BP) and pyramid plate (P) collectors of the AECF. The BP was supported by eight vertical PTFE cylinders approximately 4cm high and approximately 1cm diameter, with conical tops to minimise the contact surface, reducing the probability of leakage currents. The P collector was supported by four cylinders approximately 16cm long and 26mm in diameter positioned on the corners of the pit. The blade-like edge of the P collector resulting from the requirement to weld the sides together meant that contact area was kept to a minimum as the collector rested only on its edges.

4.5.4 AECp picoammeters

Due to the especially small currents involved with measurement of J_s components (order 1pA for a collecting plate of 1m² surface area) a picoammeter must be used. A feedback picoammeter has been developed by the University of Reading Department of Meteorology, from the original design by Harrison (1995). The circuit diagram of the standard picoammeter used by this investigation is shown in Figure 4.15, with component properties given in Table 4.2. The basic principle of this feedback picoammeter is to measure the voltage drop across a 100G Ω resistor (R3) resulting from the current originating from the collector, using a very high impedance voltage follower, the MAX406 op-amp (IC1). By Ohm's Law, a 100G Ω resistor would allow a voltage of 0.1V for a 1pA current, which was found to be a compromise between resolution and range, considering the $\pm 5V$ maximum logging capability and 1mV resolution at the RUAO. This raw output voltage was calibrated to current in the laboratory using a high sensitivity commercial electrometer (Keithly 6512 electrometer). Calibration consisted of generating a current from a precision voltage supply and 10G Ω resistor, the value of which was measured using the Keithly 6512 electrometer. This known current was then passed through the picoammeter, and the output voltage was recorded. This procedure was repeated for different currents, and a line of best fit was found between input current and output voltage.

Current from the collector enters the circuit through R3 (the 100G Ω resistor) via P1, where the voltage across R3 is measured by the op-amp IC1, which lies in parallel. For a feedback picoammeter, the voltage output of IC1 is the inverse of the current input multiplied by the value of the feedback resistor, R3, which is why an inverter component (IC4) of required to account for this inversion. This feedback method allows for a low voltage burden on the input (the collecting plate), so that the voltage on the collector is not altered by the measurement. The IC2 dual op-amp serves to fix the 5V circuit supply from the initial 12V supply from the RUAO, which may be variable, so a constant reference voltage is preserved. The variable resistor VR1 is added to allow the gain from IC1 to be changed if required.

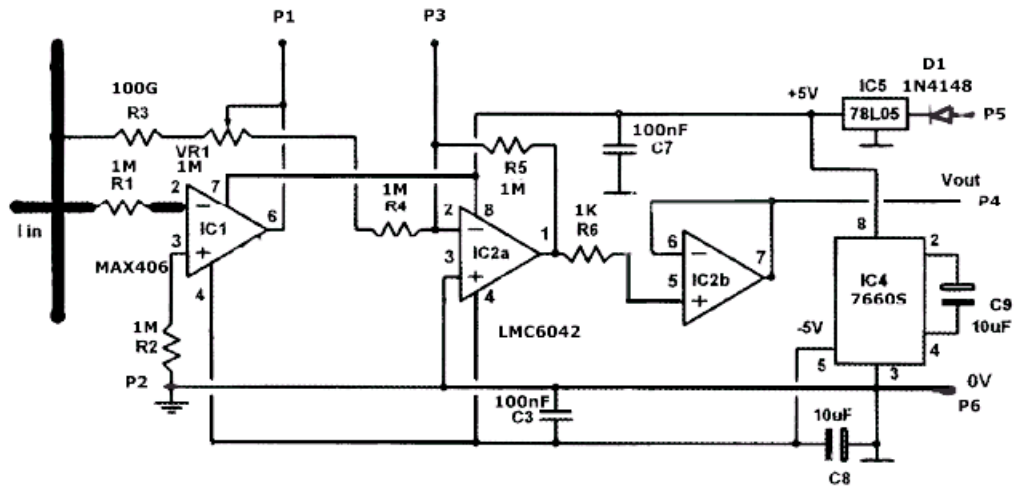


Figure 4.15 Circuit diagram for the picoammeters used in the AECp. (From University of Reading, Department of Meteorology electronics laboratory technical guide number 018-3, based on the designs of Harrison, 1997b). Component details are provided in Table 4.2.

Ref	Value	Description
D1	1N4 148	Signal diode, DO35 package
IC1	MAX406	Op-amp IC, DIL8 package
IC2	LMC6042	Dual op-amp IC, DIL8 package
IC4	7660S	Inverter IC, DIL8 package
IC5	78L05	5V regulator IC, TO92 package
R1	1M	1%, 1/8 watt metal film resistor
R2	1M	1%, 1/8 watt metal film resistor
R3	100G	10%, precision ceramic resistor (LGP opto-electronics)
R4	1M	1%, 1/8 watt metal film resistor
R5	1M	1%, 1/8 watt metal film resistor
R6	1K	1%, 1/8 watt metal film resistor
VR1	1M	10%, ¼ watt, 100ppm/deg C, 6mm multi-turn top adjust potentiometer
C3	100nF	50V, 0.2in, radial ceramic capacitor
C7	100nF	50V, 0.2in, radial ceramic capacitor
C8	10uF	16V, 0.2in, radial tantalum capacitor
C9	10uF	16V, 0.2in, radial tantalum capacitor
P1-P6	1mm	PCB terminal pins, press fit
LK1		0.6mm dia solid wire link
LK2		0.6mm dia solid wire link

Table 4.2 Components used for the picoammeter described in Figure 4.15. (From University of Reading, Department of Meteorology electronics laboratory technical guide number 018-3).

Measurements at the RUAO were made at 1Hz, so any current input variations greater than half this frequency (such as high frequency J_D) must be suitably suppressed to avoid both signal aliasing and the potential for the picoammeter op-amp (IC1) to become saturated, which may result in a non-linear response. An RC time constant of the circuit is

needed that will suppress high frequency ($>0.5\text{Hz}$) noise whilst allowing the picoammeter to accurately measure changes in J_c . The RC time constant was modified by including a low-leakage polystyrene capacitor placed in parallel with the $100\text{G}\Omega$ resistor (R3), in the feedback loop of the input amplifier. As the electrical relaxation time of the atmosphere near the surface (which governs the timescale of change in J_c at the surface) is observed to be of order 1000s (e.g. Burke and Few, 1978, Bennett and Harrison, 2006a). As such, a time constant considerably less than 1000s yet large enough to suppress high frequency noise was required. This was chosen to be approximately 30s (by using a 330pF capacitor, producing a RC time constant of 33s when positioned parallel to the $100\text{G}\Omega$ resistor, R3). The 33s time constant was observed to allow all fair-weather 1s variation to be within the $\pm 5\text{V}$ logging range, unlike trials using a 3s time constant, that did not damp the high frequency noise to within this range. For the study of J_D , this 33s time constant must be considered when comparing J_D measured by this picoammeter to sensors with a shorter time constant such as the FM.

The two picoammeters used for the AECF are shown in Figure 4.16. The current collectors are connected to the picoammeters by a shielded coaxial cable; with PTFE insulation both within the cable and as the cable enters the picoammeter housing. The outer shielding is connected to ground to suppress any noise as the current flows down the cable. Since this arrangement will produce a capacitance, the length of cable between the border plate and pyramid plate collectors was kept approximately equal to avoid damping one signal more than the other.

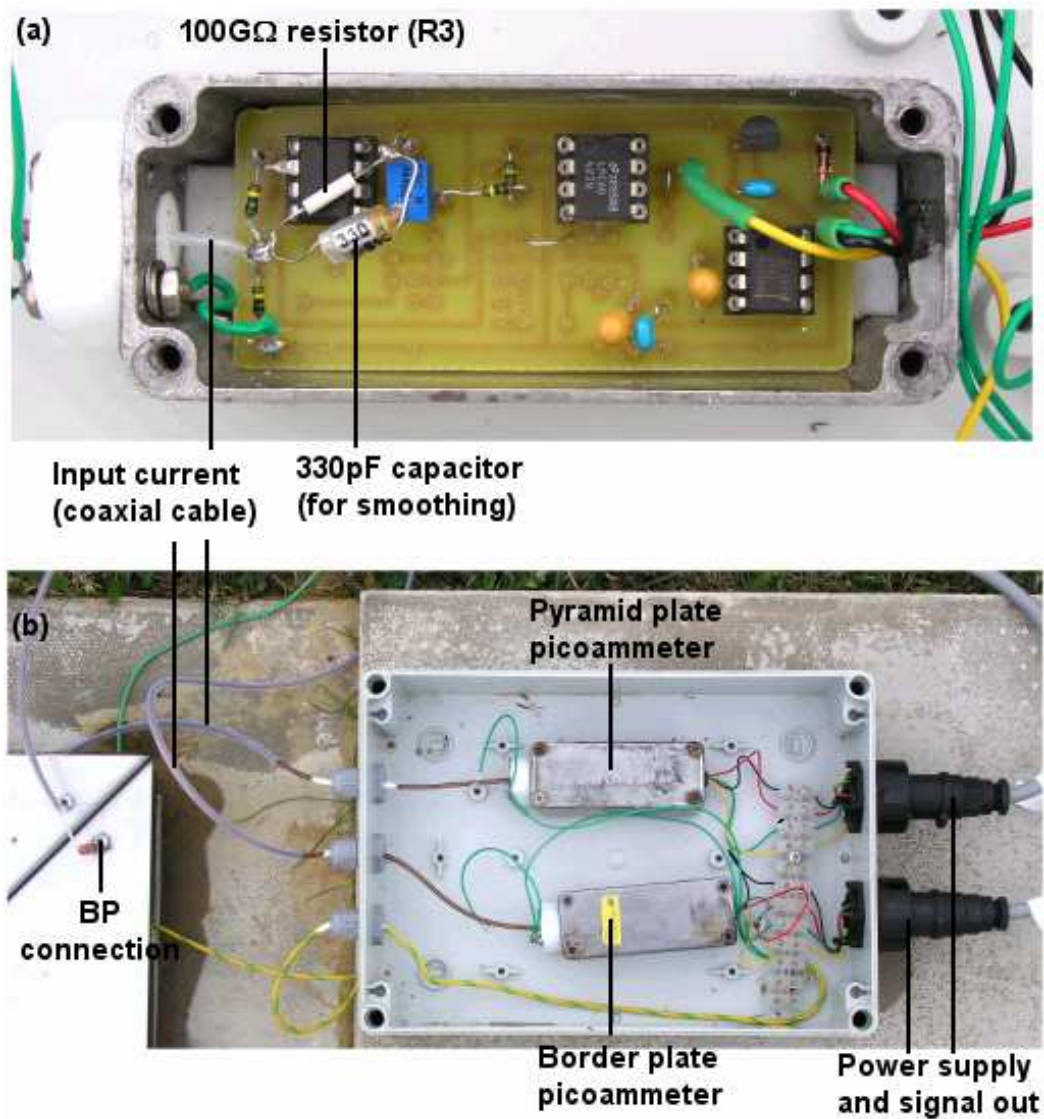


Figure 4.16 The picoammeters used for the AECF. Part (a) identifies the large value feedback resistor (R3) and smoothing capacitor of the picoammeter input stage within the circuit, and part (b) shows the two picoammeters housed in the AECF logging box, connected to the two collecting plates.

Calibration of the picoammeters was undertaken by generating a current of order 1pA using a precision voltage source and a 10G Ω resistor. The actual current produced by this method was measured using the Keithly electrometer prior to insertion into the picoammeter. The results of this calibration are shown in Figure 4.17. Although calibration incorporated the full 5V range available at the RUAO, extra data points were made around the expected typical values for I_{BP} and I_P which was considered to be around $\pm 5\text{pA}$ if values of J_C and J_D are of order 1pAm^{-2} , especially considering high frequency J_D will be suppressed by the capacitive smoothing. As can be seen in Figure 4.17, the linear relationship between input current and picoammeter output voltage holds between $\pm 30\text{pA}$,

with a slight deflection above 30pA magnitude. Despite this, the linear calibration is considered adequate for this instrument in view of the otherwise strong linear correlation in the range of expected typical input currents. Using the calibration factors determined by the least squares method, the residuals between input current and calibrated output current measurement were examined. There was no systematic relationship or correlation between input current and residual, so the error is expected to be random. The mean residual magnitude was 0.03pA and 0.04pA for picoammeters PA1 and PA2 respectively over the expected operating range of $\pm 5\text{pA}$. These uncertainties are combined when determining J_C by equation (4.6) to give an uncertainty in J_C due to the picoammeters of $\pm 0.05\text{pAm}^{-2}$.

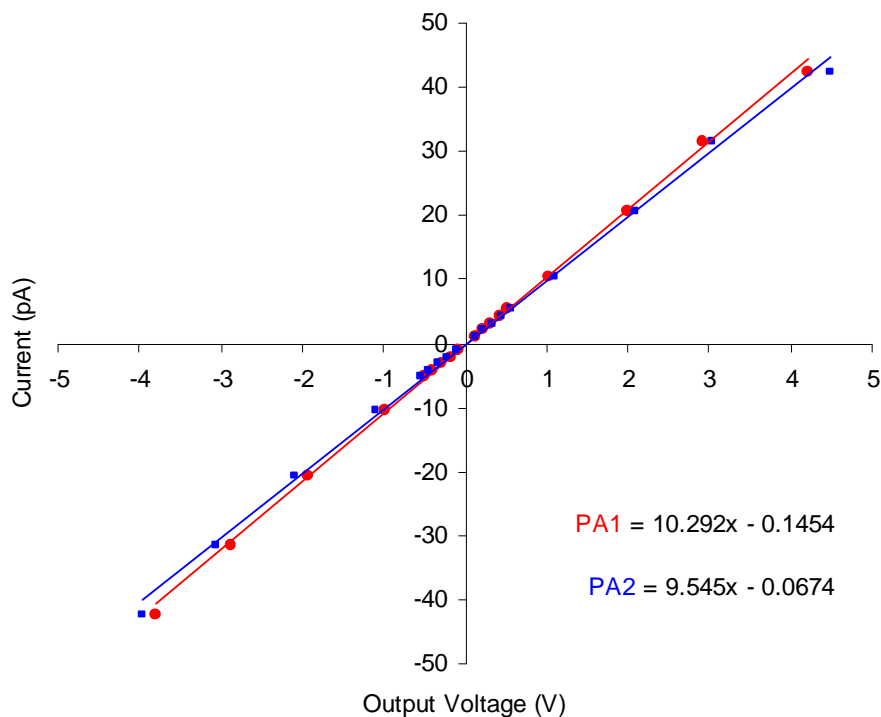


Figure 4.17 Calibration of the picoammeters using a Keithly 6512 electrometer to measure current generated by a voltage source and $10\text{G}\Omega$ resistor. The equation for the line of best-fit (using the least squares method) is given for the two picoammeters (PA1 and PA2).

In order to test for calibration drift with time, two picoammeters of this design were recalibrated 6 months later after their initial calibration and deployment in the field. The calibration was found to have changed by only 3% and 1% for the respective picoammeters during this time, demonstrating a high degree of calibration stability.

The thermal stability of the picoammeters was also investigated. A constant current was supplied into the picoammeter, which was then heated to 40°C (using an environmental chamber) then left to cool in the laboratory. Whilst cooling, the temperature of the metal picoammeter housing (also considered to be the temperature of the components within) was measured using a digital thermometer and the picoammeter output voltage corresponding to the constant current measured. A constant current was generated using a precision voltage source and 10GΩ resistor (both at constant temperature). The magnitude of this current was measured as 2.04pA. The temperature of the picoammeter once in the laboratory ranged from 32.0°C to 23.3°C. The current measured by the picoammeter showed no evidence of a trend (r value of 0.57 between the picoammeter temperature and current measurements) with a mean value of 2.04pA and standard deviation (from 6 values) of 0.012pA. Over the measured temperature range of 23.3°C to 32.0°C, the temperature sensitivity was 2fAK⁻¹.

4.5.5 Initial results from the AECF

The basic principles and initial results from the AECF are discussed in Bennett and Harrison (2006b). Example data from the BP and P collectors measured during a fair-weather period are shown in Figure 4.18, along with FM-derived PG for the same time.

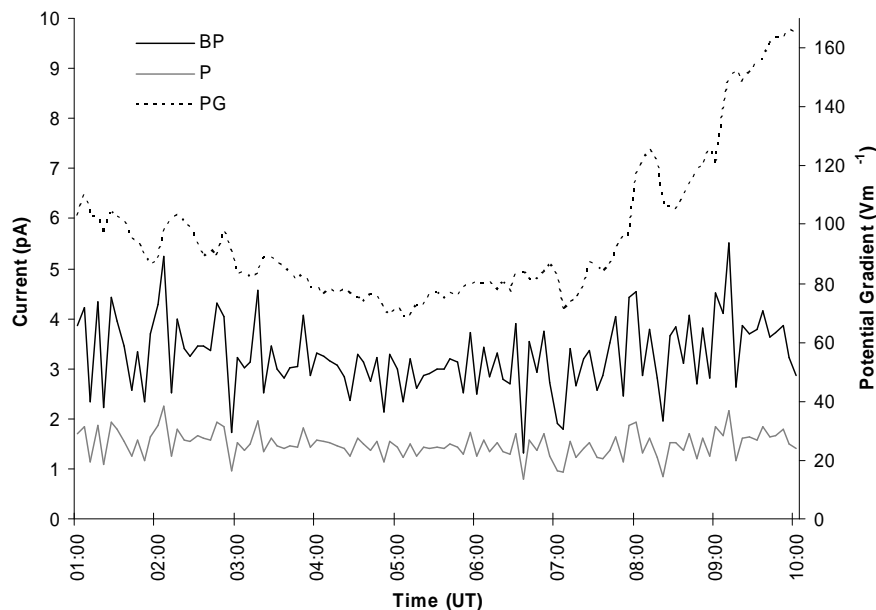


Figure 4.18 Five-minute mean current measured by the border plate (BP) and pyramid plate (P) as well as Potential gradient (PG) using a field mill 2m from the AECF, 28 January 2006. From Bennett and Harrison (2006b).

The time traces of current measured by the BP and P collectors are in good agreement, as expected from their close proximity. The BP current is higher than from P due to the larger horizontal cross sectional area of BP allowing a greater collection of J_C as described by equation (4.4). From equation (4.6) the mean J_C value can be found. For this time period, the mean was 1.76pAm^{-2} , with a standard deviation of 1.15pAm^{-2} . This result is comparable to the 1966-1979 J_C value measured using the Wilson apparatus at Kew, London (51°N, 0°W) of $1.45\pm 0.42\text{pAm}^{-2}$ (Harrison and Ingram, 2005). As previously stated J_T is expected to vary more rapidly than J_C and is likely to be responsible for much of the standard deviation.

The J_D component can be calculated theoretically from the variation of PG found by the FM (Chalmers, 1967):

$$J_{D(FM)} = -\epsilon_0 \cdot \frac{d}{dt} F \quad (4.8),$$

where ϵ_0 is the permittivity of free space, F is the potential gradient (in Vm^{-1}) and t is time (in seconds). Measurements of the displacement current J_D derived by the AECP were compared to J_D calculated theoretically using the FM and equation (4.8). Figure 4.19 shows the strong correlation between AECP and field mill-derived J_D . The correlation is significant at the 99% confidence level.

The magnitude of J_D measured by the two instruments would be the same only if both experienced the same PG, although the correlation is independent of this providing the relative change in PG remained the same. Differences in absolute PG over the AECP and FM arise as they are separated by 2m in height and 2m horizontally, and the presence of nearby grounded obstacles cause regional field distortions. No correction has been applied for this local distortion, but the gradient of Figure 4.19 indicates a factor of 1.8 between the two sensors, which is likely to have been caused by the difference in absolute PG over the instruments.

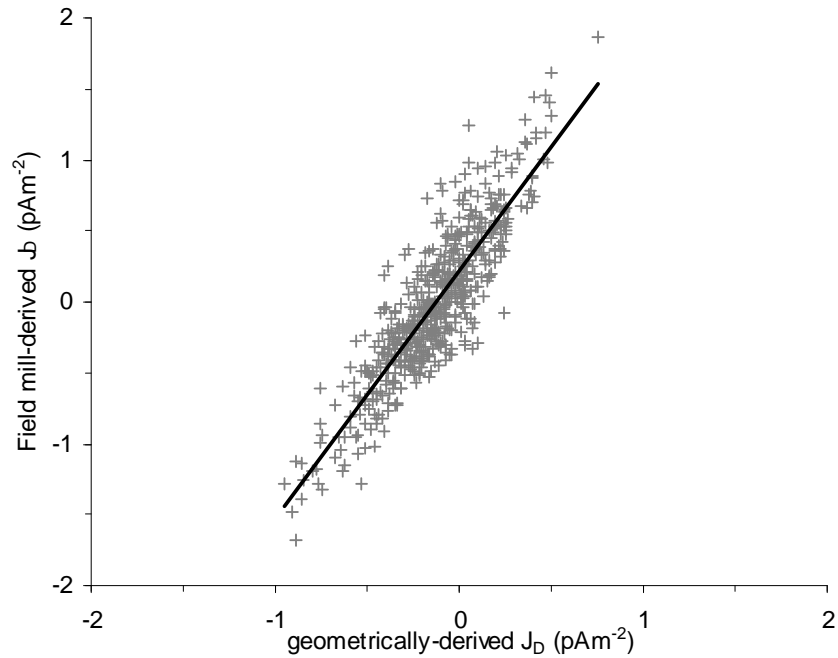


Figure 4.19 Scatter plot of field mill-derived displacement current calculated using equation (4.8) versus displacement current derived from AECP geometrical measurements and equation (4.7). Points are one-minute values between 01-10 UT 28 January 2006. From Bennett and Harrison (2006b).

4.5.6 Modelling of J_C and J_D around the AECP

Using commercial electrostatic 2D-modelling software⁴, the PG around the AECP was modelled. Modelling of the PG allows the flow of J_C to be inferred as the small ions will flow parallel to the field vectors. Additionally, from equation (4.8) it can be seen that J_D is directly proportional to the rate of change in PG. Therefore, the magnitude of PG at the collector relative to ambient PG will also be equal to the relative magnitude of J_D . By using this relationship, relative magnitude of the induced displacement current J_D received by the two collectors (BP and P) compared to that of the ambient atmosphere (without the presence of geometrical distortion) can be found.

Contours of relative PG (as a percentage of ambient) around the AECP are shown in Figure 4.20. The ground and collectors are modelled as perfect conductors (at ground (zero) potential), with the air having negligible conductivity. From this model, it can be seen that there is an enhancement of PG at the top surface of the BP by approximately

⁴ Software used was Maxwell SV version 3.1.04, by Ansoft Corporation. Details available at www.ansoft.com/maxwellsv/

25% of ambient (i.e. 125%). This is mainly due to the BP being elevated by 4cm from the surface by the insulators (Figure 4.14). The P collector is positioned in a pit below the surface so receives an average PG approximately 50% less than ambient (such as that measured by flat electrode flush with the surface).

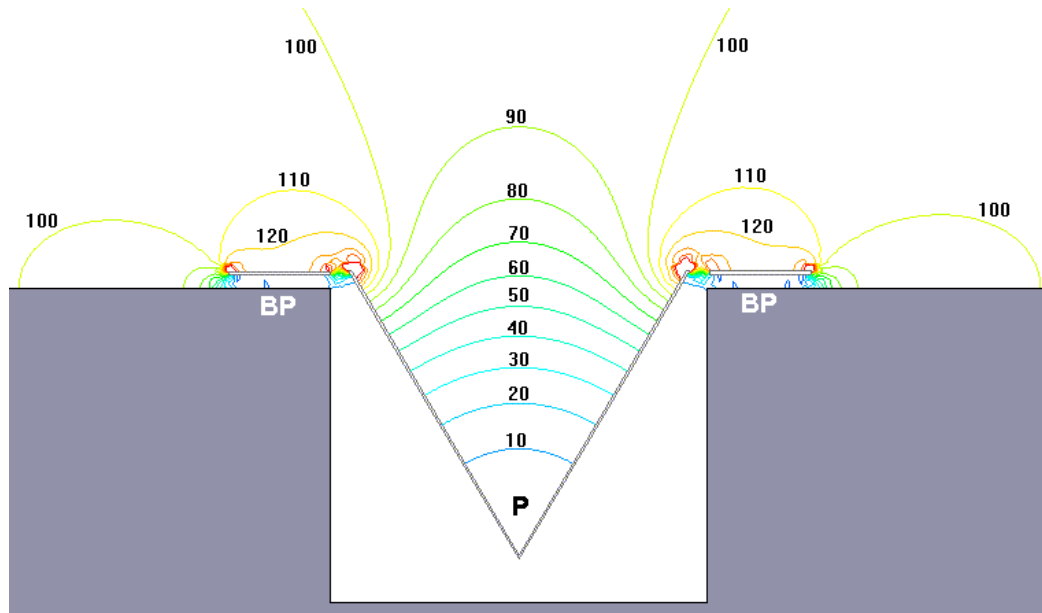


Figure 4.20 Vertical cross section of modelled PG around the AECp. The ambient PG was modelled as 100V/m so the contour values represent the percentage of ambient PG around the instrument. An enhancement of ambient PG of approximately 25% is modelled for the surface of the BP collector, with a reduction in PG around the P collector.

The fraction of mean PG received by the BP and P collectors was therefore 125/50 respectively (i.e. factor of 2.5). This factor was verified experimentally by finding the fraction of J_D measured by the two collectors on a fair-weather day. If the model was representative, J_D measured by the BP should be approximately 2.5 times larger than that measured by P. Assuming the majority of the variability in measured current from both collectors at 1Hz is due to J_D (as J_C can not change this rapidly), the gradient of a linear trendline of 1Hz BP vs P current should be approximately 2.5 for the model to be verified. For this experiment there is a requirement for the values to be measured over a timescale by which J_C is thought to be relatively constant, as it is the variability in J_D that is being considered. This timescale should therefore be less than the relaxation time of the atmosphere, of order 1000s. Consequently, the factor was calculated at 300s (5 minute) intervals. A meteorologically settled, fair-weather period was chosen when the relative humidity remained low to avoid leakage currents. The period chosen consisted of nine consecutive hours between 26-27 February 2006, within a longer period of notably settled, dry weather.

The results of this experiment are shown in Figure 4.21. It can be seen that the relative difference in J_D between BP and P is similar to the theoretical estimate of 2.5, with a measured mean of 2.66 ± 0.07 . For a relative PG of 125% on BP, this would imply a corresponding mean relative PG of 47% for P, which appears consistent with the modelled PG in Figure 4.20.

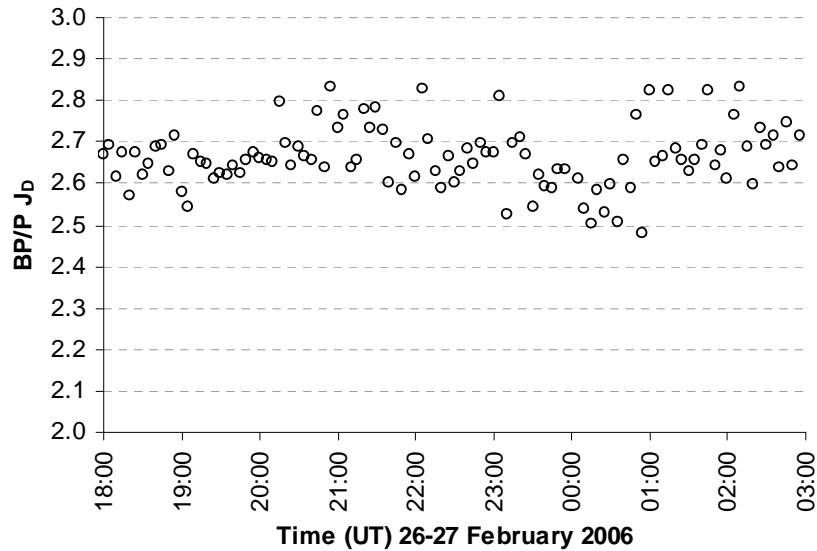


Figure 4.21 Gradients of 1Hz BP vs P current measurements for 5 minute intervals between 18UT 26 February and 03UT 27 February, 2006. During this time, the weather was fair and calm, with 1Hz current variation attributed to J_D .

This result may also help to explain the 1.8 ratio between AECP-derived J_D and FM-derived J_D of Figure 4.19, as the reduced J_D measured by the P collector will, in combination with other geometrical factors such as proximity to obstacles, cause a systematic underestimation of J_D using equation (4.7).

The implication for J_C measurements is that the AECP requires a geometrical correction factor to the 1Hz current measurements of the P collector of approximately 2.7 in order that the effect of J_D is completely removed. Although this correction factor appears relatively constant (standard deviation of 0.07 for the results in Figure 4.21), any variation would allow a small fraction of J_D to “contaminate” the J_C measurement, so re-calculation of this factor over the time period concerned would be a sensible precaution for most accurate J_C determination. In view of this correction factor, the original equations for J_C and J_D using the AECP have been modified to become:

$$J_C = \frac{I_{BP} - KI_P}{2 - K} \quad (4.9),$$

$$J_D = \frac{K}{2} \cdot \left(\frac{I_{BP} - 2I_P}{K - 2} \right) \quad (4.10).$$

Where K is the correction factor. As previously stated, these equations are only valid over time periods when J_C is constant (i.e. $< \sim 1000s$), such as using 1Hz data over five minute periods, as in Figure 4.21.

The effect on J_C resulting from distortion of PG around the AECP was also investigated. Using the same electrostatic model, PG vectors were calculated around the AECP. The current will flow parallel to these vectors so a pattern of current flow around the AECP can be derived. The results of this model are shown in Figure 4.22. From this figure it can be seen that despite the PG distortion, the current flow is near-vertical for both collectors. A key assumption of the geometrical technique is that J_C flows vertically to the collectors. This model therefore retains the assumption in the design of the AECP that the physical vertical cross sectional area of the collector is equal to the area exposed to J_C . It is noted that although the decreased and non-vertical PG vectors will cause the velocity of the small ions to decrease on entering the P collector, but conservation of charge will mean that this will be offset by an increased ion number density within the collector, therefore retaining a constant J_C within the pyramid. It is the current vector as it enters the top of the P collector that is of importance, since once the ions drift into the collector they will inevitably flow to the collector's surface.

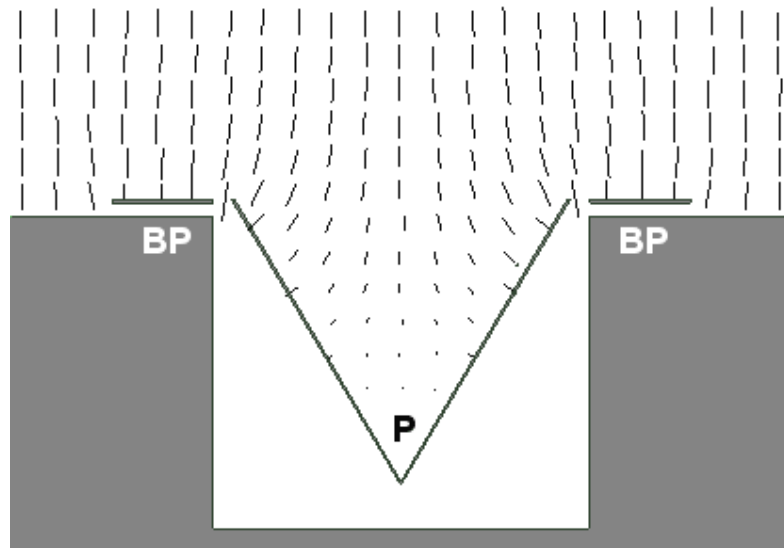


Figure 4.22 Vertical cross section of modelled PG vectors around the AECP. The direction of the conduction current J_C is parallel to these vectors (directed downward); with the line's length proportional to ion drift speed. Current remains vertical to the BP collector, verifying the assumption of a vertical current. Although current divergence is found within the P collector, the collector receives a near-vertical current.

From electrostatic modelling of the AECP it was therefore determined that although J_D is underestimated by the AECP owing to the positioning of the P collector below ground (therefore requiring a correction factor), the geometry will not affect the collection of J_C . This means that although the horizontal cross section of BP and P is proportional to the current collected as a result of vertical J_C , correction for J_D using equation (4.10) requires a corresponding correction to determine J_C , seen in equation (4.9).

Using the mean and standard error of K found from Figure 4.21 of 2.66 ± 0.07 and equation (4.9) the associated uncertainty in J_C would be $0.08J_D$. From measurements of PG made at the RUAO, the five-minute mean J_D rarely exceeds 1pAm^{-2} during fair-weather, so a cautious estimate of uncertainty due to J_D component in J_C calculation is 0.1pAm^{-2} . Combined with the 0.05pAm^{-2} picoammeter uncertainty, the total estimated uncertainty of the AECP is 0.11pAm^{-2} . The uncertainty in collector area calculation is negligible in comparison to other sources (relative uncertainty of 0.5% if collector lengths differed from expected by 5mm).

4.5.7 AECP insulator durability

Although the currents measured by the AECP appear to be free from noticeable leakage currents as shown by Figure 4.18 and Figure 4.19, significant leakage currents (enough to

saturate the output) are often present during times of high relative humidity. The connection between insulator degradation and water absorption has been investigated, the results of which are described in this section.

An example of leakage currents on both collecting plates of the AECP is shown in Figure 4.23. Leakage currents are seen to saturate the border plate (BP) during morning, and cause the pyramid plate to also have spuriously high values. A possible reason why the BP insulation allows a greater leakage current than the P insulation is that there are twice as many insulators supporting the BP than the P, and the contact area of the four P insulators is kept to an absolute minimum by allowing the pyramid's edges to rest on the cylindrical insulators.

When the relative humidity is low in the afternoon (between approx. 12-17UT in Figure 4.23) the leakage current is rapidly diminished, with current of the expected magnitude observed for both collectors. BP is approximately twice as large as P during this time owing to the larger cross sectional area. There is no reason to suspect strong correlation of leakage currents between the BP and P collectors as both have different insulators, so the close correlation between both collectors during the afternoon also suggests that J_C and J_D variation (common to both collectors) are the dominant source of variability during this time.

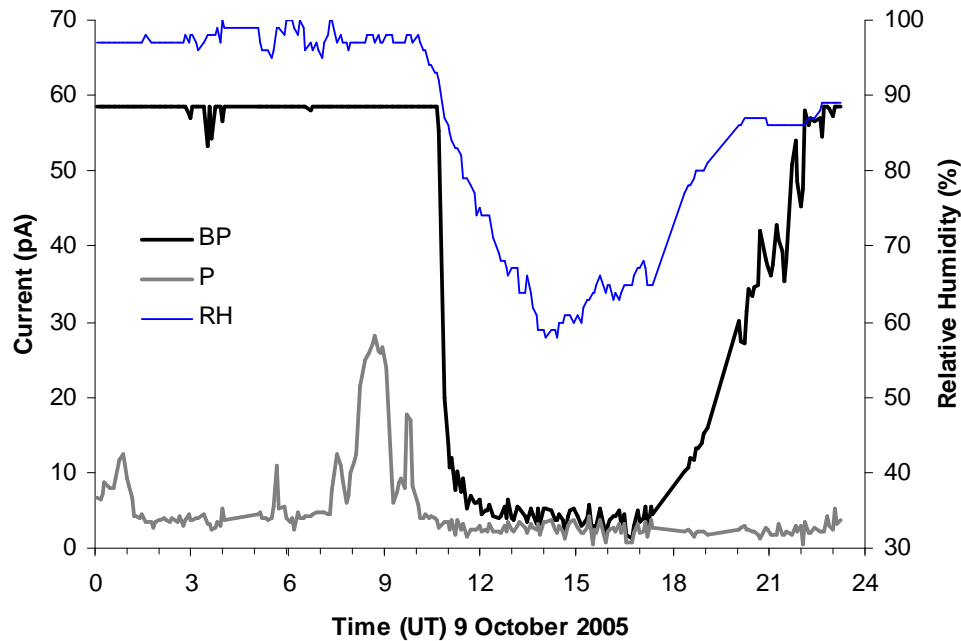


Figure 4.23 An example of leakage currents resulting from insulation water absorption on the border (BP) and pyramid (P) collecting plates of the AECF during times of high atmospheric relative humidity (RH). All measurements displayed as five-minute means.

The source of this leakage current was investigated, with a hypothesis that it was due to water absorption by the insulators and associated decrease of surface resistivity during times of high relative humidity. Despite having many beneficial properties the PTFE (like most other plastics) appears to absorb water. Once water is absorbed into the surface it is suggested to lower the resistivity and greatly degrade the quality of the insulator, allowing leakage currents to pass between the collector and ground. This was discovered by observing the coincidence between anomalous currents and high relative humidity, such as in Figure 4.23. In order to test whether sufficient water absorption by the PTFE can occur in a suitable timescale (i.e. hours) the rate of water absorption was investigated by completely immersing an initially dry PTFE cylinder of known weight and similar dimensions to the insulators in a beaker of water. The PTFE cylinder was weighed over several days and the calculated increase of mass plotted against time, shown in Figure 4.24.

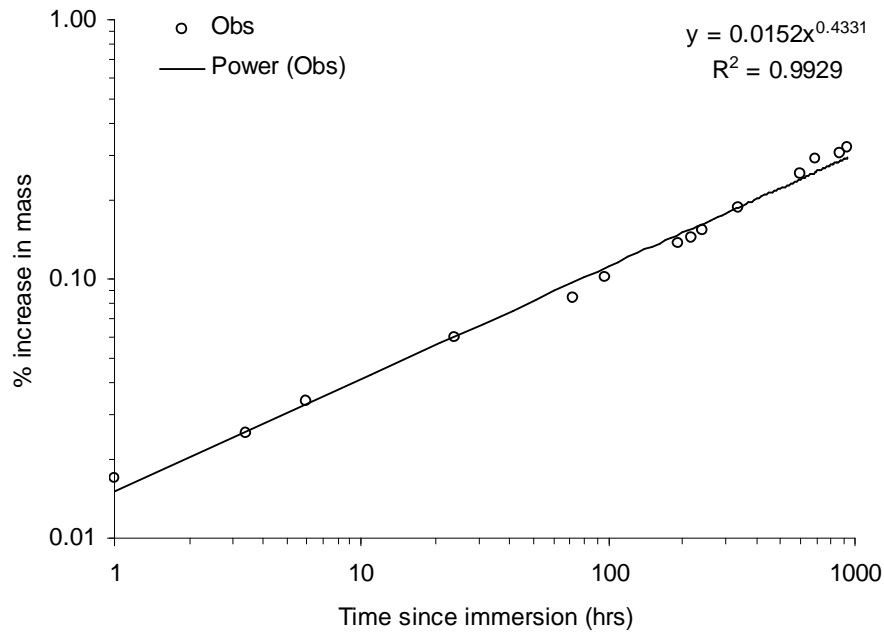


Figure 4.24 The percentage increase in mass of a PTFE cylinder of length 159mm and diameter 26mm completely immersed in water (at room temperature). The observed increase (Obs) has been modelled using a power law trendline, indicating that the percentage mass increase is approximately related to the square root of immersion time. The starting mass was 117.40g.

The mass increase with time was approximately proportional to the square root of immersion time, implying that water was rapidly absorbed in the first few hours before increasing at a slower rate after this initial absorption when the concentration gradient between the water and PTFE was reduced. Although the percentage increase is small, only a thin film of conducting medium would be required to allow a leakage current comparable or exceeding the magnitude of the picoamp signal. The results support the hypothesis that sufficient water absorption occurs to degrade the insulation. The timescale of absorption has implications for the expected nature of insulator degradation when exposed to the environment, with rapid degradation during a high moisture event such as rainfall or heavy dew, followed by a similarly fast recovery as the PTFE dries out again afterwards, as shown in Figure 4.23 at approximately 11:00UT. In the long term however, a slow overall degradation of the PTFE insulation would occur on longer timescales as more gradual yet persistent water absorption penetrates deeper into the insulator whenever there is a net absorption with time. This situation is likely to occur during the winter half of the year in mid-latitudes such as the RUAO, where relatively high rainfall and dew occurrence combined with weaker sunshine is likely to allow a daily net absorption of water.

The problem of leakage currents due to water absorption at times of high relative humidity persisted throughout the winter and even nocturnally in the summer of 2006. An additional insulator component that was highly resistive but did not absorb water was considered to reinforce the AECIP insulators. After consideration, Sapphire was the chosen material, based on its high resistivity (of order 1×10^{14} Ohm cm) and immunity to water absorption. However, Sapphire is an expensive material, so must be used sparingly. Heated Sapphire was used by Gunn (1964) for successful insulation of a marine air conductivity instrument, although the material has not been used to insulate air-Earth current instruments before.

The Sapphire reinforcements (installed from June 2006) are shown in Figure 4.25. A Sapphire ball of 3mm diameter was inserted in the end of the BP insulators to act as an impervious and resistive barrier between the BP and PTFE in the event of water absorption. The spherical shape allowed the smallest contact area to be used to support the collector and the least amount of (expensive) Sapphire. For the P insulators, a 3mm diameter Sapphire rod was positioned in between the PTFE insulator and supporting edge of the collector. Like the sphere, a rod shape allowed minimum supporting contact area.

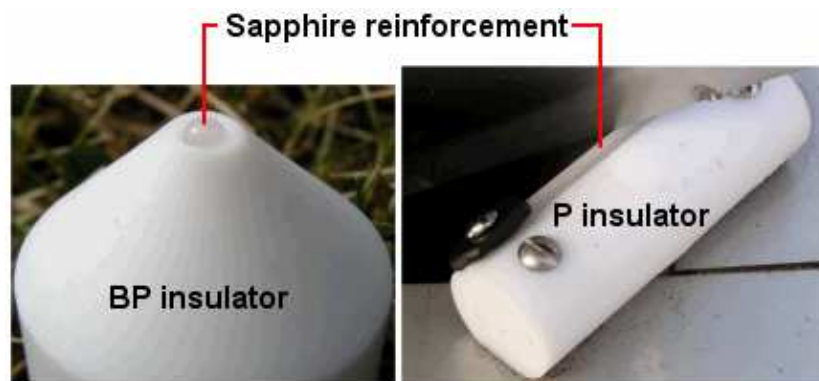


Figure 4.25 Use of additional Sapphire ball and rod to reinforce the BP and P insulators respectively, whilst retaining minimal contact area with the collector surface.

An overall improvement in BP and P reliability was seen after the additional Sapphire reinforcements were added, with longer periods of non-saturated values, although it was unclear how much of this improvement was due to the increasing amount of drier days as the summer progressed. However, despite many hours of good quality data the problem of leakage currents during the night time was still apparent. It was concluded that water absorption by the PTFE insulators that was not the only mode of degradation, but also the rapid accumulation (despite regular cleaning) of hygroscopic particles on the outside of the insulator (both PTFE and Sapphire) also a likely source of insulator degradation. This coating of foreign material such as from blowing soil, dust etc, is suspected to be

hygroscopic due to insulator breakdown during high, but not necessarily 100%, relative humidity (Figure 4.23).

4.6 The Geometrical Displacement and Conduction Current Sensor (GDACCS)

The geometric principle of J_C and J_D determination was first investigated experimentally using the AECF, with an uncertainty in J_C due to the picoammeters of $\pm 0.05 \text{ pA m}^{-2}$. Results from this instrument have been shown to compare closely to indirect determinations of J_D using a field mill (Figure 4.19), with the mean J_C from initial results being within the standard deviation of the long term mean J_C for Kew Observatory. However, despite the successful demonstration of this principle, experience using the AECF has suggested certain practical improvements to the geometrically-based method of sensing. The main areas for improvement are as follows:

- *Insulation*

The PTFE insulators work well under dry, fair-weather conditions but suffer from water absorption over time. Sapphire inserts, although impermeable to water, still permit leakage currents to arise overnight and during wet weather when humidity is high. A film of hygroscopic particles on the outside of the insulator may be to blame. Due to the size of the collecting plates, the AECF requires 12 individual insulators, increasing the probability of insulator degradation and making their regular cleaning and inspection time consuming.

- *Non-identical PG at collecting plates*

Positioning of the P collector of the AECF below the surface meant that this collector was exposed to only ~37% of the PG compared to the BP collector on the surface (Figure 4.20). Although not expected to directly affect the collection of J_C , a correction factor must be applied to the P current measurements if J_D is to be accurately determined. This correction factor appears to be relatively constant (standard deviation of under 3% of mean from Figure 4.21). Having collectors at the same PG will eliminate the need for a distortion correction factor.

In addition to these two main areas for improvement, the ease of installation and maintenance should be considered in the next design. The large size of the AECF and the consequent requirement a 1 m^3 pit makes this sensor suitable only as a permanent installation at the RUAO. Whilst the size of the collecting plates brings the benefit of a large signal-to-noise ratio, the AECF can not be temporarily installed at other sites, which

would be advantageous during fieldwork at different locations. Additionally, the pit is prone to flooding during and after heavy rain if the drainage holes become blocked or the ground waterlogged. If the water level touches the tip of the pyramid plate (15cm above the pit floor) then insulation is totally compromised. Having a low-maintenance sensor with high quality, durable insulation and simple to install would be required if measurements are to be made at remote sites.

Consideration of these points formed the basis of an improved sensor design, called the **Geometrical Displacement And Conduction Current Sensor (GDACCS)**. Calibrated picoammeters of the same design as used by the AECF (section 4.5.4) were used to record the current from both collectors.

4.6.1 The GDACCS current collectors

Like the AECF, the GDACCS has two current collecting plates, each with the same surface area, but different cross section. The requirement that both collectors experience the same PG whilst remaining flush with the surface (to avoid perturbing the ambient field) meant that the collector's vertical dimensions must be kept to a minimum. As previously discussed, a flat, horizontal plate would provide an ideal collector as it lies parallel to the equipotential plane (which is horizontal over flat, open ground) so will cause minimal PG perturbation around it when positioned flush with the surface. However, in order that the surface area is different to the horizontal cross sectional area (a requirement for the second collector), a vertical component must be present in a collector's geometry. For the AECF, this was achieved using a pyramid, although the considerable depth of this collector meant that the PG was also perturbed around it. For the GDACCS, a corrugated collector design was used instead. Corrugation allows the collector to remain as flat as possible, whilst increasing its surface area with respect to its horizontal cross section. The corrugation of this collecting plate allows it to lie close to the same equipotential plane as the flat collecting plate, thereby experiencing a similar PG. Consequently a combination of flat and corrugated collecting plates (shortened to FP and CP respectively) has been used for the GDACCS.

The dimensions of the GDACCS collecting plates were chosen to allow the sensor to be small and lightweight enough to be easily transported, whilst remaining large enough to collect a measurable current at tolerable resolution. As the output is logged at the RUAO with a resolution of 2.4mV, this would correspond to a current resolution of 0.024pA for a typical picoammeter calibration. If J_c is 1pAm^{-2} , a square, flat horizontal plate would require a minimum dimension of 16cm to provide a detectable current. This is the lower

bound on area, as the collecting plate would need to be considerably larger than this to actually observe any J_C variation. A collector approximately ten times larger in area could resolve J_C to 0.24pAm^{-2} , which is below the expected minimum fair-weather value considering those measured at Kew Observatory (Harrison and Ingram, 2005).

Available material and the ease of construction were also considered. The simplest corrugation to construct is square, so this was made from 4mm thick stainless-steel rectangular troughs of 2cm height and 4cm width, welded together at the edges. Three complete corrugations were made, with a total horizontal length of 0.261m once the plate's thickness was considered. The absolute length of these corrugations was 0.515m (i.e. if they were stretched flat). The long side of the corrugated plate was 0.535m. Consequently, the flat plate was made 0.525m square, for equal surface area. The collector dimensions and final installation of the GDACCS at the RUAO is shown in Figure 4.26.

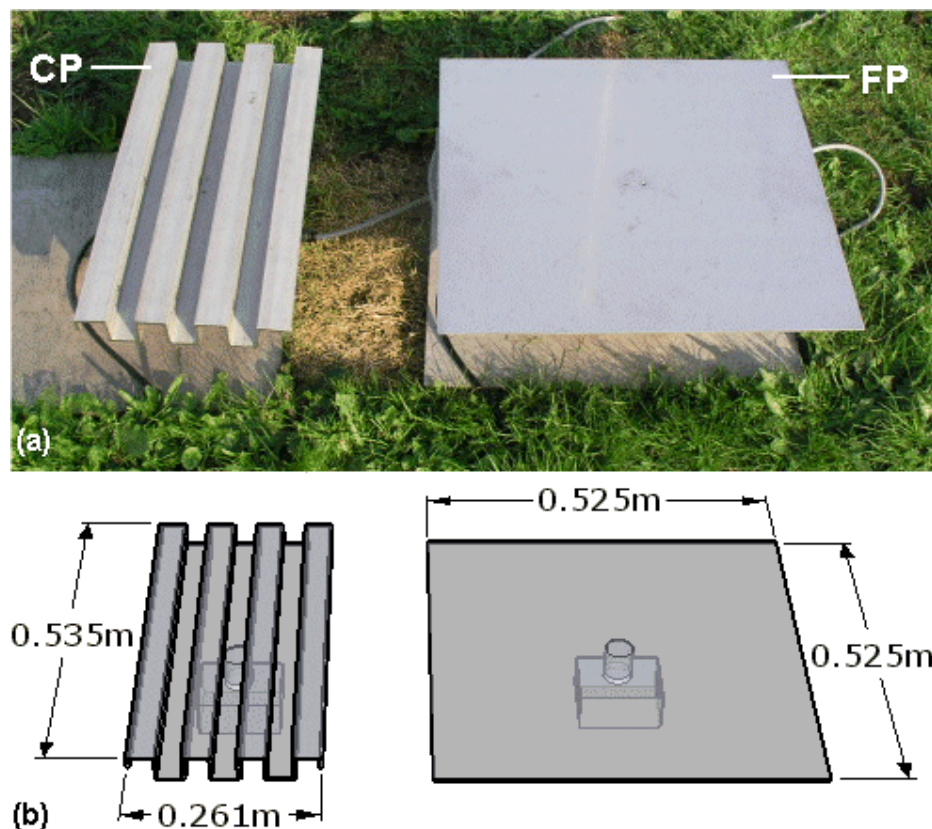


Figure 4.26 Picture and dimensions of the GDACCS. The sensor installed at the RUAO is shown in part (a) and dimensions, including the positioning of the collector support and picoammeter below the plates, can be seen in part (b).

The surface areas of both the FP and CP are 0.276m², with the vertical cross section of the CP being 0.140m². This allows an effective J_C collection area of 0.136m², which provides adequate current collection for the 2.4mV logging resolution, whilst remaining small enough to be carried by a single person.

Based on these dimensions, the equations relating the current from the collectors (I_{FP} and I_{CP} respectively, in pA) to the current density components (in pAm⁻²) are as follows:

$$J_C = \frac{I_{FP} - I_{CP}}{0.136} \quad (4.11),$$

$$J_D = \frac{I_{FP}}{0.276} - \left(\frac{I_{FP} - I_{CP}}{0.136} \right) \quad (4.12),$$

$$= 7.35I_{CP} - 3.73I_{FP} \quad (4.13).$$

4.6.2 The GDACCS collector insulation

From experience gained during operation of the AECP, insulators made of PTFE are not capable of long-term, reliable leakage current prevention, even if reinforced by Sapphire. As reliable, long-term and maintenance-free instruments would be required if measurements of J_D and J_C are to be made at remote sites, effective insulation must be devised. This insulation must be reliable in all seasons during the night as well as the day, if data on the J_C diurnal and seasonal cycles are to be found.

The cause of insulator breakdown for the AECP was suspected to be water absorption by hygroscopic material accumulated on the outside of the insulators. Although this surface coating was likely to be present during both dry and moist conditions, leakage currents were not apparent during dry, fair-weather summer afternoons (e.g. Figure 4.23), indicating that the coating would only permit a noticeable leakage current to flow when allowed to absorb moisture. A hypothesis to be tested is that if the temperature of the insulator was kept above the adjacent air temperature, water absorption by condensation on the insulator surface could be prevented, even with a coating of foreign material (providing the temperature increase is sufficient to counteract any hygroscopic tendencies). This hypothesis was tested by designing a heated insulator and observing if leakage currents still occur, the details of which is described later in this section.

As the AECP had 12 individual insulated supports, the instrument would require 12 separate heaters, which many need a considerable amount of power to keep all the heaters at a suitable temperature, as well as the need for extra cables, circuits etc.

surrounding the collectors. The most efficient design for the GDACCS would ideally have only one insulated support for each of the two collecting plates, therefore requiring only two heaters and decreasing the amount of potential leakage points between the collector and picoammeter. Two collectors were each supported by a 6cm long by 4cm diameter solid stainless steel cylinder mounted on top of the metal electronics housing box (Figure 4.27a). In between this cylinder and box there is a 2cm thick by 4cm diameter PTFE cylinder to insulate this metal support cylinder from the box (which rests directly on the ground). A solid metal rod passes through the middle of this insulator and into the box, where a rigid wire connects the conducting rod directly to the picoammeter. This allows the current from the collector to pass down through the support cylinder to the picoammeter, via the conducting rod (Figure 4.27b). The position of this support structure relative to each collecting plate is identified in Figure 4.26b. The effect of the metal support cylinder on the current measurements was not considered significant as the increase in surface area was small (under 3% of the collector surface area) and the cylinder would experience a greatly reduced PG (less than 10% of that on the collector) as it would be shielded by the collecting plate above (Figure 4.29a), thereby receiving a negligible fraction of J_C and J_D relative to the collecting plate it supports.

The PTFE insulator has shallow grooves cut along its sides to allow a heating wire to be evenly wound six times around it. A current is passed through this wire, causing it to heat up and act as a heating coil for the insulator (Figure 4.27a). For compatibility with field power supplies such as car batteries, a heater power supply of 12V was used. 0.125mm diameter Constantan resistance wire (composed of copper, manganese and nickel) was initially used for the heating coil, due to its high resistivity ($36\Omega\text{m}$) allowing the wire to heat to approximately 80°C from the 12V supply, drawing a current of approximately 0.45A. However, this wire was found to become brittle and break after a few weeks outside due to the chemical reaction of the wire with water. The Constantan wire was consequently replaced by 0.25mm diameter Nickel-Chromium wire with a resistivity of $22\Omega\text{m}$. The wire is 80cm long, so the resistance of the wire is 17.6Ω . This wire is considerably more durable, with no sign of degradation to date (following three months of continuous operation). The increased durability of the heating wire makes the GDACCS more suitable for deployment at remote sites with minimal maintenance over extended amounts of time, providing a suitable 12V power supply is available. The lower resistivity of this wire meant that more current was drawn from the 12V supply (approximately 0.65A) increasing the temperature and power requirement of the heaters (approx 8W each). As the heater temperature greatly exceeds that required to simply keep the insulator a few degrees above air temperature to avoid condensation, it is likely that the heaters will be just as effective using considerably less power.

Employing the collector support as the electrical connection to the picoammeter minimises the amount of insulation required on the instrument, with only one insulator required per collector.

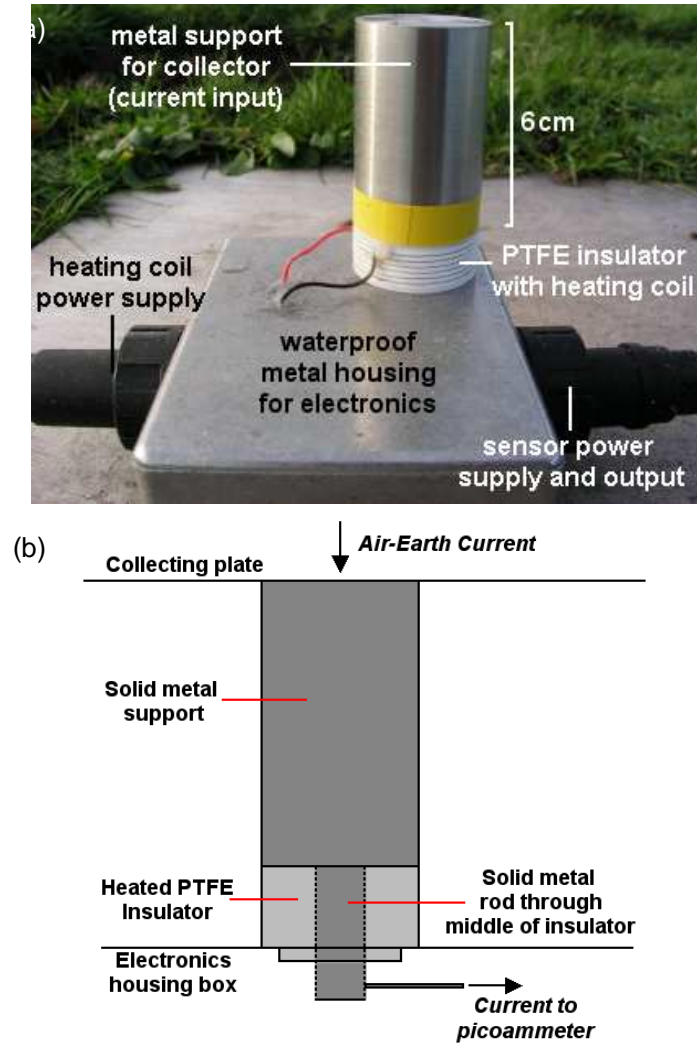


Figure 4.27 Design of the GDACCS combined collector support and current connection to the picoammeter, incorporating heated PTFE insulation. (a) shows the support mounted on the electronics housing box, with a cross-section of the support identifying the internal conducting rod shown in (b). The yellow tape shown at the base of the metal support was used as a temporary guard against bridging by water drops, until the surrounding shield was installed.

With this heated support design, the GDACCS was considerably more reliable than the AECF, with J_C and J_D being continuously recorded throughout the day and night, permitting complete diurnal cycles of fair-weather J_C to be found.

However, the instrument still suffered from occasional leakage. Three main causes of leakage were identified during operation of the GDACCS:

- Bridging of insulator by rain water
- Bridging between collector and nearby surface by a Spider's web
- Insulator surface degradation due to windblown dirt

Despite the substantial improvement in reliability due to heating of the insulator, it is still important to keep the surface clean. Although any windblown dirt accumulating on the surface of the insulator will not absorb water as it too will be heated, the conductivity of the foreign material is usually high enough to permit leakage currents. As such, the insulator should be routinely cleaned (preferably at least once a week, especially following heavy rain and/or strong wind). However, this may not be possible on remote deployment, so thin metal shielding was placed around the insulator to offer protection from windblown dirt. The shield was chosen to be metal to avoid any possible static charge which may distort the measurements. The collecting plate acts as a roof, so in combination with the shielding, should also guard against bridging of the insulator by rain water or snow, with any finer droplets being quickly evaporated on contact with the hot insulator surface.

The hot insulators appear to deter Spiders from building webs on them (as also noted by Gunn, 1964). Instead, the Spiders preferred to construct a web between the collecting plate and the nearby surface, usually from the tip of a blade of grass. Although these webs do not appear to allow a noticeable leakage current during dry conditions, they do permit leakage once the relative humidity is high. As such, their removal is required for good quality continuous measurements. The deterrence of Spiders and insects from air-Earth current instrumentation has been attempted by researchers before. Kasemir (1951a) used a form of gel to deter insects but not Spiders, whose webs he had to remove in the afternoon before the relative humidity was high enough to permit leakage through the webs in the evening. Chalmers (1967) even used a slowly rotating plate to prevent Spiders webs. Investigation into methods to reduce the incidence of leakage by Spider's webs continues.

4.6.3 Current source verification

An important verification for the GDACCS is to investigate whether the source of current variation is only from the collector, as would be expected if the instrument was operating successfully and without additional variation from leakage currents etc. This was demonstrated simply by comparing one minute mean current from the FP and CP whilst

exposed to the atmosphere as in normal operation, and then removing one of the collecting plates. The results of such an experiment can be seen in Figure 4.28. As expected, a strong linear relationship exists between the FP and CP currents as both experience the same J_D and J_C (at least proportionally) and are therefore subject to the same variation inherent in both these components. However, on removal of the FP collecting plate (leaving just the support and electronics box as in Figure 4.27a) it can be seen that the FP current output is nearly uniform, with CP variation unaffected.

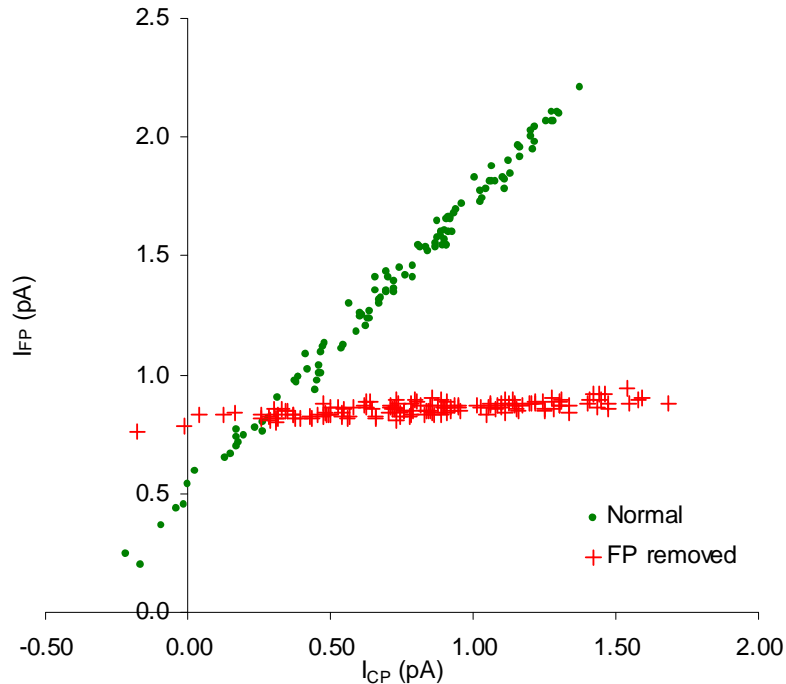


Figure 4.28 Results showing a strong linear relationship between one minute mean currents measured from the FP and CP collectors (green circles). The lack of similar variation once the FP collector is removed from the support is also shown (red crosses).

It is of particular note that although uniform, the FP current output was not zero once the FP collecting plate was removed, neither is the intercept zero when FP and CP currents are plotted in a xy scatter plot like Figure 4.28 (green circles). This implies a constant offset (as close linearity is conserved and no appreciable trend in FP is seen once the collector is removed) is present in the GDACCS. As more data was collected, it was found that this offset remained characteristic but sometimes with strong bimodal tendencies; often remaining constant for several hours before swapping quickly between one value and another, usually around sunset or sunrise. Reasons for this bimodal offset are unclear, but may be due to a form of leakage within the circuit, or a sharp change in J_T , which may change rapidly as near-surface air stability and space-charge changes during

these times (Oluwafemi et. al., 1975). This pattern of GDACCS collecting plate offset is easily recognisable in the data and can be corrected for during data processing by finding the y-intercept of FP vs CP (as seen in Figure 4.28) and subtracting this from the FP values. It is this corrected value of FP that is used to find J_C (in pAm^{-2}), such that:

$$J_C = \frac{I_{FP} - I_{CP} - y}{0.136} \quad (4.14).$$

Where y is the y-intercept (in pA) of FP vs CP (i.e. the predicted value of FP when CP=0 using a least squares line of best fit). Equation (4.13) still holds for J_D determination as this calculation is independent of any intercept.

A slight offset of similar magnitude can also be seen in some of the AECP data, but is less noticeable due to the larger current values. Another possible source of near-constant offset are contact potentials⁵ where two pieces of metal are joined. These have been minimised by using the same type of relatively inert metal (stainless steel) throughout the design, however it is possible that contact potentials exist in the instrument nonetheless.

The removal of this offset is justified by the fundamental assumption that if J_C and J_D were zero, it would be expected that current from both FP and CP should also be zero, if equations (4.11) and (4.13) are to be satisfied. As this offset is only a net offset between the FP and CP, the relative contribution from FP and CP is not known during routine operation, so no absolute correction can be applied to individual FP and CP measurements. As it is only the difference in FP and CP current that is required for J_C retrieval, removal of this net offset allows this component to be determined.

The likely uncertainty in J_C determination by the GDACCS arises from the uncertainty in current measurement by the picoammeters and calculation of the y-intercept. The picoammeter uncertainty is considered as $\pm 0.04\text{pA}$ (in accordance with the AECP as both use the same type of picoammeter). The uncertainty in y-intercept determination is dependent on the specific dataset, although using the 0.009pA standard error for the intercept seen in Figure 4.28 (green circles) this component is likely to be small. In determining J_C these three uncertainties are combined, and then divided by a factor of 0.136, as seen in equation (4.14). The uncertainty in J_C (ΔJ_C) is therefore estimated to be:

⁵ A contact potential is present when two electrically conductive materials of different electron work functions have been brought into thermal equilibrium with each other, usually through physical contact.

$$\Delta J_C = \frac{\sqrt{0.04^2 + 0.04^2 + 0.01^2}}{0.136} = 0.42 \text{pAm}^{-2} \quad (4.15).$$

The estimated uncertainty of 0.42pAm^{-2} is the uncertainty of an individual measurement. This initial estimate of uncertainty can be refined by calibration with a reference system (the AECP), which is discussed later in this section.

4.6.4 Modelling the GDACCS distortion

In order that measurements of J_C and J_D made by the GDACCS can be accurately interpreted, any characteristic features of the current outputs (such as offsets, or distortions due to geometry etc) have been investigated. Using the same electrostatics modelling software⁶ and assumptions as the AECP modelling (uniform 100V/m ambient PG, ground and collectors as perfect conductors) the PG and electric field vectors surrounding the GDACCS were modelled. The purpose of this model was to test whether both the collecting plates were likely to experience the same PG (and therefore J_D) and J_C . The results of this model are shown in Figure 4.29.

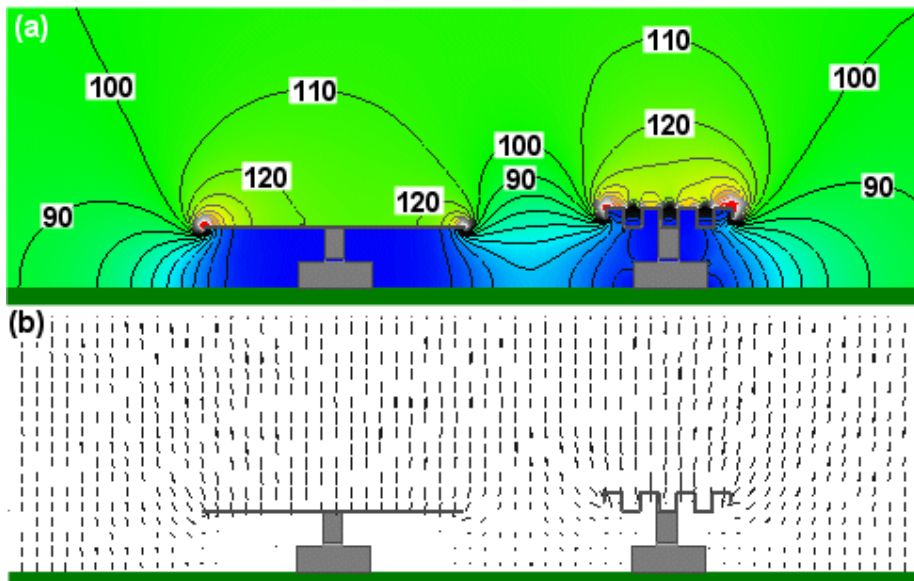


Figure 4.29 Modelled geometrical distortion of local electrical variables around the GDACCS. Part (a) shows the PG, in V/m , with contours at 10V/m intervals. Ambient (undisturbed) PG was set to 100V/m so the values displayed represent the percentage PG relative to ambient. Part (b) shows the electric field vectors, which J_C will flow parallel to. The length of the line represents its

⁶ Software used was Maxwell SV version 3.1.04, by Ansoft Corporation. Details available at www.ansoft.com/maxwellsv/

magnitude, with the line parallel to the vector direction (i.e. vertically downward above the GDACCS).

The model indicates that there is an enhancement of ambient PG above both the collecting plates. This is due to their elevation above the surface (of approximately 0.15m). The FP collector experiences a mean PG approximately 25% higher than ambient (Figure 4.29a). However, despite enhancements of up to 150% above the CP collector, the geometry of the corrugations mean that significant sections experience a reduced PG compared to ambient, with an overall mean PG adjacent to the exposed CP surface of approximately 95% of ambient (Figure 4.30). As previously found from the AECF results, this will produce a difference in J_D between the FP and CP collectors, despite having equal surface areas. From the electrostatic model, J_D from the CP is therefore expected to be approximately $95/125 = 76\%$ of that from the FP collector.

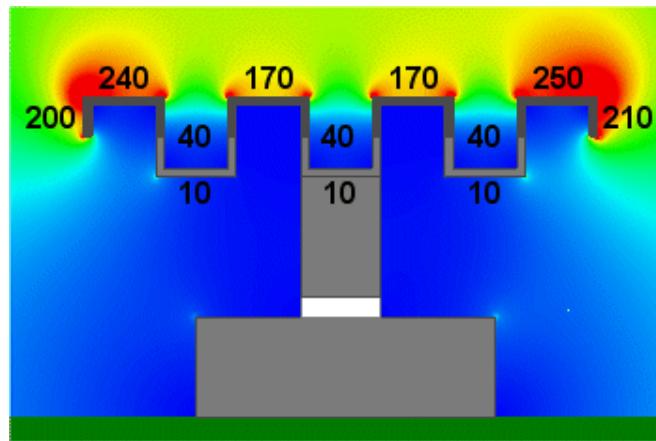


Figure 4.30 Modelled mean PG as percentage of ambient on different sections of the CP collector. The mean PG for the whole collector was found to be approximately 95% of ambient.

As for the J_C , it can be seen in Figure 4.29b that, like the AECF, the J_C generally flows vertically down to the conductors despite the distortion in PG. However, the enhanced PG near the edges of the collectors causes the nearby field vectors to face inward, converging on the plates, especially for the CP. This will act to slightly enhance the effective vertical cross sectional area of the plates, with respect to their actual cross sections. Providing the strength of this enhancement is similar for both plates (as it appears from Figure 4.29b) then this effect will be cancelled out when the difference in current is found to determine J_C using equation (4.11). However, although the consequences for J_D and J_C are likely to be relatively small, the best practise would be to place the GDACCS in a pit deep enough to allow the collectors to be flush with the

surface. This will remove the geometrical distortion and allow both collectors to be at the same potential (and experience the same J_C and J_D).

4.6.5 Verification of GDACCS model parameters

The relative magnitude of J_D on the FP and CP collectors predicted by the model (CP being 76% of FP) was verified by comparing the measured J_D on both collectors resulting from nearby lightning activity. Lightning-induced J_D was chosen as this signal is unambiguous as lightning is the only method by which a rapid ($>5\text{pAs}^{-1}$) change in current measured by the collecting plates occurs. By looking at only these signals, the uncertainty as to whether the change was due to J_C , J_T or J_D is removed. The lightning-induced J_D can be independently verified by the characteristic shape of PG change immediately after a strike using the FM.

Comparison of the change in CP and FP current over one second due to a large J_D induced by nearby lightning strikes from storms occurring at different days can be seen in Figure 4.31.

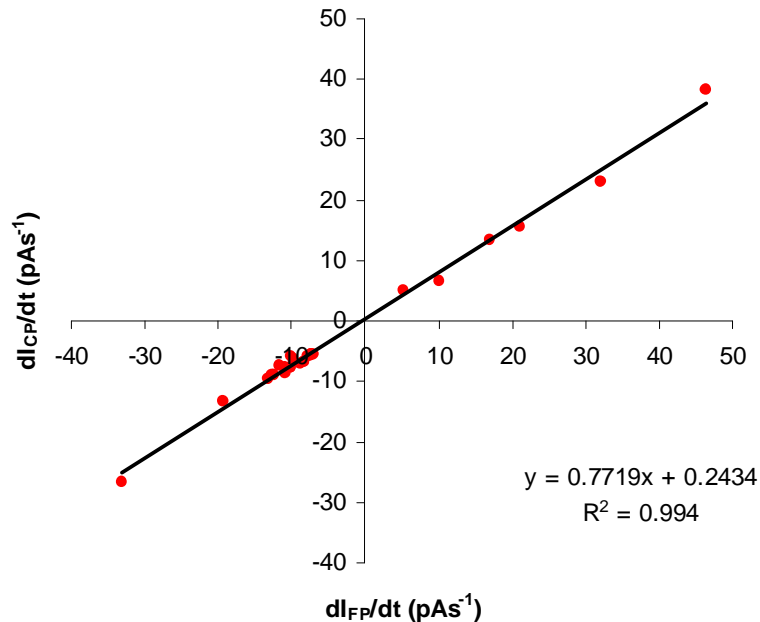


Figure 4.31 Change in FP and CP current over one second resulting from 27 nearby lightning strikes (of both positive and negative polarity), during storms on different days in October and December 2006.

The scatter plot of Figure 4.31 shows that the relationship between lightning-induced J_D was linear between the two collecting plates, and passed close to the origin. A linear

relationship of this kind is expected as both plates are experiencing the same proportional change in PG. From the gradient of this line it can be seen that the lightning-induced J_D measured by the CP is 77% of that measured by the FP. This result is in close agreement with that predicted by theory using the electrostatic model (76%) by estimating the mean relative PG that each plate is exposed to. As previously stated, although this effect is apparent when the GDACCS rests on the ground, it could be removed by positioning the GDACCS in a suitable shallow pit.

In order to verify that this difference is indeed due only to the geometrical distortion of PG caused by the different collecting plates (and not differences in picoammeter accuracy or response, for example), a displacement current was induced directly into the picoammeters via the respective support cylinders. This was achieved by simply removing the grounding from the heater coil thereby allowing a strong, high frequency systematic displacement current “noise” picked up from the power supply cable (noise source believed to be function of the 50Hz AC mains signal). As this induced current acts only on the support cylinder (as the noise is attenuated by the time it reaches the collector) both CP and FP picoammeters should change by the same amount per second as both heaters share a common power (and now noise) source. This technique is therefore independent of collector area, as only the (identical) support cylinders are affected. No evidence of this noise exists once the heater power supply is grounded, which is the usual operating condition.

The results of this experiment are shown in Figure 4.32. The characteristics of the applied noise are seen in part (a) of this figure, with a similar current change of about 5pA in amplitude and 0.3Hz frequency that is registered by both picoammeters. Part (b) demonstrates that both picoammeters are measuring the same induced current with the same magnitude, with a linear relationship that may be closely approximated as passing through the origin and with a gradient of one. This near-unity gradient can be compared with the gradient of lightning-induced J_D (Figure 4.31) to further support the hypothesis that the difference in J_D between the CP and FP is due only to the geometrical distortion of PG around the GDACCS, and not by any differences in the picoammeters or method of current registration.

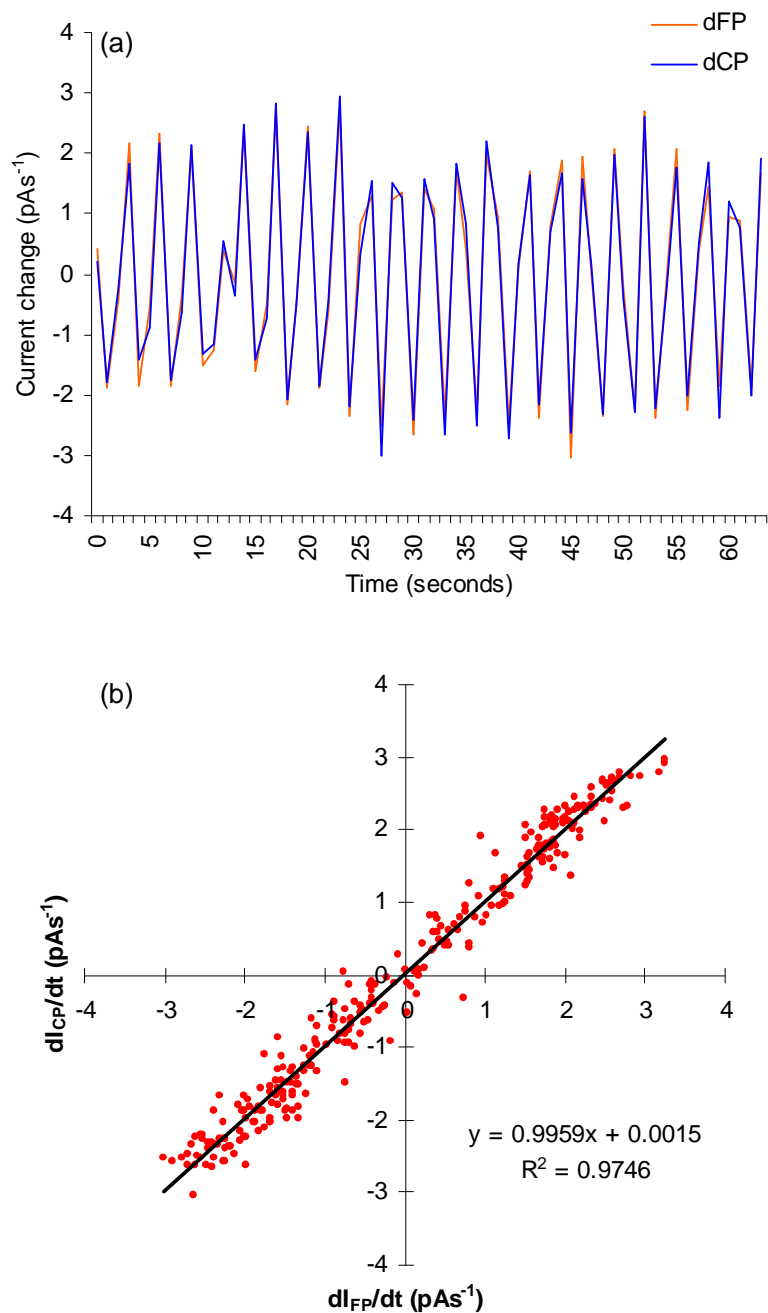


Figure 4.32 Effect of high frequency noise induced on the support cylinder from the heating coils of the FP and CP collectors. Part (a) shows the high frequency nature of the noise, with a similar current change of amplitude approximately 5pA and frequency of 0.3Hz, registered by both picoammeters. Part (b) demonstrates that both picoammeters are measuring the same induced current, with a linear relationship that may be closely approximated as passing through the origin and with a unit gradient.

4.6.6 Comparison between AECP and GDACCS measurements

Using the offset correction, J_c derived by the GDACCS was compared to that from the AECP, the results of which are shown in Figure 4.33. As can be seen, the two independent instruments are in close agreement. Such a close agreement between the two instruments considering their complete independency in both geometrical design and calibration provides confidence in the results of both.

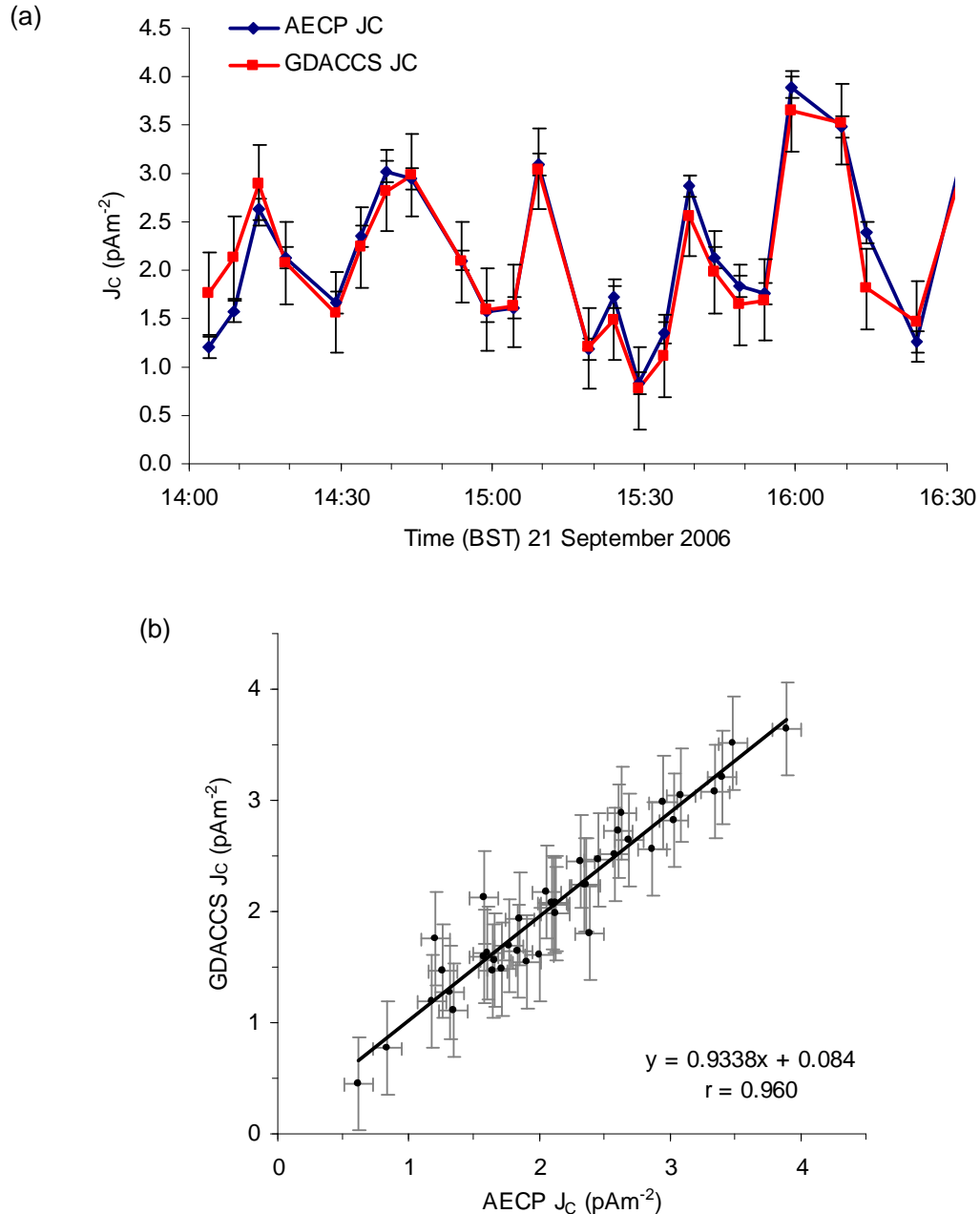


Figure 4.33 Comparison between five minute mean AECP and GDACCS derived J_c . (a) shows variation of the two J_c measurements during the time period, with (b) a scatter plot using the same values as (a) to quantifying this relationship. The correlation coefficient is shown to be 0.960, with

the equation for the least squares best fit line also displayed. The error bars identify the estimated uncertainty based on a single measurement for each instrument.

The error bars on Figure 4.33 were based on the estimated systematic uncertainty for an individual measurement ($\pm 0.11 \text{ pAm}^{-2}$ and $\pm 0.42 \text{ pAm}^{-2}$ for the pyramid and flat plate systems respectively). The lower systematic error in the pyramid data can be used to reduce the systematic error in the flat plate system. The standard error from the regression comparison of the Air-Earth Current Pyramid and the newer, corrugated plate design (the GDACCS) in Figure 4.33 is 0.17 pAm^{-2} , which, combined with the uncertainty in the AECP (0.11 pAm^{-2}) gives an uncertainty estimate in the GDACCS of 0.20 pAm^{-2} . As a result of calibration therefore, the uncertainty in the GDACCS instrument originally estimated by equation (4.15) has been improved.

4.6.7 Summary of the GDACCS

The GDACCS was designed as an improvement to the original AECP instrument, of which the theory for a geometrically-based method of J_C and J_D determination was tested. The principal features and characteristics of the GDACCS are as follows:

- Designed primarily to measure J_C at the surface by accounting for J_D , which is also measured.
- Portable sensor; designed for deployment at remote sites with minimal maintenance. Instrument requires commonly available 12V power supply. Heaters have relatively low power consumption (8W each), with the possibility of further reduction in power if necessary.
- Single, heated and shielded insulator per collector minimises leakage, increasing reliability, especially during high relative-humidity conditions.
- The sensor can be placed directly on the surface (if digging a shallow pit is not practical) and still reduce J_D “noise” affecting the J_C measurement by ~80% compared to that measured by a single collector of the same effective area. The absolute error in J_C measurement caused by J_D “noise” will vary according to the natural variability of the PG during the time of measurement. Therefore, placing the sensor’s collectors flush with the ground is advisable for most accurate results as all (not just 80%) of the J_D will then be accounted for.
- Absolute uncertainty for an individual J_C measurement is estimated at $\pm 0.42 \text{ pAm}^{-2}$, although comparison with the more accurate AECP suggests that the uncertainty in the measured five-minute mean J_C (at 1Hz) is considerably lower than this, at 0.20 pAm^{-2} .

4.7 The Electric Potential gradient And Current (EPAC) Sensor

On attending conferences relating to the study of atmospheric aerosol, it was apparent that although there was much interest in the possible use of PG and air-Earth current density in aerosol investigation, the rather specialised and often expensive equipment needed to measure these parameters was a prohibitive factor in their use by non-specialists. As such, a simple, inexpensive and highly portable sensor for the measurement of both the PG and the vertical air-earth current density was devised. The sensor is called the **E**lectric **P**otential gradient **A**nd **C**urrent (EPAC) sensor, to highlight the two atmospheric electrical parameters it measures. In addition to possible benefits to the aerosol community, such a sensor had the potential for use as an educational tool for physics teachers, thereby increasing the recognition and study of atmospheric electricity by a broader scientific community.

As the FM and GDACCS provide automatically measured values of PG and J_C respectively, the EPAC sensor (which is manually operated) was not used operationally at the RUAO and as such the full details of this sensor are not discussed here. However, the full design and operational details of this sensor, including initial results, can instead be found in Bennett and Harrison (2007a).

4.8 Discussion

The PW and PIMS are instruments that have already been proven capable of measuring the PG and σ_T respectively before the commencement of this study (Barlow, 1999 and Aplin, 2000). Once calibrated using the absolute values of PG from the PW, the commercially-purchased FM is reliable under all atmospheric conditions, and showed high levels of accuracy, resolution and thermal stability. Values of σ_T from the PIMS compared well with those found using a new, absolute method of σ_T determination using the PW. Direct measurement of J_C and J_D were first made at the RUAO using a new geometrical method of J_C and J_D discrimination by the AECF. The basic theory for the geometrical method proposed by Mukku (1984) was considered in more detail, with implied assumptions regarding PG spatial variability and vertical conduction current investigated both theoretically and by experiment. Using these results and experience of AECF operation, the AECF was improved upon by the GDACCS, which provides a portable and reliable method of J_C determination. As such, the array of instruments operating at the RUAO allows measurement of all the main atmospheric electrical parameters.

The next chapter analyses measurements made by all the instruments described in this chapter, made over several months at the RUAO, with emphasis on local sources of

variability and parameter interrelationships. Sources of variability in PG and J_C attributed to global sources are discussed further in chapter 6.

5 Analysis of local atmospheric electrical parameters

5.1 Introduction

Measurements of the potential gradient (PG), air-Earth conduction current density (J_c) total conductivity (σ_T) and small ion properties were made at the Reading University Atmospheric Observatory (RUAO) over several months. All of these parameters have been recorded simultaneously at times, although different instrumentation requirements and operating conditions meant that overlap durations differ. From these atmospheric electrical measurements and those of standard meteorological parameters, it is possible to present both an electrical “climatology” of the RUAO and a comparison between electrical and standard meteorological parameters. Additionally, inter-comparison of electrical parameters will be made and results compared to theory. The variation of PG and J_c during fog and PG variability associated with convective clouds and precipitation will also be investigated.

As emphasised in chapter 2, fair-weather J_c and PG have an ultimately global source in the thunderstorms and shower clouds that generate the global atmospheric electric circuit (Rycroft et al. 2000). However, the characteristics of these parameters are modified according to their local environment (chapter 3). These local modifications include local and columnar aerosol number concentration, variation in surface emissions of natural radioactive material and the overhead presence of charged clouds. Parameters such as total conductivity and ion properties are expected to be local in origin as terrestrial-sources of ionisation and large aerosol number concentrations dominate over the land surface. It is therefore appropriate to separate analysis of atmospheric electrical variation into that considered to be dominated by local and global sources. Investigation of atmospheric electrical variability from local sources is discussed in this chapter.

5.2 Operational times of RUAO atmospheric electrical instrumentation

The suite of atmospheric electrical instrumentation at the RUAO includes both well-established and new sensors that were developed as part of this study. Instruments such as the Programmable Ion Mobility Spectrometer (PIMS) are not primarily designed for

continuous, all-weather use and so its time and duration of deployment has to be considered by the investigator. The operational times are shown in Figure 5.1.

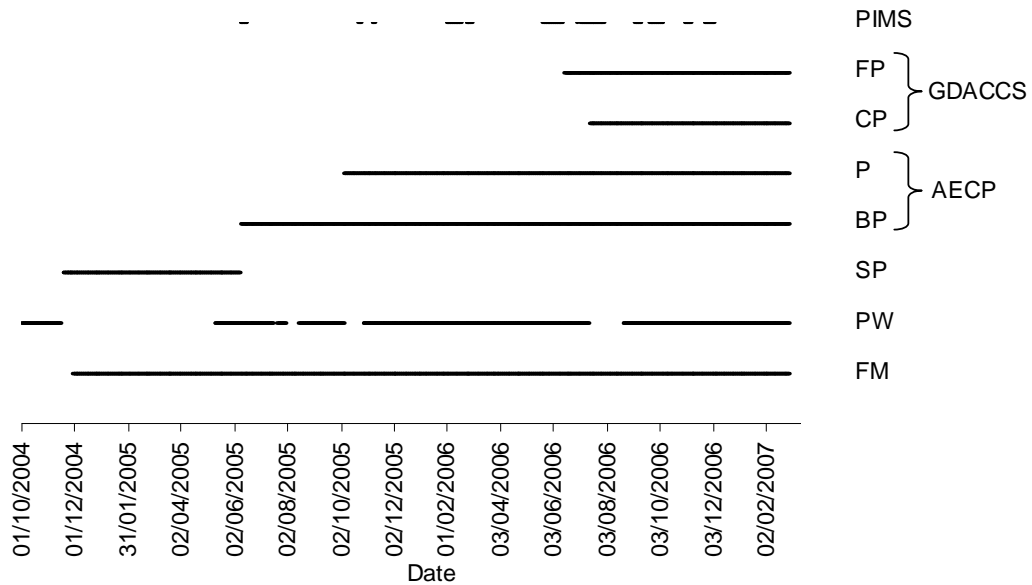


Figure 5.1 Operational times of all atmospheric electrical instrumentation at the RUAO indicated by a solid line, from the start of this investigation in October 2004. In addition to previously described acronyms (chapter 4), SP refers to a Simple Plate sensor, initially used to measure air-Earth current density.

Details on all the instruments can be found in chapter 4, except for the “simple plate” (SP). The SP was the first sensor used at the RUAO to measure the air-Earth current density, which used a stainless-steel flat square collecting plate of 1m². This was placed on a 4cm-thick sheet of polystyrene foam and connected to a picoammeter. No reliable measurements of J_s were recorded by the SP due to the continuous, large leakage currents that were permitted through the polystyrene insulation. However, the instrument served as a useful guide to further development of air-Earth current sensors, so is included in this timetable for completeness. Both the field mill (FM) and passive wire (PW) times are included, but only PG measurements from the FM are used for this analysis as the FM is more reliable than the PW, which was used only to calibrate the FM and check the calibration of the PIMS derived σ_T . As the instruments were not necessarily producing reliable measurements, the times shown in Figure 5.1 do not always reflect times of quality data. For instance, although the FM began operation on 29 November 2004, it was not until 14 April 2005 that a problem with the wiring that produced spurious results in FM output voltage was identified and resolved. From Figure 5.1 it can be seen that 2006 was the only complete year that measurements from all operational sensors were made. This year will form the basis of the RUAO atmospheric electrical climatology account, made

over one complete year as the inclusion of additional portions of the 2005 or 2007 seasons will bias the overall statistics if the parameter has a seasonal dependence. More specific analysis such as case studies or monthly diurnal cycle comparisons will not however be constrained to 2006 alone. A picture of the FM, AECP, PIMS and the FP component of the GDACCS on 12 July 2006 is shown in Figure 5.2.

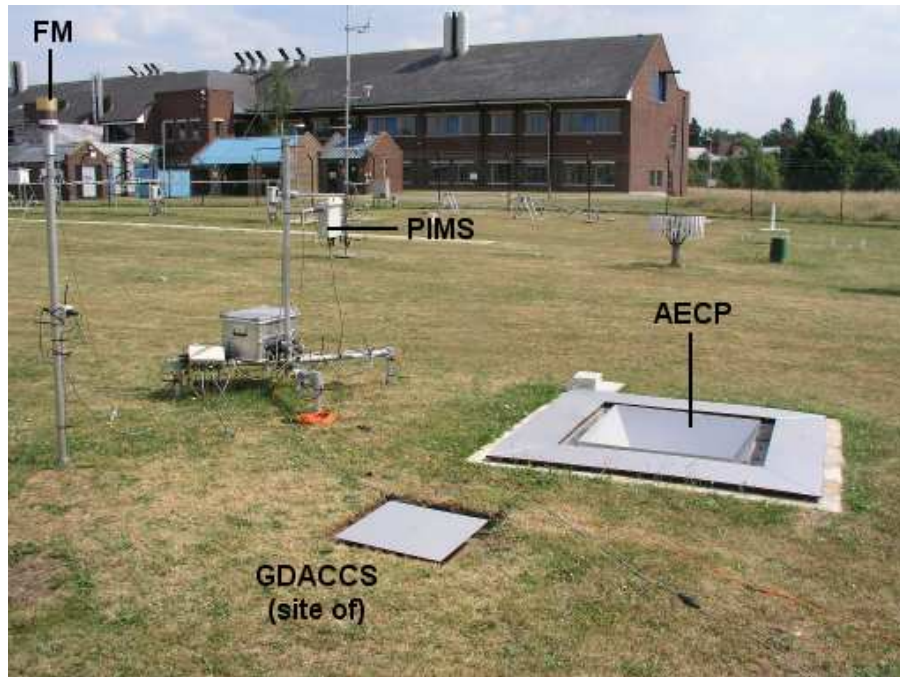


Figure 5.2 Atmospheric electrical equipment of the RUAO on 12 July 2006. Only the FP collector of the GDACCS is shown as the CP collector was not installed at the indicated location until 14 July 2006.

5.3 RUAO atmospheric electrical annual mean climatology for 2006

The parameters investigated in this section are potential gradient (PG), air-Earth conduction current density (J_C), total conductivity (σ_T), small ion number concentration (n) and small ion mobility (μ). PG was measured using the FM (calibrated by the PW). J_C was measured by the AECP from January to July (inclusive) and GDACCS from August (the first complete month of GDACCS operation). PIMS measured σ_T , n and μ . Except for the PIMS, all data is logged at the RUAO as five minute means (from one second measurements). An “hourly mean” is defined here as the mean of all the five minute averages that were logged within the hour, irrespective of how many five minute means there were. For instance, if there were 10 five-minute means available for a parameter between 14-15UT, then the hourly mean value for 14UT would be the mean of the 10

values, despite a complete hour having 12 five-minute means. Therefore an “hourly mean” will be represented by at least one five-minute mean that was measured within the hour.

5.3.1 Potential gradient (PG)

Summary graphs of hourly PG mean and standard deviation for 2006 are shown in Figure 5.3. The reliability of the FM was demonstrated to be high, operating successfully for 98.8% of this year. PG was initially recorded as five minute means, but has been processed as hourly means to reduce the size of the complete data file required for statistical analysis. However, the standard deviation of five minute means that composed of each hour were analysed, and presented in Figure 5.3b to provide an indication of PG sub-hourly variability.

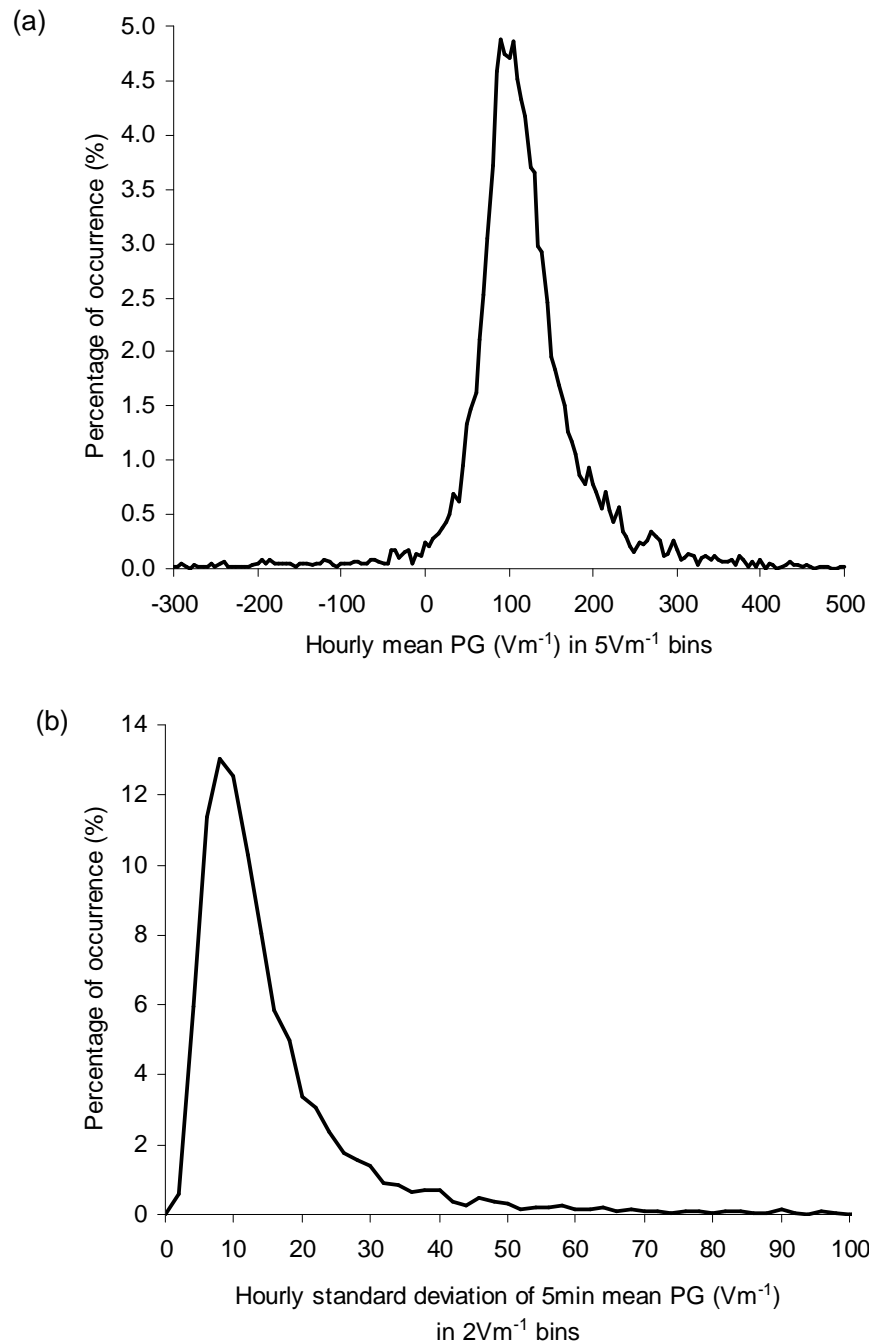


Figure 5.3 Histograms of: (a) hourly mean PG for 2006, in 5Vm^{-1} bins, from 8654 operational hours (98.8% of the total year), (b) standard deviation of the twelve five minute means used to calculate each hourly mean.

The annual mean and standard deviation of hourly mean PG was 110Vm^{-1} and 96Vm^{-1} respectively. From Figure 5.3a it can be seen that the majority of hourly mean PG lies between 50Vm^{-1} – 200Vm^{-1} (82% of measurements). A further 7% was found between 200Vm^{-1} – 300Vm^{-1} , with only 2% exceeding 300Vm^{-1} . The occurrence of a weak positive PG (0Vm^{-1} – 50Vm^{-1}) was 15%.

50Vm^{-1}) was 5%, with negative PG occurring 4% of the time during 2006. The classic definition of atmospheric electrical “fair-weather” states that there must be “no hydrometeors, no dust blowing, wind below 3 Beaufort and cloudiness below 3/10” (Israelsson, 1978). The International Commission on Atmospheric Electricity in 1965 stated a “fair-weather hour” as an hour during which any action of local generators were negligible (Israelsson, 1978). By “local generators” it was meant any local source of space-charge generation. Depending on the site, cloud amount and presence of “local generators” are difficult to record automatically (especially at night) so assumptions about the PG during fair-weather must be made so that the value itself can be the indicator of fair-weather.

From the statistics summarised in Figure 5.3a, an approximate range of PG to be described as “fair-weather” can be found for the RUAO. If it is assumed that for the majority of time the atmosphere is categorised as being fair-weather (i.e. no falling precipitation, deep convective clouds overhead, fog etc) then the range containing most PG values before the tails of the distribution are encountered could reasonably be expected to have occurred during fair-weather. For the RUAO this range of fair-weather PG is considered to be $50\text{-}300\text{Vm}^{-1}$ based on the distribution in Figure 5.3a. Experience found that weakly-disturbed weather will tend to cause a decrease in PG to a low but not necessarily negative value, so the 5% region between $0\text{-}50\text{Vm}^{-1}$ was expected not to be fair-weather, despite still being positive. However, a slight increase in PG above the mean during a weakly-disturbed weather event was rarely observed. It has also been observed that higher than usual aerosol number concentration in an otherwise fair-weather condition (assuming neutral aerosol) will increase the PG above the mean value, whilst still remaining fair-weather (as indicated by the positive skewness of the distribution of the region between $0\text{-}300\text{Vm}^{-1}$). As such, the 7% region between $200\text{-}300\text{Vm}^{-1}$ was also included as fair-weather.

The fair-weather PG ($50\text{-}300\text{Vm}^{-1}$) comprised 89% of the total PG values for 2006. Although this appears a high occurrence of “fair-weather” when perceived from a standard meteorological perspective (weather in SE England is not usually associated with having fair-weather 9 times out of 10!) it must be considered that even during a showery day which would not normally be categorised by the meteorologist as fair-weather (it would instead be termed a “rain day”), it is quite possible that for the majority of the time the convective cloud is not overhead, the PG remains positive and local electrical fair-weather exists, with only short (although often vigorous) PG excursions into the disturbed-weather category as the showers pass overhead. A “thunder day” only needs one thunderclap too.

From Figure 5.3b it can be seen that 2006 had an 89% occurrence of sub-hourly standard deviations being less than 40Vm^{-1} . Of these occurrences, 95% were when the PG was considered “fair-weather” using the $50\text{-}300\text{Vm}^{-1}$ hourly mean definition. This suggests that fair-weather PG is also associated with low sub-hourly variability, in addition to the range of absolute values of PG.

PG variability

A spectral analysis for hourly mean PG between 1 May 2005 and 1 March 2007 found using a Lomb Periodogram (Lomb, 1976) is presented in Figure 5.4. From this figure it can be seen that the dominant cycles in PG are semi-diurnal, diurnal and annual, with a variety of intra-annual cycles exceeding one day, that have significances exceeding 99%. Significance is tested against white noise.

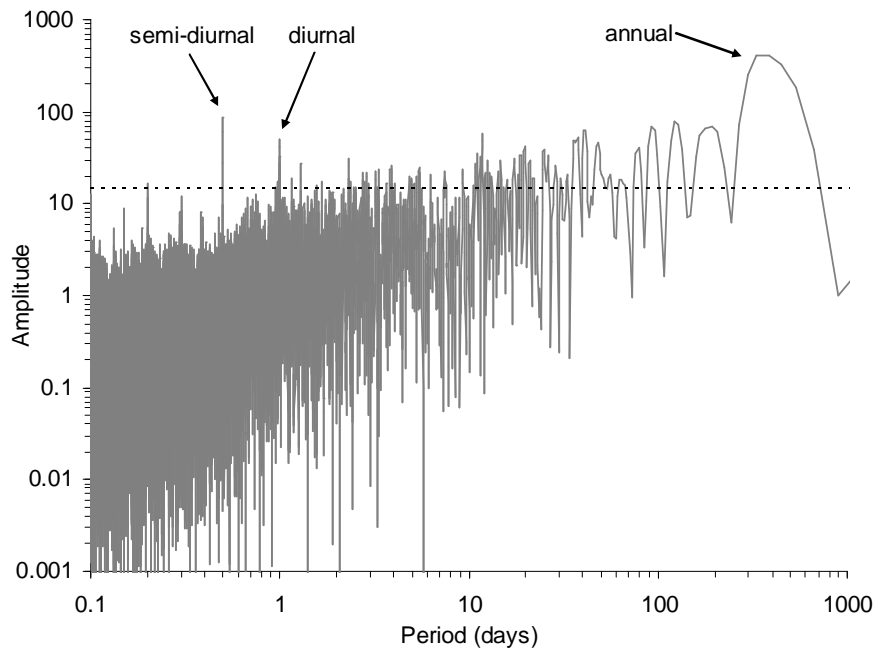


Figure 5.4 Periodogram of hourly mean PG between 1 May 2005 and 1 March 2007, with prominent cycles identified. Dashed line represents the 99% significance threshold amplitude for white noise.

5.3.2 Air-Earth conduction current density (J_C)

The air-Earth current density (J_C) measurements used for the 2006 climatology were from the Air-Earth Current Pyramid (AECF) between 1 January and 31 July. Once the Geometrical Displacement and Conduction Current Density Sensor (GDACCS) began operation, J_C measurements from this sensor were used (from 1 August to 31 December).

By combining these two datasets it is possible to examine a complete set of J_C measurements for 2006. As the absolute measurements from the GDACCS have been shown to correspond well to those of the AECF, there is not expected to be any systematic offset.

The histogram of hourly mean J_C for 2006 is shown in Figure 5.5. The annual median of hourly mean J_C was 2.05pAm^{-2} . Due to leakage currents some of the hourly means appear to deviate unrealistically from this median result, so in this case the annual mean including all measurements is not instructive. However, the values representative of J_C are clearly evident as a distribution within the range of -5pAm^{-2} to 10pAm^{-2} , as shown in Figure 5.5. This range represents 62% of the total number of hourly means (5378hrs out of 8671hrs), once saturation values are removed. Although leakage currents are usually clearly observed by an often sharp, unphysical step change in J_C as the insulation is breached, it must be considered that some of the shape of the distribution in Figure 5.5 may be attributed to a leakage current component superimposed on the actual distribution of J_C . A turbulent current density component (J_T) may also be present in the distribution. The magnitude of J_T during fair weather conditions is investigated in the next subsection.

However, the distribution is not unlike that found by Israelsson and Tammet (2001), who reported a mean J_C at their Swedish site between 1993 and 1998 of 2.44pAm^{-2} and a broad distribution, with standard deviation of 5.57pAm^{-2} . This J_C was measured indirectly, using PG from a field mill and conductivity from bipolar Gerdien condensers. Their higher median J_C is likely to be due to their lower aerosol number concentration (both at the surface and in the column, lowering R_C) and higher geomagnetic latitude compared to Reading.

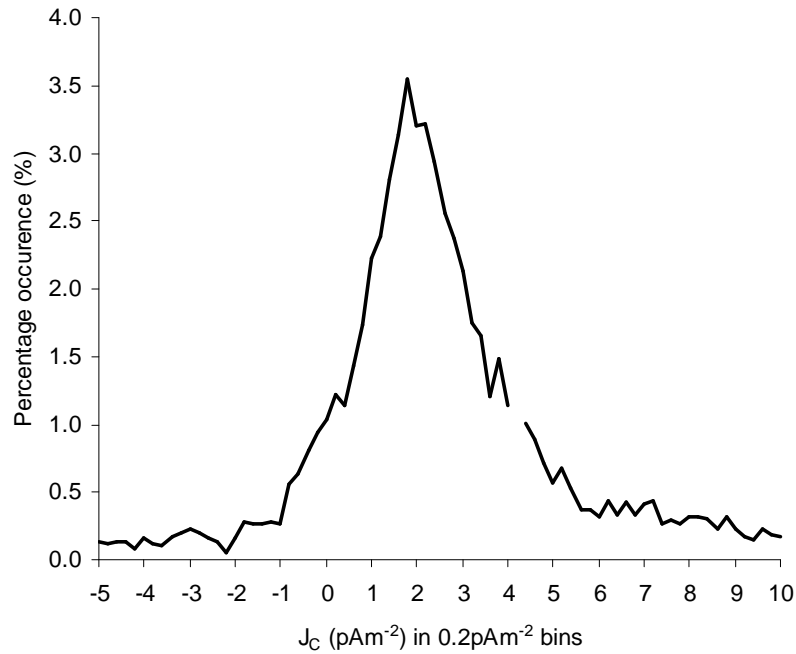


Figure 5.5 Histogram of hourly mean J_C for 2006, derived from the AECP until 31 July, and GDACCS thereafter. The 4.2pAm^{-2} bin has been removed as difference of saturation outputs from the AECP collectors (BP and P) produce a spurious J_C of 4.1pAm^{-2} , which otherwise would appear as a large spike in the histogram.

During fair-weather, J_C will be positive. For the observations at Kew, London which seems reasonable to regard as being the longest and most reliable fair-weather J_C dataset to date, a 1966-79 mean and standard deviation of 1.41pAm^{-2} and 0.42pAm^{-2} respectively was found (Harrison and Ingram, 2005). The minimum and maximum value of this fair-weather J_C distribution were approximately 0.4pAm^{-2} and 2.6pAm^{-2} . Considering these observed limits on fair-weather J_C for an urban site of similar geomagnetic latitude to the RUAO (although Kew in 1966-79 was likely to have been more polluted than present day Reading), the range of J_C observation at the RUAO considered as fair-weather (and with no leakage current) is $0.5\text{-}3.0\text{pAm}^{-2}$.

J_C variability

A spectral analysis for hourly mean fair-weather J_C between 1 January 2006 and 1 March 2007 using a Lomb Periodogram is presented in Figure 5.6. From this figure it can be seen that the dominant cycles for J_C are diurnal and annual, with no significant periods less than one day. Additionally, a prominent 10.9-day cycle can be seen in Figure 5.6, which is also evident as one of the dominant intra-annual PG cycles, seen in Figure 5.4.

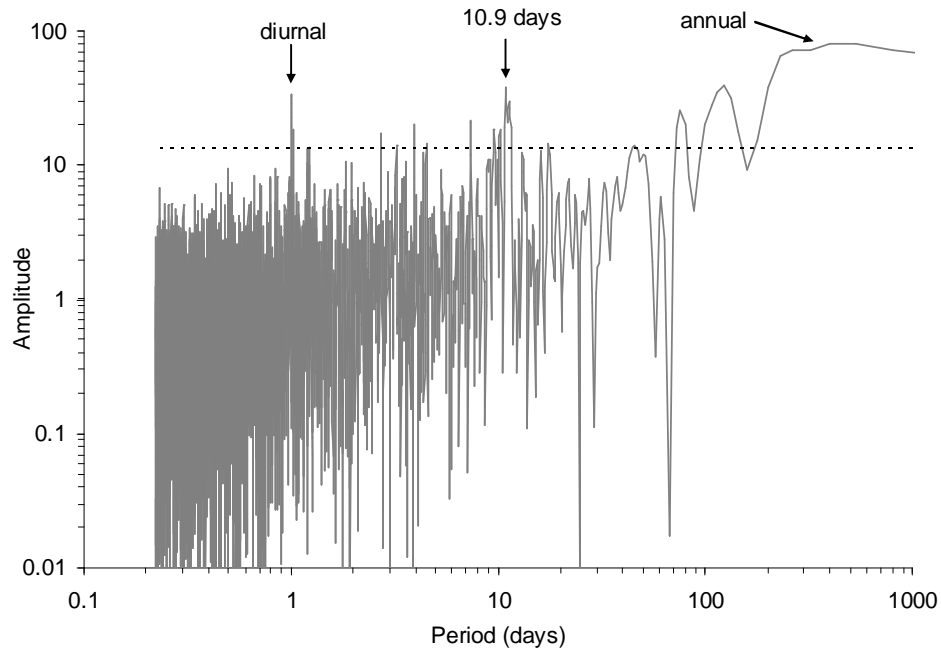


Figure 5.6 Periodogram of hourly mean fair-weather J_C between 1 January 2006 and 1 March 2007, with prominent cycles identified. Dashed line represents the 99% significance threshold amplitude for white noise.

5.3.3 Measurement of the turbulent current density (J_T)

The turbulent current density (J_T) is hypothesised to be small compared to J_C during fair weather conditions, thereby allowing its contribution to directly measured vertical current density to be neglected (Gherzi, 1967). This hypothesis was tested experimentally using established theory on J_T calculation using turbulence theory applied by previous researchers (e.g. Bent and Hutchinson (1966), Vitta (1974), Oluwafemi et al (1975)). As J_T is the vertical flux of space charge density due to air turbulence, it can be calculated using the micrometeorological approach of high-frequency (>1Hz) turbulence and space-charge sampling. The two parameters required are the space charge density (ρ_{SC}) and coincident vertical wind speed (w) at the same height (w is positive for upward motion). The deviations of each parameter from their mean with time is required for the Reynold's Averaging technique used for turbulent flux calculation (Stull, 1988). These deviations are denoted by a prime (') superscript. Using this method, the mean J_T ($\overline{J_T}$) is found by:

$$\overline{J_T} = \langle w' \rho_{SC}' \rangle \quad (5.1).$$

Space charge density (ρ_{SC}) is calculated from the vertical gradient of PG (denoted as F in the equation) using the method applied by Bent and Hutchinson (1966):

$$\rho_{sc} = -\epsilon_0 \cdot \frac{dF}{dz} \quad (5.2).$$

The PG gradient was measured using two JCI131 field mills positioned at the top of different height masts at the RUAO. As a vertical gradient is required, the two masts were positioned as close together as possible; horizontally separated by approximately 3m. One mast was at a height of 3m and the other at 10m above the ground. The vertical wind speed was measured using a sonic anemometer positioned at the top of a third mast at a height in between the two PG masts (7.2m). A picture showing the relative positioning of the three masts can be seen in Figure 5.7. All three instruments were sampled simultaneously at 4Hz to provide sufficient time resolution to incorporate the turbulent eddies considered to contribute to the surface vertical flux (e.g. Rooney and Claxton, 2006).

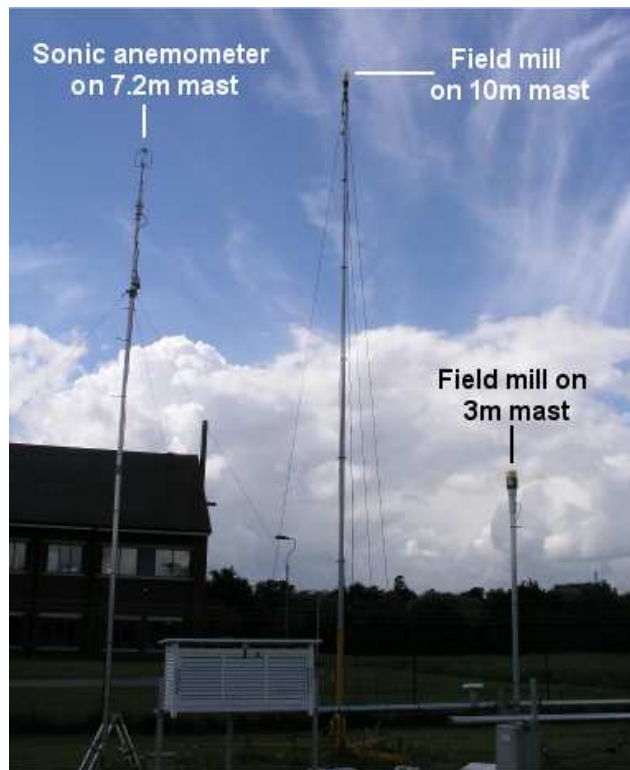


Figure 5.7 Equipment layout at the RUAO for J_T measurement during 15 June 2007

The results of two samples of J_T taken during different meteorological conditions over periods of 15 and 30 minutes are shown in Table 5.1. A negative J_T implies that positive space charge is moving upwards. This is consistent with upward turbulent transfer of a net positive ionic space charge adjacent to the surface that results from the electrode effect

(Hoppel et al. 1986). From these results, it can be seen that the mean J_T measured over 15 minutes during fair-weather conditions was an order of magnitude less than a typical J_C of 1pAm^{-2} . The J_T measured during fair weather on 14 June 2007 is less than the uncertainty in J_C using the AECF and GDACCS instruments. The increased convective activity on 15 June 2007 (deep cumuli seen in Figure 5.7) may have been responsible for the increased J_T as space charge was transported vertically by convective mixing, although as the typical variability of J_T is not known, it is unclear whether the difference in J_T was due to meteorological conditions or inherent variability. Although more samples of J_T would be required to fully characterise J_T at the RUAO, the initial results are in agreement with the hypothesis that J_T is small compared to J_C during fair weather (e.g. Gherzi, 1967).

Sample Duration	Mean J_T	Meteorological conditions
15 minutes (14/6/07)	-0.1pAm^{-2}	Fair weather, overcast
30 minutes (15/6/07)	-0.2pAm^{-2}	Strongly convective

Table 5.1 Mean and standard deviation of J_T for samples made on different days, calculated from 4Hz measured PG gradient and vertical wind speed.

5.3.4 Total conductivity (σ_T)

Total conductivity (σ_T) (determined by the sum of positive and negative conductivity, $\sigma_+ + \sigma_-$) was measured by the Programmable Ion Mobility Spectrometer (PIMS) on various occasions throughout 2006, totalling 4248 individual measurements. The PIMS was operated in current-measurement mode (Aplin 2000) using an 18-step bias voltage sequence from -18.51V to $+17.85\text{V}$ and processed in accordance to Harrison and Aplin (2007). A histogram of total conductivity for the 2006 measurements is given in Figure 5.8.

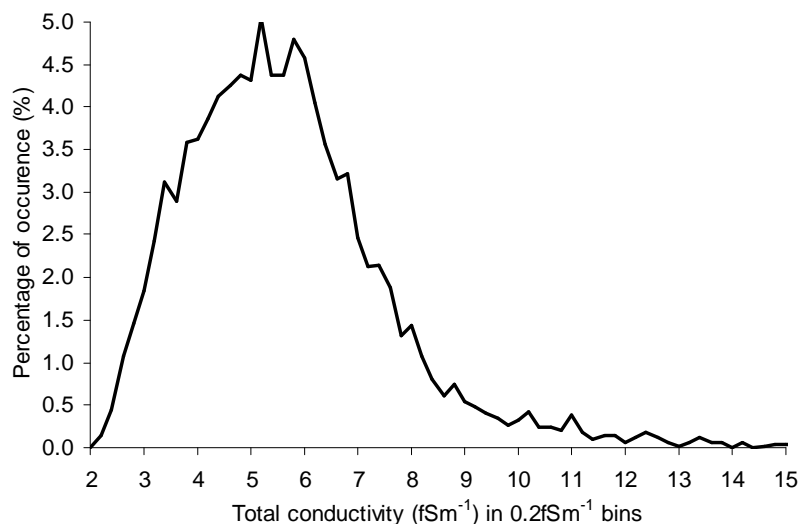


Figure 5.8 Histogram of total conductivity (σ_T) from small ions for 2006. Any PIMS σ_T data below 2fSm^{-1} or above 20fSm^{-1} was considered spurious and excluded from the dataset.

The annual mean and standard deviation of σ_T for 2006 were 5.7fSm^{-1} and 2.3fSm^{-1} respectively. Like previous atmospheric electrical variables, the dataset is positively skewed. Unlike PG and J_C , σ_T can not be negative. As the parameter is related to local small ion number concentration and mobility and not (directly at least) to J_C or remote charge regions it is more resistant to meteorological changes such as the passage of convective cloud or precipitation. However, falling precipitation will remove both ions and aerosol, which are the controlling factors of σ_T (via the steady-state ion balance equation, Harrison and Carslaw, 2003). Like PG, σ_T will be affected by local variation of aerosol number concentration and ionisation rate. The extended positive tail is likely to represent times of abnormally low aerosol number concentration or high surface ionisation rate at the RUAO, both of which are known to vary over a range of timescales (Hoppel et al. 1986). Additionally, σ_T is most sensitive to variations in aerosol number concentration for high values of σ_T , corresponding to a broader range of σ_T towards the higher portion of the distribution for any given absolute variation in aerosol.

Only small ions with mobilities $>0.95\text{cm}^2\text{V}^{-1}\text{s}^{-1}$ for positive ions and $>0.99\text{cm}^2\text{V}^{-1}\text{s}^{-1}$ for negative ions are sampled by the PIMS2 instrument that was used throughout 2006. It is small ions that are expected to contribute the most to total conductivity due to their high ionic mobility compared to the larger ions. However, at sites with high surface aerosol number concentrations ($>10,000\text{cm}^{-3}$), large ions may contribute a significant component of the total conductivity (Dhanorkar and Kamra, 1997). If this occurs at the RUAO, the σ_T measured by the small-ion PIMS may be an underestimate of the actual σ_T at the site if

sufficient number concentrations of large ions with mobilities less than approximately $0.9\text{cm}^2\text{V}^{-1}\text{s}^{-1}$ exist.

σ_T variability

A spectral analysis for hourly mean σ_T for 2006 found using a Lomb Periodogram is presented in Figure 5.9. It can be seen that the dominant cycles for σ_T are semi-diurnal and diurnal. An annual cycle may be inferred although resolution is low at these timescales due to the dataset being only one year in duration. There are several prominent intra-annual cycles, including the ~11-day cycle that is also evident in the PG and J_C periodograms. As this 11-day cycle is found in parameters that are dominated by local, near-surface effects (σ_T) and J_C , which is affected by the whole column and global properties, it is likely that this cycle is related to boundary-layer processes which influence aerosol number concentration and terrestrial ionisation rate profiles and near-surface values. However, σ_T at the surface will have a small (~20%) contribution from cosmic ray ionisation, which is also a dominant factor in the determination of columnar resistance, suggesting that a quasi-11-day periodic variability in cosmic ray intensity may provide a possible explanation for the similar 11-day periodicity observed in J_C , PG and σ_T .

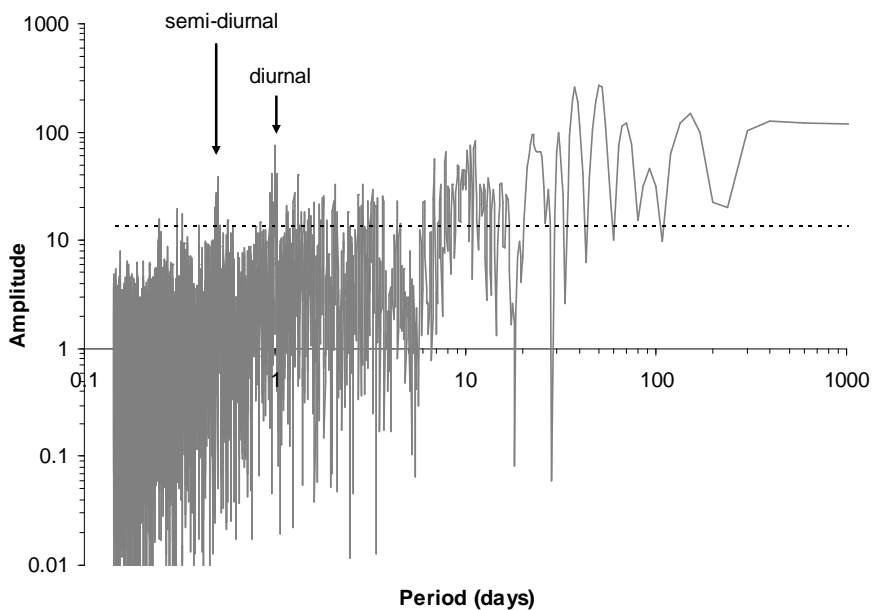


Figure 5.9 Periodogram of hourly mean σ_T for 2006, with prominent cycles identified. Dashed line represents the 99% significance threshold amplitude for white noise.

5.3.5 Small ion number concentration and mobility

In addition to calculating σ_T , the PIMS also derives bipolar small ion number concentrations and mobilities. Histograms of these parameters for 2006 are shown in Figure 5.10 (each histogram uses data from 4248 measurements).

The distribution of small ion number concentration shown in Figure 5.10a, has a mean and standard deviation for positive and negative ions (in cm^{-3}) of 105 ± 56 and 86 ± 48 respectively. The 1.22 ratio of these means is similar to that found by previous studies in an urban environment (MacGorman and Rust, 1998). Both distributions are positively skewed, so the positive and negative medians of 96 and 75 respectively may be more indicative of the majority of small ion concentrations during 2006. A broader number concentration distribution is observed for the positive small ions compared to negative.

A clear distinction between the average positive and negative ion mobilities is identified by Figure 5.10b, with positive and negative mobility means (in $\text{cm}^2\text{V}^{-1}\text{s}^{-1}$) of 1.78 and 2.38 respectively (ratio of 0.75). The higher negative small ion mobility was expected as negative small ions tend to be lighter (and therefore more mobile in a PG) than their positive counterparts (MacGorman and Rust, 1998). The standard deviations are very similar however, being $0.84\text{cm}^2\text{V}^{-1}\text{s}^{-1}$ for both polarities. Although the tail of the mobility histogram reduces to near-zero occurrences below mobilities of about $0.5\text{cm}^2\text{V}^{-1}\text{s}^{-1}$, it must be remembered that the PIMS was only configured to sample small ions of mobilities exceeding approximately $0.9\text{cm}^2\text{V}^{-1}\text{s}^{-1}$, so this reduction is not necessarily reflective of the true ion population. Small ion mobilities measured in an urban environment in Estonia by Hörrak et al. (1994) were lower than those measured at the RUAO, at 1.1 and $1.8\text{cm}^2\text{V}^{-1}\text{s}^{-1}$ for positive and negative small ions respectively (ratio of 0.61). Later measurements in a rural area of Estonia by Hörrak et al. (2000) of hourly mean ion mobilities for 14 months in 1993-1994 had a mean of 1.36 and $1.53\text{cm}^2\text{V}^{-1}\text{s}^{-1}$ for positive and negative ions respectively (ratio of 0.89). The positive to negative ion mobility ratio for the RUAO of 0.75 lies between that found by Hörrak et al. (1994, 2000) at the urban and rural locations. If the difference between the ratios is a function of the aerosol number concentration (through selective ion-aerosol attachment) then this may suggest that the RUAO is in between the urban and rural regimes, and with smaller (more mobile) small ions than those measured in Estonia.

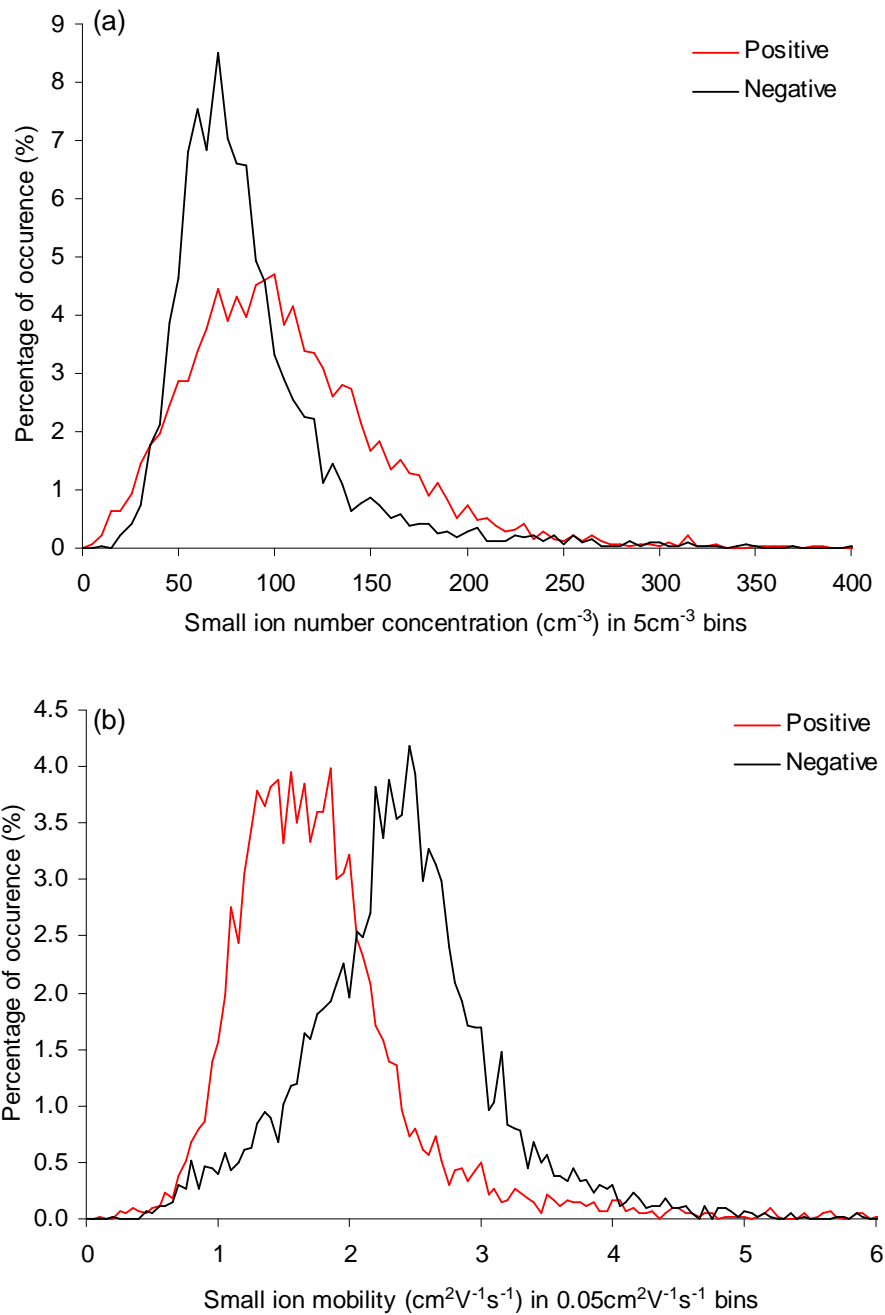


Figure 5.10 Histograms of small ion (a) number concentration and (b) mobility for positive and negative ions during 2006.

A summary of the combined annual mean and cumulative distribution percent points of atmospheric electrical statistics for the RUAO during 2006 are provided in Table 5.2. The negative value of J_c measured at the 1% occurrence level is expected to represent times of disturbed weather.

	1%	25%	Median	75%	99%	Mean	St. Dev
PG (Vm^{-1})	-242	80	107	141	371	110	96
J_C (pAm^{-2})	-3.9	1.0	2.0	3.8	9.4	2.3	2.5
σ_T (fSm^{-1})	2.5	4.2	5.4	6.6	15.8	5.7	2.3
n₊ (cm^{-3})	16	68	96	132	291	105	56
n₋ (cm^{-3})	27	58	75	98	276	86	48
μ_+ ($cm^2V^{-1}s^{-1}$)	0.7	1.3	1.7	2.0	5.1	1.8	0.8
μ_- ($cm^2V^{-1}s^{-1}$)	0.7	1.9	2.4	2.7	4.8	2.4	0.8

Table 5.2 Summary statistics for atmospheric electrical parameters measured at the RUAO during 2006. J_C has been constrained to -5 to 10pAm⁻² to remove suspected leakage values whilst containing the fair-weather distribution of Figure 5.5.

5.4 RUAO atmospheric electrical diurnal and seasonal variations

Dominant diurnal and seasonal cycles are seen for both PG, J_C and σ_T using the Lomb periodogram analysis in the previous section. The mean diurnal and seasonal variations of PG, J_C and σ_T have been further investigated for the RUAO during 2006, the results of which are presented in this section.

5.4.1 Potential gradient (PG)

Variations in PG during fair and disturbed weather are treated separately due to their difference sources. The monthly mean fair-weather ($50Vm^{-1} < PG < 300Vm^{-1}$) diurnal cycles were calculated for 2006 and displayed as a contour plot in Figure 5.12. These monthly fair-weather PG diurnal cycles are also displayed as a contour plot in Figure 5.12 to emphasise seasonal trends in diurnal variation throughout 2006. Due to the large sample size (~300 five-minute fair-weather PG values for each hour during a month), the standard error attributed to the hourly means used to produce the monthly mean diurnal variations (Figure 5.11) are low compared to the amplitude of the diurnal variations (Table 5.3). Therefore, the calculated diurnal variations are expected to be robust. Error bars are therefore not included in Figure 5.11 and Figure 5.12a due to their small amplitude.

The general feature of the monthly mean diurnal variations are that all have a morning peak. The time and amplitude varies seasonally, occurring at approximately 7UT in the summer and 9UT in winter. The cause of this morning peak in fair-weather PG is not expected to be global in origin as although the peak occurs around the time of the Asian thunderstorm maxima in the Carnegie curve (Whipple and Scrase, 1936) the magnitude of

the observed peak is too great to be solely attributed to this. Instead, local factors are expected to cause this morning peak, which has been reported by several investigators in the past (e.g. Scrase (1934), Mani and Huddar (1972), O'Connor (1976), De et al. (2006)).

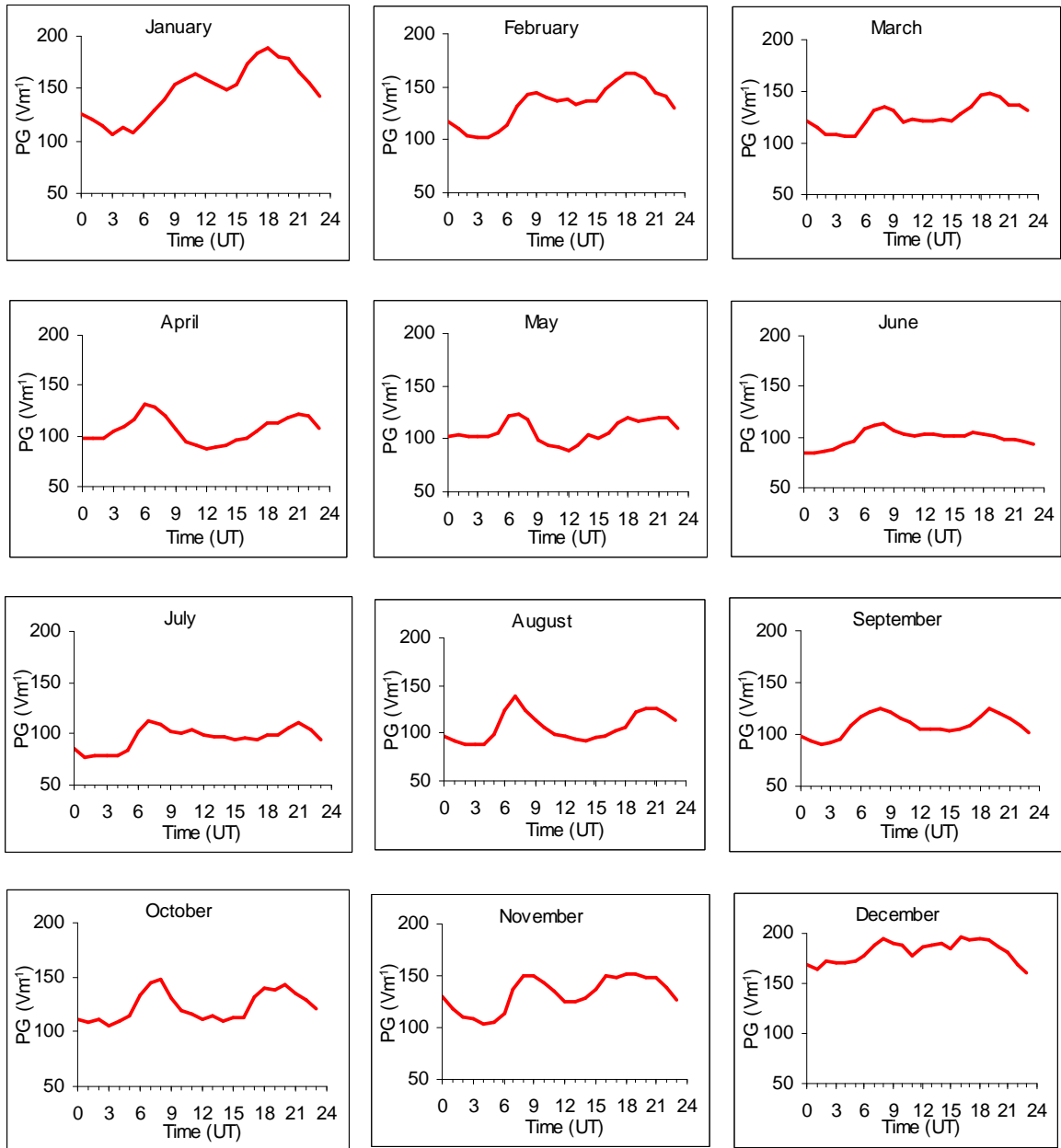


Figure 5.11 Monthly mean fair weather PG recorded at the RUAO during 2006.

Mean hourly standard error (Vm^{-1})	
Jan	2.7
Feb	2.5
Mar	2.5
Apr	1.8
May	2.0
Jun	1.6
Jul	1.5
Aug	1.6
Sep	1.8
Oct	2.3
Nov	2.8
Dec	4.4

Table 5.3 The standard error in monthly mean PG diurnal variation during 2006 (averaged over all hours), as shown in Figure 5.11.

The local factors can be either decrease σ_T by an increase in aerosol, which increases the PG for a constant J_C (Harrison, 2005b) or the elevation of positive space change by initial convection currents after sunrise (Chalmers, 1967). The former is expected to be the dominant process at polluted urban sites (Whipple, 1936) and the latter for unpolluted sites (O'Connor, 1976). The RUAO is urban, so the morning peak in PG is expected to be due mainly to a corresponding increase in aerosol. Such an increase in PM_{10} (mass concentration of aerosol particles $<10\mu\text{m}$ in diameter) was observed during the time of PG morning maximum in the annual mean diurnal variation of PM_{10} for Reading during 2004 (Latha and Highwood, 2006).

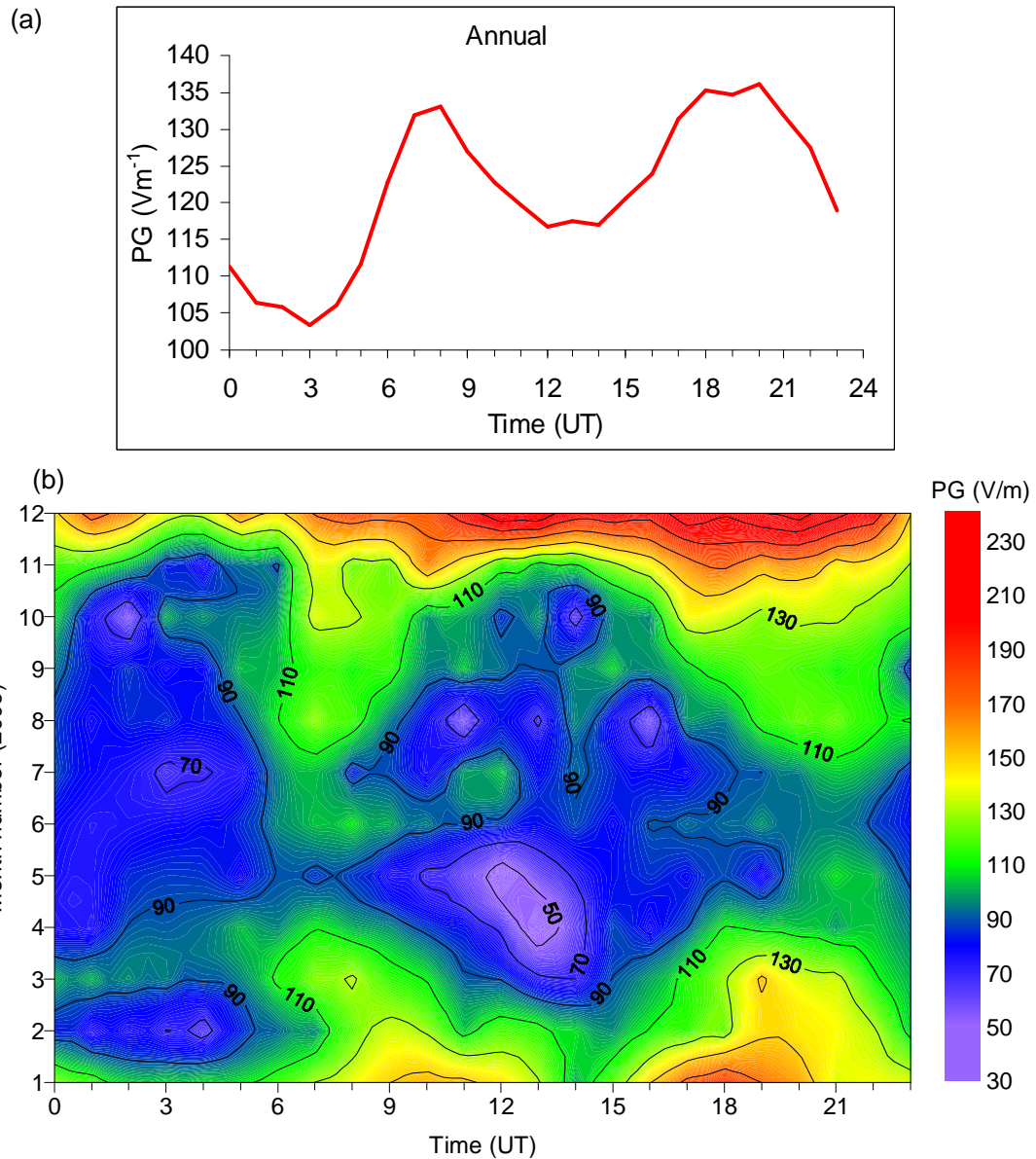


Figure 5.12 (a) Annual mean diurnal cycle and (b) contour plot of monthly fair-weather PG diurnal variations for 2006.

A secondary maximum in PG occurs in the early evening at around 18UT during winter and 20UT for summer. The time of this peak coincides with the second maximum in annual average PM_{10} mass concentration for Reading (Latha and Highwood, 2006) so may also be attributed to the diurnal variation in local aerosol concentration. However, this evening peak also coincides with the time of PG maximum for the Carnegie curve, which is representative of surface PG variation due to global thunderstorm activity. The observed evening peak in PG exceeds that of the morning one at the RUAO during winter in 2006, with only a weak evening maximum occurring in June and July. The two maxima

in the PG diurnal cycles produce the prominent semi-diurnal cycle seen by spectral analysis in Figure 5.4.

A minimum of PG is observed to occur at approximately 03UT for all fair-weather monthly mean diurnal cycles (Figure 5.11). The minimum coincides with both the minimum PM_{10} mass concentration for Reading (Latha and Highwood, 2006) and that of the Carnegie curve. Like the evening PG maximum, the similarity in times between minimum times of local PM_{10} and the globally representative Carnegie curve creates ambiguity between the relative influence of global and local sources of the 03UT PG minimum. A secondary minimum in PG is observed to occur during all months, but is especially pronounced in late spring and summer (Figure 5.12). The source of this secondary minimum can be attributed to local sources as there is no evidence of such a pronounced afternoon minimum in the Carnegie curve. The local source is expected to be due to increased convection in the afternoon that deepens the boundary layer and increases upward ventilation of near-surface aerosol (Scrase, (1936), Serrano et al. (2006)). As a result, PM_{10} is observed to also have a minimum during the early afternoon (Latha and Highwood, 2006). Lower aerosol concentration increases conductivity and reduces PG (for constant J_C). This reduced PG due to low aerosol concentration is likely to be reduced further by a corresponding decrease in J_C . As no aerosol is lost from the column during this convective ventilation process, J_C will continue to reduce with increasing aerosol columnar load (due to increasing R_C) as more aerosol is moved aloft by convection. The combination of a lower J_C and increased conductivity at the surface caused by a change in the aerosol number concentration vertical profile is hypothesised to be the most likely source of the observed afternoon minimum of PG at the surface, demonstrated by the columnar resistance model in chapter 6.

The monthly mean and standard deviation of fair weather (FW) hourly mean PG for the month are shown in Figure 5.13. The reduced mean PG during the summer is evident in this figure. Additionally, the standard deviation of hourly mean FW PG is lowest for the summer months. The lower monthly mean and standard deviation during the summer is likely to be due to seasonal variation of surface aerosol number concentration (Märcz and Harrison (2003), Adlerman and Williams, (1996)). The increased occurrence of mist and fog during the winter half of the year will also contribute to the increased aerosol number concentration. Like other sources of aerosol, mist and fog will increase the surface PG for a given J_C , and the increased frequency of occurrence during the winter is likely to also contribute to the increased monthly standard deviation, as the more extreme PG variability associated with times of disturbed weather (showers, thunderstorms etc) are not included.

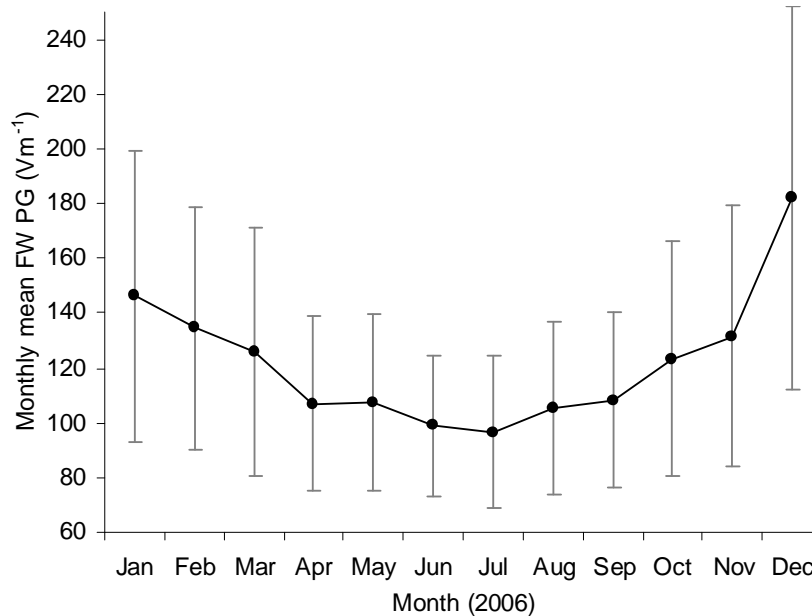


Figure 5.13 Monthly mean fair-weather (FW) PG for 2006, including standard deviation of hourly mean FW PG values observed during the month.

Diurnal variation of PG standard deviation

When considering all the PG measurements made during 2006, not just those of fair-weather, strong variability of PG on sub-diurnal timescales are found. The standard deviation within hourly mean PG (derived from 5 minute means) used to produce Figure 5.3b are shown in Figure 5.14 as a function of time and day of year for 2006. The results of Figure 5.3b are used to generate a colour key for Figure 5.14 to indicate times when PG sub-hourly variability is typical of settled, fair-weather conditions (green), and unsettled (white through to red). It can be seen that during January to March there is a higher occurrence of slight PG disturbance indicated by the white/light grey colour, especially in the morning (6-10UT) and evening (16-19UT) This is expected to be due to the onset and dissipation of mist and fog, which will cause variability in PG by decreasing near-surface air conductivity as small ions become attached to the suspended water droplets. More extreme PG variability occurs during the passage of convective cloud, especially Cumulonimbus clouds which are often highly electrically charged (MacGorman and Rust, 1998). Figure 5.15 shows the mean diurnal cycle of PG standard deviation for 2006. It is found that the greatest sub-hourly variability occur between 13-16UT inclusive. The standard errors in the calculated hourly means indicate that this maximum is greater than that which may be attributed to natural variability alone. This maximum is due to the early/mid afternoon being the time of greatest convective activity over the RUAO, especially during the summer half of the year when convective cloud formation due to local surface heating by the sun is strongest.

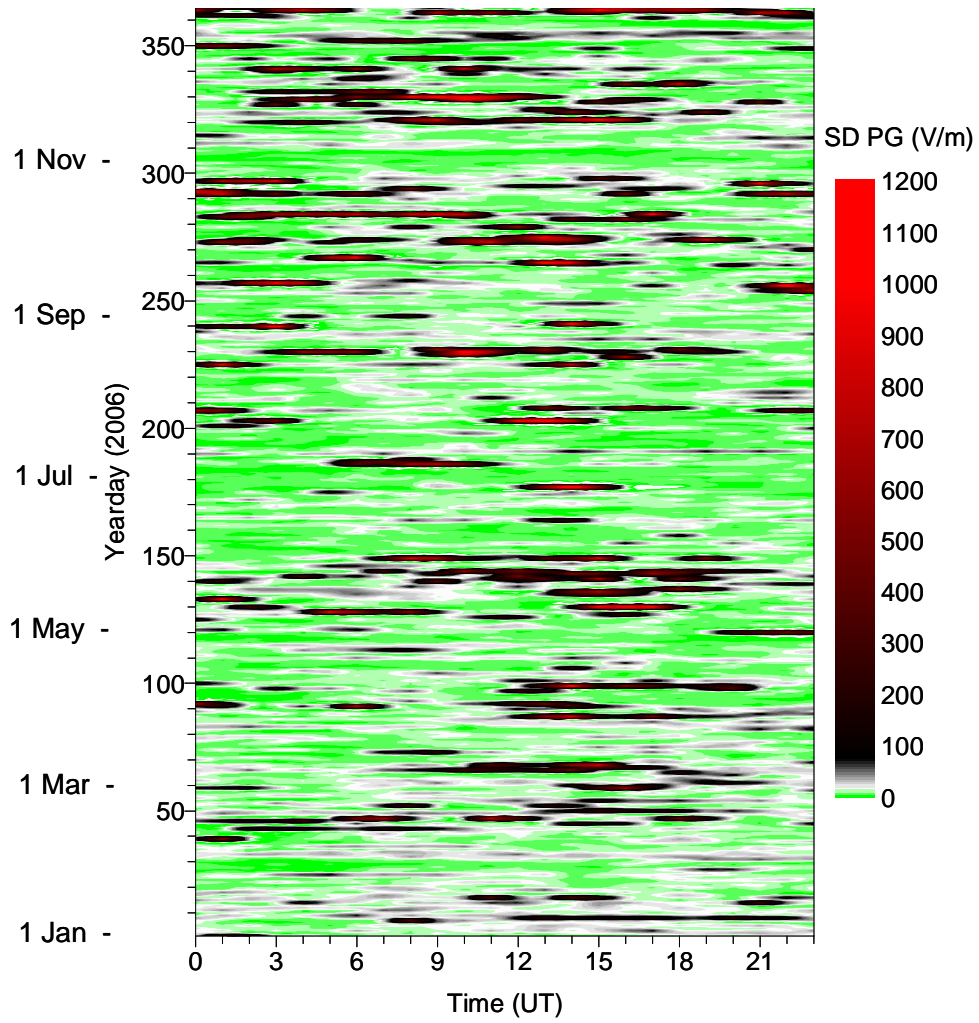


Figure 5.14 Standard deviation of the twelve five minute means that were used to calculate each hourly mean value for 2006, displayed as a function of time and day of year. The colour key was chosen to indicate times of typical and high PG sub-hourly variability.

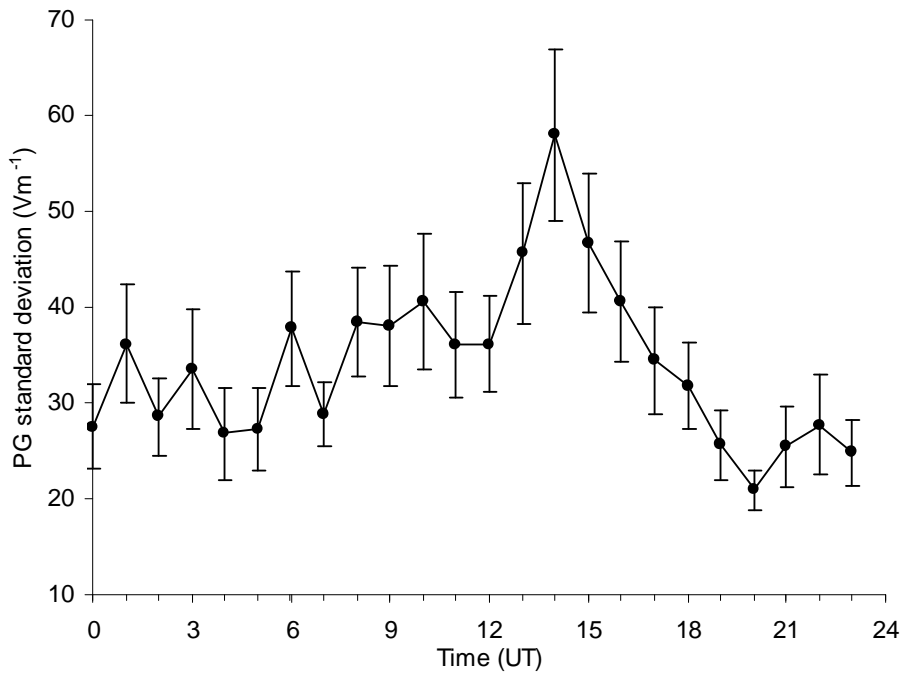


Figure 5.15 Mean diurnal cycle of five minute PG standard deviation within an hour for all PG measurements in 2006, including standard error bars.

5.4.2 Air-Earth conduction current density (J_C)

Measurements of J_C during 2006 were made at the RUAO using the Air Earth Current Pyramid (AECF) from the months January to July (inclusive) and the Geometrical Displacement and Conduction Current Sensor (GDACCS) from August until December. Due to leakage currents affecting the AECF, the amount of fair-weather ($0.5 < J_C < 3.0 \text{ pA m}^{-2}$) measurements made during one month were considered too few to be statistically reliable, especially during the night. Therefore the J_C data has been divided into seasons (not months) to assess any changes to the mean fair-weather diurnal variation of J_C throughout the year. These mean seasonal diurnal variations of J_C are shown in Figure 5.16.

In general, diurnal cycles of J_C do not appear to be as distinct as those of PG, nor do they show similar tendencies. Variability within the winter (Dec, Jan, Feb) J_C diurnal cycle is lowest, due mainly to the lack of J_C reduction during the night, which is observed for the other seasons. However, the comparatively large standard errors of the hourly means imply that the diurnal variation of this season is somewhat ambiguous. The magnitude of J_C between 11-16UT is similar for all seasons, with all but summer (June-August) displaying a steady decrease during this time. For the summer, although J_C decreases from 09-13UT, it increases again from 14UT to form a shallow maximum between 18-

21UT. A more prominent morning maximum occurs at 08UT during the summer, following a minimum value at 05UT. The lower standard error during summer (due to more fair-weather values) compared to the other seasons imply that more confidence can be attributed to this diurnal variation. There are no immediate similarities between the seasonally averaged diurnal variation of J_C and the Carnegie curve during 2006. This suggests that local variations (R_C in the case of J_C) are important in determining the diurnal variation of J_C . However, using the GDACCS in winter 2007, there is a noticeable similarity between monthly mean J_C and the Carnegie curve, which will be discussed in Chapter 6.

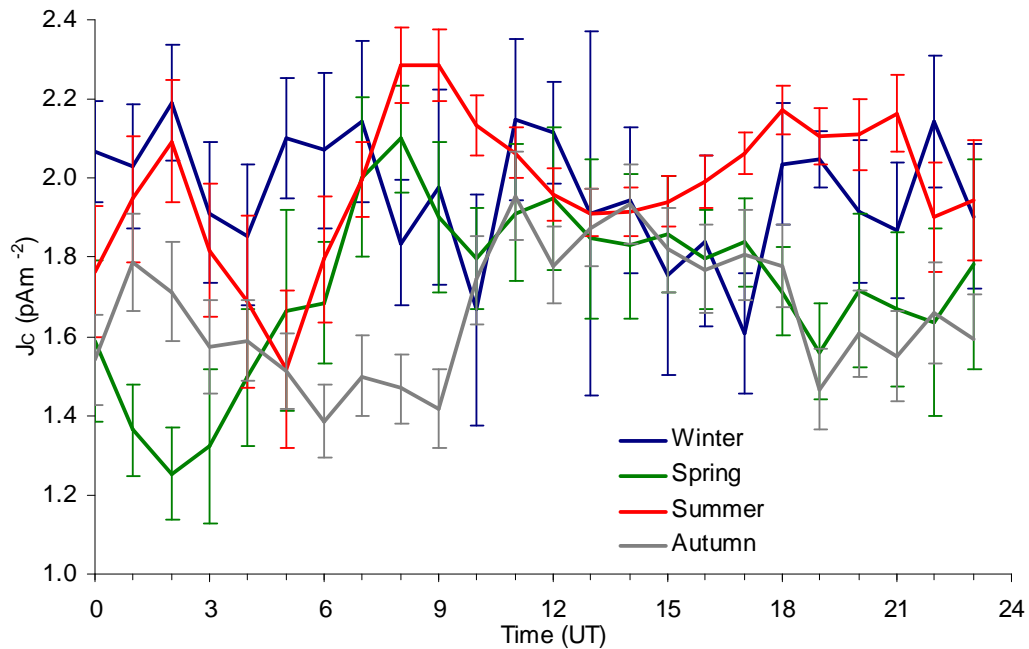


Figure 5.16 Seasonal mean diurnal variation of fair-weather J_C for 2006. Seasonal definitions are Winter (Dec,Jan,Feb), Spring (Mar-May) Summer (Jun-Aug) and Autumn (Sep-Nov). Standard error bars are included.

The annual average J_C diurnal variation is shown in Figure 5.17. It can be seen that there is a distinct minimum between 04-05UT (valid for the displayed standard errors) and a broader maximum between 10-12UT. It should however be noted that the standard errors are smaller than the instrument error of the AECF at 0.11pAm^{-2} , although this error estimate is still less than the amplitude of the diurnal variation. J_C then reduces gradually throughout the afternoon between 12-20UT before decreasing more rapidly towards the 05UT minimum. Unlike the annual mean PG diurnal variation (Figure 5.11), the J_C cycle displays no double peak during times of expected high surface aerosol concentration seen by the annual mean diurnal variation of PM_{10} (Latha and Highwood, 2006). This further suggests that it is the local conductivity and not the R_C that causes the PG double peaks.

According to the measurements of Sagalyn and Faucher (1956) the R_C should be greatest around 14 local time, which would act to decrease J_C for a given V_I . However, J_C is near the daily maximum during this time (Figure 5.17) and the maximum in V_I (Carnegie curve) is not until the evening for the time zone of the RUAO, so the time of the observed maximum is not immediately obvious. The minimum of J_C at 04-05UT is near to that of the Carnegie (03-04UT) so may be (at least partially) related to characteristics of the global circuit.

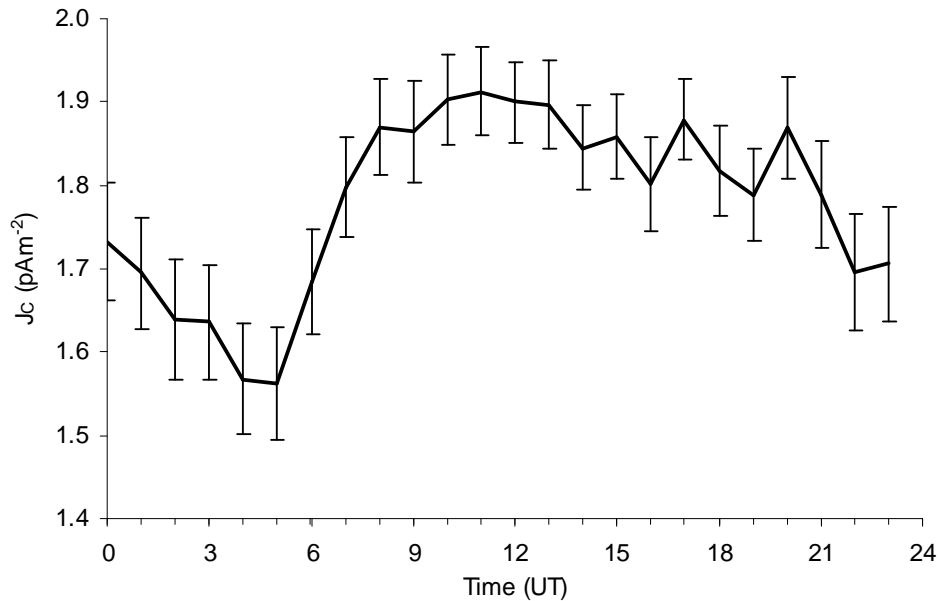


Figure 5.17 Annual mean fair-weather J_C diurnal variation for 2006, including standard error.

The monthly mean and standard deviation of J_C is shown in Figure 5.18. Unlike the PG, the monthly mean J_C appears to have no distinct annual shape. The largest monthly mean J_C was January, although a broad maximum also occurred in the summer. The months of October-December experienced the lowest J_C . No obvious differences in standard deviation are visible, although the lowest deviations occurred during the J_C maxima at January and July, and the highest near Equinox, during April and October. This seasonal variation in J_C does have some qualitative similarities to that measured in Hawaii between 1977-1983 (Adlerman and Williams, 1996), with a maximum J_C in summer and minima around the Spring and Autumn equinox. Secondary maxima around the equinox was also found for Kew (Harrison and Ingram, 2005).

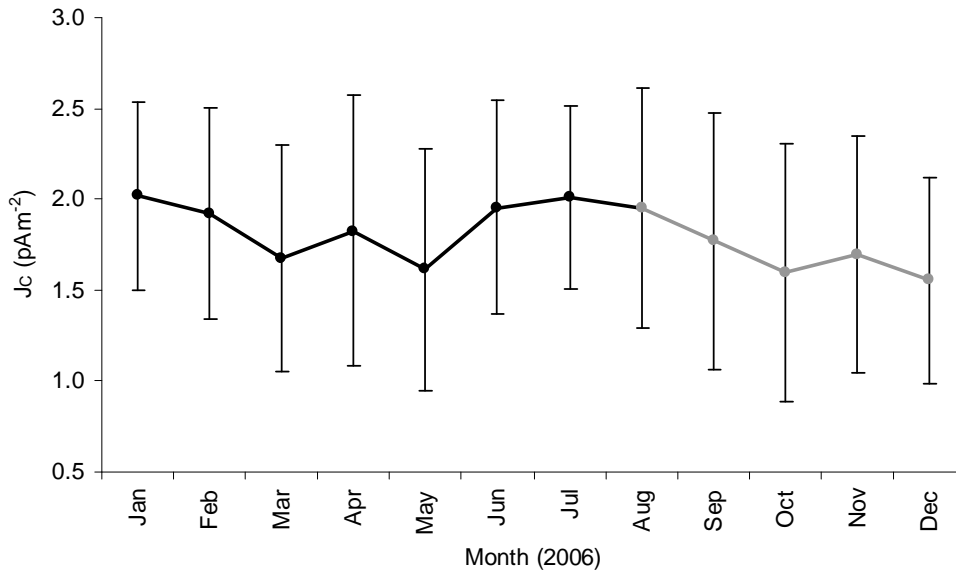


Figure 5.18 Monthly mean fair-weather J_c and standard deviation of hourly measurements within the month. The grey line (August to December) represents measurements made by GDACCS.

5.4.3 Total conductivity (σ_T)

Total conductivity, σ_T , was measured using the PIMS throughout 2006. As the PIMS was not suited to prolonged exposure to environmental conditions, not all the months were sampled for long enough to be considered representative (i.e. <3 days in the month were not considered significant, with many months being sampled at least half of the days). The number of PIMS samples for each month is given in Table 5.4. The largest amount of PIMS samples were for July, with PIMS operating successfully during all but one of the days.

	<i>Jan</i>	<i>Feb</i>	<i>Mar</i>	<i>Apr</i>	<i>May</i>	<i>Jun</i>	<i>Jul</i>	<i>Aug</i>	<i>Sep</i>	<i>Oct</i>	<i>Nov</i>	<i>Dec</i>
<i>Samples</i>	0	908	32	0	317	286	1605	0	557	189	354	0

Table 5.4 Number of PIMS samples made during each month of 2006. Each sample represents a single PIMS measurement cycle, lasting approximately 18 minutes. Months in italics were not used for monthly statistics due to under/lack of sampling.

The seasonal diurnal variations of σ_T during 2006 are shown in Figure 5.19. The standard errors associated with these mean values imply that although the small variations between adjacent hours are unlikely to be significant, the broader diurnal shapes have amplitudes sufficient to be confident of their presence in reality. The basic variation for all seasons includes a morning minimum at between 04-07UT for the Spring and Summer,

and approximately two hours later in the Autumn and Winter. The diurnal σ_T maximum is most pronounced in Spring, at 11UT, with more broader maxima observed during this time for Summer, beginning earlier at 8UT. Autumn maximum is also broad, and of a similar shape to that of the Summer, although beginning later at 10UT. The maximum of σ_T during the Winter is not as broad as the Autumn and begins more gradually; rising steadily from the minimum to a maximum at 14UT before falling more sharply to the lowest value of the day at 18UT.

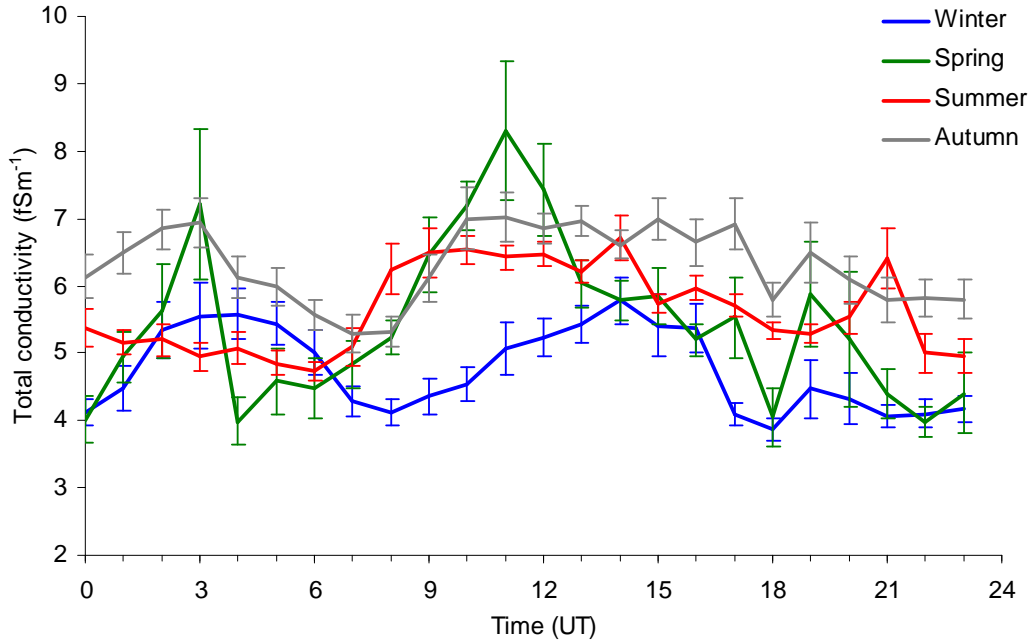


Figure 5.19 Seasonal mean diurnal variation of σ_T during 2006. Months used were restricted to data availability (Table 5.4), with Winter (Feb), Spring (Mar, May), Summer (Jun, Jul) and Autumn (Sep, Oct, Nov). Standard error bars included.

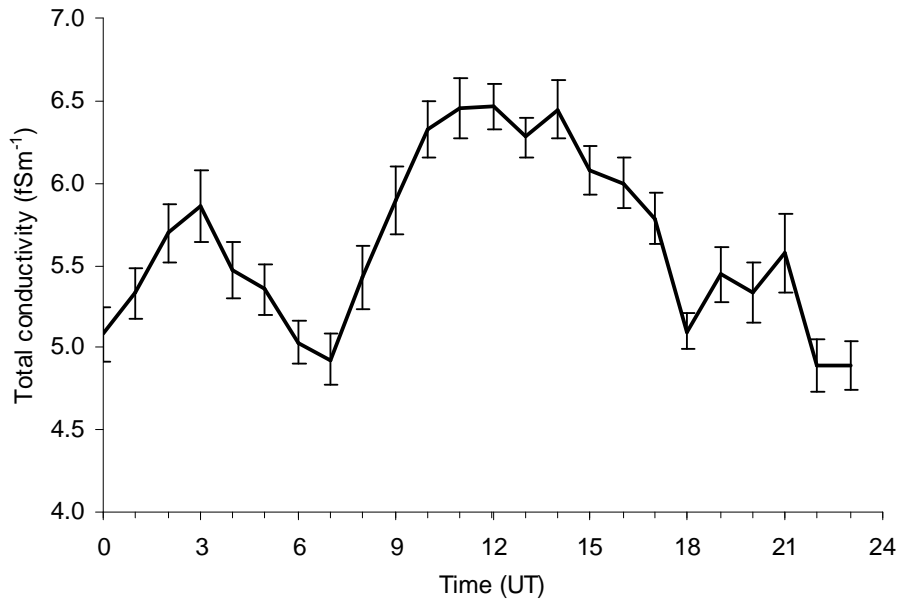


Figure 5.20 Annual mean σ_T diurnal cycle for 2006, including standard error bars.

The annual mean variation of σ_T for 2006 is shown in Figure 5.20, where a minimum value at 07UT and mid day maximum between 10-14UT are observed. This mid day maximum value occurs at a similar time as the maximum of annual mean J_C in Figure 5.17.

The diurnal cycle of σ_T will be related to the diurnal cycle of local aerosol number concentration and ion production rate, for constant ion mobility. Terrestrial sources of ionisation dominate over those of cosmic origin for ion pair production near the land surface (Hoppel et al. 1986). Neither ionisation rate nor natural radioactive gasses such as Radon were measured at the RUAO during 2006 (Geiger counters installed at the RUAO during 2005 were retired from regular service in 2006 due to technical difficulties and Radon concentration has never been measured, although typical values indicated a mean surface ionisation rate of $8\text{cm}^{-3}\text{s}^{-1}$). However, it is aerosol number concentration that is expected to be the dominant source of ion (and therefore σ_T) variability as the ion-aerosol attachment process dominates over ion recombination as the main source of ion loss near the surface of an urban site.

A hypothesis for the variation of σ_T seen in Figure 5.19 and Figure 5.20 is that the enhanced surface ventilation of aerosol by convection generated by solar heating of the surface will reduce the aerosol number concentration during the afternoon on days with near surface static instability. The reduction in afternoon aerosol concentration will allow more ion number concentrations to exist near the surface and a correspondingly higher σ_T as seen in Figure 5.20. The aerosol will accumulate near the surface during more stable

times such as early morning when a nocturnal inversion is likely to prevent upward ventilation of aerosol. The aerosol will accumulate under this inversion until sunrise when convection begins to extend the height of the boundary layer. This is likely to explain the σ_T minimum at 07UT, as it is this time just before the onset of convection that aerosol concentration will be highest. The diurnal variation of Radon concentration is also explained by diurnal variation of atmospheric stability and convection by Kataoka et al. (1998), as both aerosol and Radon are considered as passive tracers for this purpose.

The mean diurnal variation of σ_T for July 2006 is compared with that of total small ion number concentration and mobility for the same time period in Figure 5.21a. The purpose of this comparison is to assess whether the variability in σ_T is due more to variations of small ion number concentration or mobility (the two parameters that determine σ_T). From Figure 5.21a it is clear that ion number concentration is the dominant source of σ_T variability, as shown by the near-identical diurnal variations, with ion mobility remaining relatively constant throughout the day. As aerosol number concentration is expected to be the main source of small ion variability for an urban site such as the RUAO, the variation in aerosol number concentration should be proportional to the inverse of conductivity, as increased aerosol will reduce ion number concentration and therefore σ_T . Although the diurnal variation of aerosol number concentration for July 2006 is not known, the aerosol mass concentration was regularly measured using a Dusk Trak instrument. This is an optical device so will not be responsive to aerosol in the ultra fine aerosol region, which is unfortunately the region of the aerosol distribution with the highest number concentration (Pruppacher and Klett, 1997). However, the Dust Trak aerosol mass concentration will however indicate times of greatest aerosol loading by larger particles (the instrument is equivalent to a PM_{15} counter, measuring the combined mass of aerosol with diameters $<15\mu\text{m}$). The instrument was calibrated for Arizona road dust size distribution.

The mean diurnal variation of σ_T (plotted on a reverse axis for ease of comparison) and aerosol mass concentration is shown in Figure 5.21b. The similarity of these diurnal variations indicates that variation of aerosol concentration is the dominant source of σ_T variability, through the process of ion-aerosol attachment. The dominance of aerosol number concentration in determining total conductivity was also demonstrated by the discovery of a close empirical relationship between total conductivity and visibility using data from 11 years of observations at Kew, London (Brazenor and Harrison, 2005).

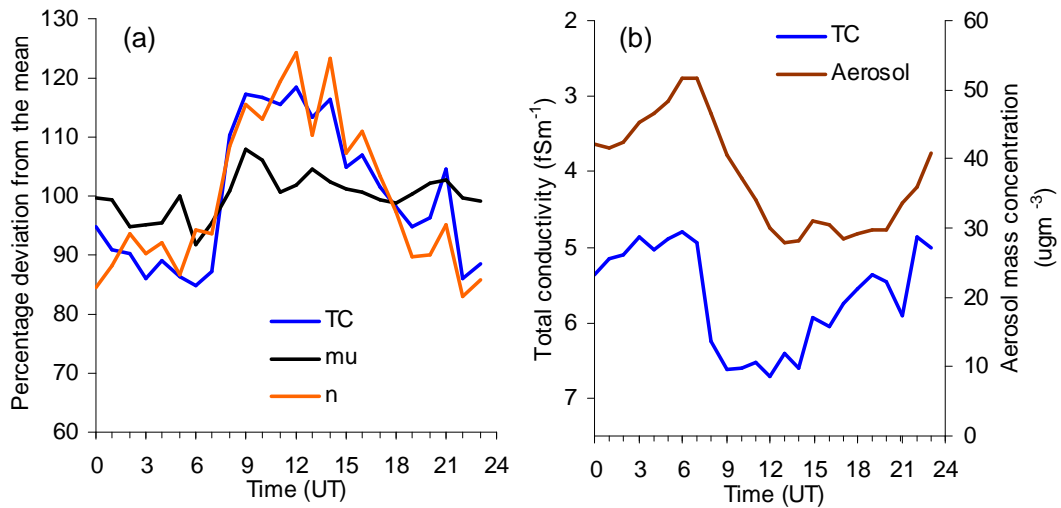


Figure 5.21 Diurnal variation as percentage of mean for July 2006 of (a) total conductivity (TC), total small ion number concentration (n) and mean small ion mobility (μ). Diurnal variation of total conductivity (with axis reversed) and aerosol mass concentration for July 2006 are shown in (b).

The reduction in aerosol mass concentration (and associated increase in σ_T) during the afternoon in July 2006 reinforces the hypothesis of surface aerosol ventilation by convection, and an increase in aerosol concentration (decreasing σ_T) in the early morning (07UT) before the nocturnal temperature inversion that trapped the aerosol near the surface is eroded.

The monthly mean and standard deviation of σ_T during 2006 is shown in Figure 5.22. Although the dataset is incomplete, it can be inferred that mean σ_T is highest during the Autumn and lowest in Winter. This is likely to be due to lower aerosol number concentrations in late summer (Serrano et al. (2006), Adlerman and Williams, (1996)).

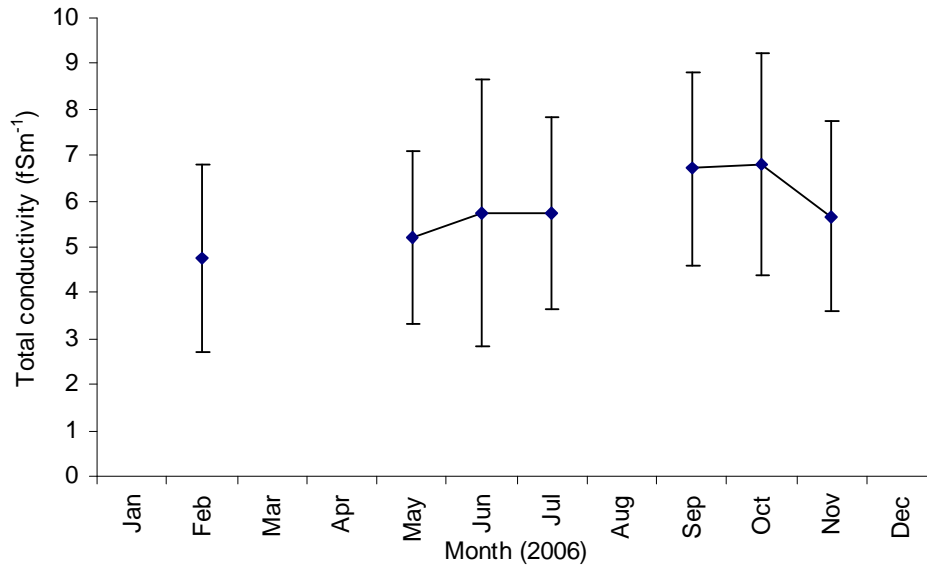


Figure 5.22 Monthly mean σ_T and standard deviation of samples within the month, for 2006. Number of samples per month are provided in Table 5.4.

5.5 Inter-comparison of atmospheric electrical parameters

A comparison between fair-weather PG, J_C and σ_T will be made to assess the validity of Ohm's Law at the RUAO. If Ohm's Law is valid during fair-weather, the three parameters should be related by:

$$J_C = \sigma_T F \quad (5.3),$$

where F represents PG. Therefore J_C should be directly proportional to σ_T and PG when one parameter is kept constant, and PG should be directly proportional to the inverse of σ_T (i.e. resistivity, ρ) for constant J_C . As the absolute values of the electrical parameters may be distorted by local factors such as nearby grounded objects, more confidence is given to the variability. Therefore to remove possible inconsistencies due to absolute offsets, a comparison of the coincident variability between a pair of parameters will be made, rather than an attempt to quantifiably demonstrate equation (5.3) by measuring two parameters and comparing the predicted value using (5.3) with the observed third parameter. The three hypotheses to be tested are therefore:

1. $J_C \propto F \Big|_{\text{constant } \sigma_T}$
2. $F \propto \sigma_T^{-1} \Big|_{\text{constant } J_C}$

$$3. J_C \propto \sigma_T \Big|_{\text{constant } F}$$

The Ohmic assumption required for equation (5.3) and the acceptance of the three hypotheses is expected to be valid during fair weather, when there are no sources of charge separation, both at the surface and within the column. The month of July 2006 will be used as a case study for inter-comparison of PG, J_C and σ_T as this month has the greatest intensity of PIMS σ_T measurements and was warm and dry (fair-weather) promoting conditions when AECF leakage currents are expected to be at a minimum. July had the most fair-weather hours for J_C for the entire measurement period (Figure 5.1), with 383 hours. Due to the high median J_C for July (2.8pAm^{-2}) when coincident values of σ_T were available, J_C between 0.5pAm^{-2} and 4.0pAm^{-2} were considered as fair-weather and leakage-free, compared to the standard upper limit of 3pAm^{-2} when annual mean statistics are considered.

A scatter-plot comparing fair-weather PG and J_C for July 2006 is shown in Figure 5.23. The values were chosen when σ_T was between $5\text{-}6\text{fSm}^{-1}$, near the median value (Figure 5.8) for optimisation between maximising the amount of data points available whilst keeping σ_T as uniform as possible. As expected by the Ohmic assumption of equation (5.3), there is a linear relationship between PG and J_C with a statistical confidence exceeding 99%. This means that the Ohmic assumption is valid over the month when applied to columnar (not surface) properties, as keeping uniform σ_T effectively removes variability in J_C and PG attributed to near-surface conductivity changes, leaving only columnar (R_C) and global (V_I) variability linking the two parameters. Therefore hypothesis 1 can be accepted, although the considerable scatter away from the linear trend line shown in Figure 5.23 demonstrates that, although a significant contributor, sources other than J_C and also contribute to fair weather PG variability, given constant σ_T . These additional sources are expected to be space charge.

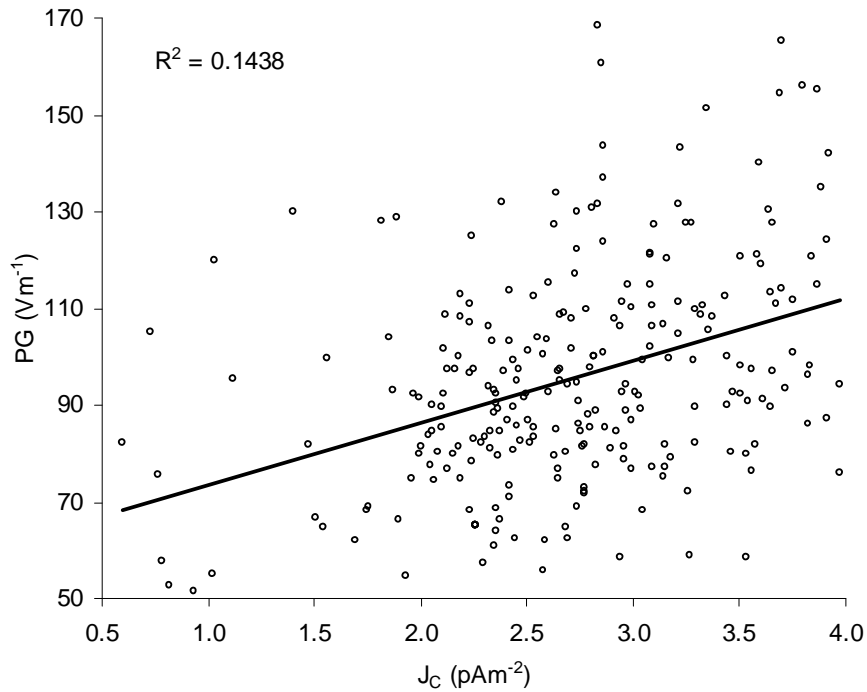


Figure 5.23 PG versus J_C for July 2006, as five minute means. Values were chosen when σ_T was approximately $\pm 5\%$ of the median, at $5\text{-}6\text{fSm}^{-1}$.

A scatter-plot comparing fair-weather resistivity (σ_T^{-1}) and PG for July 2006 is shown in Figure 5.24. The values were chosen when J_C was between $2.7\text{-}2.9\text{pAm}^{-2}$. The linear relationship observed is statistically significant, with a confidence exceeding 99%. This means that in addition to the purely columnar variation of Figure 5.23, exclusively near-surface variability (Figure 5.24) is also Ohmic during the month, as J_C is kept uniform, which acts to filter R_C or V_I variability from PG. This result means that hypothesis 2 can be accepted.

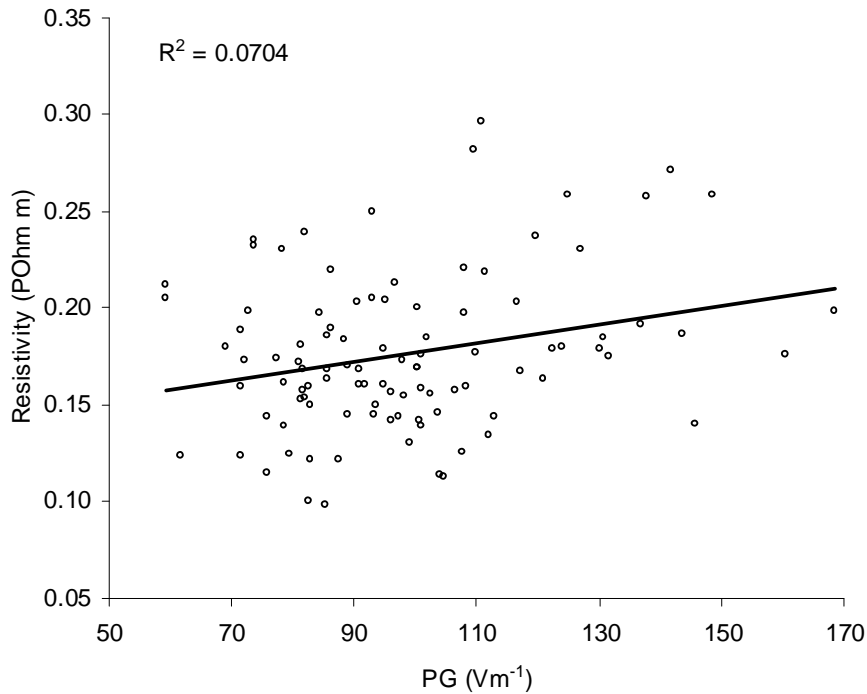


Figure 5.24 Resistivity (σ_T^{-1}) versus PG for July 2006. Values were chosen when J_C was approximately $\pm 5\%$ of the median, at $2.7\text{-}2.9\text{pA}\text{m}^{-2}$. PG values are five minute means corresponding to the time of σ_T , which represents an average of approximately 18 minutes.

A scatter-plot comparing fair-weather σ_T and J_C for July 2006 is shown in Figure 5.25. The values were chosen when PG was between $90\text{-}100\text{Vm}^{-1}$. It can be seen that there is no significant linear correlation between σ_T and J_C , unlike that expected from equation (5.3), therefore hypothesis 3 is rejected in this instance. This implies that the Ohmic assumption does not, on average, apply simultaneously at the surface and in the whole atmospheric column during the month, which is necessary for σ_T to be directly proportional to J_C for a constant PG. This result suggests that a satisfaction of Ohm's Law at the surface (i.e. PG variation proportional to that of surface resistivity) does not necessarily mean that it can be simultaneously applied to the atmospheric column (PG varying in accordance with J_C). Although hypothesis 3 should be accepted under strictly Ohmic conditions, this hypothesis is most sensitive to minor deviations from Ohms Law as it requires any change in surface conductivity (even if it only affected the immediate area of the field mill) to have a proportional effect on the entire atmospheric column, R_C . In reality, deviations in σ_T that cause a noticeable change in PG may be have a negligible effect on R_C (and therefore J_C) even if the variability of atmospheric electrical parameters can generally be regarded as Ohmic, as demonstrated by the acceptance of hypotheses 1 and 2. The different sensitivity of PG and J_C to changes in surface σ_T is why a vertical profile model requires at

least two resistors; one for the surface boundary layer and the other for the free atmosphere (Harrison and Bennett, 2007a, 2007b).

In addition to Ohmic (electrodynamic) generation of PG as J_C flows through a resistor, there can be an electrostatic component which by definition would be independent of any current flow. An example of this is the variation of PG due to the overhead passage of charged clouds (MacGorman and Rust, 1998) or local space-charge (Chalmers, 1967) which occurs independently of J_C variation and therefore violates the Ohmic assumption of equation (5.3). It is the presence of charged particles above the PG sensor that is expected to have caused the deviation from Ohm's Law during fair-weather, as the PG would have both electrodynamic (Ohmic) and electrostatic (non-Ohmic) sources.

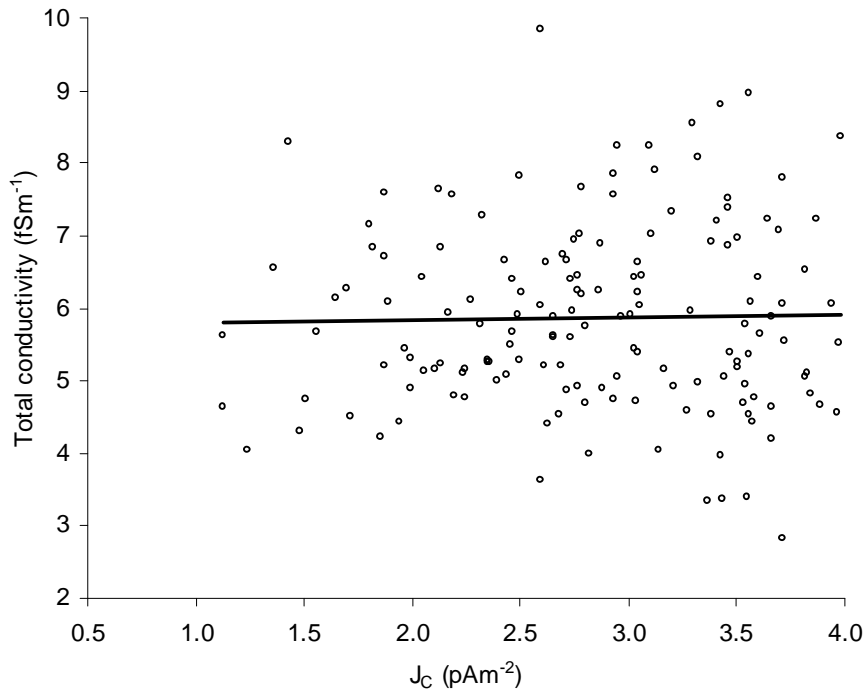


Figure 5.25 σ_T versus J_C for July 2006. Values were chosen when PG was approximately $\pm 5\%$ of the median, at $90\text{-}100\text{Vm}^{-1}$. J_C values are five minute means corresponding to the time of σ_T , which represents an average of approximately 18 minutes. R^2 value of 0.0004.

In summary, the Ohmic assumption that relates PG, J_C and σ_T measured at the RUAO during July 2006 can, on averaging timescales of one month, be applied separately to near-surface variability (PG varying in accordance with local air conductivity) and columnar/global variability (PG varying in accordance with J_C). Although PG variability is attributed to both J_C and σ_T , the main source of PG variability is J_C , due to the greater statistical significance. However, there is no evidence to suggest that the Ohmic

assumption applies simultaneously to both surface and columnar/global variability on monthly averaging timescales. It is suggested however that at times when local space-charge variability is low, allowing PG variation to be exclusively electrodynamic, the Ohmic assumption will apply to both local and columnar/global properties. A summary of results of the hypothesis testing is given in Table 5.5.

Ohmic Hypothesis	Result
$J_C \propto F \Big _{\text{constant } \sigma_T}$	Accepted
$F \propto \sigma_T^{-1} \Big _{\text{constant } J_C}$	Accepted
$J_C \propto \sigma_T \Big _{\text{constant } F}$	Rejected

Table 5.5 Results of the hypothesis testing for the validity of Ohm's Law in measured atmospheric electrical parameters at the RUAO during fair weather in July 2006.

5.6 Comparison between fair-weather atmospheric electrical and standard meteorological parameters

Hourly mean values of fair-weather atmospheric electrical (J_C , PG and σ_T) and standard meteorological parameters for 2006 were analysed. The standard meteorological parameters chosen were dry-bulb temperature (T_{dry}), relative humidity (RH), mean horizontal (non-directional) wind speed (U) and aerosol mass concentration. T_{dry} and RH were measured at the RUAO in a Stevenson screen, U measured by a cup anemometer positioned 2m above the ground. Aerosol mass concentration was measured by a laser photometer (Dust Trak) with an inlet tube positioned approximately 3m above the surface.

The correlation coefficients and their statistical significance for the hourly mean results for 2006 are shown in Table 5.6. The significance is calculated using Fisher's exact test (Fisher, 1922), which has the advantage of applying to small samples, regardless of the sample characteristics. However, the test assumes independency of each consecutive data point. Autocorrelation has been performed on the atmospheric electrical datasets used in this analysis and the independent assumption was found to be justified. It can be seen that with the exception of J_C versus U and aerosol, all correlations are significant at the 99% confidence level. The reason for these close correlations is expected to be due to all the parameters having a seasonal variation, which dominates the correlation results. For example, the high PG during the winter (due to increased aerosol number concentration and occurrence of fog) will correspond to a low dry-bulb temperature and produce a negative correlation. J_C and σ_T are relatively high in summer (Figure 5.18 and Figure 5.22) and so produce a positive correlation with temperature. Significant inter-

correlations between the meteorological parameters is seen (Table 5.7), which is reflected in the sign change of the correlations of Tdry and RH and the same sign for Tdry and U with atmospheric electrical parameters (Table 5.6).

	J_C	PG	σ_T
Tdry	0.121 (>99%)	-0.417 (>99%)	0.247 (>99%)
RH	-0.192 (>99%)	0.257 (>99%)	-0.168 (>99%)
U	-0.004 (16%)	-0.100 (>99%)	0.289 (>99%)
Aerosol	0.025 (64%)	-0.125 (>99%)	-0.145 (>99%)

Table 5.6 Correlation coefficients and corresponding confidence levels for hourly mean surface fair-weather atmospheric electrical and standard meteorological parameters during 2006. Tdry is dry bulb temperature, RH is relative humidity, U is mean wind speed at 2m and aerosol represents the aerosol mass concentration measured by the Dust Trak instrument. A total of 512 coincident data points for each parameter was used.

	Tdry vs RH	Tdry vs U	RH vs U	Aerosol vs Tdry	Aerosol vs RH	Aerosol vs U
Correlation (confidence)	-0.599 (>99%)	0.185 (>99%)	-0.337 (>99%)	0.222 (>99%)	0.051 (94%)	-0.342 (>99%)

Table 5.7 Correlation coefficients and corresponding confidence levels for hourly mean standard meteorological parameters used to compare against PG, J_C and σ_T during 2006.

In order to remove the dominant seasonal influence on the correlations, a shorter time period which would not be strongly affected by seasonal variability was used. The time period chosen was July 2006, which was the month containing the highest number of fair-weather atmospheric electrical recordings. As July is near the annual maximum of temperature, the daily variability in temperature is most likely to be dominated by diurnal variation than any underlying seasonal trends. The correlation coefficients for July 2006 are given in Table 5.8. In contrast to the correlations calculated for an annual time period, the monthly period shows more correlations below the 99% confidence interval. The majority of variation is expected to be diurnal or semi-diurnal for both the meteorological and atmospheric electrical parameters, as this has been shown by spectral analysis to be the dominant source of periodic variability at timescales less than one month.

	J_C	PG	σ_T
Tdry	-0.047 (83%)	-0.014 (32%)	0.318 (>99%)
RH	0.001 (2%)	0.020 (44%)	-0.178 (>99%)
U	-0.109 (>99%)	0.043 (79%)	0.304 (>99%)
Aerosol	0.001 (2%)	0.042 (67%)	0.058 (82%)

Table 5.8 Correlation coefficients and corresponding confidence levels for five minute mean surface fair-weather atmospheric electrical and standard meteorological parameters during July 2006. Tdry is dry bulb temperature, RH is relative humidity, U is mean wind speed at 2m and aerosol represents the aerosol mass concentration measured by the Dust Trak instrument. A total of 548 coincident data points for each parameter was used.

The diurnal variations of the meteorological and atmospheric electrical parameters during July 2006 are shown in Figure 5.26 and Figure 5.27 respectively. For the meteorological parameters, this variation can be explained by atmospheric boundary layer processes, with the governing source being changes to the surface long wave radiation budget. The vertical sensible heat flux near the surface is closely related to the temperature gradient between the ground and dry-bulb air temperature at Stevenson screen height (Bennett, 2004). The convection associated with the surface heating increases the depth of the boundary layer, with increased convection also increasing the mean wind speed (Stull, 1988). If the surface is dry (as is common during periods of extended fair-weather such as July 2006) then the increase in temperature will produce a corresponding decrease in relative humidity. Therefore, Tdry is inversely proportional to RH (Figure 5.26). The time of strongest convection typically occurs when near-surface air temperature (Tdry) is greatest, explaining the proportionality of Tdry with wind speed, U. As the boundary layer deepens, the upward ventilation of near-surface aerosol increases, causing the observed reduction in aerosol concentration (Figure 5.26).

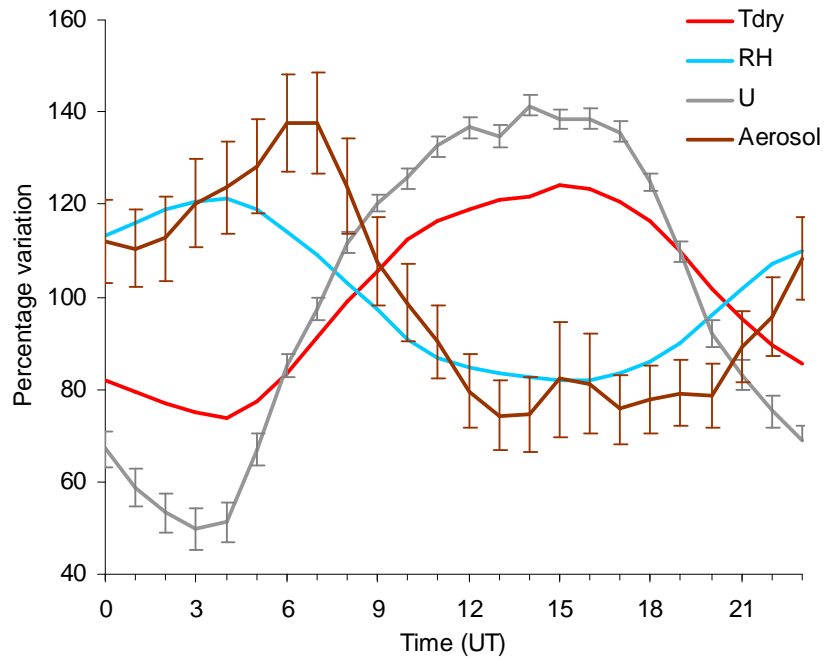


Figure 5.26 Mean diurnal variation of the standard meteorological parameters during July 2006, as a percentage of the mean. Standard error bars have been included for mean wind speed (U) and aerosol, but omitted from Tdry and RH due to their small size (<1%).

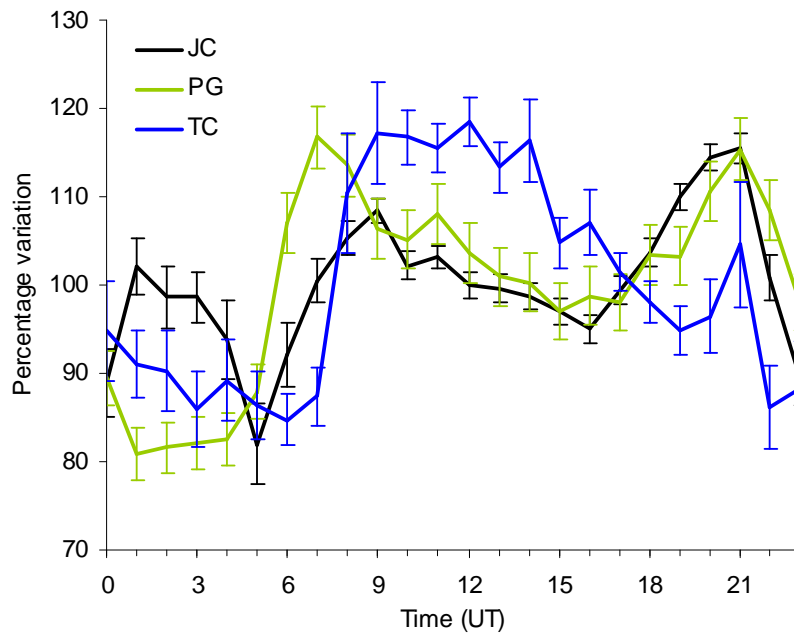


Figure 5.27 Mean diurnal variation of atmospheric electrical parameters during July 2006, as a percentage of the mean. Standard error bars included.

The diurnal variation of these meteorological parameters due to boundary-layer processes significantly influences the variation of total conductivity, σ_T . σ_T is governed by the ion-

balance equation which, over an urban surface, is dominated by the terrestrial ionisation rate (i.e. concentration of Radon gas) and aerosol number concentration. Both these factors will be influenced by boundary-layer convective motion, with a reduction in Radon and aerosol number concentrations occurring near the surface as convection intensifies. For an urban site such as the RUAO, the dominant source of ion number concentration variability (and therefore variability in σ_T) is likely to be aerosol number concentration, which reduces during the time of greatest convection (Figure 5.26). This inverse relationship is seen by comparison of the observed diurnal variations of aerosol mass concentration and σ_T (Figure 5.21b), despite the lack of a statistically significant correlation (Table 5.8), which will be discussed in greater detail later in this section.

Variability of PG is attributed both to local (σ_T) and global/columnar sources (J_C), so is not as dependent on boundary-layer variability as σ_T . The global component of PG variability explains the lower correlation between the PG and local meteorological parameters compared to σ_T . Although changes to the aerosol vertical profile will affect J_C , these changes are unlikely to be adequately represented by the surface meteorological observations alone, as demonstrated by the lack of significant correlation. The global source of J_C (and therefore PG) variability is the ionospheric potential (V_i) which will be independent of the surface meteorological values, contributing to the lack of significant correlation for J_C for Tdry, RH and aerosol. The only significant meteorological correlation for J_C was with mean wind speed, U (Table 5.8). During fair-weather, U increases with increased convective activity. This convection also increases the height of the boundary layer which will may also increase the amount of aerosol in the column, increasing R_C and lowering J_C . Although this would account for the negative correlation, it is not possible to test this hypothesis without data on the diurnal variation of the aerosol number concentration profile (not just surface parameters) at the RUAO. Similar results were found by Bhartendu (1971) and Israelsson and Oluwafemi (1975) who calculated coherence coefficient spectra between atmospheric electrical and standard meteorological parameters and found the maximum coherence was the diurnal component for all cross-comparison spectra.

To assess whether the meteorological parameters affect σ_T individually (and not just because they are a function of boundary-layer processes), the correlations for July 2006 were recalculated for σ_T keeping all but the parameter in question as constant as possible, to limit their influence. A suitably narrow range was chosen, incorporating the modal value for maximum number of available data points. The results of this is shown in Table 5.9.

	σ_T vs Tdry	σ_T vs RH	σ_T vs U	σ_T vs aerosol
Correlation (confidence)	0.108 (23%)	-0.188 (40%)	0.427 (93%)	0.049 (12%)

Table 5.9 Correlation between σ_T and isolated meteorological parameters for July 2006, with the remaining parameters set at a narrow range to limit their influence. These ranges were chosen to include the modal value, and were $20^\circ\text{C} < \text{Tdry} < 22^\circ\text{C}$, $6\% < \text{RH} < 67\%$, $2\text{ms}^{-1} < \text{U} < 3\text{ms}^{-1}$ and $10\mu\text{gm}^{-3} < \text{aerosol} < 15\mu\text{gm}^{-3}$.

From the results of the independent correlation analysis in Table 5.9, it appears that none of the meteorological parameters are correlated with σ_T with a confidence interval exceeding 95%. However, as aerosol number concentration is expected to be the governing factor that links meteorological diurnal variations with σ_T via the ion-balance equation, and appears negatively correlated in diurnal variation, the lack of a significant statistical correlation is investigated further.

The values for aerosol are specifically those of the aerosol mass concentration. However, it is the aerosol number concentration that is theoretically linked to σ_T through the process of ion-aerosol attachment. Therefore, a correlation between aerosol mass concentration and σ_T (as in Table 5.9) would only be expected to be significant providing the aerosol mass concentration is directly proportional to the number concentration. The validity of this assumption depends on the aerosol size distribution, with a direct proportionality existing only if this size distribution remains constant with time. Although it is not possible to directly assess this assumption with the available data, the variability of this size distribution can be limited by certain assumptions about what causes variability in the aerosol mass concentration. Figure 5.28 shows a histogram of aerosol mass concentration for July 2006 (the period under investigation). It can be seen that the histogram is strongly positively skewed. For the high mass concentration events, it is more likely that moderate amounts of additional large aerosol particles were present (such as dust) rather than an extreme excess of smaller ones required to generate the same increase in combined aerosol mass. However, although these episodes of increased amounts of large aerosol particles cause a significant increase in aerosol mass concentration, they may have little effect on aerosol number concentration (ultra fine aerosol is most abundant). This will produce a large change in aerosol mass concentration that may not be registered by σ_T as the number concentration was not significantly increased.

In order to minimise this suggested deviation of aerosol mass from number concentration, the data has been filtered to remove the effects of excessive mass concentrations (the

positive tail of the distribution), with only mass concentrations less than $30\mu\text{gm}^{-3}$ considered in the correlation. As can be seen in Figure 5.28, this represents 54% of the total values for July 2006. The correlations were recalculated (keeping other known sources of variability constant) and the results are shown in Table 5.10.

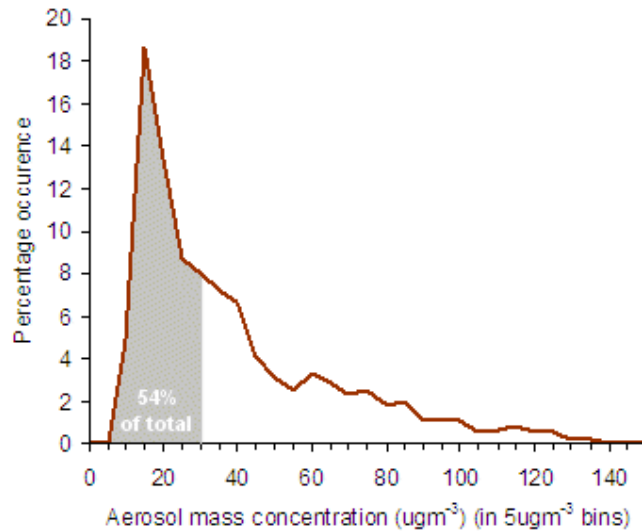


Figure 5.28 Histogram of aerosol mass concentration measured at the RUAO by the Dust Trak instrument for July 2006, with the aerosol mass $<30\mu\text{gm}^{-3}$ corresponding to 54% of total aerosol samples highlighted.

	0-30 μgm^{-3} Aerosol vs J_c	0-30 μgm^{-3} Aerosol vs PG	0-30 μgm^{-3} Aerosol vs σ_T
Correlation (confidence)	0.028 (37%)	-0.059 (16%)	-0.140 (>99%)

Table 5.10 Correlation coefficients for aerosol versus atmospheric electrical parameters during July 2006, using aerosol mass concentrations less than $30\mu\text{gm}^{-3}$. To test PG, J_c was kept between 2.2-2.4 pAm^{-2} and σ_T between 5-6 fSm^{-1} .

From Table 5.10 it can be seen that once the aerosol mass concentration has been filtered to remove events of high concentration (expected to depart significantly from the assumption of mass and number proportionality), the statistical significance for σ_T has increased to exceed the 99% confidence level. The negative correlation coefficient is expected, as increased aerosol concentration will reduce the concentration of small ions and therefore lower the conductivity. As with the correlation using all the aerosol data, there were also no significant correlations between J_c and PG with aerosol below $30\mu\text{gm}^{-3}$.

Summary of significant independent correlations

Independent correlations (i.e. correlation that exists when all other correlated variables are kept constant) have been investigated for atmospheric electrical (J_c , PG and σ_T) and standard meteorological parameters (Tdry, RH, U and aerosol). The total conductivity, σ_T , is the only electrical parameter that correlates with aerosol mass concentration, for concentrations below $30\mu\text{gm}^{-3}$ (expected to be most representative of the number concentration). This correlation is in agreement with the conclusion of Harrison (2006b) that σ_T can be used to estimate aerosol number concentration. Observed significant correlations of σ_T versus Tdry, RH and U are not valid independently, as their correlation is instead an effect of similar diurnal variability to aerosol. Although PG does not independently correlate with aerosol, its close correlation to σ_T means that it is likely to respond to a change in aerosol, although the form of the response will be dependent on any coincident change in J_c . Other than PG, J_c also correlates independently with mean wind speed, U. This negative correlation is suggested to be due to both parameters being related to boundary-layer convection. A summary of the significant (>95% confidence level) independent correlations is given in Table 5.11.

	J_c	PG	σ_T
J_c	-----	✓ +	✗
PG	✓ +	-----	✓ -
σ_T	✗	✓ -	-----
Tdry	✗	✗	✗
RH	✗	✗	✗
U	✓ -	✗	✗
Aerosol	✗	✗	✓ -

Table 5.11 Summary of significant (>95%) independent correlations (tick mark) for the atmospheric electrical and standard meteorological parameters investigated. The sign of the correlation (+ or -) is displayed next to the tick mark.

5.7 Disturbed-weather case studies

Fair-weather values of J_c , PG and σ_T have been investigated in regards to inter-correlations and correlations with standard meteorological parameters, and it is the fair-weather values that are used to create a climatology for the RUAO. However, the greatest variability in all three electrical parameters is often found during disturbed weather. This variability can be used to monitor and investigate meteorological process. The following section describes the variation of J_c and PG during fog, convective cloud and precipitation. Reliable measurements of σ_T have not been made using the PIMS during disturbed weather, due to leakage currents.

5.7.1 Fog

The presence of a layer of fog will have the same effect as an aerosol layer on the atmospheric electrical parameters (providing the fog is uncharged), as both are associated with the presence of suspended particles that remove small ions by attachment. The water droplets will remove ions by attachment and decrease the total conductivity, σ_T , which will produce a corresponding increase in PG for a given J_C . The effect of fog on J_C will largely depend on the fog depth, as J_C is dependent on the columnar resistance (R_C), not just changes in local conductivity. If the fog is shallow, then the effect on J_C is likely to be negligible in comparison to the change observed in σ_T and PG.

The effect of a shallow (100m) layer of fog on σ_T , PG (both 1m above the surface) and J_C is considered theoretically using the vertical profile columnar resistance model (chapter 3), as although the model is designed for fair-weather conditions, the presence of a neutrally-charged aerosol (fog) layer is within the modelling capabilities. The fog is modelled as an aerosol layer of uniform number concentration extending from the surface to 100m. This layer is superimposed on a typical fair-weather aerosol profile and the relative change in the parameters is calculated. The number concentration of the fog was chosen to reduce σ_T by approximately 20% in accordance with that observed in cloud (MacGorman and Rust, 1998).

Model output	Relative value due to fog, as % of the value for fog-free conditions
R_C	102%
J_C	98%
PG (1m)	434%
σ_T (1m)	22%

Table 5.12 Modelled atmospheric electrical parameters due to a 100m deep layer of fog, relative to the values for fog-free conditions.

From Table 5.12 it is shown that the introduction of a 100m deep aerosol layer representing fog has little effect on R_C and therefore J_C , but greatly increases PG in the fog (1m above the surface), for a chosen σ_T reduction to approximately 20% of the fog-free value.

Such a predicted increase in PG due to the presence of fog at the RUAO can be seen in Figure 5.29 (Bennett and Harrison, 2007b). Fog is present at the RUAO from 0800BST on 9 September 2005, with the dry-bulb temperature (T_{dry}) equalling the dew point temperature (T_{dew}). In the absence of droplet number density information the minimum of

T_{dry} is expected to be when the fog is most dense (Duynderke, 1991), which occurs at approximately 0820BST. This corresponds with the time of highest PG, as would be expected if the droplet (i.e. aerosol) number concentration increases, decreasing the conductivity (assuming J_C remains constant). As the fog thins (T_{dry} increases), the PG falls until the fog dissipates at approximately 0930BST, followed shortly by the air becoming subsaturated, identified by the divergence of T_{dry} and T_{dew}.

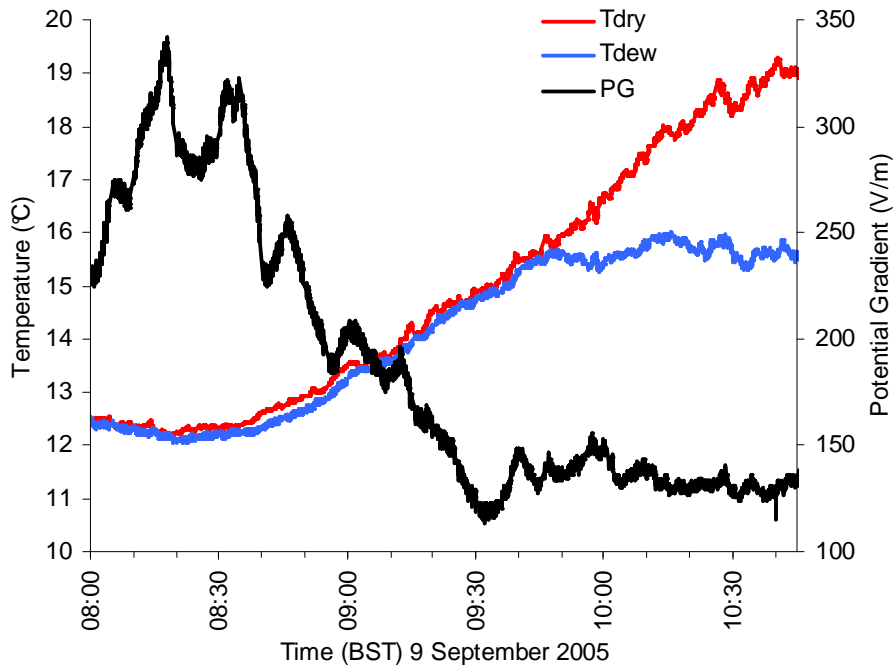


Figure 5.29 PG at the RUAO before and after fog (identified by the difference in dry-bulb and dew point temperatures, T_{dry} and T_{dew} respectively). Measurements were made every second (Bennett and Harrison, 2007b).

The RUAO experienced successive days of near-continuous fog during December 2006, with PG and J_C measured during the foggy period between 19-21 December 2006 shown in Figure 5.30a. The presence of fog is identified by the high relative humidity in Figure 5.30b, which indicates breaks in the otherwise continuous fog during approximately 00-06UT and 12-18UT on 19th. During these breaks in the fog, the PG reduces to fair-weather values ($\sim 200\text{Vm}^{-1}$) but is otherwise in excess of the 300Vm^{-1} designated upper limit of “fair-weather”, even reaching 800Vm^{-1} on occasions when the fog is likely to be thickest. The variability is also higher during the foggy conditions, with a mean sub-hourly standard deviation of 49Vm^{-1} , exceeding the typical fair-weather median of 11Vm^{-1} . Both an increase in the mean and variability of PG during fog has been reported in the past (e.g. Chree, 1919, Hoppel et al. 1986).

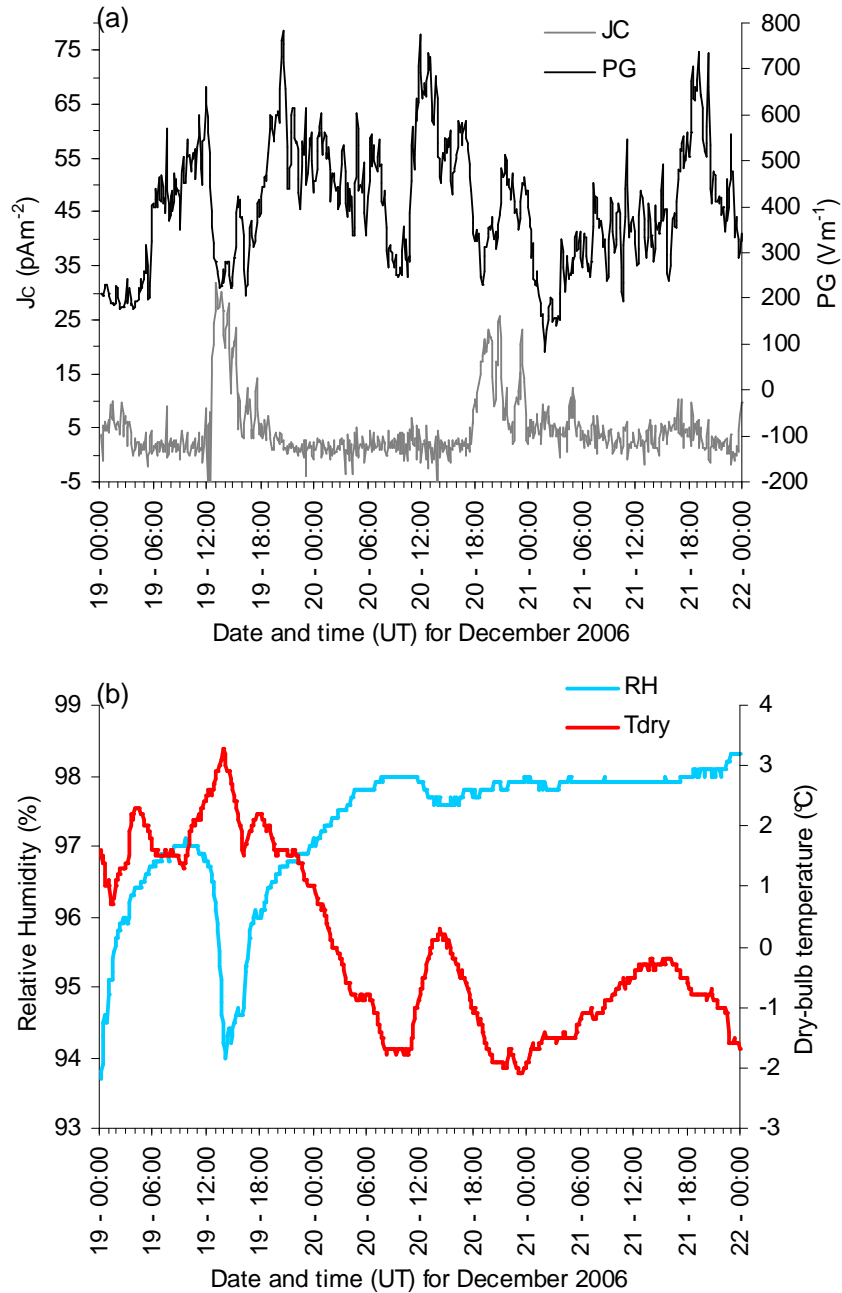


Figure 5.30 (a) J_C and PG during three days of near-continuous fog at the RUAO between 19-21 December 2006, with (b) corresponding Tdry and RH. Values are five minute means.

In contrast, the mean and standard deviation of J_C during this time is comparable to that of fair-weather, except during 12-18UT on the 19th and 18-23UT on 20th. These large deviations in otherwise fair-weather J_C are discussed later in this subsection. A positive, steady J_C during fog was also reported by Burke and Few (1978), with an increase before dissipation. Reason for this increase was suggested to be due to a reduction in R_C as the

fog layer thinned (Burke and Few, 1978), which implies their observation occurred during fog deep enough to noticeably effect R_C . Scrase (1933) also reported steady J_C during fog, but increased variability on some occasions during fog formation and dissipation.

The effect of fog on the distribution of PG and J_C measurements are shown in Figure 5.31. Comparisons of the histograms of J_C during the foggy period of 19-21 December 2006 indicate little change from the distribution of all fair-weather values made during 2006 (Figure 5.31a), except for higher occurrences of J_C between $3-7\text{pAm}^{-2}$, which is linked to the short but excessive increases in J_C seen in Figure 5.30a. The modal bin is 0.2pAm^{-2} lower for J_C during fog compared to the 2006 fair-weather distribution, suggesting a slight reduction in J_C during fog, in accordance with the predictions of the model.

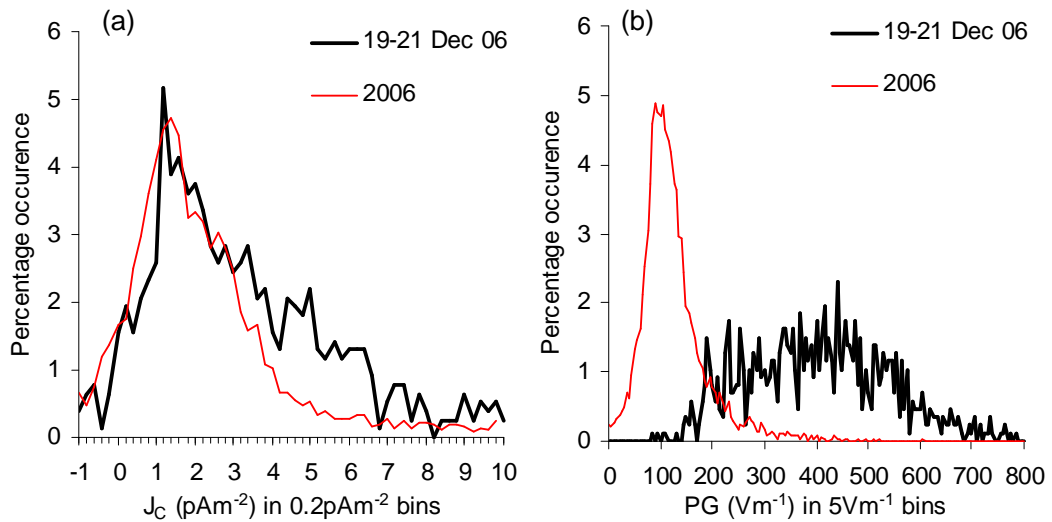


Figure 5.31 Comparison of histograms during the foggy days of 19-21 December 2006 with the mean histogram for 2006 for (a) J_C and (b) PG.

In contrast to the similarity between foggy and fair-weather conditions found for J_C , there is a marked difference in the distribution of PG measurements, seen in Figure 5.31b. The median value increases to approximately 400% of that for fair-weather. The broader PG distribution during the fog signifies the greater variability compared to fair-weather conditions.

The sharp increase in an otherwise steady J_C observed during 12-18UT on the 19th and 18-23UT on 20th begins during the dissipation of fog on the 19th, seen by the reduction in RH for this time in Figure 5.30b. It is unclear if the second increase on the 20th is also associated with fog dissipation, but may be more likely to have occurred during fog formation or thickening considering T_{dry} is reducing during this time. Usually such rapid

and excessive increase in J_C when precipitation is not present suggests an insulation failure, with associated leakage current. However, considering the two incidents occur in a period of otherwise good quality J_C measurements, the events are investigated further.

The J_C increase coincides with a rapid decrease in PG (due to fog dissipation) but the J_C change is in the opposite sense, so is not an effect of J_D and is too large to be associated with a coincident change in V_I . One possible reason for the rapid change of J_C is due to the presence of space charge (i.e. charged fog droplets). Although no space charge sensors were operational during the fog, there is a marked response in the passive wire (PW) during the times of J_C increase (Figure 5.32b). The PW often suffers from leakage currents during disturbed weather that prevent the wire from reaching the potential of the air. However, it is usually responsive to rapid changes in potential (i.e. will show a transient increase in potential during a rapid rise in PG, even if it is not capable of holding at the correct atmospheric potential). If the fog droplets were charged, then their charge would be transferred to the PW as they collide with the wire, changing the potential. The same effect may be seen in the J_C measurements as charged droplets collide with the collecting electrodes. The second J_C excursion (18-23UT on 20th) is associated with a decrease in the PW, not an increase like the first. One difference between the first and second events is that the first event occurred when T_{dry} was above 0°C, and the second when T_{dry} was below (Figure 5.32a). The GDACCS is heated so supercooled fog droplets will not freeze on contact, although the PW is not heated, so fog droplets below 0°C may freeze on contact. The phase of hydrometeors is expected to be associated with different charge polarity (Adkins 1959), so the difference in the response of the PG may be due to the temperature of the droplets impacting on the wire. To summarise, it is suggested that the rapid increase in current density measured by the GDACCS and PW during fog dissipation is due to the sedimentation of positively charged droplets onto the electrodes. However, when the droplets are below freezing (i.e. supercooled) they transfer a negative charge to the electrode as they freeze on contact with the metal if it is also below freezing (the unheated PW) but if not allowed to freeze on contact (such as for the GDACCS electrodes, which are heated), they transfer a positive charge.

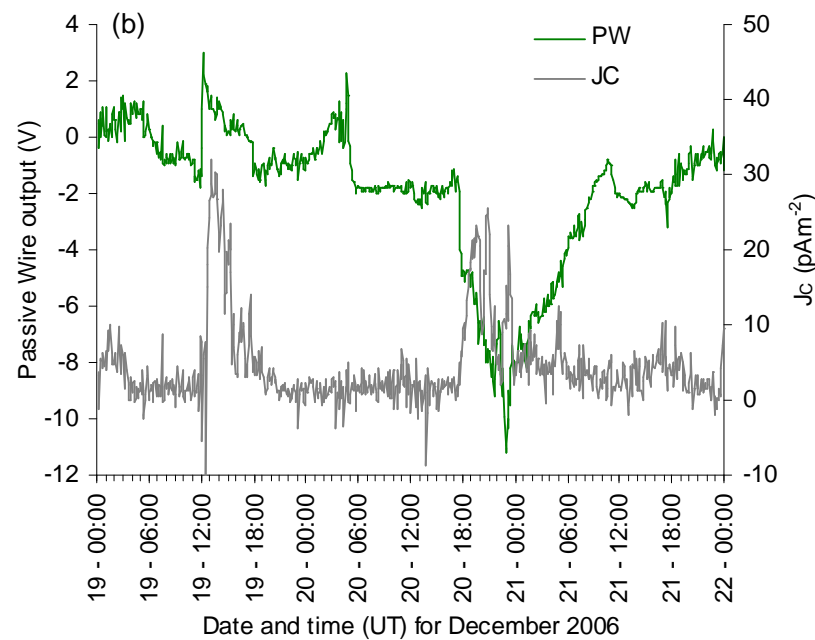
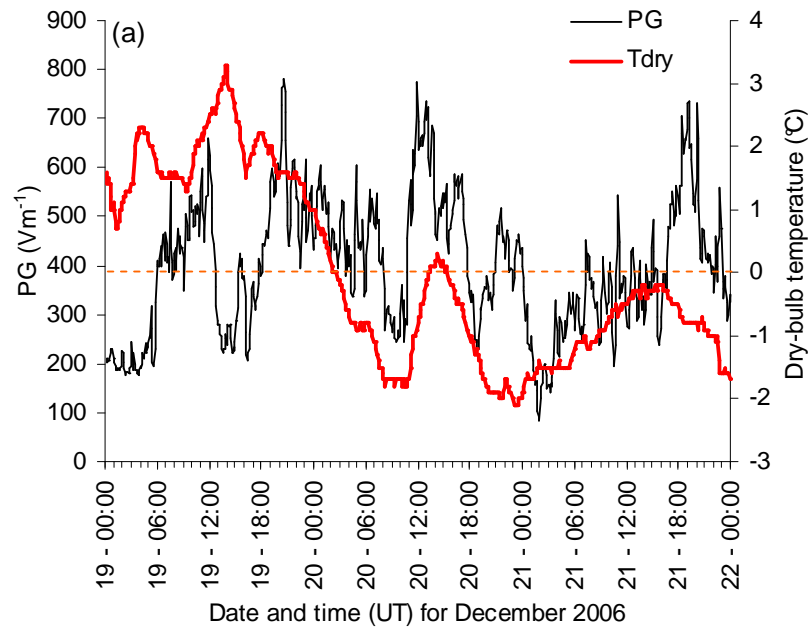


Figure 5.32 (a) Temperature and PG and (b) J_c and voltage on the passive wire (PW) during the foggy days of 19-21 December 2006.

5.7.2 Convective cloud

All cloud will have a distribution of charge within it due to the change in conductivity between clear and cloudy air causing sign-dependent ion concentrations at the cloud edges. Additionally, further charge separation occurs within the cloud that intensifies the charged regions, the details of which are discussed by MacGorman and Rust (1998).

Convective clouds generally are more charged than stratiform ones (MacGorman and Rust, 1998), with Cumulonimbus cloud generating a PG strong enough to cause electrical breakdown, seen as lightning. The cloud charges cause the PG to vary as they pass overhead, with the size of these rapid (order one minute) variations often exceeding the strength of fair-weather PG by an order of magnitude, and of both signs. The source of this change in PG due to charged cloud is therefore electrostatic, with a remote charge source, in contrast to the electrodynamic (i.e. Ohmic) mechanism that generates the fair-weather PG, resulting from J_C and σ_T . As such, Ohm's Law does not apply in this non-fair weather situation. An example of the rapid variation in PG during the passage of convective clouds over the RUAO (separated by periods of fair-weather) is shown in Figure 5.33. Convective cloud over land typically occurs in the afternoon, and it is these variations in PG from the passing of convective cloud that produces the greatest standard deviation in the PG diurnal cycle, seen in Figure 5.15.

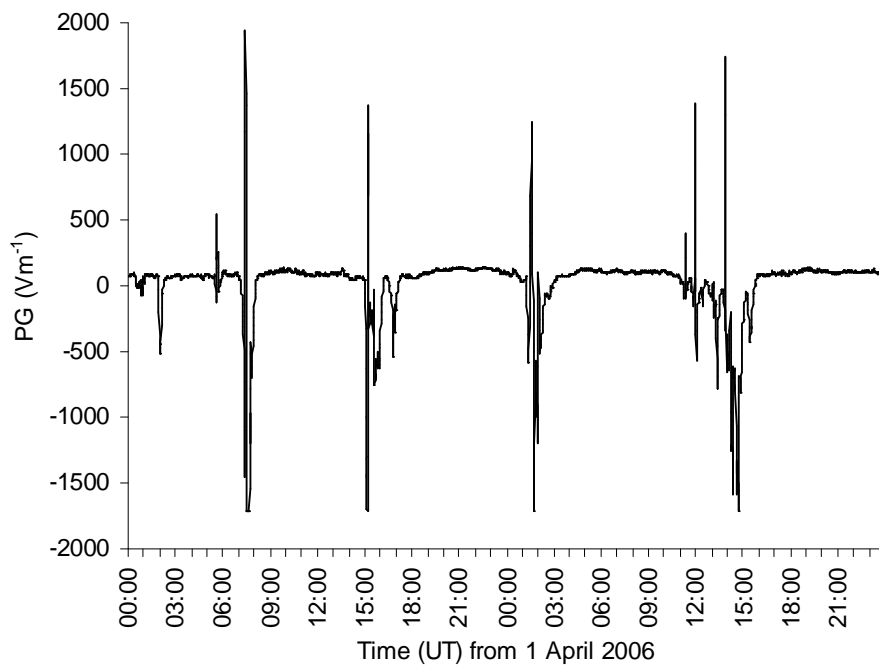


Figure 5.33 PG (as 1minute means) during the passage of convective clouds over the RUAO, separated by periods of fair-weather, between 1-2 April, 2006.

Effect of lightning on PG

In addition to changes in PG due to charge regions within clouds, lightning discharges also cause rapid (order seconds) and characteristic fluctuations in PG (Figure 5.34). As the actual lightning stroke lasts for less than one second (MacGorman and Rust, 1998) the observed change in PG results from the redistribution of charge within the cloud (and

ground). An initial increase in PG implies removal of negative charge above the sensor (negative polarity lightning), with a positive strike causing the PG to rapidly decrease initially, before returning to a similar value as before the strike over approximately 2 minutes. A detailed account of PG changes due to lightning is provided by MacGorman and Rust (1998).

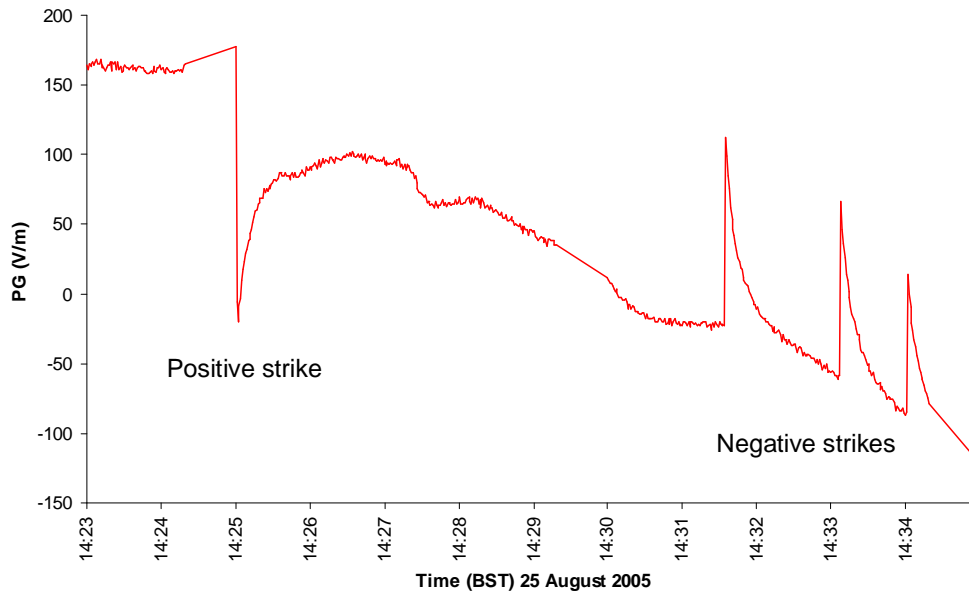


Figure 5.34 PG during positive and negative polarity lightning, near to (order 10km) the RUAO on 25 August, 2005.

PG and cloud radar observations

In order to further investigate rapid PG change resulting from the overhead passage of cloud, a JCI 131 electrostatic field mill was mounted on top of a meteorological mast, calibrated at the RUAO to measure PG at 1m. The mast was installed approximately 100m from the cloud radars at Chilbolton in Southern UK (51.144°N, 1.437°W). More information on this radar facility can be found at www.met.rdg.ac.uk/radar/chilbolton.html. The field mill can be seen installed near the 25m diameter dish of the large 3GHz Chilbolton Advanced Meteorological Radar (CAMRa) in Figure 5.35. The actual radar used for this investigation was the much smaller 35GHz Cloud radar (Copernicus) located adjacent to the CAMRa identified in Figure 5.35. The cloud radar measures the “radar reflectivity factor” which is proportional to the sixth power of particle diameter. Therefore higher values of radar reflectivity factor indicate larger particles. These large particles may be either cloud droplets or hydrometeors (raindrops or large ice crystals). The radar reflectivity data was provided by Ewan O’Connor, Reading University.



Figure 5.35 Field mill measuring PG positioned approximately 100m from the Chilbolton cloud radar facility. Picture taken by Stephen Gill.

The effect of the overhead passage of an isolated shallow Cumulonimbus cloud on the PG is seen in Figure 5.36. From the coincident values of cloud radar reflectivity (provided as time-height plots) it is observed that PG reaches a minimum when the cloud is directly overhead. There are two maxima in PG that occur immediately before and after the minimum. These occur when the edge of the cloud is overhead. A possible explanation for this PG pattern is that the cloud contains a vertical charge dipole, with a negative charge at the cloud base and positive near the cloud top. Such an arrangement would cause the PG to rise as the cloud nears the surface observation point, as the influence of the positive top is felt before and after the negative base. The negative base then becomes more dominant as the cloud is directly overhead, due to its closer proximity to the surface. The ratio of PG maxima to minima will depend on the relative magnitudes of the charge regions and their vertical separation, allowing basic information on charge distribution within a cloud to be gained from PG variation as it passes overhead. Gherzi (1967) used vertical pulses of 3cm wave band radar to investigate the pronounced and rapid changes in PG due to the overhead passage of convective cloud. The investigation showed that clouds with a large radar reflectivity factor (due to suspended rain droplets within the cloud) also produced a prominent change in surface PG, and that the radar pulse itself did not affect the measured PG (Gherzi, 1967).

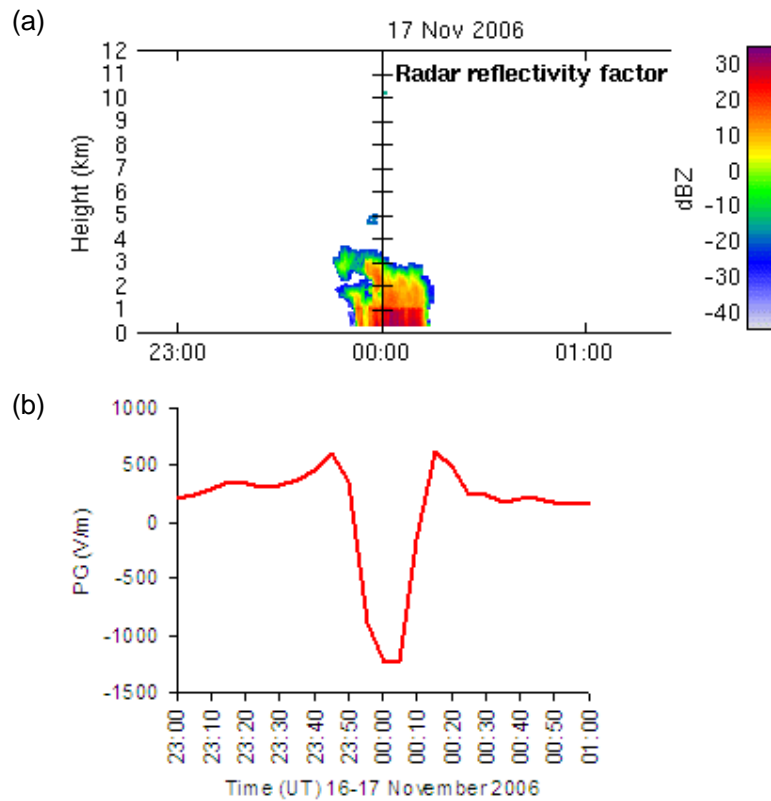


Figure 5.36 (b) PG (5min means) during the passage of an isolated shallow Cumulonimbus cloud identified by (a) the cloud radar reflectivity factor (the intensity of radar signal reflected from the cloud droplets) over the Chilbolton Observatory around midnight 17 November 2006.

Modelling charge distributions within a cloud

A simple electrostatic model has been used to reproduce the PG at the surface below an isolated Cumulonimbus cloud that passed over the RUAO on 28 July 2005 (Bennett and Harrison, 2007b), using Maxwell SV, the same commercially available electrostatic modelling software package used to model PG and J_C around the J_C sensors. This allowed the location and size of charged regions within the cloud to be investigated, by determining the simplest charge arrangement that would produce the observed change in PG. A uniform cloud velocity over the site, and no temporal change in charge structure during the surface observations was assumed. Cloud base and height were estimated from radiosonde ascents.

The two-dimensional representation of the cloud used consisted of two square charged regions adjacent to each other at 500m above the surface, with sides of 500m length and charge +0.20mC and -0.22mC. A further charged region of the same dimensions and -0.15mC was placed 2500m vertically above the top of the positive cloud base region to represent charge near the middle of the cloud. Although the cloud top was also likely to be

charged (MacGorman and Rust, 1998), the approach adopted was to seek the simplest charge structure to represent the observed PG change as the cloud passed over. The effect of charges located at greater heights was neglected, as these would have less effect on the surface response. A background PG of 100Vm^{-1} was assumed. Figure 5.37a shows the charge distribution assumed for the cloud.

The comparison between the observed PG and that predicted using the electrostatic model is given in Figure 5.37b, which shows good agreement between observed and modelled PG changes. It indicates that the variation in PG is consistent with a tri-polar charge structure within the cloud, unlike the cloud in Figure 5.36, which associated PG variation could be explained by a vertical dipolar arrangement. However, in Figure 5.37 at approximately 10.5km on the x -axis scale, the observed PG deviates significantly from the model. This appears to have been due to rainfall, which occurred as the cloud passed over the PG sensor. Since the rain drops falling were charged, the rainfall further modified the charge distribution within the cloud with time. PG perturbations will also have resulted from the charged rain beneath the cloud base. Convective rainfall has generally been observed to cause rapid fluctuation in PG and will be discussed in a later section.

Modelling of the likely location and charge of different regions with a convective cloud provides a new method of inferring cloud properties from the surface, under suitable assumptions for the cloud evolution, cloud extent and cloud propagation speed.

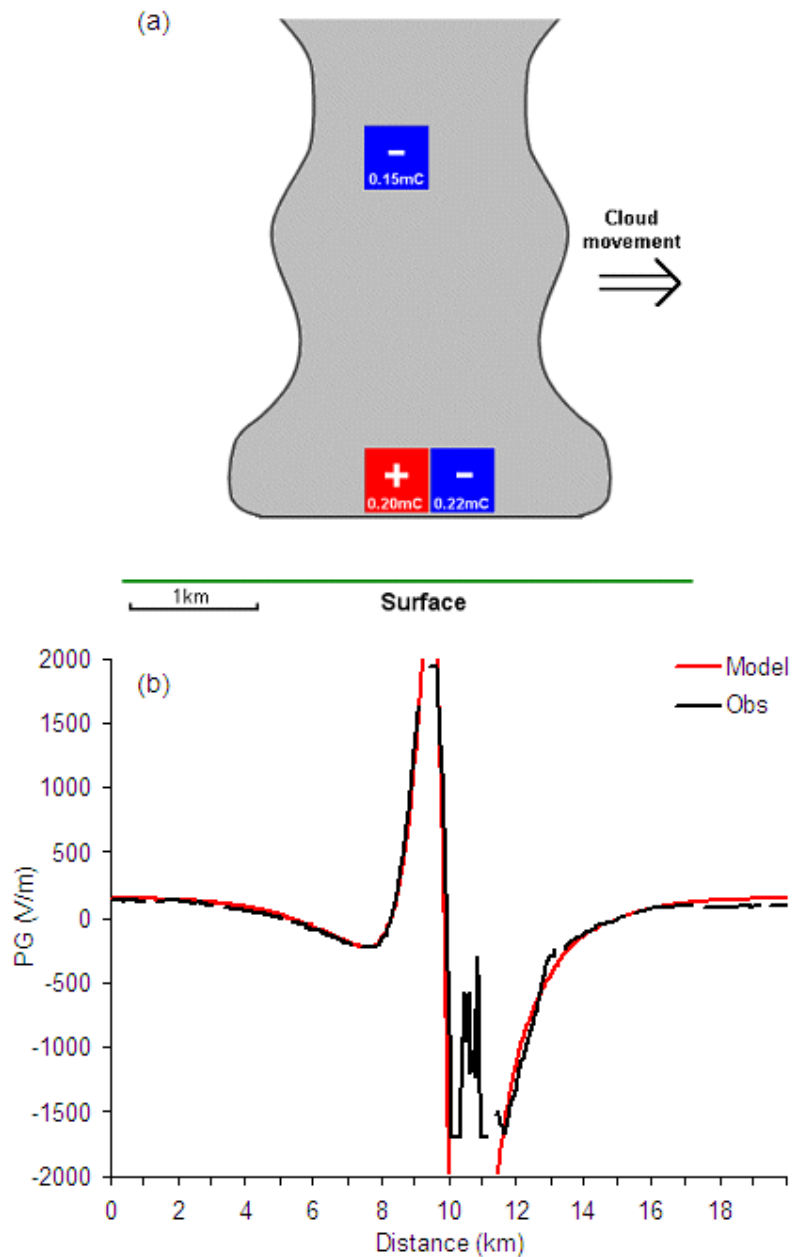


Figure 5.37 (a) Schematic of the modelled charge distribution of an isolated Cumulonimbus cloud that passed over the RUAO on 28 July 2005, with (b) a comparison between modelled and observed PG at 1m. The x-axis “horizontal distance” represents the location of the cloud when PG observation began, found by converting the measurement times to distance, assuming a constant cloud speed of 8.3ms^{-1} (Bennett and Harrison, 2007b).

During more complex cloud structure situations than that of an isolated Cumulonimbus cloud, the PG is observed to vary rapidly in both positive and negative directions on successive occasions as multiple charge structures associated with a variety of different cloud cells passing in close proximity. An example of complex PG perturbations occurred when cold, warm and occluded fronts (with associated cloud structures) passed over the

Chilbolton Observatory between 19-20 November 2006 in close proximity to each other, as shown in Figure 5.38.

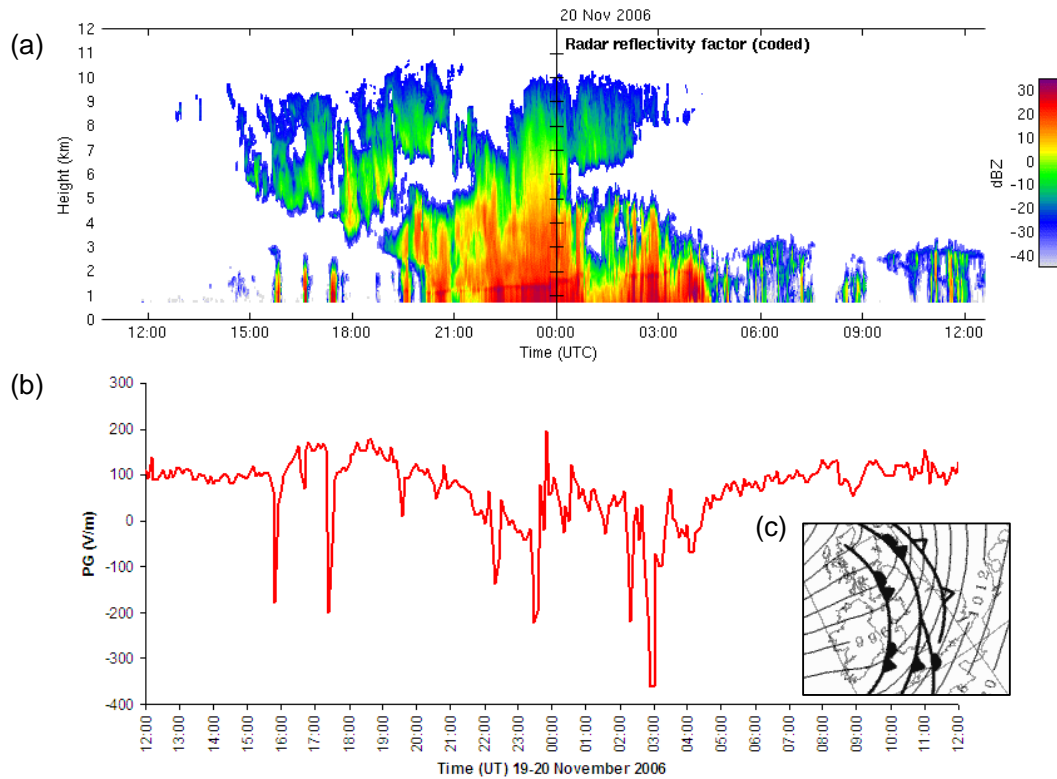


Figure 5.38 (b) PG (5min means) during the passage of a complex cloud structure identified by (a) the cloud radar reflectivity factor over the Chilbolton Observatory between 12UT on 19 and 12UT on 20 November 2006. The complexity was caused by the arrival of multiple fronts during this time, identified in (c), the section of UK Met. Office synoptic chart for midnight on 20 November 2006.

5.7.3 Precipitation

In addition to charged regions within clouds, precipitation is also charged (MacGorman and Rust, 1998) and therefore will affect the PG. The phase of the precipitation (i.e. rain or snow) is often associated with a difference charge sign. As described by Adkins (1959) dry snowflakes are usually negatively charged and therefore cause the PG to increase as negative charge is brought to the surface. Rainfall and wet snow is found to be generally positively charged, bringing positive charge to the surface and lowering the PG. In both cases, increased precipitation rates will produce larger deviations in the PG (Adkins, 1959). An example of the effect of rainfall on the PG is seen in Figure 5.39. The PG is at fair-weather values before the arrival of the rainfall at 1030UT on 22 September 2006 (mean of 173Vm^{-1} with a standard deviation of 18Vm^{-1} between 0900-1030UT). The rainfall was measured by a tipping-bucket rain gauge, and remained steady and moderate

(approximately 1.5mmhr^{-1}) between 1030 and 1400UT. During this time the PG is negative (mean of -145Vm^{-1}) and the standard deviation increases to 134Vm^{-1} . The moderate rainfall turns heavier between 1400 and 1500UT (13.7mmhr^{-1} average). During this period of heavier rainfall the PG fluctuates rapidly in both signs (standard deviation of 1189Vm^{-1}). When the rainfall becomes light between 1500-1600UT (0.8mmhr^{-1} average) the PG still displays large, rapid fluctuations (standard deviation of 984Vm^{-1}). This implies that the rapid fluctuations of PG observed between 1400-1600UT are more a result of charged regions within the cloud and not of the precipitation itself, as the standard deviation of PG was similar for both the heavy and light rainfall times. A further oscillation in PG was observed around 17:00UT, but no rainfall was detected. This suggests a non-precipitating cloud passing overhead during this time, possibly of a tripolar charge structure as the oscillation looks similar to that of Figure 5.37.

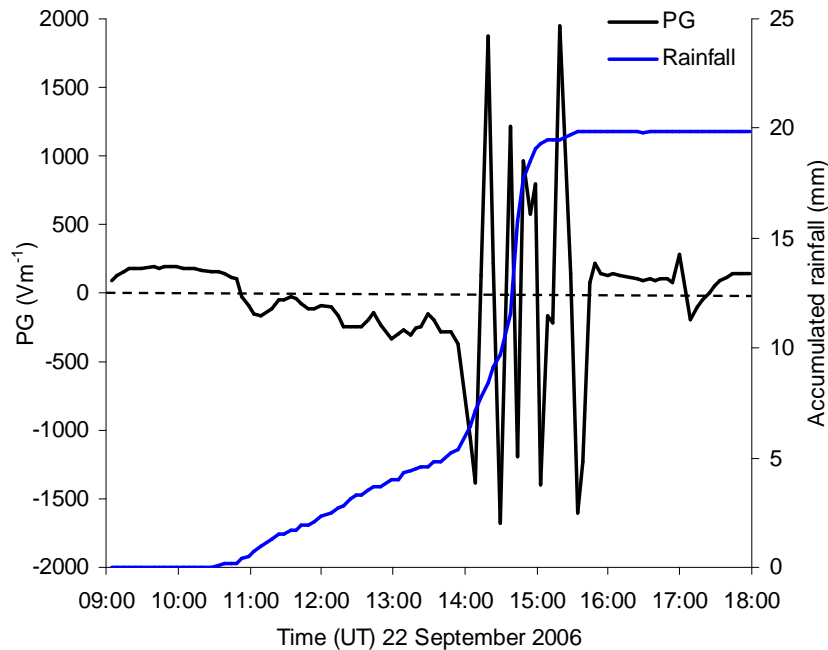


Figure 5.39 PG and accumulated rainfall amount at the RUAO during steady moderate rainfall (1030-1400UT) and heavy rain (1400-1500UT) on 22 September 2006. Data are five minute means.

In accordance with the observations of Adkins (1959) and Gherzi (1967), the PG was seen to increase during a snow shower at the RUAO on 28 February 2006 (Figure 5.40). Global shortwave solar radiation (S_g) is used as an indicator of the time of maximum snowfall, which would lower the radiation intensity as the snowflakes reflect some of the short wave solar radiation before reaching the sensor. The heavy snow shower was observed to occur between 1530-1533 UT, with the heaviest fall occurring at the time of lowest S_g , which corresponds to the time of maximum PG. The standard deviation of PG

during the snow shower is lower compared to that during the rain shower in Figure 5.39 (Bennett and Harrison, 2007b). This is suggested to be due to three reasons;

- The fall speed of the snowflakes will be considerably lower than that of rain drops, so high frequency (order seconds) variation would be smoother compared to more rapid changes in intensity compared to rainfall.
- As the snowflakes will take longer to fall from the cloud base to the surface, they have more time for charge exchange with the air (and possibly each other) which may promote a more uniform charge per snowflake (and therefore less charge variability reaching the surface) compared to rain drops, which will have less time for charge modification.
- By the time the snow reaches the surface, the parent cloud (or at least the region of greatest charge density) may have moved sufficiently away from the overhead direction to not cause rapid PG distortions, as seen superimposed on the PG variation due to rainfall in Figure 5.39.

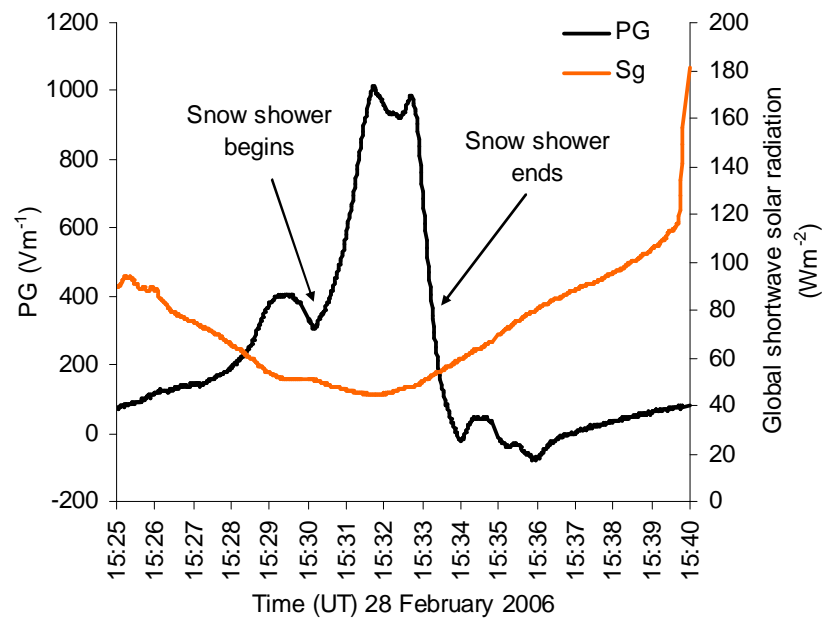


Figure 5.40 PG and global shortwave solar radiation (Sg) during a snow shower between 15:30 and 15:33UT on 28 February 2006 (Bennett and Harrison, 2007b).

5.8 Discussion

A climatology of atmospheric electrical parameters at the RUAO has been presented for 2006. Diurnal cycles of fair-weather PG, J_C and σ_T for annual and seasonal timescales have been produced, all of which are likely to be influenced by either local, columnar or global meteorological variations. Ohm's Law was found to be obeyed (on average) during fair-weather independently near the surface and for the atmospheric column. The presence of space charge was a suggested reason for Ohm's Law not being observed, affecting the value of surface PG independently of that due to Ohmic processes. During disturbed weather, the PG was observed to vary greatly (by an order of magnitude) due to the overhead passage of convective cloud, with precipitation also producing weaker changes. Rainfall was observed to produce a different characteristic PG than snowfall, with steady rain generally associated with negative PG and snowfall producing a strongly positive PG. The presence of fog increased PG to approximately 400% of fair-weather values and increased the variability. However, there was negligible change in J_C during fog compared to fair-weather, except for short periods expected to be during fog dissipation, when space charge carried by fog droplets was inferred to cause an increase in the observed current density. The next chapter compares measured PG and J_C with both the Carnegie curve and coincident measurements made at remote sites to assess the influence of global sources on PG and J_C variability.

6 Observation of the global atmospheric electric circuit

6.1 Introduction

Measurements of PG and J_C provide an opportunity to monitor the intensity of global thunderstorm activity from one point on the Earth's surface, through the global electric circuit. However, variability in these measurements can not usually be attributed only to the global circuit, but also to changing meteorological conditions, such as those that affect the aerosol number concentration vertical profile. These local sources of variability in J_C and PG often dominate measurements made at urban sites, as identified in chapter 5.

To observe variability attributed to more global sources, a site with low variability in meteorological conditions known to affect surface J_C and PG must be used. As the aerosol number concentration is often the dominating source of local variability (Alderman and Williams (1996), Harrison and Ingram (2005)), a globally-representative site is usually one of consistently low air pollution (and therefore low variability) such as oceanic, arctic or mountain observatories (Chalmers, 1967). The low-pollution site used for this investigation will be Lerwick, in the Shetland Islands of Scotland. This site has a record of hourly J_C and PG measurements over several years during the 1960s to early 1980s. Air pollution is low due to its remote location away from any large settlements and surrounded by the Atlantic Ocean, making it ideal for investigation of global sources of surface electrical variability.

In addition to analysis of data from the low-pollution site of Lerwick, an attempt will be made to retrieve the diurnal cycle of ionospheric potential (i.e. the global circuit) from measurements made at a relatively polluted urban site (the RUAO), using the columnar resistance model to account for both measured and estimated boundary-layer diurnal variation.

J_C is considered as the parameter measured at the surface that is most representative of the global circuit (e.g. Chalmers (1967), Dolezalek (1978)). This is because fair-weather J_C is a function only of R_C and V_I (the latter being the intensity of the global circuit), whereas PG has the additional dependence on local σ_T . The hypothesis that J_C is a more globally-representative parameter than surface PG will be investigated, including whether PG at an urban site can be used to represent global circuit variability at all.

When comparing the diurnal variation of J_C and PG to the Carnegie curve in order to quantify the degree of global circuit representation, only averaged data of at least one month shall be used, as the Carnegie curve is not necessarily representative of global variation during any particular day (Dolezalek (1972) and observational evidence presented by Harrison (2004b)).

To assess global circuit variability at timescales less than one month, comparison of surface PG measured simultaneously at different measurement sites will also be made. This will test whether similar PG variations to the RUAO are observed at three other stations 47km, 118km and 1370km from the RUAO. Apart from global variations in V_I , PG will only be affected by the local variability in surface total conductivity of the immediate (order metres) vicinity of the PG sensor, or from the atmospheric column immediately above the sensor. This means that any coincident PG variability between the different sites would be due to common variability of the global circuit (V_I), providing coincident local variation can be neglected. Long-range correlations in coincident measurements of the global atmospheric electric circuit have previously been found by Anderson (1967) and Harrison (2004b) and attributed to the universal variation in V_I .

Three methods will therefore be used to investigate variations of the global circuit. These are (1) using PG and J_C variation at a single low-pollution site, (2) measurements of PG, J_C and aerosol mass concentration at a polluted site combined with an R_C model to separate local and global sources of variability and (3) the use of two sites several kilometres apart to detect coincident variations from a common global source.

6.2 Diurnal variations of fair-weather PG and J_C at Lerwick

Lerwick is a small town on the Shetland Islands, Scotland (60.1°N, 1.2°W), approximately 970km North of the RUAO. The remoteness of this island location means that the site has low concentrations of air pollution and therefore may be considered as a globally-representative site (Harrison, 2003). Details of this Met. Office site at Lerwick including measurement and atmospheric electrical apparatus for PG are given by Harrison (2003).

Potential gradient

The mean diurnal variations of Lerwick PG 1968-1973 and the standard Carnegie curve (Gish, 1939) are shown in Figure 6.1. It can be seen that the variation of the two curves are in close agreement (correlation coefficient r of 0.965) although the mean value of PG at Lerwick exceeds that of the Carnegie by 21Vm^{-1} .

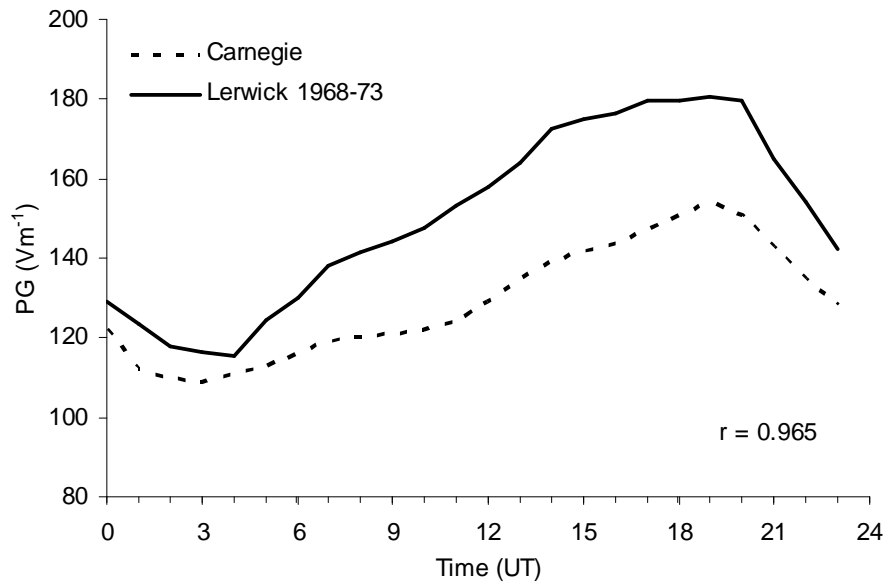


Figure 6.1 Comparison of mean diurnal PG measured at Lerwick during 1968-73 and that of the standard Carnegie curve (adapted from Harrison, 2003).

The higher PG at Lerwick compared to Carnegie may be attributed to a difference in ionospheric potential (V_i) between the duration of the Carnegie Cruises (1915-1921 and 1928-29) and the Lerwick data (1968-73). J_c that ultimately drives fair-weather PG is a function of geomagnetic latitude (higher towards the poles), so the geographic position of Lerwick and the Carnegie cruises may also have contributed to this difference. Another suggestion to the source of the higher PG is that the mean aerosol number concentration was greater in Lerwick than during the Carnegie cruises. This is a likely explanation for at least a component of this difference as the Carnegie was in the open ocean, well away from land and associated sources of pollution. Although Lerwick is considered a clean-air site compared to other land stations, a small amount of locally generated aerosol and pollution advected from the mainland is likely. Using the columnar resistance model for 60°N and assuming cosmic radiation as the only source of ionisation (away from land-based sources of radioactive gasses) a surface PG difference of 21Vm^{-1} would equate to a 25% increase in surface aerosol number concentration (1480cm^{-3} from 1180cm^{-3}), for an ionospheric potential of 250kV. This represents a small absolute change in aerosol number concentration so it is not unreasonable to expect that such a difference would exist between Lerwick and the open ocean.

Considering the diurnal variability as a percentage of the mean, the relative variability at Lerwick can be directly compared to the Carnegie. Figure 6.2 shows the difference between Lerwick and Carnegie PG percentage variability. It is evident from this that the

Lerwick PG was proportionally lower during the night and higher during the daytime compared to the Carnegie.

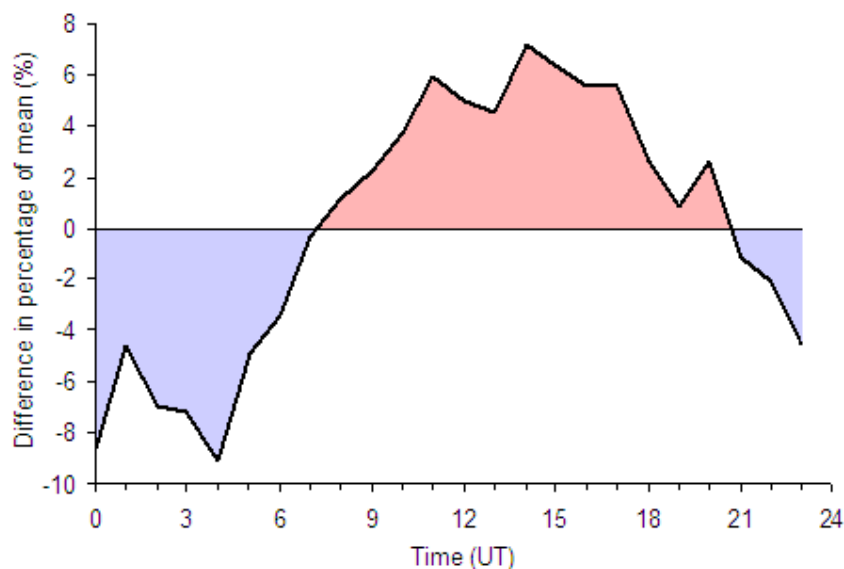


Figure 6.2 Difference between Lerwick and Carnegie PG diurnal variation, as a difference in percentage variation from their respective means.

The time of maximum and minimum percentage difference between Lerwick and Carnegie PG are 14UT and 04UT respectively. These times coincide with times of maximum and minimum air temperature at Lerwick, which would suggest a local (boundary-layer) influence on Lerwick PG in addition to the global signal, or uncorrected thermal drift in the instrumentation. However, the deviation in diurnal variability from the Carnegie is small (<10%) and a clear association with the globally-representative Carnegie curve is found in the PG measurements of this relatively unpolluted site. Further analysis of the Lerwick PG data, including monthly and annual variations are discussed by Harrison (2003).

Conduction current density

In addition to PG measurement, the Lerwick site measured J_c directly using a horizontal plate collector. Measurement of J_c began later than PG, with the first complete year of tabulated observation being 1979, with 1983 being the last (although paper-tape records began in 1969). The mean diurnal variation of Lerwick J_c between 1979-83 is shown in Figure 6.3.

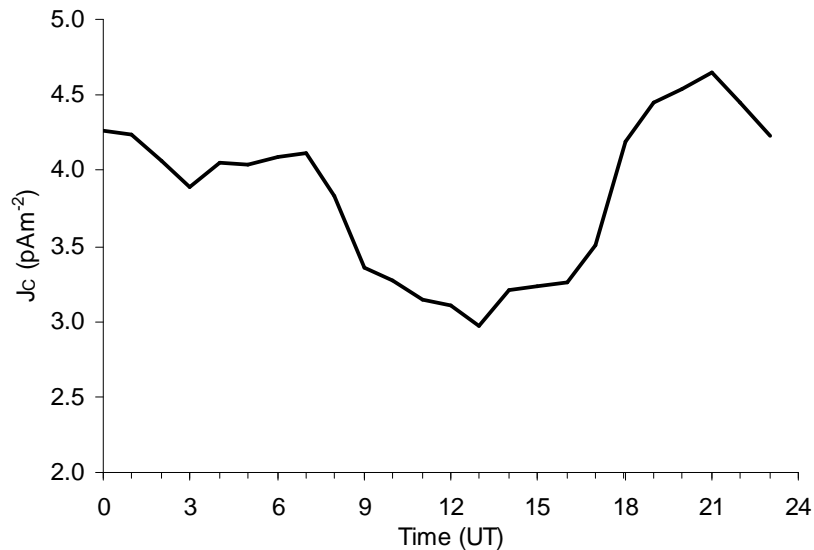


Figure 6.3 Mean J_C diurnal variation for Lerwick between 1979-1983.

Unlike PG, the mean diurnal variation of Lerwick J_C does not resemble that of the standard Carnegie curve. Additionally, the mean J_C is somewhat high compared to the six year mean of 2.44pAm^{-2} measured at a relatively unpolluted (although continental) site of similar geomagnetic latitude (Israelsson and Tammet, 2001). A possible explanation for the lack of a correlation between Lerwick J_C and the Carnegie and the anomalously high mean is that the instrument suffered from leakage currents. The most likely occurrence of leakage currents would be during the night, when the relative humidity is high and dirty or bridged insulators would absorb water and permit a leakage current to flow to (or from) the collecting plate. The increased J_C during the night and minimum value around the expected time of lowest humidity during the early afternoon suggests this may be a likely explanation. The mean Lerwick PG diurnal cycle between 1979-83 closely follows the Carnegie curve (like that during 1968-73, Figure 6.1). Assuming no coincident local sources of variability exists, the variation of the PG is therefore expected to have changed in accordance with Ohm's Law through changes in J_C . Considering PG follows the Carnegie curve but J_C does not implies that the diurnal cycle of J_C is incorrect, since it is the source of Ohmic PG variability. The relative deviation of the J_C diurnal cycle from that of the PG during the same time (1979-83) is shown in Figure 6.4. From this figure it is seen that J_C is too low during the day and too high during the night, in accordance with that expected by humidity-dependent leakage currents. From the anomalously high mean J_C , it appears more likely that J_C is always too high due to leakage, but even more so during the higher nocturnal relative humidity. Unlike the minor deviation of PG from the Carnegie curve, the J_C diurnal cycle differs by up to $\sim 30\%$, making the Lerwick J_C

measurements unsuitable for estimation of the global circuit diurnal cycle, due to suspected leakage currents.

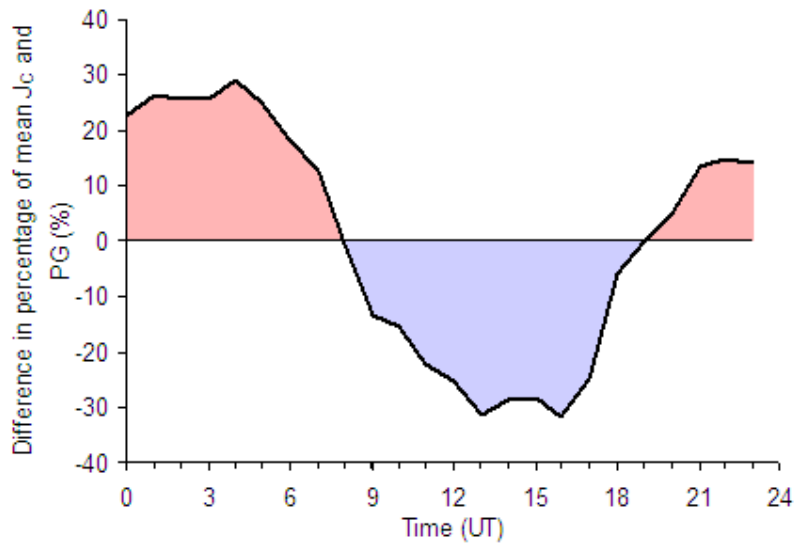


Figure 6.4 Difference in J_C and PG diurnal variations for Lerwick, between 1979-1983. Values expressed as a difference in percentage variation from their respective means.

6.3 RUAO fair-weather PG and J_C diurnal cycles compared to those of the Carnegie

The Reading University Atmospheric Observatory (RUAO) is an urban site within a large town. Therefore the site would not be considered as unpolluted enough to be globally representative. However, under certain conditions when the aerosol number concentration or ionisation rate vertical profiles do not vary considerably with time, variations in J_C and PG may well exhibit global characteristics. This section compares the mean fair-weather diurnal cycles of PG and J_C with the Carnegie curve to identify times (both sub-diurnally and seasonal) when more globally representative signals can be found.

Potential Gradient

The mean diurnal variation of fair-weather PG during 2006 is compared to the standard Carnegie curve, both as percentages of their respective means, in Figure 6.5. Despite some obvious deviations, the RUAO mean diurnal cycle shares the same minimum and maximum times as the Carnegie, although a distinct double-peak exists in the RUAO PG variation.

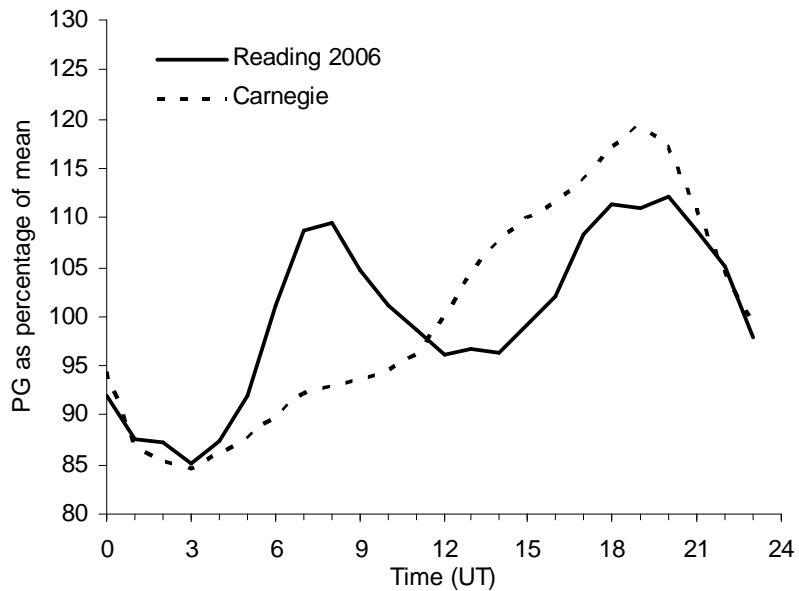


Figure 6.5 Mean diurnal fair-weather PG for Reading (RUAO) during 2006 and the standard Carnegie curve, as a percentage of the mean.

The difference between these two cycles is shown in Figure 6.6. The main deviation of the RUAO PG from the Carnegie curve is observed between 6-10UT, when the PG increases by up to 17% more than that of the Carnegie. As described in chapter 5, similar increases have been measured during this time at many polluted urban sites, such as at Kew, London (Scrase, 1933) which was attributed to the increase in anthropogenic sources of aerosol number concentration. A modern equivalent may be vehicle exhaust emissions during the morning “rush-hour” traffic (Bent and Hutchinson, 1966). However, space-charge density variations during this time (the “sunrise effect” described by Chalmers, 1967) may also contribute to local PG deviation during this time. The reduction in PG below that of the Carnegie between 12-20UT may be attributed to an increased loading of the atmospheric column with aerosol elevated from the surface by convection, increasing the R_C and therefore decreasing J_C and PG through Ohm’s Law. Again, the effect of space charge has not been quantified but may also contribute to a lowering of PG at the surface if a sufficient quantity of negative space charge is present above the PG sensor. Despite these deviations, the RUAO PG corresponds closely to the Carnegie variation during the night, keeping to within 5% between 20-05UT. Based on this analysis, the RUAO PG measurements are, on average, most likely to be globally representative between these times. The most likely explanation for this is that local sources of variation are lower during the night, when static stability within the boundary layer is high, suppressing convective motion that alters the aerosol number concentration and terrestrial ionisation rate by vertical mixing.

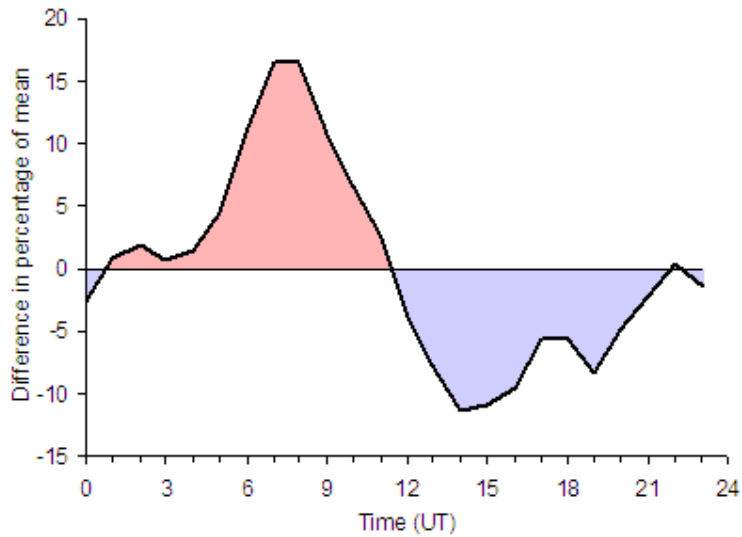


Figure 6.6 Difference between PG (as percentage of mean) for RUAO 2006 and Carnegie.

The difference between the diurnal variations of percentage RUAO PG and the Carnegie curve is seasonally dependent, as seen by the mean differences during each month averaged between May 2005 and March 2007 (Figure 6.7). Although most months show a similar general pattern of higher RUAO PG compared to Carnegie in the mid-morning and lower during the afternoon, the magnitude of the differences during the winter is less than half that during the summer.

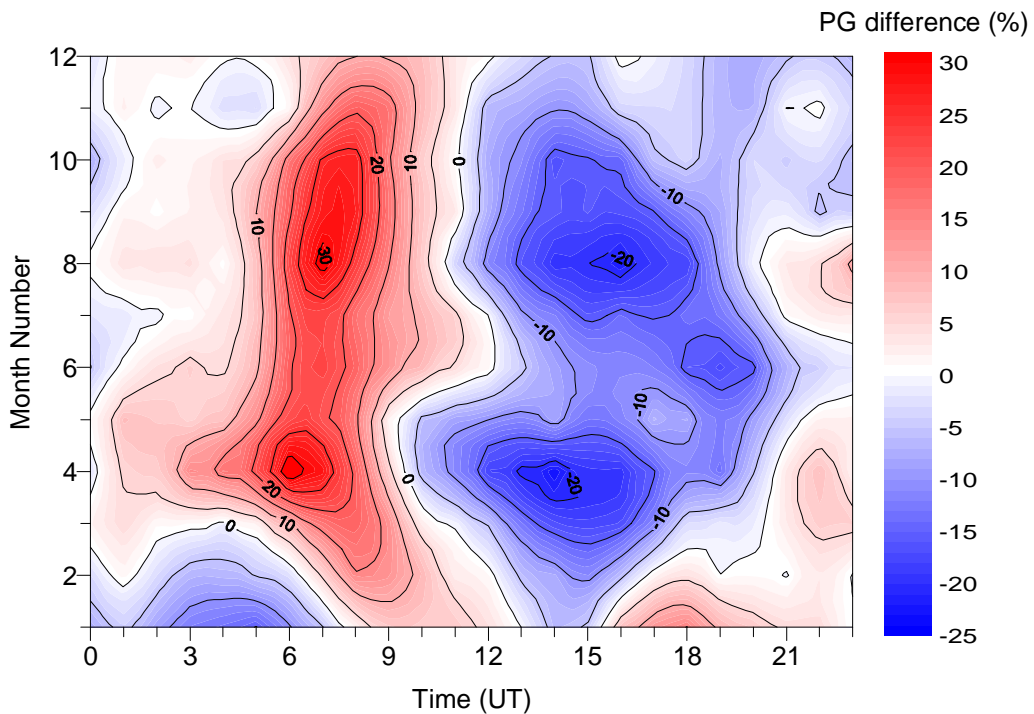


Figure 6.7 Difference between percentage RUAO monthly mean fair-weather PG with the standard Carnegie curve, for each hour. Monthly means averaged between May 2005 and April 2007.

To quantify the increased similarity between RUAO PG and the Carnegie curve during the winter compared to summer, the average monthly correlations are shown in Figure 6.8. From this figure it can be seen that the highest correlations are during the winter, and lowest during summer. This suggests that globally representative PG is more likely to occur between November to January. The increased agreement between surface PG and the Carnegie curve during the winter was also found by Harrison (2004b), who calculated daily correlations between the Carnegie curve and PG measurements from a low-pollution site on Mount Wank in Hungary. Autocorrelation of the hourly values representing the Carnegie curve show that the decorrelation time is approximately 6 hours, implying only 4 degrees of freedom for correlation significant confidence level tests. Only 4 independent pairs of data (24 hours divided by 6 hour decorrelation time) strictly means that a correlation coefficient of 0.95 would be required for 95% confidence. Therefore confidence level statistics are not appropriate for identifying similarities between diurnal variations to the Carnegie curve. Instead, visual inspection is used; checking for similarity in amplitude and timing of principal maxima and minima.

Like the times of close correlation within a diurnal cycle, it is the intensity of convection that is the most likely cause of this seasonality in occurrence of globally-representative PG. During the winter, the boundary layer is less dynamic compared to the summer, so there is less diurnal variability in aerosol number concentration and terrestrial ionisation rate vertical profiles. This means that both R_C and surface σ_T are less variable, allowing global variation attributed to changes in Ionospheric potential to become the dominant source of J_C and PG variability. Similar seasonality in globally-representative PG has been reported by Israelsson and Tammet (2001), Märcz and Harrison (2003) and Serrano et al. (2006). All these authors cite reduced boundary-layer variability during winter as the main cause of this effect.

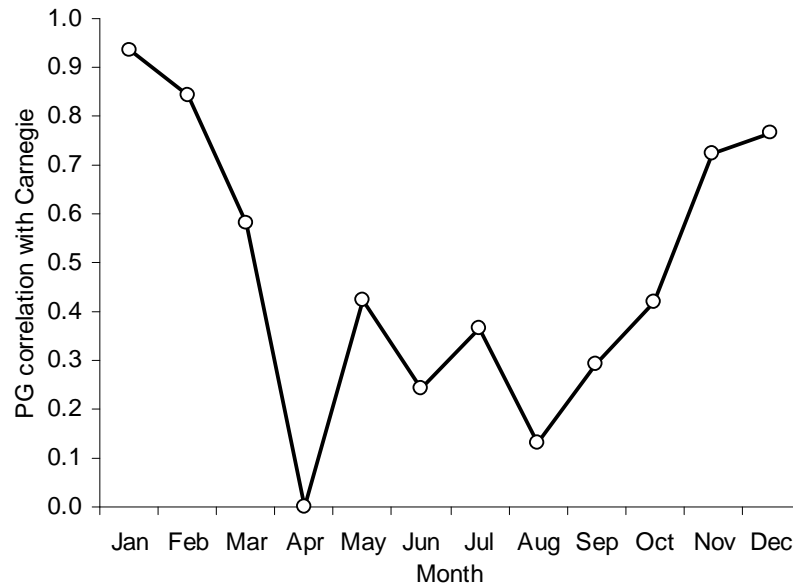


Figure 6.8 Correlation of RUAO monthly mean fair-weather PG with the standard Carnegie curve. Monthly correlations averaged between May 2005 and April 2007.

In summary, the times when the PG is most likely to be globally representative at the RUAO are between November and January, and between 20-05UT, corresponding to the times of minimal boundary-layer variability. During some individual days, especially in the winter, the PG does appear to correspond to the Carnegie curve, implying that globally-representative PG can occur throughout the day at the RUAO (assuming that the global circuit variation corresponded to the Carnegie curve during that particular day). An example of such an occurrence is shown in Figure 6.9, with a correlation coefficient of hourly RUAO PG with the standard Carnegie curve of 0.872 for 23 January 2007. This day was overcast (thin stratocumulus), calm (daily mean and standard deviation of wind speed at 2m was $1.4 \pm 0.5 \text{ms}^{-1}$) and had a small temperature range (daily mean temperature of 2.0°C with a standard deviation of 0.9°C). All these factors indicate only weak convection with minimal boundary-layer evolution, allowing global variability in PG to exceed local effects. Although the minimum in observed PG occurs at the same time as the Carnegie curve, the reduced relative PG between 0-6UT may have been due to increased terrestrial ionisation rate from Radon trapped near the surface due calm wind conditions and a shallow nocturnal temperature inversion. The short deviations in observed PG were likely to be a result of weak charge differences within the Stratocumulus cloud base passing over the site. However, the Carnegie curve is only a guide to expected global circuit diurnal variation at daily timescales, so the contribution of global and local effects on the PG during this day can not be precisely quantified.

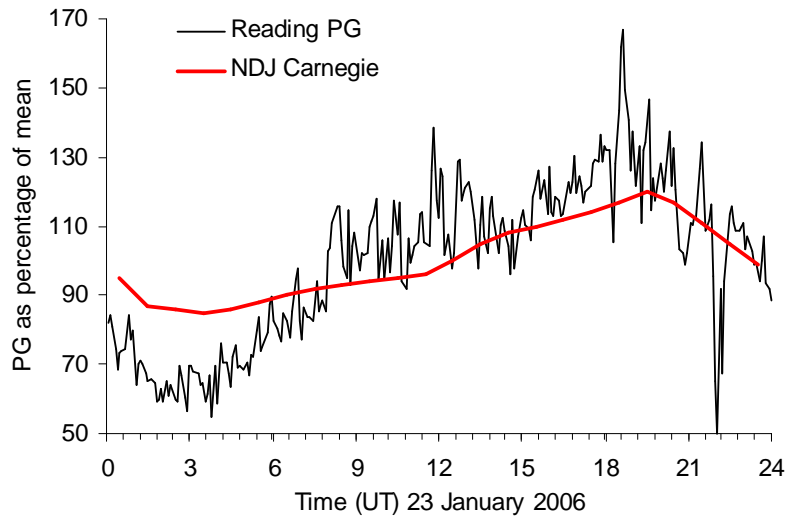


Figure 6.9 Five minute mean PG measured at the RUAO during 23 January 2006. The standard Carnegie curve is shown for comparison. Both data are shown as percentages of their respective means.

Conduction current density

The conduction current density, J_C is considered to be the most globally representative parameter measured at the surface (e.g. Kasemir (1951), Dolezalek (1978) Israelsson and Tammet (2001)). However, J_C is inherently difficult to measure directly due to the problem of leakage currents and the small currents involved. Consequently, despite the benefits of J_C for monitoring of the global circuit, PG is usually the preferred parameter as its measurement is comparatively simple and uses well established instrumentation. The hypothesis that J_C is more globally representative than PG is investigated by comparing the monthly mean J_C and PG diurnal cycles for the RUAO during times of strong and weak PG correlation with the Carnegie curve.

From Figure 6.8 it was found that the most globally representative PG diurnal variation occurred in January, and the least in April. Due to the lack of adequate fair-weather J_C measurements for April, the second least globally-representative month (August) was used instead, which contained more fair-weather days. Figure 6.10 shows the comparison between fair-weather J_C and PG mean diurnal variation for January 2007 and the mean November-January Carnegie curve (averaged over all cruises), all as a percentage of their respective means. Although both J_C and PG are closely correlated with the Carnegie curve during this time (0.93 for PG and 0.87 for J_C) confirmed by visual inspection of the amplitude and phase of the diurnal cycles, it is J_C that is more proportional, with PG being too low during the early morning minimum and too high during the maximum. The mean

and standard deviation of absolute J_C deviation from Carnegie was $6.0\% \pm 4.0\%$ compared to $7.8\% \pm 4.8\%$ for PG. This result is in accordance with the theory that J_C is more globally representative than PG, as it is less affected by local (boundary-layer) variability.

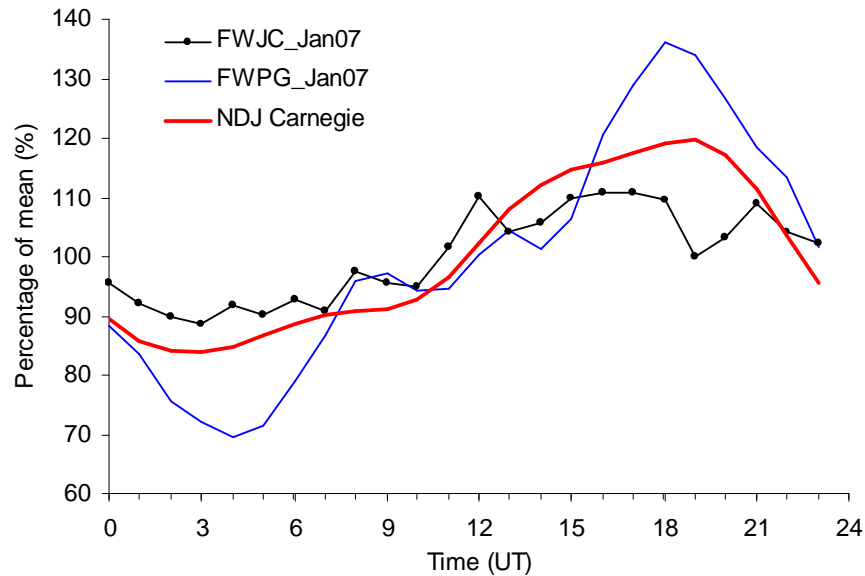


Figure 6.10 Comparison of fair-weather J_C and PG mean diurnal variation for January 2007 and the mean November-January Carnegie curve (averaged over all cruises). The standard errors associated with the J_C and PG monthly means are $\sim 2\%$.

The same comparison was made for August 2006, which is a month where the PG was not significantly correlated with the Carnegie curve (Figure 6.8). The comparison is shown in Figure 6.11. The large increase in PG above the Carnegie variation between 5-10UT and decrease between 11-19UT is not as pronounced in the J_C cycle. However, the time of maximum PG corresponds closer to the Carnegie than the J_C data. Despite this, J_C follows the Carnegie more closely than PG, with a mean and standard deviation of absolute J_C deviation from Carnegie of $7.2\% \pm 5.6\%$ compared to $10.1\% \pm 9.1\%$ for PG.

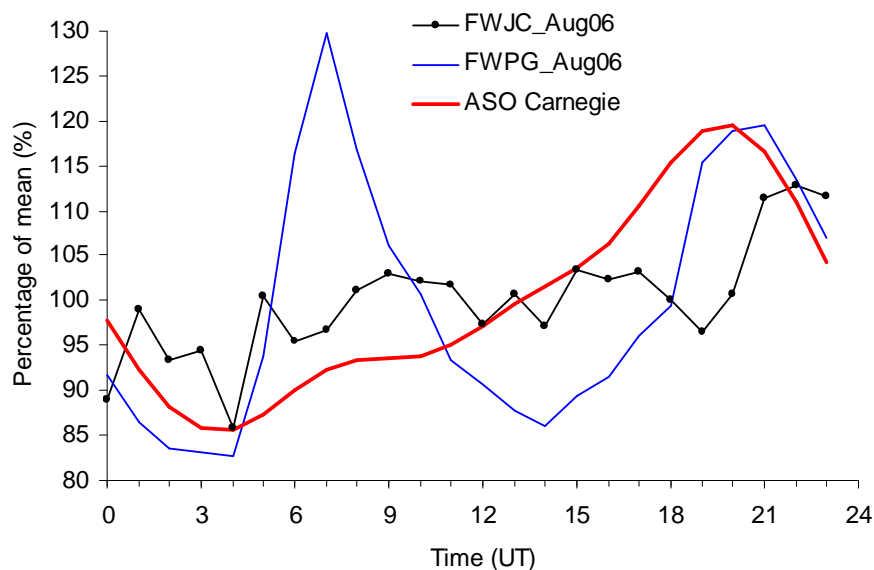


Figure 6.11 Comparison of fair-weather J_C and PG mean diurnal variation for August 2006 and the mean August-October Carnegie curve (averaged over all cruises). The standard errors associated with the J_C and PG monthly means are $\sim 2\%$.

By comparing the mean percentage diurnal variations of J_C and PG with the seasonal Carnegie curve, it was demonstrated that J_C more closely relates to the Carnegie curve (and therefore variation of the global circuit) than PG for the two months investigated. However, this is not always found to be the case, such as when the duration of fair-weather J_C in a month is too short to be statistically representative (i.e. due to leakage currents that were often present before the introduction of heaters). For months with long fair-weather J_C measurements that allow calculation of a J_C diurnal variation over a significant fraction of the month (such as during August 2006 and January 2007), the hypothesis that J_C is more globally representative than PG appears valid. However, more months containing long-duration fair-weather J_C throughout the year are required for a more thorough assessment of whether J_C is indeed more globally representative than PG for the RUAO site all year round.

6.4 Retrieval of global circuit diurnal variation from measurements made at a polluted site

As previously discussed in chapter 5, local factors often dominate over global sources of variability in J_C and PG measured at urban sites. The main source of local variability is the aerosol number concentration profile, which is modified throughout the day by convection. This effect is most apparent during the summer months, when convection is strongest.

The loss of global (Carnegie-like) signals from the monthly mean diurnal variation during the summer was shown by Figure 6.8.

One application of the simple columnar model theory is to provide a basis for the synthesis of surface atmospheric electrical measurements made simultaneously at several European sites, as discussed in detail by Harrison and Bennett (2007b). Assuming V_i to be common above all the sites, the theoretical J_c present in the absence of a boundary layer R_c can be found by extrapolation of surface atmospheric electrical parameters. However, this method of global circuit variability detection requires simultaneous measurement of PG and J_c over several independent sites, and the uncertainty in this type of retrieval is expected to be large (Harrison and Bennett, 2007b). However, retrieval of global variability at a single urban site can be made if an R_c model is used in combination with local meteorological observations to successfully compensate for local sources of PG and J_c variability. It is this method that will be discussed in this subsection.

A month when local sources are expected to have contributed significantly to the overall PG and J_c variability is July 2006, where the lack of a significant correlation to the Carnegie curve for both PG and J_c is found. This, together with sufficient atmospheric-electrical data (particularly PIMS-derived σ_T), make July 2006 a suitable case study for retrieval of global circuit mean diurnal variation by combining the atmospheric electrical and aerosol data with the columnar resistance model. The global circuit intensity is proportional to the ionospheric potential (V_i), so it is the diurnal variability of this parameter that is to be retrieved using the model. The measured mean atmospheric electrical parameters and dry-bulb temperature for the RUAO during July 2006 are given in Table 6.1.

JUL 06	J_c	PG	σ_T	μ_+	μ_-	T_s
Mean	2.1pAm ⁻²	96.1Vm ⁻¹	5.7fSm ⁻¹	1.8cm ² V ⁻¹ s ⁻¹	2.2cm ² V ⁻¹ s ⁻¹	21.0°C

Table 6.1 Observed monthly mean fair-weather atmospheric electric parameters and dry-bulb temperature for July 2006.

In order to model the observed monthly mean J_c and PG, estimation of the mean ionospheric potential (V_i) and aerosol number concentration profile were required. V_i was assumed to be 250kV, based on the approximate mean V_i calculated by Markson (2007). Using the Ohmic assumption, the total conductivity based on the mean J_c and PG should be 21.9fSm⁻¹. However, the observed σ_T measured by the PIMS was only 5.7fSm⁻¹. This large discrepancy may be due to either reduced PG due to negative space charge aloft, or

under sampling of the ion population (and therefore σ_T) by the PIMS, which only measures ions with mobilities exceeding approximately $0.95\text{cm}^2\text{V}^{-1}\text{s}^{-1}$ (Bennett and Harrison, 2006a), or indeed a combination of the two. However, as the PIMS is known to sample only the small ion contribution to σ_T , it was the absolute values of PG and J_C that were used to estimate the aerosol vertical profiles. However, since only the relative variation of V_I is to be modelled, it is the relative and not absolute observed variability of σ_T , PG and J_C that is of importance, with the absolute values being used only as a guide to realistic model parameters. The background aerosol profile component was assumed to be small but with a large scale height. As this component will not be modelled to have a diurnal variation, its inclusion in the model is only to produce non-zero aerosol number concentrations above the troposphere. The modelled parameters used to most accurately represent the mean value of J_C and PG (with σ_T assumed to be uniformly under sampled) are shown in Table 6.2. The scale heights of terrestrial ionisation (z_{si}) and boundary-layer aerosol number concentration (z_{BL}) were assumed equal. Using these parameters, J_C was modelled as 2.2pAm^{-2} and PG as 97Vm^{-1} (for a assumed V_I of 250kV), in close relation to the observed means for July 2006.

Model	P_s	T_s	Q_0	z_{si}	N_{0BG}	N_{0BL}	z_{BG}	z_{BL}
Value	1013hPa	21°C	$8\text{cm}^{-3}\text{s}^{-1}$	1200m	200cm^{-3}	8000cm^{-3}	10000m	1200m

Table 6.2 Model parameters used to simulate the mean electrical conditions of July 2006.

Although the absolute values of J_C and PG were used to generate realistic values of the mean aerosol number concentration profile for July 2006, it is the relative variability of the observed values that is of importance in retrieval of the diurnal cycle of relative V_I . For absolute values more observations are required, such as the actual absolute σ_T or surface aerosol number (not mass) concentration, and the height of the boundary-layer (perhaps from radiosonde ascents or estimations from an integrated meteorological numerical model such as the Met. Office Unified Model). Of course, absolute values of V_I could be found without a model if coincident determinations of R_C (such as from observed σ_T vertical profiles) and J_C are measured.

The steps used to retrieve V_I from measured diurnal cycles of J_C , PG and σ_T are as follows:

Step 1

Diurnal variation of aerosol number concentration, N_{0BL} , (relative to the daily mean) is assumed equal to measured aerosol mass concentration diurnal cycle, with a daily mean of 8000cm^{-3} (Table 6.2). Using this value of N_{0BL} the model is run for Q_0 of $8\text{cm}^{-3}\text{s}^{-1}$ for

each hour to calculate the diurnal variation of σ_T . This is compared to variation of the measured σ_T , with difference between modelled and measured σ_T relative variability used to find relative variability in Q_0 , which is adjusted for each hour until the diurnal cycle of modelled σ_T equals that measured at the RUAO.

Step 2

The model is run for each hour using the corresponding values of retrieved Q_0 and measured N_{0BL} , as well as the estimated boundary layer height, z_{BL} . All other model input parameters are kept constant.

Step 3

As V_I was kept constant in step 2, all variability in modelled J_C and PG is attributed to local effects (variation of ionisation rate and aerosol number concentration profiles). The diurnal variation of V_I is retrieved by subtracting this modelled local diurnal cycle of J_C and PG from the observed J_C and PG diurnal cycles.

For step 1, the variability of σ_T is independent of V_I but dependent instead on surface ionisation rate and aerosol number concentration. Therefore the observed relative diurnal variation of σ_T and aerosol mass concentration (assumed to be proportional to number concentration) was used to estimate the relative diurnal variation of surface terrestrial ionisation using the model. The boundary layer height was assumed to vary with the same relative amount as that found for an urban environment of similar geographical latitude and time of year (from Harrison and Aplin, 2003, based on direct observation of boundary layer height by Dupont et al., 1999), but with a mean height of 1200m (Table 6.2). To estimate the uncertainty in V_I calculation based on this chosen diurnal boundary layer height variation, error bars of 10% of the daily mean height (i.e. 120m) were placed on two sample times marking the first and last quarter of the cycle, (and also near boundary layer height maximum and minimum) at 06UT and 18UT. In order to calculate (and eventually subtract) the local component of J_C and PG variability, V_I is kept constant.

A summary of parameters kept constant and those with a modelled diurnal cycle is given in Table 6.3.

Kept constant	Diurnal variation
Cosmic ray ionisation profile	Boundary layer aerosol profile
Temperature profile	Terrestrial ionisation rate profile
Surface pressure	
Background aerosol profile	
Surface ion mobility	
Ionospheric potential	

Table 6.3 Modelled parameters and profiles that were kept constant and those with an assumed diurnal cycle.

Diurnal temperature and pressure variations were shown to have negligible effect on the atmospheric electrical parameters so their values are kept constant. No significant diurnal variability in ion mobility was observed for July 2006 so they too remain constant. The cosmic ray intensity and background aerosol number concentration profiles are not expected to have a significant diurnal cycle, so are also assumed to be constant with time, leaving only the diurnal cycles of boundary layer aerosol and terrestrial ionisation rate profiles as considered significant local sources of diurnal variability in J_C , P_G and σ_T .

For step 2, the columnar resistance model was run for each hour of the day based on the observed diurnal variation of surface aerosol mass (assumed equal to number) concentration and boundary layer scale height. The difference between observed and modelled σ_T (which kept the unknown surface terrestrial ionisation rate Q_0 variation constant) was used to retrieve the percentage diurnal variation of Q_0 by changing this parameter until the modelled σ_T was equal to the observed relative variation for each hour. These diurnal variations are seen in Figure 6.12.

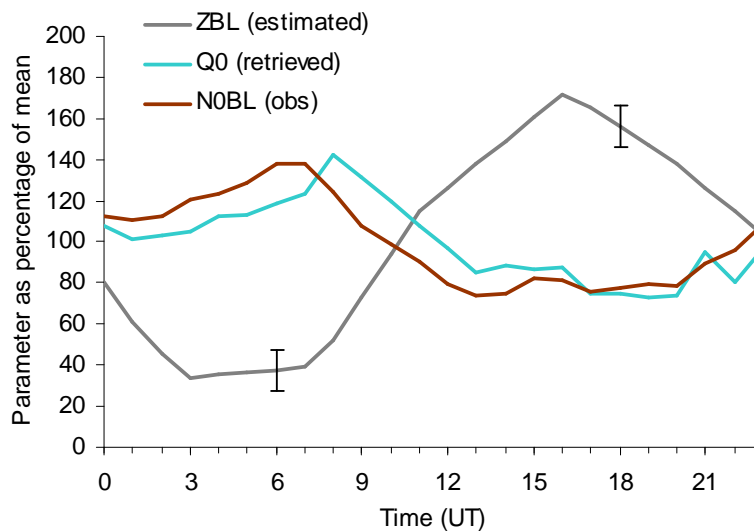


Figure 6.12 Estimated diurnal variation of boundary layer height (z_{BL}) based on Dupont et al. (1999), including height error bars of $\pm 10\%$ of mean, with observed variation of surface aerosol

mass concentration (assumed to be proportional to number concentration). The retrieved diurnal cycle of surface terrestrial ionisation rate from observed σ_T and N_{OBL} is also shown. All values are relative to their respective means.

It can be seen that the retrieved terrestrial ionisation rate (Q_0) diurnal cycle is similar in relative magnitude and form to that of the surface aerosol number concentration (N_{OBL}), demonstrating that both are likely to be governed by boundary layer ventilation, as assumed. The modelled diurnal variation of J_C and PG using these diurnal variations and a constant V_1 are shown in Figure 6.13. As the global component (V_1) is kept constant, the modelled cycles are based only on local sources of variability.

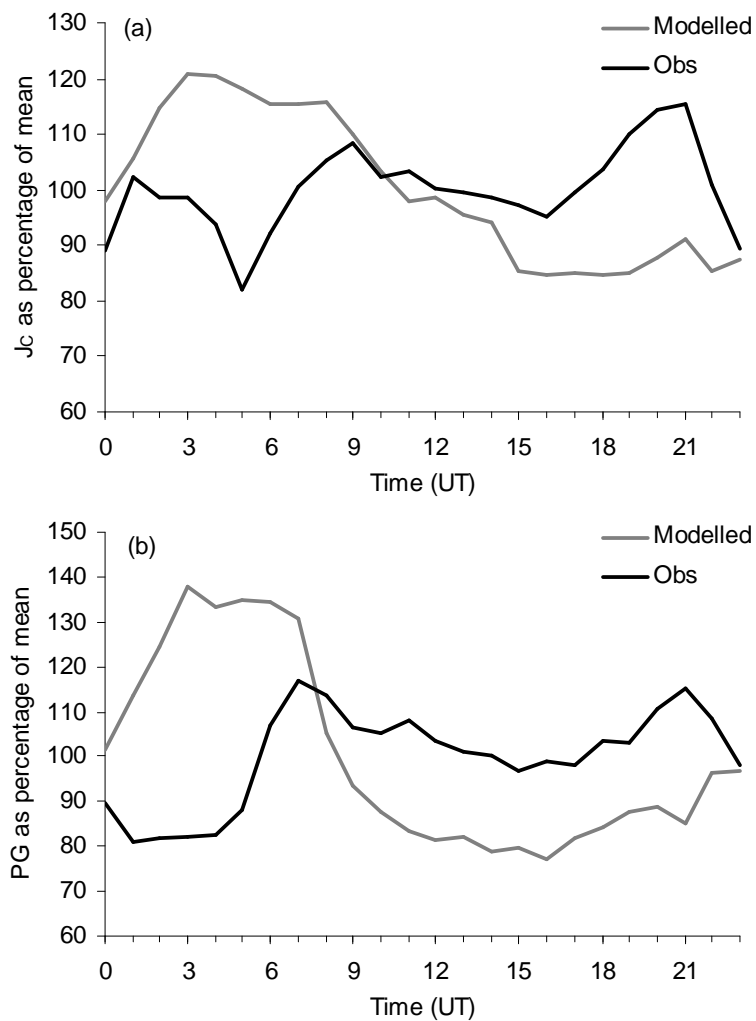


Figure 6.13 Observed and modelled (a) J_C and (b) PG for July 2006 assuming no diurnal variation of V_1 (i.e. the local component of modelled variability) as a percentage of their respective means.

In order to retrieve the diurnal variation of V_I from the observed variation of J_C and PG, (step 3) the local contribution must be removed. This was done by determining the V_I diurnal cycle that produced the closest fit between modelled and observed J_C and PG. Preference was given to accurate fitting of J_C as the contribution of space charge (which can not be modelled by the fair-weather columnar resistance model) to PG diurnal cycle was not known. The modelled diurnal cycle of V_I that produced the best fit to the observations for July 2006 is shown in Figure 6.14.

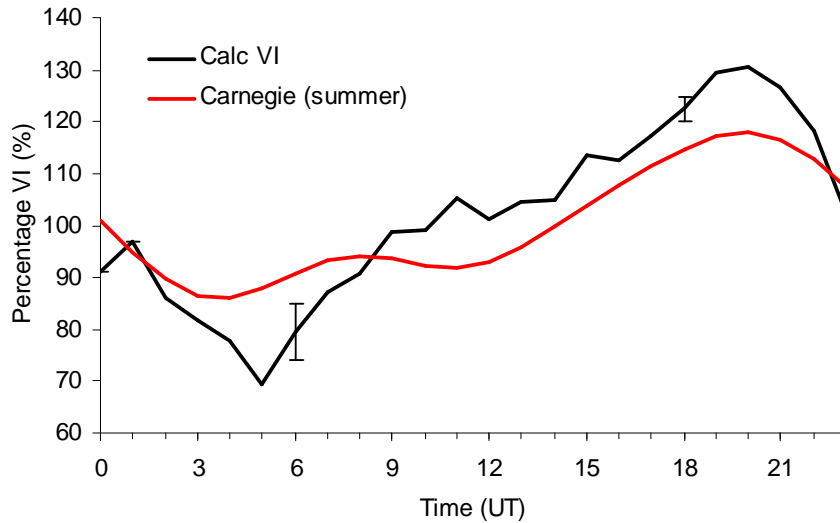


Figure 6.14 Retrieved V_I diurnal cycle based on J_C , PG and σ_T variability for July 2006, and the summer Carnegie curve. Error bars on V_I used to assess the uncertainty in boundary layer height at 06UT and 18UT are shown.

The retrieved V_I diurnal cycle agrees closely (correlation coefficient of 0.906) to that of the mean summer Carnegie curve, which is the expected diurnal variation of the global electrical circuit, with a similar amplitude and phase (Figure 6.14). The error bars used to represent the uncertainty in boundary layer diurnal variation indicate that the retrieved V_I cycle is robust to this uncertainty, with a 6% and 2% uncertainty in V_I percentage variation at 06UT and 18UT respectively, given a 10% uncertainty in boundary layer height (as a percentage of daily mean) at these times. The time of maximum deviation from the Carnegie curve occurs between 03-07UT. This is likely to be due to leakage currents affecting the J_C results, as this was the time with the least number of leakage-free J_C measurements were observed, as the AECF was susceptible to leakage currents during times of high humidity such as early morning. Therefore, this time may have been inadequately represented in the calculation of monthly mean J_C diurnal cycle.

The V_I diurnal variation was retrieved by preferentially matching observed and modelled J_C as this was considered more reliable than PG, which despite having the local effects of aerosol and terrestrial ionisation rate removed, may still have an unknown contribution due to space charge. Subtracting the relative variation of Observed and modelled PG (Figure 6.15), a variation closely resembling that of the difference between the unpolluted Lerwick PG and Carnegie curve (Figure 6.2). This further suggests that the effect of boundary-layer aerosol and terrestrial ionisation rate variability has been successfully removed by the model (or at least reduced to that of Lerwick), and that the difference between PG from an unpolluted (globally representative) site and the Carnegie curve is not due likely to be due to aerosol or ionisation rate variability, with the local cycle of space charge being a possible explanation for this difference, as temperature variation alone would be too small to account for the observed differences.

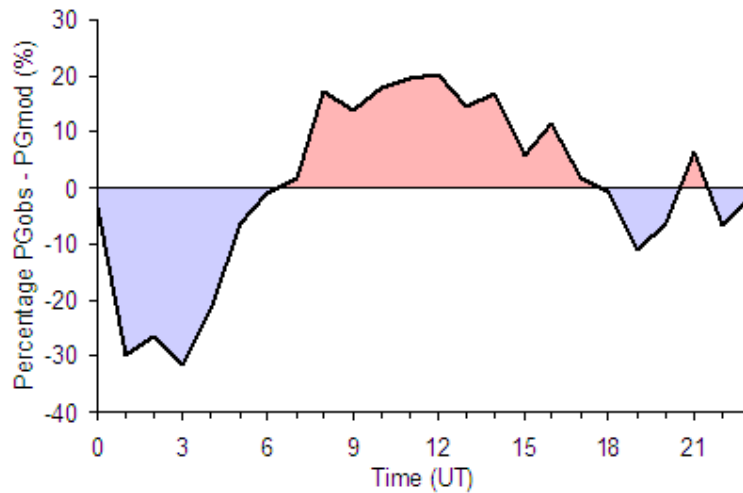


Figure 6.15 Difference between observed and modelled PG (relative to the mean) for July 2006, once the effect of aerosol and terrestrial ionisation rate variability is removed.

To summarise, it has been demonstrated that a time-dependent fair-weather columnar resistance model is capable of retrieving the monthly mean diurnal variation of V_I from surface measurements of J_C , PG and σ_T providing information on the surface aerosol number concentration and boundary-layer height is known. This retrieved V_I is demonstrated to be considerably more globally representative than the surface measurements of J_C or PG on their own, as seen in Table 6.4 where the correlation coefficient with the summer Carnegie is greatest for the retrieved V_I than directly observed J_C and PG. Therefore globally-representative data can be retrieved from polluted urban sites such as the RUAO, providing some information on the otherwise dominant local sources of variability is known. However, surface PG measurements at both clean and polluted sites may also be subject to a significant electrostatic component of diurnal

variability, expected to be due to space charge. Therefore, J_c is still expected to be the most reliable source of global variability, once local (columnar) sources of variability are accounted for.

JULY 2006	J_c	PG	Retrieved V_I
Correlation with summer Carnegie	0.46	0.41	0.91

Table 6.4 Correlation coefficients for the mean diurnal variation of J_c , PG and retrieved V_I for July 2006.

6.5 Simultaneous observations of PG at Reading, Durlston Head and Chilbolton

A JCI131 electrostatic field mill was installed on the top of a mobile meteorological mast (2.5m above the surface) and positioned at both Durlston Head and Chilbolton Observatory (at different times). Durlston Head was chosen primarily as this is the site used for the MSc student fieldtrip, allowing the students to gain experience in interpretation of PG data whilst providing an additional site for comparison with the RUAO. The rural, coastal location is also a useful contrast to the urban, inland RUAO site. The Chilbolton Observatory site was used due to its cloud radar facility, which was used to acquire information on overhead clouds that caused associated variation in PG. Additionally, the site is easily accessible from Reading allowing regular data collection and maintenance, and was situated in a rural, inland location. The field mill used to measure PG at both remote sites was calibrated at the RUAO to be equal to that for 1m above the ground, in accordance with the field mill permanently installed at the RUAO. Comparisons between the PG measured at the two mobile sites and coincident measurements at the RUAO will be made in this section, with the aim of identifying times of similar PG variability that may be attributed to a common global source. A map showing the locations of the RUAO, Chilbolton Observatory and Durlston Head is given in Figure 6.16.

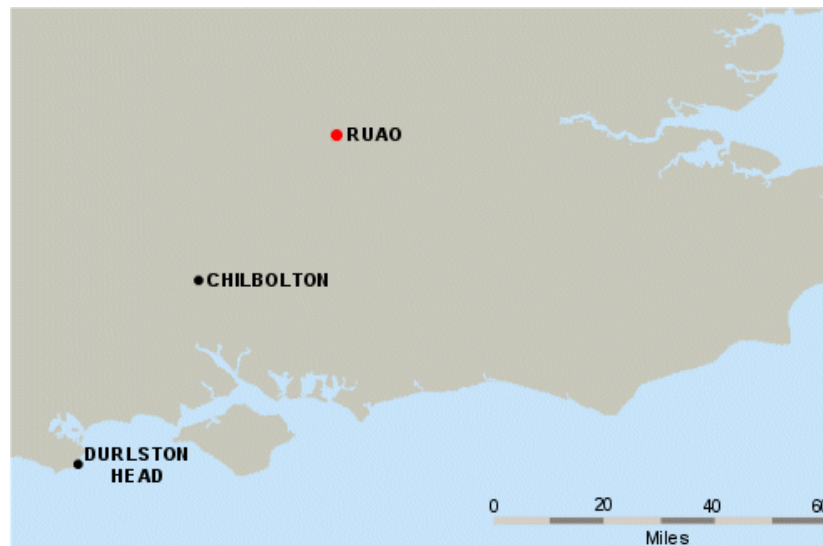


Figure 6.16 Map of South East England showing location of the RUAO, Chilbolton Observatory and Durlston Head.

Durlston Head

Observations of PG were made at the coastal site of Durlston Head, Dorset (118km SW of the RUAO, Figure 6.16) during 24-31 October 2006. The site is coastal; on the top of a small hill (80m AMSL) approximately 200m from the sea to the SE, with rural land to the NW. Further details of the site and specific examples of PG variation due to local meteorological processes have been discussed by Bennett and Harrison, 2007b.

A comparison between the five minute mean fair-weather PG coincident values at the RUAO and Durlston Head is shown in Figure 6.17. From these results it is clear that PG at the two sites do not vary in unison throughout the observation period as would be expected if both were dominated by the same global source (i.e. if local meteorological effects were small). Local factors therefore are expected to have dominated the PG variability at both sites for the five minute mean time resolution. Both the mean and standard deviation of PG at Durlston Head ($170 \pm 72 \text{Vm}^{-1}$) are larger than that at the RUAO ($129 \pm 50 \text{Vm}^{-1}$). As Durlston Head is in a rural location by the coast, it would be expected that the aerosol number concentration would be lower than that for an urban site such as the RUAO. Lower aerosol number concentration implies lower PG as the total conductivity would be higher. However, from these results it can be seen that this is not the case. A possible explanation as to why the coastal site had a greater and more variable PG than the RUAO is that space charge may have been advected over the Durlston Head field mill, generated by nearby wave breaking along the shoreline. Blanchard (1966) reported that breaking waves were found to generate positive space charge that increased the mean and variability of PG when the wind direction brought air from the nearby surf zone.

It is this variability due to locally-generated space charge that is expected to have masked any positive correlation in the five minute mean PG at Durlston and Reading. The PG mean and variability at Durlston Head was observed to drop noticeably when the wind direction changed from inshore to offshore (Bennett and Harrison, 2007b), seen between year days 299.8 and 300.4 in Figure 6.17a.

The mean fair-weather PG diurnal variations during 24-31 October RUAO and Durlston Head comparison is shown in Figure 6.18, including the Carnegie curve. From this figure the average time of greatest residual between RUAO and Durlston Head PG occurred between 04-13UT. However, both sites show a similar relative PG outside of this time, with the variation also being similar to the standard Carnegie curve during the night, between 17-04UT. This time coincided with a broad minimum in mean wind speed at Durlston Head, which may have reduced the flux of space charge over the sensor, allowing a greater proportionality of PG variability to be generated by the global sources.

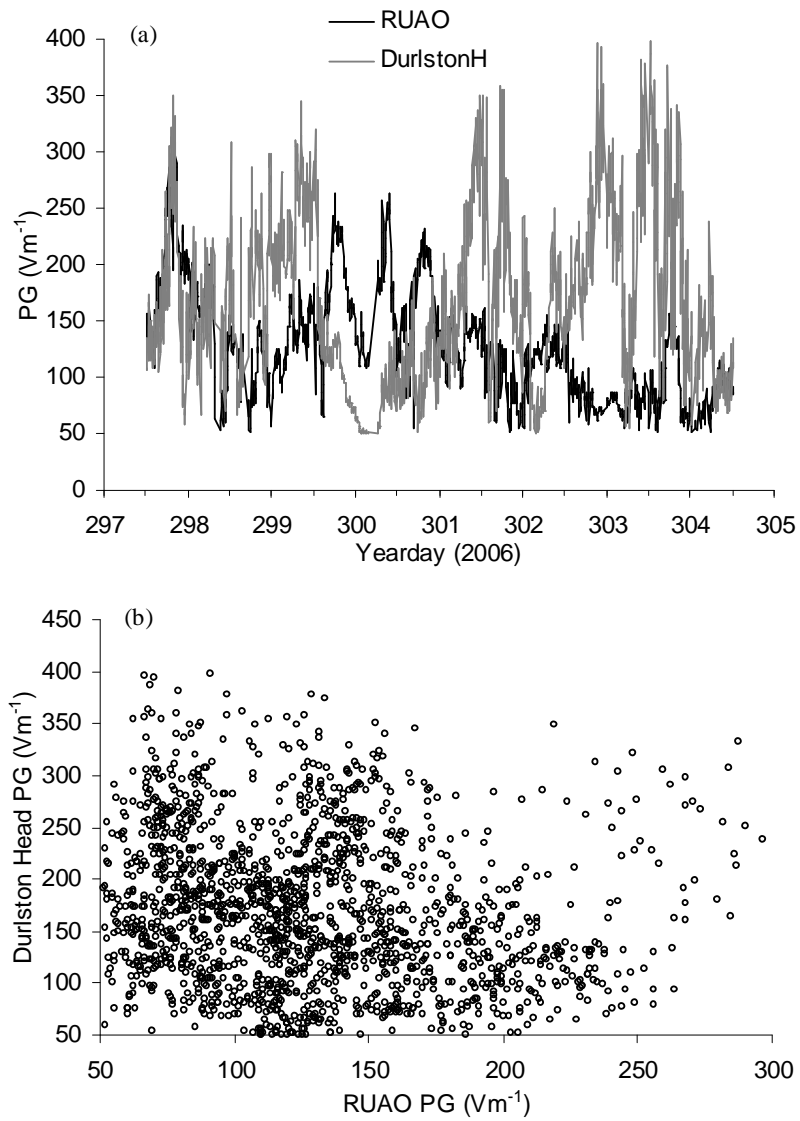


Figure 6.17 Five minute mean fair-weather PG measured simultaneously at the RUAO and Durlston Head between 24-31 October 2006 (year days 297-304 respectively), showing (a) the PG with time and (b) a scatter plot comparing PG from the two sites.

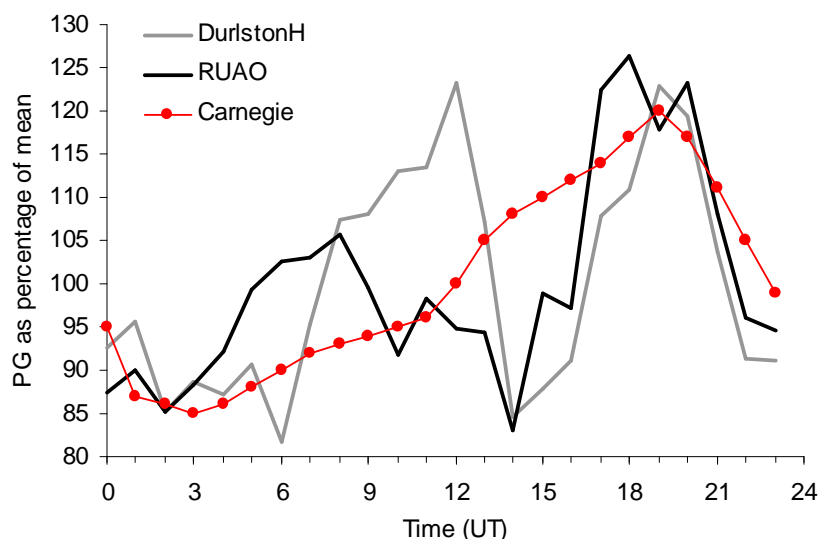


Figure 6.18 Mean diurnal cycles for PG measured at the RUAO and Durlston Head between 24-31 October 2006, compared to the standard Carnegie curve. Values are expressed as a percentage of their respective means.

Chilbolton Observatory

As discussed in chapter 5, PG was measured at the Chilbolton Observatory, Hampshire (47km SW of the RUAO) between 1 November and 4 December, 2006. The five minute mean PG is compared to that of the RUAO during this period in Figure 6.19a. Decorrelation of the Chilbolton PG data occurred after 40 steps from 3470 values, therefore permitting 87 degrees of freedom (independent data pairs) in the correlation. The correlation coefficient between Chilbolton and RUAO fair weather PG was 0.443, which for 87 degrees of freedom has a p value of 2×10^{-5} (i.e. confidence >99.9%). As both the RUAO and Chilbolton are inland sites, they are not subject to wave-breaking space charge like Durlston Head. Therefore, both sites have a similar mean and standard deviation fair-weather PG during this period, with the RUAO and Chilbolton statistics being $134 \pm 48 \text{Vm}^{-1}$ and $112 \pm 44 \text{Vm}^{-1}$ respectively. The 22Vm^{-1} difference in mean PG is likely to be due to the RUAO having a generally higher aerosol number concentration than the more rural site of Chilbolton.

The significant correlation between the two sites implies that either (1) both are affected by a similar but largely independent local effect (such as boundary layer evolution) or (2) they share a common (global) source of variability. It is likely that both of these effects occurred throughout the period, what is not easy to determine however is their relative importance. If the mean diurnal fair-weather PG cycles are compared (Figure 6.19b) the close correspondence between the two sites can be seen. By comparing the cycles with that of the standard Carnegie curve it appears that both sites have a PG maximum at or

near that of the Carnegie at 19UT, and follow the general trend of the curve until 06UT. During the daytime, between 06-17UT the RUAO and Chilbolton diurnal cycles do not follow that of the Carnegie, although their close correspondence with each other persists. From this diurnal pattern it is suggested that the positive correlation between RUAO and Chilbolton PG is due to similar variability of local sources during the day (such as boundary-layer evolution) but may tend to share a more global source nocturnally, between 19-06UT, when the boundary layer aerosol and ionisation rate is less variable. To test whether correlation between Chilbolton and RUAO PG was higher during the night, the data was divided into two halves (as approximately equal number of data pairs would be required for a fair statistical comparison), one for data between 07-18UT (1748 pairs) and the other for 18-07UT (1722 pairs). Correlation between Chilbolton and RUAO fair weather PG for 18-07UT was 0.49 compared to 0.38 outside of these times, demonstrating the increased correlation during the night. With decorrelation occurring after 40 steps of autocorrelation, these correlations correspond to p values of 8.3×10^{-4} and 1.3×10^{-2} for 18-07UT and 07-18UT data respectively. This represents a factor of 16 decrease in statistical p value during the nocturnal hours compared to the day, demonstrating that although both p values were statistically significant at the 99% confidence level, the significance greatly increased during the night.

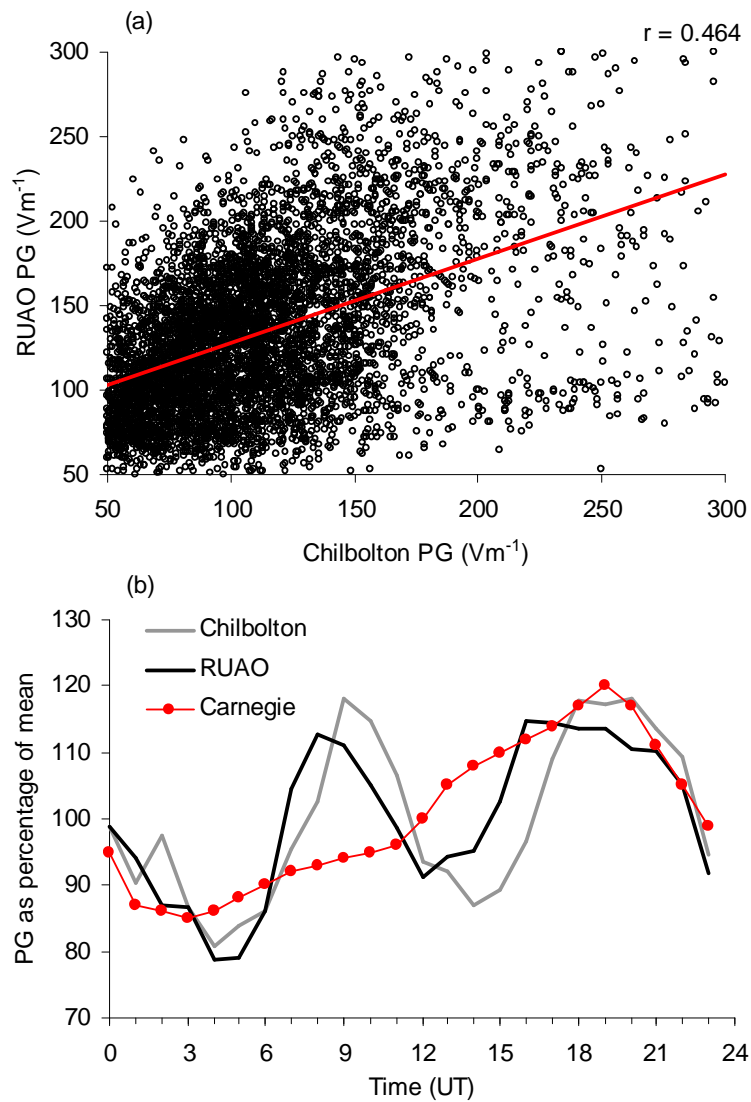


Figure 6.19 (a) Scatter plot between five minute mean coincident fair-weather PG for the RUAO and Chilbolton Observatory between 1 November and 4 December 2006. (b) The mean fair-weather PG diurnal variation for the two sites and the standard Carnegie curve, as a percentage of their respective means.

An example of the combination of global and local effects on the PG at Chilbolton occurred on 21 November 2006. From Figure 6.20a it can be seen that the variation in Chilbolton PG closely follows the standard Carnegie curve (although the magnitude of PG variability is three times that of the Carnegie). Additionally, there are short periods of rapid PG change that coincide with times of overhead convective cloud, identified by the cloud radar (~100m from the field mill) RHI plot of Figure 6.20b. Like when the Carnegie curve was evident in 24 hours of RUAO PG (Figure 6.9), the diurnal cycle of temperature was relatively steady at Chilbolton during 21 November 2006, with a daily mean and standard deviation of 5.1°C and 0.9°C respectively. The RUAO was in the same showery air mass

so was also affected by overhead convective cloud on occasions during this time. However, it can be seen that both sites fair-weather PG correspond closely during this day (Figure 6.21), suggesting that in the absence of overhead convective cloud, PG variability was mainly due to global sources, based on the assumption that the global circuit varied in accordance with the standard Carnegie curve.

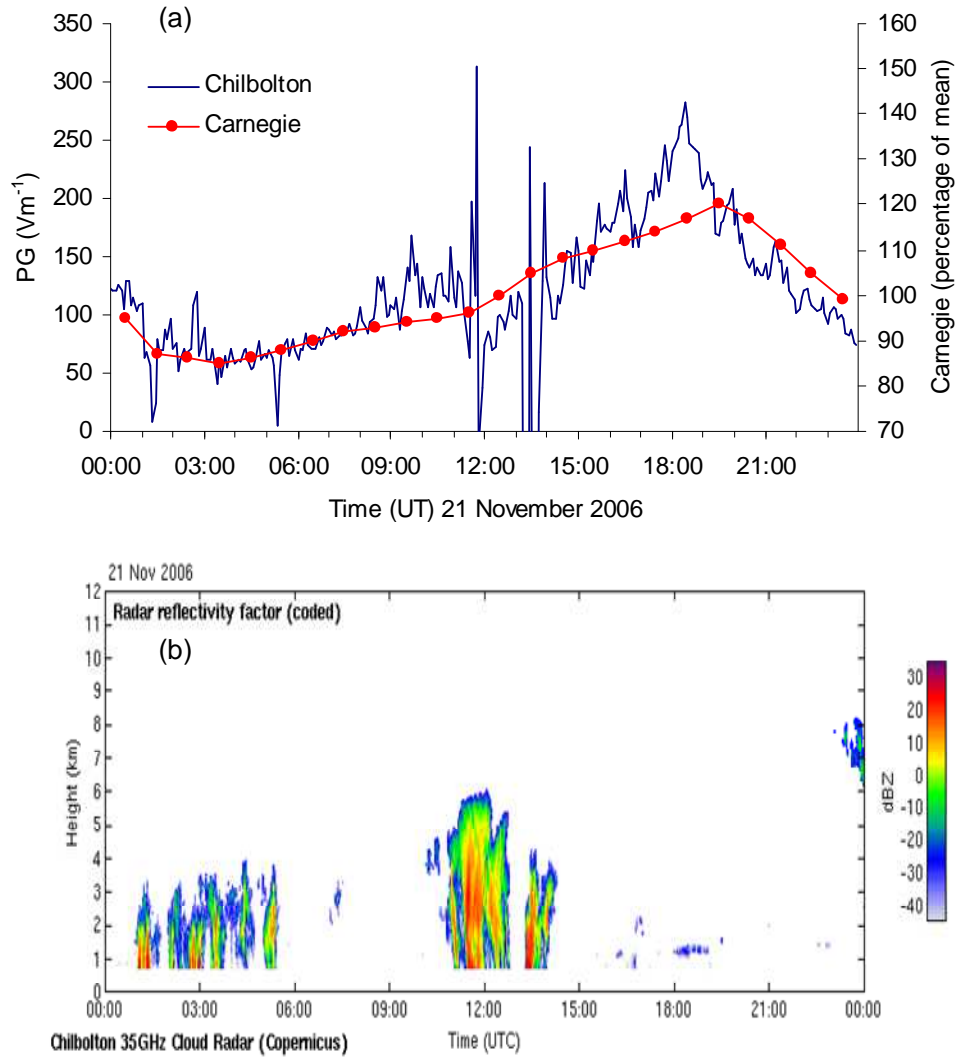


Figure 6.20 (a) PG measured at Chilbolton on 21 November 2006 compared to the Carnegie variation. Vertical scales have been adjusted to show the similarity in variation, although the magnitudes are different, with variability in Chilbolton PG about the mean being three times that of the Carnegie. The corresponding RHI radar reflectivity factor is shown in (b) identifying convective cloud as the source of rapid PG deviations from the Carnegie curve.

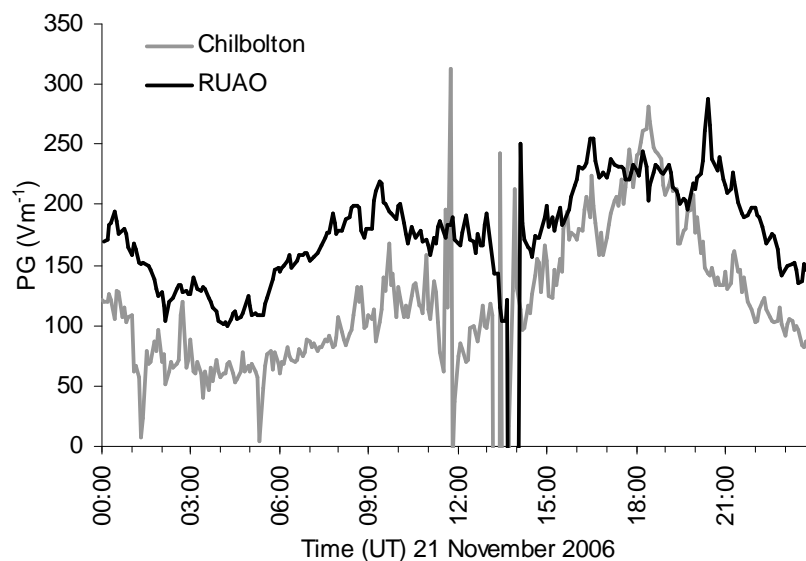


Figure 6.21 Five minute mean fair-weather PG for the RUAO and Chilbolton Observatory during 21 November 2006.

6.6 Comparison between RUAO and Nagycenk fair-weather PG

Hourly mean PG has been recorded at Nagycenk, Hungary (47.6°N, 16.7°E - approximately 1370km ESE of the RUAO) since 1962. Like Lerwick, Nagycenk is considered to be a low-pollution site, although semi-urban. Details of the Nagycenk site, operating procedure and PG records are provided by Märcz and Harrison (2003).

Fair-weather PG monthly mean diurnal cycles measured at Nagycenk and the RUAO between July 2005 and December 2006 were compared, and the mean annual correlations between the two sites monthly diurnal cycles are shown in Figure 6.23. With the exception of June, the seasonal variation in correlation appears similar to that of the correlations between RUAO and Carnegie monthly diurnal variation (Figure 6.8). For correlations between the RUAO and the Carnegie/Nagycenk PG, it is the winter that produces the greatest correlations, with more independent variability observed during the summer. This result is consistent with the explanation that the low variability of aerosol and ionisation rate profiles during the summer allows the global component of PG variability to be dominant over local effects. This global dominance is therefore common to the RUAO, Nagycenk and Carnegie diurnal variability, which produces the high correlation found during the winter.

An example of close (January 2006) and poor (August 2006) correlation between the PG diurnal cycles at the RUAO and Nagycenk are shown in Figure 6.22. From this figure, it is

also evident that the mean PG at Nagycenk is consistently lower than that of the RUAO (by approximately a factor of three). The reason for this is likely to be due to lower aerosol number concentration at Nagycenk. When both sites correlate significantly during January 2006, the variation is similar to that of the globally-representative Carnegie curve.

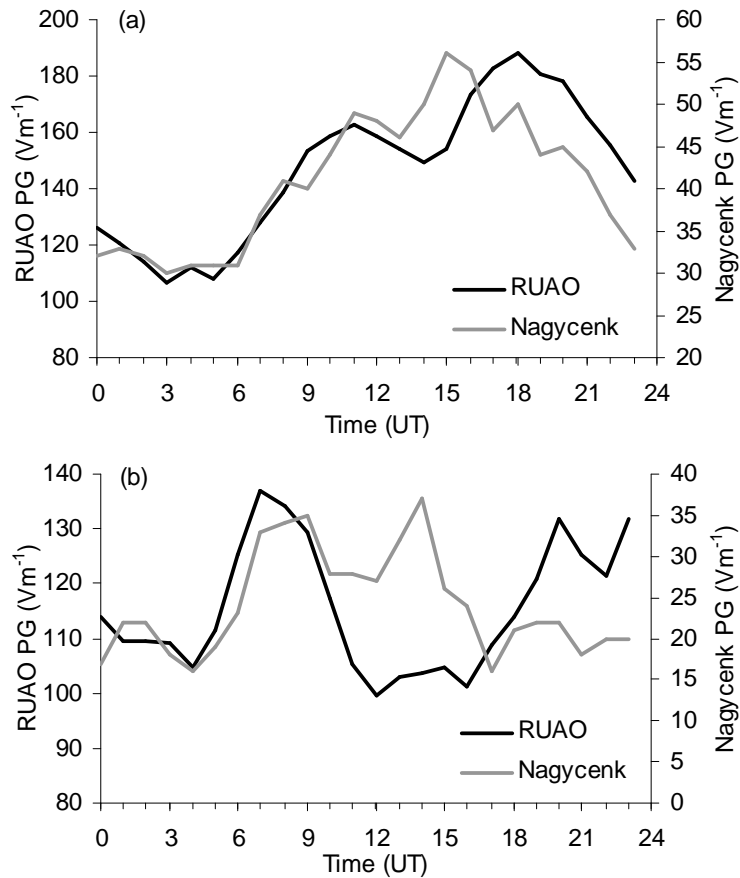


Figure 6.22 Mean fair-weather PG diurnal cycle for the RUAO and Nagycenk during (a) January 2006 and (b) August 2006.

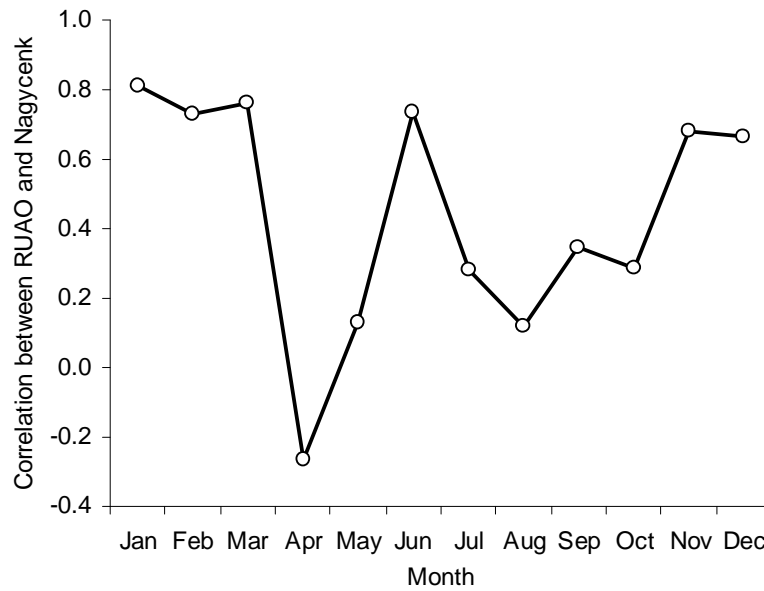


Figure 6.23 Correlation of RUAO and Nagycenk monthly mean fair-weather PG diurnal cycles. Monthly correlations averaged between July 2005 and December 2006.

Like the differences between diurnal PG for the RUAO and the Carnegie curve, a seasonal pattern between the RUAO and Nagycenk monthly mean diurnal PG is evident (Figure 6.24) with greater residuals in summer than winter. This result demonstrates the closer correlation between the two sites during the winter compared to summer as seen in Figure 6.23.

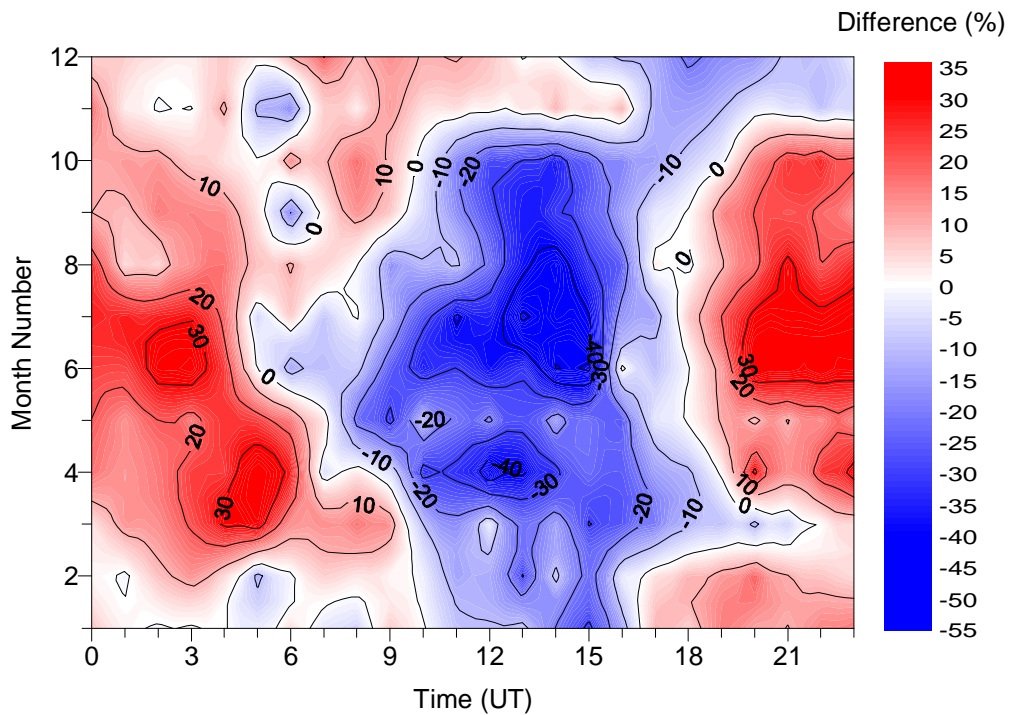


Figure 6.24 Difference in percentage RUAO and Nagycenk monthly mean fair-weather PG diurnal cycles. Monthly differences for each hour averaged between July 2005 and December 2006.

A comparison between the RUAO, Nagycenk and Chilbolton Observatory mean fair-weather PG diurnal cycle during November 2006 is shown in Figure 6.25. During this time, all three sites correlate closely with each other, although as discussed in the previous section, it is only the times between approximately 16-04UT that also show a similar close association with the Carnegie curve during November 2006. Outside of this time, the close association between the three sites is expected to be due more to similar local effects (Nagycenk is only 1hour 11mins East of the RUAO) than each being affected by a common global signal.

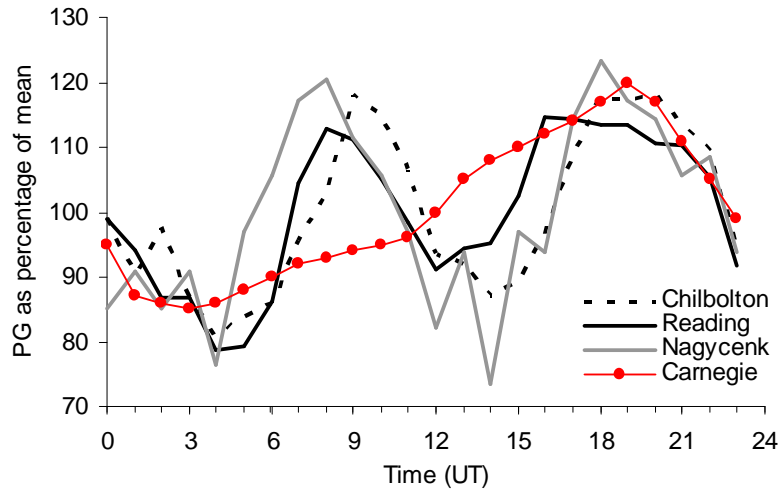


Figure 6.25 Mean fair-weather PG diurnal variation for the RUAO, Nagycenk and Chilbolton Observatory during November 2006, along with the standard Carnegie curve. Values are shown as a percentage of their respective means.

Although the correlation between the RUAO and Nagycenk is low during August 2006, it can be seen that a similarity in variability does exist between 0-10UT. Märcz and Harrison (2003) identified that the dawn hours (0-4UT) in the Nagycenk PG record were most likely to be globally representative, a finding also valid for the RUAO data. Therefore, a comparison of an hourly mean PG value during the dawn (i.e. 03UT, which is the mean PG between 03-04UT) for each fair-weather day may give a positive correlation during all seasons on account of similar global variations at timescales greater than one day (although differences between the value of PG at 03UT for the two sites relative to the daily mean does appear to still have a seasonal dependence, seen in Figure 6.24). The correlation between 03UT mean fair-weather PG for the RUAO and Nagycenk is shown in Figure 6.26a. From this it is demonstrated that a significant correlation exists between fair-weather PG at the RUAO and Nagycenk at 03UT during July 2005 to December 2007. Assuming PG variability during 03UT was not significantly influenced by coincident local sources of variability during this time, the strong correlation further suggests a common global source for the magnitude of PG during the early morning, not just for the diurnal variability, despite an observed seasonal difference during this time.

A time plot of daily RUAO and Nagycenk 03UT fair-weather PG is shown in Figure 6.26b, smoothed over 10 days to more easily identify seasonal trends. From this, a common seasonal cycle is observed, with the highest PG occurring during winter, and lowest in summer. If the statistically significant positive correlation between 03UT PG was due to global circuit variation alone, then this seasonal variability would be expected to be that of the global electric circuit. However, Adlerman and Williams (1996) point out that aerosol

number concentration (Aitken nuclei) are highest in winter. As the PG will increase with increasing aerosol number concentration, it was suggested that for surface land sites, the seasonal cycle of PG was due more to the local concentration of Aitken nuclei than any seasonal effect of the global circuit. This suggests that the significant correlation in daily fair-weather PG at 03UT between the RUAO and Nagycenk may be due to similarities in seasonal aerosol number concentration, and not due to influences of global circuit. However, this does not affect the conclusion that PG variability during the early morning is most globally representative, rather that the day-to-day comparison in absolute PG strength during this time is influenced more by local than global affects.

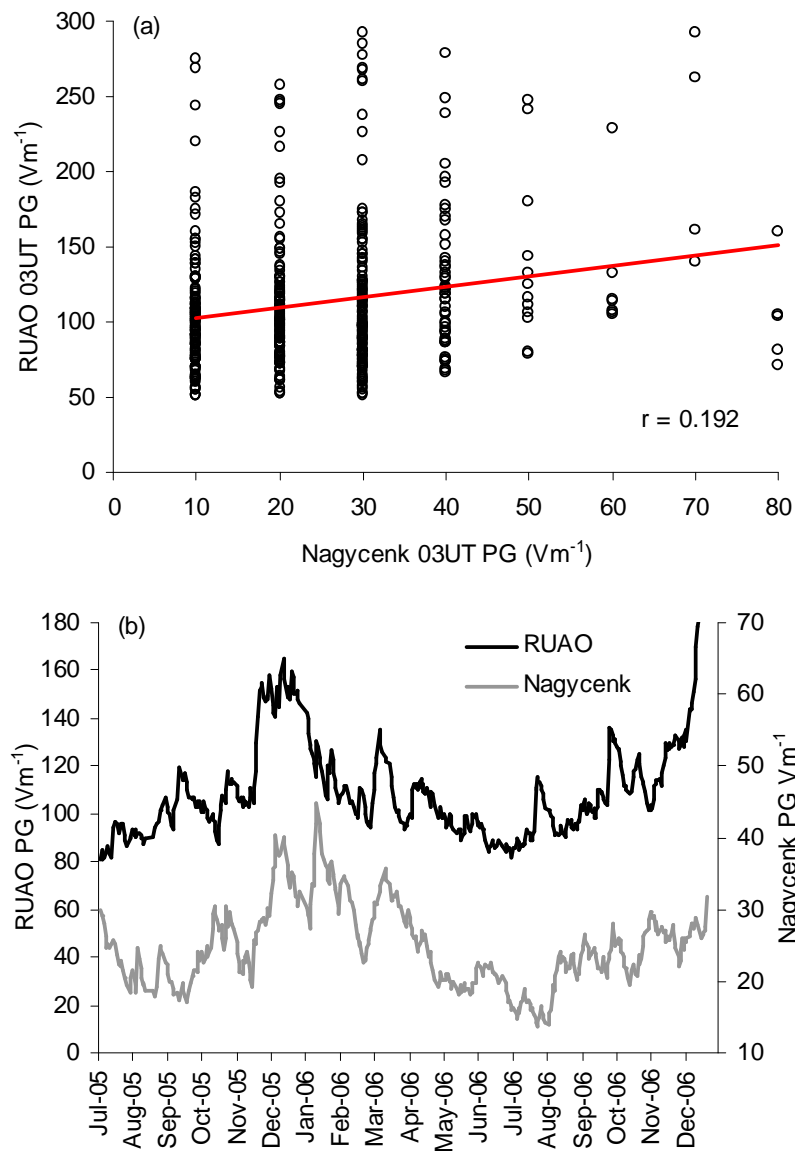


Figure 6.26 Comparison between RUAO and Nagycenk fair-weather PG at 03UT between July 2005 and December 2006, as (a) a scatter plot and (b) over time, with the latter smoothed over 10 days.

The RUAO data is currently too short to investigate long term (inter-annual) trends in PG. However, a long-term decrease in the winter (Dec-Feb) dawn (01-04UT) Nagycenk PG was reported by Märcz and Harrison (2003) throughout the analysed period 1962-2001. A similar decrease was also reported at the low-pollution site of Eskdalemuir, Scotland. Although the variation of aerosol number concentration for Nagycenk was not known during this time (and visibility used as a proxy for aerosol number concentration for Eskdalemuir), Märcz and Harrison (2003) hypothesised that the long-term decrease was global, caused by a decrease in galactic cosmic rays during this time, causing the thunderstorm-electrosphere resistance to increase, decreasing the ionospheric potential and therefore surface PG.

6.7 Discussion

Diurnal mean fair-weather PG measured at the low-pollution site of Lerwick averaged over 1968-1973 corresponds closely to the Carnegie curve, which is considered representative of the global circuit. Measurements made at the RUAO of the monthly mean fair-weather PG diurnal cycle are concluded to be globally representative throughout the day during the winter (December to January) but only during approximately 19-04UT at other times of the year, when local sources of variability are less dominant. During these times, high positive correlations between other sites such as Nagycenk in Hungary, 1370km away from the RUAO, and 47km away in Chilbolton are apparent. Similarities between these sites outside of these more globally-representative times are suggested to be due to similar times of local variability. In the case of the coastal site at Durlston Head, Dorset, strong sources of local PG variability (space-charge generated from breaking waves nearby) prevented any significant correlation between the site and the RUAO. However, even for this coastal site there was evidence for more global variability between 19-04UT, which was hypothesised to be due to the wind that brought the space-charge being weaker during this time. Although similarities between seasonal PG changes at the RUAO and Nagycenk did exist, implications for a common global source were suspect as the effect of seasonal variability in local aerosol number concentration at both sites would also provide an explanation for the similarity in observed trends.

Although the agreement between fair-weather J_C and PG monthly mean diurnal variation with the Carnegie curve is not close during the summer months at the RUAO, it has been demonstrated that globally-representative variability can be retrieved using a columnar resistance model, provided there are observations or estimations of the diurnal variation of boundary-layer height and surface parameters such as aerosol number concentration and

total conductivity. Once variability in PG due to aerosol and terrestrial ionisation rate have been accounted for by the model, the difference in RUAO PG from the Carnegie curve is similar to that found for the Lerwick PG. This demonstrates that global circuit variations are embedded within the J_c and PG variability at an urban site, but knowledge of local boundary-layer changes in aerosol number concentration, terrestrial ionisation rate and boundary-layer height are required for extraction of information on global circuit diurnal variability.

7 Conclusions and suggestions for further work

This chapter summarises the main investigations and conclusions drawn from the thesis, as a brief outline followed by more detailed descriptions separated into measurement, instrumentation and data analysis components. Suggestions for further work in the research areas investigated during this study are also provided.

7.1 Overview of studies completed

- A columnar resistance model was developed and used to separate global and local sources of variability in fair-weather monthly mean potential gradient (PG) and air-Earth conduction current density (J_C) diurnal variations measured at the RUAO.
- Two new J_C sensors have been designed and operated at the RUAO, which provide the first practical examples of an entirely new approach to measurement of J_C using the geometrical method.
- Mean diurnal variation of potential gradient, conduction current density and total air conductivity have been measured and analysed for each season.
- Atmospheric electrical parameters were found to be largely independent of more routine meteorological parameters (temperature, relative humidity and wind speed). Total air conductivity was dependent on aerosol number concentration, through the process of ion-aerosol attachment.
- Surface PG was demonstrated to be sensitive to convective cloud, fog, rain and snow (all of which produced separate PG characteristics), making PG measurement beneficial for nowcasting of these events.
- Ohm's Law applies to the atmospheric electrical parameters measured at the RUAO, for averaging timescales of several fair-weather days. The presence of space-charge or disturbed weather caused non-Ohmic variability in PG and J_C at timescales of minutes.
- A spectral "window" was identified where diurnal variability in surface PG and J_C measurements were most likely to be dominated by global sources. The duration

of this window ranged from 0-4UT for both parameters during summer, to all day during the winter for J_C and all except for 9-11UT in the case of PG, when local sources dominated.

- Based on modelled sensitivities of surface J_C and PG to the aerosol number concentration and ionisation rate profiles, a shallow boundary layer was found to be most favourable for global circuit monitoring using J_C , with a deep, uniformly varying boundary layer preferred for PG.

7.2 Summary of measurement findings

Atmosphere electrical instrumentation

The passive wire and Programmable Ion Mobility Spectrometer (PIMS) are instruments that have already been proven capable of measuring the PG and σ_T respectively before the commencement of this study (Barlow, 1999 and Aplin, 2000). Once calibrated using the absolute values of PG from the passive wire, the commercially-purchased field mill was reliable under all atmospheric conditions, and showed high levels of accuracy, resolution and thermal stability. Values of small ion conductivity from the PIMS compared well with those found using a new, absolute method of σ_T determination using the passive wire.

The Air-Earth Current Pyramid (AECF) system, and the improved compact version, the Geometrical Displacement and Conduction Current Sensor (GDACCS) provide the first practical examples of an entirely new approach to measurement of the air-Earth current density using the geometrical method. The GDACCS instrument provides a low maintenance, reliable method for continuous measurements of the conduction current density and displacement current density. It can be installed at the surface with little site preparation and no assumptions about the local air conductivity are required. The absolute accuracy of the AECF and GDACCS J_C measurements are 0.11pAm^{-2} and 0.20pAm^{-2} respectively.

Measurement of atmospheric electrical parameters

A climatology of atmospheric electrical parameters at the RUAO has been presented for 2006. Diurnal cycles of fair-weather PG, J_C and σ_T for annual and seasonal timescales have been produced, all of which are likely to be influenced by either local surface, columnar or global meteorological variations.

Variability in PG was statistically demonstrated to be independent of dry-bulb temperature, relative humidity, wind speed and aerosol mass concentration when considered in isolation. J_C was also independent of the standard meteorological parameters except for a negative correlation with mean wind speed. Total air conductivity σ_T was independent of all meteorological parameters except low values of aerosol mass concentration.

It is the pronounced diurnal variation of aerosol number concentration (and to a lesser extent, terrestrial ionisation rate) due to convective boundary layer height evolution that was considered to be the main cause of the total conductivity diurnal cycle. The dominant source of variability in total conductivity was small ion number concentration, not mobility. As PG was found to be significantly proportional to σ_T , this local effect also indirectly contributes to the diurnal variation of PG. The diurnal variation of J_C was due to a combination of columnar and global effects.

During disturbed weather, the PG varied greatly (by an order of magnitude) due to the overhead passage of convective cloud, with precipitation also producing weaker changes. The presence of fog increased PG to approximately 400% of fair-weather values and increased the variability. However, there was negligible change in J_C during fog compared to fair-weather.

7.3 Summary of R_C model

A fair-weather columnar resistance (R_C) model has been produced using theoretical assumptions on the interaction of cosmic and terrestrial ionisation, small ions, aerosol and the atmospheric vertical structure. Once R_C was known, the air-Earth conduction current density (J_C), potential gradient (PG) and total air conductivity (σ_T) at 1m can be calculated for a given value of ionospheric potential (V_i). The model ionisation rate and conductivity profiles are in good agreement with observed profiles. This model allows quantitative assessment of the influence of the aerosol, ionisation and temperature profiles on the surface measurements of J_C , PG and σ_T . By modifying the profiles that vary according to the evolution of the boundary layer, the relative contribution of local and global effects on the atmospheric electrical observations at the surface can also be investigated.

7.4 Discussion of applicability of Ohm's Law

It has been demonstrated that significant correlations exist between five-minute mean surface measurements of J_C and PG (for constant σ_T) as well as PG and σ_T (for constant J_C), which were in accordance to that expected by Ohm's Law. The close correlation

between air conductivity, small ion and aerosol number concentrations demonstrated that the modulation of ion number concentration by aerosol attachment was the dominant source of variability in surface air conductivity at the RUAO. Despite Ohm's Law being valid on average over one month, deviation from the Ohmic assumptions were regularly observed at higher frequencies; causing scatter throughout the monthly data about the otherwise linear relationships. The reason for these times of non-Ohmic correspondence in the electrical parameters is considered to be the presence of space charge (ρ_{SC}). Space charge would impose an electrostatic field in addition to that generated by J_C and σ_T through Ohm's Law which would perturb the PG from its Ohmic state. Additionally, any turbulent transfer of space charge to the J_C sensor would constitute a turbulent current density (J_T) which would be indistinguishable from the Ohmic conduction current density, J_C . Ohm's Law is therefore considered to be fulfilled for long averaging timescales (order days) although not for timescales of minutes, where perturbations of otherwise Ohmic PG and J_C due to space charge are important.

7.5 Insights into the global circuit

Atmospheric conditions required for global circuit monitoring

Monitoring of variability in the global circuit from surface measurements of PG and J_C in an urban environment are usually obscured by local sources of variability. The dominant source of local variability is aerosol number concentration, both at the surface and in the atmospheric column. Ionisation rate changes also contribute to surface electrical variability, but to a lesser extent than aerosol.

Both PG and J_C measured at the surface will respond to changes in the global circuit intensity through a change in ionospheric potential. However, the criteria for these two surface parameters to be used for global circuit monitoring is different. For shallow ($\sim 500\text{m}$) boundary layers, J_C will be more globally representative than surface PG as any changes in aerosol number concentration will be of small vertical extent compared to the entire atmospheric column. As J_C will vary by R_C , this variation will be small for the shallow boundary layer. However, as PG will also vary according to the total conductivity immediately surrounding the sensor, it will be more susceptible to the surface aerosol variability, irrespective of boundary layer height.

For cases when σ_T and R_C have similar relative variability, such as when aerosol number concentration varies uniformly with height over a deep boundary layer (which determines the majority of columnar resistance), PG will be more globally representative than J_C . This

is due to the tendency for a cancellation of the local and columnar sources of PG variability, which act in the opposite sense.

Spectral “window” on global circuit variability

It is apparent from surface PG and J_C measurements made both at the RUAO and other sites that there are time intervals when variability from global sources is most likely to dominate over local effects. These spectral “windows” on the global circuit are identified by the monthly mean diurnal variations; an averaging time long enough for the Carnegie curve to adequately represent diurnal variation of the global circuit. For mean diurnal timescales of all seasons, the early morning (~0-4LT) offered atmospheric conditions most favourable for detection of the global circuit in PG and J_C measurements. The reduced diurnal variability of aerosol number concentration and terrestrial ionisation rate profiles during the winter allowed the global component of PG and J_C variability to dominate over local effects for a greater extent of the day compared to other seasons. The seasonal variation in aerosol number concentration over urban sites prevented an unambiguous assessment of seasonal variability of the global circuit, so only information on the diurnal cycle is currently available.

For times outside the natural spectral window of global circuit monitoring, global variability can be retrieved from PG and J_C mean diurnal variation using a columnar resistance model, providing the diurnal variation of σ_T , surface aerosol concentration and boundary layer height is known.

The conditions most likely to produce globally representative surface measurements at the RUAO are summarised in Table 7.1.

Parameter	Season	Time of day	Boundary layer depth	Met. conditions
J_C	Winter	All day possible	Shallow, steady with time	Calm, no precipitation or convective cloud
	Equinox	0-4UT		
	Summer	0-4UT		
PG	Winter	All day except 7-11UT	Deep, steady with time	Calm, vertically uniform aerosol number conc., RH<100% no precipitation or convective cloud
	Equinox	0-4UT		
	Summer	0-4UT		

Table 7.1 Summary of conditions most favourable to the observation of global circuit variability in surface measurements of J_C and PG at the RUAO.

7.6 Further work

As part of the suggested research topics outlined in chapter 1, i.e. modelling, data collection and analysis with the overall objective to investigate the interaction of atmospheric electricity and climate, this present study has suggested that the following aspects would benefit from further investigation.

Modelling

A key scientific question to be answered is whether the effect of space charge (both ionic and charged aerosol) can be effectively incorporated in the vertical profile model. The departure from an otherwise fair-weather model would allow modelling of surface atmospheric electrical parameters during disturbed weather, and quantitatively investigate the influence of space charge and turbulent current density on surface PG and J_C , allowing the observed non-Carnegie diurnal variations to be replicated. A coupled boundary layer-atmospheric electrical model that simulates convectively-driven changes to the aerosol and ionisation rate profiles would allow more accurate determination of surface/columnar sources of J_C and PG variability. By modelling and compensating for these local effects, including space charge, it may be possible to retrieve global signals from polluted sites such as the RUAO on a daily basis during all seasons, not just from fair-weather monthly means as demonstrated by this study.

Instrumentation

A focus of future instrumentation development could be investigation of the offset observed in the current collected by the electrodes of air-Earth current density measurements, which requires an offset correction before the magnitude of current density can be found. This offset is expected to be largely due to either a constant voltage offset from contact potentials within the instrument, or a persistent leakage current. Modifications to the instrument to reduce the effect of both would be advantageous. Further investigation into the prevention of spider's webs on the J_C sensors would be beneficial for long term continuous measurement. As identified in Table 7.1, it is the winter when global variations are most likely to occur in RUAO PG and J_C measurements, so these sensors must be capable of continuous measurement during cold, moist conditions.

An instrument capable of continuously measuring the true total conductivity (not just the small ion component as measured by the PIMS) would be a useful addition to the RUAO instrument suite, as well as continuous measurement of space charge density. With such measurements, it would be possible to quantify the Ohmic fulfilment in terms of absolute values, not just significant correlations.

Observations

Measurement of atmospheric electrical vertical profiles (not just surface measurements) would be useful for model accuracy assessment and development, including the possibility of directly determining the columnar resistance (and therefore ionospheric potential using measured J_C). This will be possible if inexpensive, balloon-borne atmospheric electrical sensors capable of operating in the conditions expected during the ascent (extreme cold, high and low humidity, cloud etc) are developed.

Continuous, long term measurements of PG and J_C at a low-pollution site would offer a useful comparison to those of the RUAO, and may serve as a reference source for “real-time” variability of the global circuit, without the need to average over several days to be confident of a Carnegie-like diurnal cycle. Using times of J_C or PG correlation between two clean-air sites (preferably displaced by many degrees longitude so their local diurnal variations are not in phase) it may be possible to observe sub-diurnal variations of the global circuit. The continuation of atmospheric electrical measurements both at the RUAO and in low-pollution sites will eventually allow investigation of inter-annual and decadal changes to both local and global sources of variability; vital if the effect of climate change on the global electric circuit is to be studied.

A key benefit of atmospheric electrical measurements even when they are not giving global-circuit data, is the additional insight provided into cloud and atmospheric physical processes. More investigation into the effect of local meteorological conditions on J_C , PG and σ_T will enable a more quantitative use of atmospheric electrical measurements for meteorological research in areas such as nowcasting, aerosol studies, convective clouds and boundary-layer processes. Short-period (order minutes) variability in J_C due to the passage of convective cloud is now possible using the geometrical method, as the requirement for ~ 1000 s measurement lag using the more traditional “matching circuit” method is not required.

Appendix A

The following code was used to generate the columnar resistance model used for this thesis (although values used for the constants may vary depending on application).

```
/* This program is designed to return the columnar resistance, conduction
current, PG and total air conductivity at 1m */

/* NOTE: Requires FOUR csv files to read in - ZSA, SIR, SAC and VI data.
Assumes ZSQ=ZSA */

#include <iostream>
#include <fstream>
#include <stdlib.h>
#include <cmath>

using namespace std;

/* List of Constants */

#define pi          3.14159265 /* Pi */
#define EC          1.6e-19   /* Elementary charge C */
#define R           287.053   /* Gas constant for dry air J/K.Kg */
#define TELR       0.0065    /* Tropospheric Env. lapse rate K/m */
#define TPELR      0.0        /* Tropopausal Env. lapse rate K/m */
#define SELR       -0.0015   /* Stratospheric Env. lapse rate K/m */
#define TPZ        11000     /* Tropopausal base altitude m */
#define SZ         20000     /* Stratospheric base height m */
#define SDT        273       /* Standard temperature (for mobility) K */
#define SDP        101300    /* Standard pressure (for mobility) Pa */
#define SDPK       1.80      /* Standard positive ion mobility cm/s */
#define SDNK       2.20      /* Standard negative ion mobility cm/s */
#define K          1.38e-23  /* Boltzmann's constant J/K */
#define E          8.85e-12  /* Permittivity of free space F/m */
#define U          1.66054e-27 /* Atomic mass unit Kg */
#define g          9.81      /* Gravitational acceleration ms-2 */

/* Atmospheric properties data input */

#define GML         50        /* Geomagnetic latitude deg*/
#define ST          294       /* Surface temperature K*/
#define SP          101300    /* Surface pressure Pa*/
#define BAC         200       /* Background aerosol concentration at the
surface ppcc */
#define ZBA         10000     /* Background aerosol scale height m */
#define AR          0.05      /* Aerosol radius um */
#define PIM         147       /* Pos ionic mass amu */
#define NIM         80        /* Neg ionic mass amu */
#define MMA         29        /* Molecular mass of air amu */
#define AD          2200      /* Aerosol density Kg/m^3 */

/* Defining the vertical profile to be modelled */

#define z1          0         /* lowest limit of altitude range */
#define zh          50000    /* highest limit of altitude range */
#define dz          1         /* altitude resolution */

double suminvtemp=0.0;

#include <iostream>
#include <stdlib.h>
```

```

using namespace std;

double func(double z, unsigned int ZBL, double SAC, double SIR);

int main()
{
    fstream outfile, blfile, sacfile, sirfile, vifile;
    unsigned int ZBL;
    double SAC;
    double VI;
    double SIR;

    /* Input data part */

    sacfile.open("SAC_for_BL.csv", ios_base::in);
    blfile.open("BL_height.csv", ios_base::in);
    vifile.open("VI.csv", ios_base::in);
    sirfile.open("SIR_for_BL.csv", ios_base::in);

    if (!blfile.is_open())
    {
        cout << "Unable to open BL_height.csv" << endl;
        return 1;
    }
    outfile.open("BL_and_VI_vary_same_BL_results.csv", ios_base::out);
    if (!outfile.is_open())
    {
        cout << "BL_and_VI_vary_same_BL_results.csv" << endl;
        blfile.close();
        return 1;
    }

    blfile >> ZBL;
    sacfile >> SAC;
    sirfile >> SIR;
    vifile >> VI;

    if (blfile.eof())
    {
        cout << "Input file was empty!" << endl;
        blfile.close();
        outfile.close();
        return 1;
    }

    outfile << "Surface temperature (K)," << ST << endl;
    outfile << "Surface pressure (Pa)," << SP << endl;
    outfile << "Aerosol radius (um)," << AR << endl;
    outfile << "Background aerosol surface conc. (cm-3)," << BAC <<
endl;
    outfile << "Background aerosol scale height (m)," << ZBA << endl;
    outfile << "Geomagnetic latitude (degrees N)," << GML << endl <<
endl;

    outfile << "SAC,SIR,ZBL,VI,Rc,Jc,PGL,TCl" << endl;

    while (!blfile.eof(), !sacfile.eof(), !sirfile.eof(),
!vifile.eof())
    {

```

```

double colres = 0.;
double ndiv=(zh/dz);

double h=(zh - z1)/ndiv;

    /* Do the sum as you go in the loop, then tack
    on the trapezoidal "correction" at the end */

    double z;
for(int i = 0; i < ndiv ; i++ )
{
    z = z1 + i*h;
    if (i%2==0)
    {
        colres = colres + 2*func(z, ZBL, SAC, SIR);
    }
    else
    {
        colres= colres + 4*func(z, ZBL, SAC, SIR);
    }
}

colres = (h/3)*(colres+func(zh, ZBL, SAC, SIR)+func(z1, ZBL,
SAC, SIR));

double colrespeta=colres/(1e15);
double Jc=(VI/colres)*1e12;
double PG1=VI*(func(1, ZBL, SAC, SIR)/colres);
double TC1=(1/(func(1, ZBL, SAC, SIR)))*1e15;

    outfile << SAC << "," << SIR << "," << ZBL << "," << VI <<
    "," << colrespeta << "," << Jc << "," << PG1 << "," << TC1 << endl;
    blfile >> ZBL;
    sacfile >> SAC;
    sirfile >> SIR;
    vifile >> VI;
}

outfile.close();
blfile.close();
sacfile.close();
sirfile.close();
vifile.close();

return 0;

} /* End of integrating program */

double func(double z, unsigned int ZBL, double SAC, double SIR)
{
    double SD=SP/(R*ST);          /* Surface air density calculation*/
    double colatitude=90-GML;    /* Geomagnetic colatitude calculation*/

    if (colatitude<30)
        colatitude=30;

    if (colatitude>150)
        colatitude=150;

    colatitude=colatitude*((2*pi)/360); /* Convert to radians */

```

```

/* Ionisation formulae */

double cos4theta=pow((cos(colatitude)),4);
double Q0=(1.5+(0.533*cos4theta));
double Qa=(15+(17.778*cos4theta));
double Qmax=(93.5+(730*cos4theta));
double zmax=16+(24.889*cos4theta);
double za=6;
double sa=-za/(log(Q0/Qa));
double sb=(zmax-za)/sqrt(-log(Qa/Qmax));

double temperature, invtemp, preinvtemp, air_density, pressure,
aerosol, positive_ion_mobility, negative_ion_mobility, ionisation_rate,
positive_ion_concentration, negative_ion_concentration,
positive_conductivity, negative_conductivity, resistance, PEIAAC, NEIAAC,
PIRC, NIRC;

    if (z<=TPZ)
/* Temp calculation and logic */

    temperature = ST-(z*TELR);

    if (z>TPZ && z<SZ)

    temperature = ST-(TPZ*TELR)-((z-TPZ)*TPELR);

    if (z>=SZ)

    temperature = ST-(TPZ*TELR)-((SZ-TPZ)*TPELR) -((z-SZ)*SELR);

    if (z>z1)
    {
    invtemp=1/temperature;
    preinvtemp=suminvtemp;
    suminvtemp=preinvtemp+invtemp;
    }
    else
    suminvtemp=0.0;

    if (z>z1)
    {
    pressure=SP*exp(-(((dz*g)/R)*suminvtemp));
    }
    else
    pressure=SP;
    air_density = pressure/(R*temperature);

positive_ion_mobility = SDPK*(SDP/pressure)*sqrt(temperature/SDT);
negative_ion_mobility = SDNK*(SDP/pressure)*sqrt(temperature/SDT);

    aerosol=SAC*exp(-(z/ZBL))+BAC*exp(-(z/ZBA));

/* Cosmic ionisation calculations and logic */
    if (z<(za*1000))

    ionisation_rate=SIR*exp(-(z/ZBL))+Qa*exp(((z/1000)-za)/sa);

    if (z>=(za*1000) && z<(zmax*1000))

ionisation_rate=SIR*exp(-(z/ZBL))+Qmax*exp(-pow((((z/1000)-zmax)/sb),2));

    if (z>=(zmax*1000) && z<30000)

```

```

ionisation_rate=SIR*exp(-(z/ZBL))+Qmax*((z/1000)/zmax)*exp(-
(0.5*pow((z/1000)/zmax),2))+0.5);

    if (z>=30000)

ionisation_rate=SIR*exp(-(z/ZBL))+Qmax*(30/zmax)*exp(-
(0.5*pow((30/zmax),2))+0.5);

    double
ion_production_rate=ionisation_rate*(air_density/(SDP/(R*SDT)));

/* Equations related to resistance calculation (below) */

PEIAAC=((4*pi*(positive_ion_mobility/10000)*K*temperature*(AR/1000000))/E
C)*1000000; /* Pos effective ion aerosol attach coef */

NEIAAC=((4*pi*(negative_ion_mobility/10000)*K*temperature*(AR/1000000))/E
C)*1000000; /* Neg effective ion aerosol attach coef */

/*Equations needed for recombination coefficient calc. */

    double a=(pow((EC),2))/(6*pi*E*K*temperature);
    double cp=sqrt((8*K*temperature)/(pi*PIM*U));
    double cn=sqrt((8*K*temperature)/(pi*NIM*U));
    double lp=((8*positive_ion_mobility*1e-
4)/(3*EC))*sqrt((K*temperature*(PIM*U)*(MMA*U))/((MMA*U)+(PIM*U)));
    double lneg=((8*negative_ion_mobility*1e-
4)/(3*EC))*sqrt((K*temperature*(NIM*U)*(MMA*U))/((MMA*U)+(NIM*U)));

    if (z<40000)

        PIRC=(pi*pow((a),2)*sqrt(pow((cp),2)+pow((cn),2))*(2-
(lp/(2*a))*(1-exp(-(2*a)/lp)))-(lneg/(2*a))*(1-exp(-
((2*a)/lneg)))))*1e6+0.00000013*exp((z-47000)/47000);

    if (z>=40000)

        PIRC=0.00000013;

    if (z<40000)

        NIRC=(pi*pow((a),2)*sqrt(pow((cp),2)+pow((cn),2))*(2-
(lp/(2*a))*(1-exp(-(2*a)/lp)))-(lneg/(2*a))*(1-exp(-
((2*a)/lneg)))))*1e6+0.00000013*exp((z-47000)/47000);

    if (z>=40000)

        NIRC=0.00000013;

/* Equations related to resistance calculation (below) */

positive_ion_concentration=(PEIAAC*aerosol-
sqrt(pow((PEIAAC*aerosol),2)+4*PIRC*ion_production_rate))/(-2*PIRC);

negative_ion_concentration=(NEIAAC*aerosol-
sqrt(pow((NEIAAC*aerosol),2)+4*NIRC*ion_production_rate))/(-2*NIRC);

    positive_conductivity=EC*(positive_ion_concentration*1000000)*(posi
tive_ion_mobility/10000);

    negative_conductivity=EC*(negative_ion_concentration*1000000)*(nega
tive_ion_mobility/10000);

```

```
        resistance=(1/(positive_conductivity+negative_conductivity));  
    }  
    return resistance;  
}
```

Appendix B

This appendix details the calibrations applied to the raw voltage outputs of the sensors where required, and the duration of calibration validity.

Sensor	Duration using calibration	Calibration	Notes
JCI131 Field Mill (FM)	01/05/05-16/01/07	$PG = 387.0 \cdot V + 12$	Calibration change as field mill height moved from 2m to 3m. Negligible absolute difference between different field mills.
	17/01/07 - present	$PG = 248.5 \cdot V - 1$	
Border Plate (BP)	Throughout	$I = 10.30 \cdot V - 0.09$	
Pyramid Plate (P)	Throughout	$I = 9.60 \cdot V - 0.05$	
Corrugated Plate (CP)	12/06/06 – 29/01/07	$I = 10.30 \cdot V - 0.14$	
	30/01/07 - present	$I = 10.61 \cdot V + 0.002$	Recalibration
Flat Plate (FP)	17/07/06 – 29/01/07	$I = 14.30 \cdot V - 0.05$	
	30/01/07 - present	$I = 14.44 \cdot V - 0.04$	Recalibration

Table A1 Calibrations for the instrumentation used during this study. The raw voltage of the instrument is labelled V , in units of volts. PG (potential gradient) units are Vm^{-1} and current I is in μA . The equations used to calculate the current density components (i.e. J_c) are given in chapter 4.

References

Adamson, J., (1960). The compensation of the effects of potential-gradient variations in the measurement of the atmospheric air-earth current, *Quarterly Journal of the Royal Meteorological Society* **86** 252-258.

Adkins, C. J., (1959). Measurement of the atmospheric potential gradient on a Canadian glacier, *Quarterly Journal of the Royal Meteorological Society* **85**(363) 60-64.

Adlerman, E. J. and Williams, E. R., (1996). Seasonal variation of the global electric circuit, *Journal of Geophysical Research* **101** D23 29679-29688.

Anderson, R. V., (1969). Universal Diurnal Variations in the Air-Earth Current Density, *Journal of Geophysical Research* **74**(6) 1697-1700.

Anderson, R. V., (1967). Measurement of worldwide diurnal atmospheric electricity variations, *Monthly Weather Review* **95**(12) 899-904.

Aplin, K. L., (2000). PhD Thesis. University of Reading, UK.

Aplin, K. L. and Harrison, R. G., (2001). A self-calibrating programmable mobility spectrometer for atmospheric ion measurements, *Review of Scientific Instruments* **72**(8) 3467-3469.

Aplin, K. L. and McPheat, R. A., (2005). Absorption of infra-red radiation by atmospheric molecular cluster-ions, *Journal of Atmospheric and Solar-Terrestrial Physics* **67** 775-783.

Aplin, K. L., Harrison, R. G. and Bennett, A. J., (2005). Effect of the troposphere on surface neutron counter measurements, *Advances in Space Research* **35** 1484-1491.

Barlow, J. F., (1999). PhD Thesis. University of Reading, UK.

Bhartendu, (1971). Relation of the Atmospheric Potential Gradient with Meteorological Elements-Cross Power Spectral Analysis, *Pure and Applied Geophysics* **88**(1) 210-227.

Beccaria, G., (1775). *Della elettricite terrestre atmosferica a cielo sereno*, Turin.

- Belova, E., Kirkwood, S. and Tammet, H. (2001). The effect of magnetic substorms on near-ground atmospheric current. *Annales Geophysicae*, **18** 1623-1629.
- Bent, R. B. and Hutchinson, W. C. A., (1966). Electric space charge measurement and the electrode effect within the height of a 21 m mast, *Journal of Atmospheric and Terrestrial Physics* **28** 53-73.
- Bennett, A. J., (2004). *MSc dissertation*, University of Reading, Reading, UK.
- Bennett, A. J. and Harrison, R. G., (2006a). In situ calibration of atmospheric air conductivity instruments, *Review of Scientific Instruments* **77** 016103.
- Bennett, A. J. and Harrison, R. G., (2006b). Surface determination of the air-earth electrical current density using co-located sensors of different geometry, *Review of Scientific Instruments* **77** 066104.
- Bennett, A. J. and Harrison, R. G., (2006c). Retrieval of columnar aerosol properties by surface measurement of the air-earth current *Proc. 17th annual conference, The Aerosol Society*, London, 28th-29th March 2006.
- Bennett, A. J., and Harrison., R. G., (2007a). A simple atmospheric electrical instrument for educational use, *Advances in Geosciences*, in press.
- Bennett, A. J. and Harrison, R. G., (2007b). Atmospheric electricity in different weather conditions, *Weather*, in press.
- Blanchard, D. C., (1966). Positive Space Charge from the Sea, *Journal of the Atmospheric Sciences* **23** 507-515.
- Brazenor, T. J. and Harrison, R. G., (2005). Aerosol modulation of the optical and electrical properties of urban air, *Atmospheric Environment* **39** 5205-5212.
- Bricard, J., (1965). Action of radioactivity and of pollution upon parameters of atmospheric electricity Coroniti S.C. (ed.) *Problems of Atmospheric and Space Electricity*, Elsevier.
- Bunker, J., (1982). Sailing the Magnetic Fields: Carnegie, a Sea-Going Observatory, Plotted the Forces That Sent Compasses Awry, *Surveyor* **16**(4) 28-31.

Bürgesser, R. E., Pereyra, R. G. and Avila, E. E., (2006). Charge separation in updraft of convective regions of thunderstorm, *Geophysical Research Letters* **33** L03808.

Burke, H. K. and Few, A. A., (1978). Direct Measurements of the Atmospheric Conduction Current, *Journal of Geophysical Research* **83**(C6) 3093-3098.

Burns, G. B., Frank-Kamenetsky, A. V., Troshichev, O. A., Bering, E. A. and Reddell, B. D., (2005). Interannual consistency of bi-monthly differences in diurnal variations of the ground-level, vertical electric field, *Journal of Geophysical Research* **110** D10106.

Byrne, G. J., Benbrook, J. R. and Bering, E. A., (1993). Ground-Based Instrumentation for Measurements of Atmospheric Conduction Current and Electric Field at the South Pole, *Journal of Geophysical Research* **98**(D2) 2611-2618.

Canton, J., (1753). A Letter to the Right Honourable the Earl of Macclesfield, President of the Royal Society, concerning Some New Electrical Experiments. *Philosophical Transactions* **48**, 780-785.

Chalmers, J. A., (1967). *Atmospheric Electricity (2nd Edition)*, Pergamon Press Ltd.

Chree, C., (1919). Electric Potential Gradient and Atmospheric Opacity at Kew Observatory, Proceedings of the Royal Society of London. Series A, Containing Papers of a Mathematical and Physical Character **95**(668) 210-234.

Chubb, J. N., (1990). Two New Designs of "Field Mill" Type Fieldmeters not Requiring Earthing of Rotating Chopper, *IEEE Transactions of Industry Applications* **26**(6) 1178-1181.

Clement, C. F. and Harrison, R. G. (1991). Charge distributions on aerosols Electrostatics 1991: Invited and contributed papers From the Eighth International Conference, Held at the University of Oxford 10-12 April 1991, Edited by B. C. O'Neill, Inst. Phys. Conf. Ser. **118** 275-281.

Cobb, W. E., (1967). Evidence of a solar influence on the atmospheric electric elements at Mauna Loa Observatory, *Monthly Weather Review* **95**(12) 905-911.

Crozier W. D., (1963) Measuring Atmospheric Potential with Passive Antennas *Journal of Geophysical Research* **68**(18) 5173-5179.

De, S. S., De, B. K., Adhikari, S. K., Sarkar, S. K., Bera, R., Guha, A. and Mandal, P. K., (2006). A report on some specific features of the atmospheric electric potential gradient in Kolkata, *Indian journal of physics and proceedings of the Indian Association for the Cultivation of Science* **80**(2) 167-172.

Del Guasta, M., (2002). Daily cycles in urban aerosols observed in Florence (Italy) by means of an automatic 532–1064nm LIDAR *Atmospheric Environment* **36** 2853-2865.

Dhanorkar, S. and Kamra, A. K., (1997). Calculation of electrical conductivity from ion-aerosol balance equations, *Journal of Geophysical Research* **102**(D25) 30,147-30,159.

Dolezalek, H., (1978). The application of atmospheric electricity concepts and methods to other parts of meteorology, *World Meteorological Organisation Technical Note* **162** 130pp.

Dolezalek, H., (1972). Discussion of the Fundamental Problem of Atmospheric Electricity, *Pure and Applied Geophysics* **100** 8-43.

Dupont, E., Menut, L., Carissimo, B., Pelon, J. and Flamant, P., (1999). Comparison between the atmospheric boundary layer in Paris and its rural suburbs during the ECLAP experiment. *Atmospheric Environment* **33** 979-994.

Duykerke, P. G., (1991). Radiation Fog: A Comparison of Model Simulation with Detailed Observations, *Monthly Weather Review* **119** 324-341.

Everett, J. D., (1868). Results of observations of atmospheric electricity at Kew Observatory, and at Kings College, Windsor, Nova Scotia *Phil. Trans. Roy. Soc. Lond. A.* **158**, 347-361.

Fisher, R. A., (1922). On the interpretation of χ^2 from contingency tables, and the calculation of P", *Journal of the Royal Statistical Society* **85**(1) 87-94.

Fleming, J. A., (1949). *Physics of the Earth VIII - Terrestrial Magnetism and Electricity*, Dover publications, New York.

Füllekrug, M., (2004). The contribution of intense lightning discharges to the global atmospheric electric circuit during April 1998. *Journal of Atmospheric and Solar-Terrestrial Physics* **66** 1115-1119.

Füllekrug, M., and Fraser-Smith, A. C., (1997). Global lightning and climate variability inferred from ELF magnetic field variations, *Geophysical Research Letters* **24**(19) 2411-2414.

Füllekrug, M., Fraser-Smith, A.C., Bering, E.A. and Few, A.A., (1999). On the hourly contribution of global cloud-to-ground lightning activity to the atmospheric electric field in the Antarctic during December 1992. *Journal of Atmospheric and Solar-Terrestrial Physics* **61** 745-750.

Gerdien, H., (1905a). Messungen der Dichte des vertikalen elektrische in der freien Atmosphäre bei der Ballonfahrt am 11 V 1905 *Nachrichten von der Gesellschaft der Wissenschaften zu Göttingen* **1905**, 258-270.

Gerdien, H., (1905b). Messungen der Dichte des vertikalen elektrische in der freien Atmosphäre bei der Ballonfahrt am 30 VIII 1905 *Nachrichten von der Gesellschaft der Wissenschaften zu Göttingen* **1905**, 447-458.

Gherzi, E., (1967). Atmospheric Electricity at Brébeuf College Geophysical Observatory in Montréal, Canada, *Pure and Applied Geophysics* **67**(1) 239-265.

Gish, O. H., (1939). Atmospheric electricity In: Fleming, J.A. (Ed), *Terrestrial Magnetism and Electricity*. Dover, New York.

Gish, O. H., (1944). Evaluation and interpretation of the columnar resistance of the atmosphere, *Terrestrial Magnetism and Atmospheric Electricity* **36** 159-160.

Gringel, W., (1978). Untersuchungen zur elektrischen Luftleitfähigkeit unter Berücksichtigung der Sonnenaktivität und der Aerosolteilchenkonzentration bis 35km Höhe, Dissertation, Universität Tübingen, FRG.

Gringel, W., Hofmann, D.J., Rosen, J. M. (1983). Measurements of mobility, small ion recombination and aerosol attachment coefficients to 33km, unpublished manuscript.

Gringel, W., Leidel, J. and Mülheisen, R., (1978). The air-earth current density at the water surface and in the free atmosphere above the ocean *Meteor Forschungsergebn. Reihe B* **13** 41-52.

Gringel, W., Rosen, J. M. and Hofmann, D. J., (1986). *The Earth's Electrical Environment*, Ch. 12, Studies in Geophysics. National Academy Press, U. S. A.

Gunn, R., (1954). Diffusion charging of atmospheric droplets by ions and the resulting combination coefficients *Journal of Meteorology* **11** 339-347.

Gunn, R., (1955). The statistical electrification of aerosols by ionic diffusion *J. Colloid Sci* **10** 107-119.

Gunn, R., (1964). The Secular Increase of the World-Wide Fine Particle Pollution, *Journal of the Atmospheric Sciences* **21** 168-180.

Hamilton, R. A., (1969). Air-earth current measurements, *Journal of Atmospheric and Terrestrial Physics* **31** 207-210.

Harrison, H., (2006a). Atmospheric electric fields at the Kennedy Space Center, 1997-2005: No evidence for effects of global warming or modulation by galactic cosmic rays, *Geophysical Research Letters* **33** L10814.

Harrison, R. G., (1992). *PhD Thesis*, Imperial College, London, UK.

Harrison, R. G., (1995). A Portable Picoammeter for atmospheric electrical use *Inst. Phys Conf Ser.* No 143: Section 7 223. Paper presented at 9th Int. Conf on Electrostatics, York, 2-5 April 1995.

Harrison R. G., (1997a) An antenna electrometer system for atmospheric electrical measurements *Rev. Sci. Inst.* **68**(3) 1599-1603.

Harrison, R. G., (1997b). A noise-rejecting current amplifier for surface atmospheric ion flux measurements, *Review of Scientific Instruments* **68**(9) 3563-3565.

Harrison, R. G., (2002). Twentieth century secular decrease in the atmospheric electric circuit *Geophysical Research Letters* **29**(14) DOI 10.1029/2002GL014878.

Harrison, R. G., (2003). Twentieth-century atmospheric electrical measurements at the observatories of Kew, Eskdalemuir and Lerwick, *Weather* **58**(1) 11-19.

Harrison, R. G., (2004a) *Institute of Physics Conference Series* **178**(7) 337.

Harrison, R. G., (2004b). Long-range correlations in measurements of the global atmospheric electric circuit, *Journal of Atmospheric and Solar-Terrestrial Physics* **66** 1127-1133.

Harrison, R. G., (2004c). The global atmospheric electrical circuit and climate, *Surveys in Geophysics* **25** 441-484.

Harrison, R. G., (2005a). Meteorological radiosonde interface for atmospheric ion production rate measurements *Review of Scientific Instruments* **76**, 126111
doi:10.1063/1.2149005.

Harrison, R. G., (2005b). Columnar resistance changes in urban air, *Journal of Atmospheric and Solar-Terrestrial Physics* **67** 763-773.

Harrison, R. G., (2006b). Urban smoke concentrations at Kew, London, 1898-2004, *Atmospheric Environment* **40** 3327-3332.

Harrison, R. G. and Aplin, K. L., (2003). Nineteenth century Parisian smoke variations inferred from Eiffel Tower atmospheric electrical observations, *Atmospheric Environment* **37** 5319-5324.

Harrison, R. G. and Aplin, K. L., (2007). Water vapour changes and atmospheric cluster ions, *Atmospheric Research* doi: 10.1016/j.atmosres.2006.12.006.

Harrison, R. G. and Bennett, A. J., (2007a). Cosmic ray and air conductivity profiles retrieved from early twentieth century balloon soundings of the lower troposphere *Journal of Atmospheric and Solar-Terrestrial Physics* **69** 515-527.

Harrison, R. G. and Bennett, A. J., (2007b). Multi-station synthesis of early twentieth century surface atmospheric electricity measurements for upper tropospheric properties *Advances in Geosciences*, in press.

Harrison, R. G. and Carslaw, K. S., (2003). Ion-aerosol-cloud processes in the lower atmosphere, *Reviews of Geophysics* **41**(3) 1012.

Harrison, R. G. and Ingram, W. J., (2005). Air-earth current measurements at Kew, London, 1909-1979, *Atmospheric Research* **76**(1-4) 49-64.

- Hays, P. B. and Roble, R. G., (1979). A Quasi-Static Model of Global Atmospheric Electricity 1. The Lower Atmosphere, *Journal of Geophysical Research* **84**(A7) 3291-3305.
- Hess, V. F., (1912). Über Beobachtungen der durchdringenden Strahlung bei sieben Freiballonfahrten *Phys.Zeitschr.* 13 1084.
- Hoppel, W., (1967). Theory of the electrode effect *Journal of Atmospheric and Terrestrial Physics* **29** 709-721.
- Hoppel, W., Anderson, R. V. and Willett, J. C., (1986). *The Earth's Electrical Environment*, Ch. 11, Studies in Geophysics. National Academy Press, U. S. A.
- Hörrack, U., Iher, H., Luts, A., Salm, J. and Tammet, H., (1994). Mobility spectrum of air ions at Tahkuse Observatory *Journal of Geophysical Research* **99**(D5) 10697-10700.
- Hörrack, U., Salm, J. and Tammet, H., (2000). Statistical characterization of air ion mobility spectra at Tahkuse Observatory: Classification of air ions *Journal of Geophysical Research* **105**(D7) 9291-9302.
- Israelsson, S., (1993). The effects of wind and evaporation on space charge formation at the ground, *Journal of Atmospheric and Terrestrial Physics* **56**(1) 1-8.
- Israelsson, S., (1978). On the Conception 'Fair Weather Condition' in Atmospheric Electricity, *Pure and Applied Geophysics* **116** 149-158.
- Israelsson, S. and Oluwafemi, C., (1975). Power and cross-power spectral studies of electric parameters under fair-weather conditions in the atmospheric surface layer, *Boundary-Layer Meteorology* **9** 21-32.
- Israelsson, S. and Tammet, H., (2001). Variation of fair weather atmospheric electricity at Marsta Observatory, Sweden, 1993-1998, *Journal of Atmospheric and Solar-Terrestrial Physics* **63** 1693-1703.
- Kamra, A. K., Deshpande, C. G. and Gopalakrishnan, V., (1994). Challenge to the assumption of the unitary diurnal variation of the atmospheric electric field based on

observations in the Indian Ocean, Bay of Bengal, and Arabian Sea, *Journal of Geophysical Research* **99**(D10) 21043-21050.

Kasemir, H. W., (1951). An apparatus for simultaneous registration of potential gradient and air-earth current (description and first results), *Journal of Atmospheric and Terrestrial Physics* **2** 32-37.

Kasemir, H. W., (1955). Measurement of the air-earth current density. *Wentworth Conf.*, 91-95.

Kasemir, H. W., (1972). Atmospheric Electric Measurements in the Arctic and Antarctic, *Pure and Applied Geophysics* **100** 70-80.

Kasemir, H. W., (1977). Theoretical problems of the global atmospheric electric circuit. In *Electrical Processes in Atmospheres*, H. Dolezalek and R. Reiter, eds., Dr. Dietrich Steinkopff Verlag, Darmstadt, 423-439.

Kataoka, T., Yunoki, E., Shimizu, M., Mori, T., Tsukamoto, O., Ohhashi, Y., Sahashi, K., Maitani, T., Miyashita, K., Fujikawa, Y. and Kudo, A., (1998). Diurnal variation in radon concentration and mixing-layer depths, *Boundary-Layer Meteorology* **89**(2) 225-250.

Krumm, H., (1962). Der weltzeitliche Tagesgang der Gewitterhäufigkeit, *Zeitschrift für Geophysik* **28** 85-104.

Latha, K. M. and Highwood, E. J., (2006). Studies on particulate matter (PM₁₀) and its precursors over urban environment of Reading, UK, *Journal of Quantitative Spectroscopy and Radiative Transfer* **101** 367-379.

Lomb, N. R., (1976). Least-squares frequency analysis of unequally spaced data *Astrophys Space Sci* **39** 447-462.

Mani, A. and Huddar, B. B., (1972). Studies of Surface Aerosols and their effects on Atmospheric Electric Parameters, *Pure and Applied Geophysics* **100** 154-166.

Makino, M. and Ogawa, T., (1985). Quantitative Estimation of Global Circuit, *Journal of Geophysical Research* **90**(D4) 5961-5966.

Márcz, F. and Harrison, R. G., (2005). Further signatures of long-term changes in atmospheric electrical parameters observed in Europe, *Annales Geophysicae* **23**(6) 1987-1995.

Márcz, F. and Harrison, R. G., (2003). Long-term changes in atmospheric electrical parameters observed at Nagycent (Hungary) and the UK observatories at Eskdalemuir and Kew, *Annales Geophysicae* **21** 1-8.

Mareev, E. A., Israelsson, S., Knudsen, E., Kalinin, A. V. and Novozhenov, M. M., (1996). Studies of an artificially generated electrode effect at ground level, *Annales Geophysicae* **14** 1095-1101.

Markson, R., (1976). Ionospheric Potential Variations Obtained From Aircraft Measurements of Potential Gradient, *Journal of Geophysical Research* **81**(12) 1980-1990.

Mauchly, S. J., (1921). Note on the Diurnal Variation of the Atmospheric-Electric Potential Gradient *Physic. Rev.* **18** p.161, 477.

Mauchly, S. J., (1926). Atmospheric-electric results obtained aboard the Carnegie, 1915-1921, Carnegie Institute, Washington 175(3) 197-211.

McCracken, K. G., Beer, J. and McDonald, F. B., (2004). Variations in the cosmic radiation, 1890-1986, and the solar and terrestrial implications, *Advances in Space Research* **34** 397-406.

McDaniel E. W. (1964) *Collision phenomena in ionized gases* Wiley, New York.

Mukku, V. N. R., (1984). A design for eliminating displacement currents in the air-earth current measurement, *Journal of Physics* **17**(E) 629.

Neher, H. V., (1967). Cosmic ray particles that changed from 1954 to 1958 to 1965, *Journal of Geophysical Research* **72** 1527-1539.

Nickolaenkoko, A. P., Hayakawa, M. and Sekiguchi, M., (2006). Variations in global thunderstorm activity inferred from the OTD records, *Geophysical Research Letters* **33** L06823.

O'Connor, W. P., (1976). Seasonal Changes in Diurnal Variation of Potential Gradient at Fargo, North Dakota, *Pure and Applied Geophysics* 114 933-943.

Ogawa, T., (1985). Fair-Weather Electricity, *Journal of Geophysical Research* **90**(D4) 5951-5960.

Oluwafemi, C. O., Ungethüm, E., Israelsson, S., Knudsen, E. and Hultberg, A., (1975). On the influence of eddy-motion on air-earth current density, *Atmospheric Environment* **9** 673-681.

Pruppacher, H. R. and Klett, J. D. (1997) *Microphysics of Clouds and Precipitation*. Kluwer Academic Publishers.

Price, C. and Melnikov, A., (2004). Diurnal, seasonal and inter-annual variations in the Schumann resonance parameters, *Journal of Atmospheric and Solar-Terrestrial Physics* **66** 1179-1185.

Reddell, B. D., Benbrook, J. R., Bering, E.A., Cleary, E. N. and Few, A. A., (2004). Seasonal variations of atmospheric electricity measured at Amundsen-Scott South Pole station, *Journal of Geophysical Research* **109** A09308.

Retalis, D. A., (1991). Study of the Air-earth Electrical Current Density in Athens, *Pure and Applied Geophysics* **136** 217-233.

Rishbeth, H., (2006). F-region links with the lower atmosphere?, *Journal of Atmospheric and Solar-Terrestrial Physics* **68** 469-478.

Roble, R. G. and Tzur, I. (1986). *The Earth's Electrical Environment*, Ch. 15, Studies in Geophysics. National Academy Press, U. S. A.

Rooney, G. G. and Claxton, B. M., (2006). Comparison of the Met Office's surface exchange scheme, MOSES, against field observations, *Quarterly Journal of the Royal Meteorological Society* **132**(615) 425-446.

Rosen, J. M., Hofmann, D. J., Gringel, W., Berlinski, J., Michnowski, S., Morita, Y., Ogawa, T. and Olson, D., (1982). Results of an International Workshop on Atmospheric Electrical Measurements, *Journal of Geophysical Research* **87**(C2) 1219-1227.

- Rosen, J. M. and Hofmann, D. J., (1981). Balloon-Borne Measurements of Electrical Conductivity, Mobility, and the Recombination Coefficient, *Journal of Geophysical Research* **86**(C8) 7406-7410.
- Rycroft, M. J., Israelsson, S. and Price, C., (2000). The global atmospheric electric circuit, solar activity and climate change, *Journal of Atmospheric and Solar-Terrestrial Physics* **62** 1563-1576.
- Sagalyn, R. C. and Faucher, G. A., (1954). Aircraft investigation of the large ion content and conductivity of the atmosphere and their relation to meteorological factors, *Journal of Atmospheric and Terrestrial Physics* **5** 253-272.
- Sagalyn, R. C. and Faucher, G. A., (1956). Space and time variations of charged nuclei and electrical conductivity of the atmosphere, *Quarterly Journal of the Royal Meteorological Society* **82** 428-445.
- Sapkota, B. K. and Varshneya, N. C., (1990). On the global atmospheric electrical circuit, *Journal of Atmospheric and Terrestrial Physics* **52**(1) 1-20.
- Scrase, F. J., (1934). Observations of atmospheric electricity at Kew Observatory, *Meteorological Office Geophysical Memoirs* **60**(3) 3-27.
- Scrase, F. J., (1933). The air-earth current at Kew Observatory, *Meteorological Office Geophysical Memoirs* **58**(1) 3-31.
- Serrano, C, Reis, A. H., Rosa, R. and Lucio, P.S., (2006). Influences of cosmic radiation, artificial radioactivity and aerosol concentration upon the fair-weather atmospheric electric field in Lisbon, *Atmospheric Research* **81** 236-249.
- Shreve, E. L., (1970). Theoretical Derivation of Atmospheric Ion Concentrations, Conductivity, Space Charge Density, Electric Field and Generation Rate from 0 to 60km, *Journal of the Atmospheric Sciences* **27** 1186-1194.
- Simpson, G.C., (1949). Atmospheric Electricity during Disturbed Weather, *Geophys. Memoirs No. 84*.
- Stull, R. B., (1988). *An Introduction to Boundary Layer Meteorology* Kluwer Academic Press.

- Stull, R. B., (2000). *Meteorology for Scientists and Engineers*, 2nd ed. Brooks/Cole.
- Takagi, M. and Kanada, M., (1972). Global Variation in the Atmospheric Electric Field, *Pure and Applied Geophysics* **100** 44-53.
- Tammet, H., Israelsson, S., Knudsen, E. and Tuomi, T. J., (1996). Effective area of a horizontal long-wire antenna collecting the atmospheric vertical current, *Journal of Geophysical Research* **101** 29671-29677.
- Thompson, S. P., (1910). *The Life of William Tomson*, Vol. I, MacMillan.
- Thomson, J. J., (1924). Recombination of gaseous ions, the chemical combination of gases and monomolecular reactions *Phil. Mag.* **47**, 337-378.
- Thompson, W., (1859). On the Necessity for incessant Recording, and for Simultaneous Observations in different Localities, to investigate Atmospheric Electricity, *29th Meeting, British Association for the Advancement of Science* (Aberdeen).
- Thomson, W., (1872). *Reprint of papers on Electrostatics and Magnetism* (Section XVI, Atmospheric Electricity). Macmillan, London.
- Tinsley, B. A. and Zhou, L. (2006). Initial results of a global circuit model with variable stratospheric and tropospheric aerosols, *Journal of Geophysical Research* **3** D16205.
- Uchikawa, K., (1972). On the Seasonal Variations of the Atmospheric Electric Elements, *Pure and Applied Geophysics* **100** 54-59.
- Usoskin I. G., Mursula, K., Solanki, S. K., Schüssler, M. and Kovaltsov, G. A., (2002). A physical reconstruction of cosmic ray intensity since 1610, *J. Geophys. Res.*, **107** (A11), 1374.
- Vitta, P. B., (1974). The effect of eddy diffusion on the atmospheric electric current, *Journal of Atmospheric and Terrestrial Physics* **36** 1277-1282.
- Watson, W. M., (1746). Observations upon So Much of Monsieur Le Monnier the Younger's Memoir, Lately Presented to the Royal Society, as Relates to the

Communicating the Electric Virtue to Non-Electrics, *Philosophical Transactions* (1683-1775) **44** 388-395.

Whipple, F. J. W., (1929). On the association of the diurnal variation of electric potential gradient in fine weather with the distribution of thunderstorms over the globe, *Quarterly Journal of the Royal Meteorological Society* **55**(229) 1-17.

Whipple, F. J. W. and Scrase, F. J., (1936). Point Discharge in the Electric Field of the Earth *Geophysical Memoirs* **68** Meteorological Office, HMSO, London.

Wilding, R. J., and Harrison, R. G., (2005). Aerosol modulation of small ion growth in coastal air, *Atmospheric Environment* **39** 5876-5883.

Williams, E. R., (1992). The Schumann Resonance: A Global Tropical Thermometer, *Science* **256** 1184-1187.

Williams, E. R. and Satori, G., (2004). Lightning, thermodynamic and hydrological comparison of the two tropical continental chimneys, *Journal of Atmospheric and Solar-Terrestrial Physics* **66** 1213-1231.

Wilson, B., (1753). A Letter to the Right Honourable the Earl of Macclesfield, President of the Royal Society, from Mr. Benjamin Wilson, F.R.S. concerning Some Electrical Experiments, Made at Paris, *Philosophical Transactions*, **48** 347-349.

Wilson, C. T. R., (1906). On the Measurement of the Earth-Air Current and on the Origin of Atmospheric Electricity, *Cambridge Proc. Phil. Soc.* **13**(6) 363-382.

Wilson C. T. R., (1960). Reminiscences of my early years. *Notes and Recollections of the Royal Society of London* **14**(2), 163-173 .

Woessner, R. H., Cobb, W. E. and Gunn, R., (1958). Simultaneous measurements of the positive and negative light-ion conductivities to 26km *Journal of Geophysical Research* **63** 171-180.